Propriétés d'écoulement de suspensions concentrées de particules de PVC et leur lien avec la physico-chimie du système

Guillaume Chatté

THÈSE DE DOCTORAT

de l'Université de recherche Paris Sciences et Lettres
PSL Research University

Préparée à l'ESPCI Paris

Flow properties of PVC-particles concentrated suspensions and their relation to the physico-chemistry of the system

Ecole doctorale n°397

PHYSIQUE ET CHIMIE DES MATERIAUX

Spécialité CHIMIE DES MATERIAUX

COMPOSITION DU JURY :

M. HEBRAUD Pascal
IPCMS – Univ. Strasbourg, Président du jury

Mme. GUAZZELLI Elisabeth
IUSTI – Univ. Aix-Marseille, Rapporteuse

Mme. LEMAIRE Elisabeth
LPMC – Univ. Nice Sophia-Antipolis, Rapporteuse

Mme. KOLB Evelyne
PMMH – ESPCI Paris, Examinatrice

M. BOQUILLON Nicolas
TARKETT, Invité

M. LEQUEUX François
SIMM – ESPCI Paris, Directeur de thèse

Mme. PANTOUSTIER Nadège
SIMM – ESPCI Paris, Co-directrice de thèse

Soutenue par Guillaume **CHATTÉ**
le 18 septembre 2017

Dirigée par **François Lequeux et Nadège Pantoustier**

ESPCI PARIS PSL

"Vivre simplement pour que les autres puissent simplement vivre"
-Mohandas Karamchand Gandhi

Acknowledgements

This PhD thesis is the outcome of the last three years of very interesting and challenging work. The work would not have been the same without the help of many people that I would like to thank.

First I would like to express my sincere gratitude to my supervisors: Guylaine Ducouret, François Lequeux and Nadège Pantoustier for helping me a lot during my researches these last three years (and a half):

Guylaine, thank you for all the rheology knowledge and know-how you transferred to me; and also for your wise advices in daily life and also in more difficult moments.

François, thank you for your guidance and your fantastic capacity to synthesize complex results. It helped me a lot to step back and guide the work in the most promising directions. Thus, discussions with you were empowering to go further in the research.

Nadège, thank you for your constant implication at any time but also for your expertise in chemistry, it helped me a lot to investigate this aspect of the problem.

I would also like to give a special thank to Annie Colin: you brought new insights on the topic and boosted investigations on related topics like for example the origin of shear thickening. You and the collaborations you enabled also helped me a lot and have enriched this work.

I want to express my gratitude to all people who welcomed me in their laboratory through collaborations: Sébastien Manneville and Brice St Michel at E.N.S. Lyon for ultrasonic coupled with rheology; Nicolas Lenoir at Placamat and Guillaume Ovarlez at L.O.F. (Bordeaux) for X-ray radiography coupled with rheology; Lydéric Bocquet, Jean Comtet, Antoine Nigues and Alessandro Siria for the A.F.M. measurements at the particle scale (E.N.S. Ulm in Paris) and Yasmina Abdesselam and Jean-François Agassant for the capillary experiments in C.E.M.E.F. (Sophia-Antipolis). I learned a lot during those collaborations and discovered by the way other approaches to rheology.

As regards to the industrial partner, I am grateful to Nicolas Boquillon who supervised me at Tarkett: thank you for the regular scientific discussions, the constant following of the PhD and also your help to build bridges between this academic work and industrial applications. I also thank you for having introduced me in the R& I center (Wiltz) as well as in different Tarkett plants. Besides, I really appreciated the freedom you gave me for conducting this research work. Moreover, such a work would not have been possible without Richard Peres and Anne-Christine Ayed who decided to fund the PhD. I express my gratitude to them for trusting me. From Tarkett, I would also offer my thanks to several people for having followed carefully the ongoing work through regular steering committees: Nicolas Boquillon, Richard Peres but also Yasmina Abdesselam, Jean-François Agassant, Diego Gourdin, Reinhold Hoff, Jean-Yves Simon. I also thank Daniel Guebel, Nicolas Hinck, Agnès Parmentier, Johnny Poncin, Alain Sonnet and Christelle Toussaint for their help in organizing my

regular visits to Tarkett R& I center. More generally, I thank all colleagues from Tarkett I met during those years.

At SIMM laboratory, I am also grateful to many people: Christian Fretigny for welcoming me in the lab during those years; Ludovic Olanier and Alexandre Lantheaume for their nice support and work in building several experimental setups for my PhD; Flore Lasaone, Mohammed Hanafi and Armand Hakopian for their help. I also thank all students, friends, and colleagues I met in SIMM for their support, help and the good atmosphere at work. It was a real pleasure to work with you. Furthermore, I thank interns who contributed partially to this work: Clément Goubault, Chloé Guilloteau and Cyprien Poirier.

Furthermore, I would like to express my heartfelt thanks to the members of the Jury who accepted to evaluate my work.

Outside the professional side, I am grateful to my friends who supported me: friends I met in school and high school but also friends I met during the years at ESPCI. Especially François Bargain, "binome", former roommate and fellow PhD student. I also thank my family, especially my brother Thibaut and my parents for supporting and helping me through the years from the very beginning until now. Finally, I am very grateful to Charlotte whose love and support whatever it happens (especially during the last months!) are always a source of energy and happiness.

Contents

1 Rheology of concentrated suspensions **5**

1.1 Non-dimensional numbers 5
1.2 Simple scaling? 6
1.3 Role of repulsive forces 8
1.3.1 Suspension stabilization 8
1.3.1.1 Electrostatic stabilization 8
1.3.1.2 Steric stabilization 9
1.3.1.3 Combining steric and electrostatic stability 10
1.3.2 Shear-thickening 10
1.3.2.1 Description 10
1.3.2.2 Order-disorder transition 11
1.3.2.3 Dilatancy 11
1.3.2.4 Hydroclustering 12
1.3.2.5 Stress-induced friction scenario 13
1.3.2.6 Tuning shear thickening 17
1.4 Role of attraction 19
1.4.1 Different attractive interactions 19
1.4.2 Tuning attractive interactions with formulation 20
1.4.3 Capillary bridges 21
1.4.4 Thixotropy and microstructure 22
1.5 Normal stress differences 23
1.6 Shear-induced particle migration 25
1.7 Beyond shear-thickening: rheology at high shear rate 27
1.8 Focus on plastisol suspensions 28
1.8.1 Formulation 28
1.8.1.1 Poly-Vinyl-Chloride (PVC) powder 28
1.8.1.2 Filler 29
1.8.1.3 Plasticizer 29
1.8.1.4 Surfactants 30
1.8.2 Ageing 30
1.8.3 Rheological behaviour 31
1.8.4 Impact of formulation on rheology 32

1.8.4.1 Surfactant . . . 32
1.8.4.2 PVC granulometry . . . 33
1.8.4.3 Water . . . 33
1.8.4.4 Dispersing liquid . . . 34
1.8.4.5 Filler effect . . . 34
1.8.5 Normal stresses difference . . . 35
1.9 Conclusion . . . 35
1.10 Summary . . . 37

2 Materials and experimental methods **39**
2.1 Characterisation of the raw materials . . . 39
2.1.1 PVC powders . . . 39
2.1.2 Surfactant on PVC 2 powder . . . 39
2.1.2.1 Identification . . . 41
2.1.2.2 Quantification . . . 42
2.1.3 Plasticizer . . . 42
2.1.4 Fillers . . . 44
2.1.5 Cornstarch . . . 47
2.2 Sample naming . . . 47
2.3 Dispersion protocole . . . 47
2.4 Surfactant-modified PVC . . . 50
2.5 Granulometry . . . 50
2.6 Plasticizer absorption value . . . 50
2.7 Rotational rheometer . . . 51
2.7.1 Used rheometers . . . 51
2.7.2 Basic of rheometry . . . 52
2.7.2.1 Cone and plate . . . 52
2.7.2.2 Plate and plate . . . 53
2.7.2.3 Couette cell . . . 53
2.8 Capillary rheometer . . . 53
2.8.1 Need for capillary rheometer . . . 53
2.8.2 Basics of capillary rheometry . . . 55
2.8.3 Commercial capillary rheometer . . . 56
2.8.3.1 Bagley pressure correction . . . 57
2.8.3.2 Mooney analysis: slip at the wall . . . 58
2.8.3.3 Weissenberg-Rabinowitsch correction for non-Newtonian fluids . . . 59
2.8.3.4 Conclusion . . . 60
2.8.4 In-house-built capillary rheometer . . . 60
2.8.4.1 Device presentation . . . 60
2.8.4.2 Results for D2 at 60% . . . 61
2.8.4.3 Results for D1 at 60% . . . 62
2.9 Ultrasonic velocimetry . . . 62

2.10 X-ray tomography . . . 63
2.11 Summary . . . 66

3 Suspension of PVC particles in a plasticizer 67
3.1 Rheological characterization of the system . . . 67
3.1.1 Linear rheology . . . 67
3.1.2 Flow curves . . . 67
3.1.3 Normal stresses differences . . . 69
3.1.4 Discontinuous shear thickening (DST) . . . 71
3.1.4.1 Stress-control sweep . . . 71
3.1.4.2 Onset stress for shear thickening . . . 71
3.1.4.3 Time-resolved data . . . 72
3.1.5 Capillary rheometer . . . 73
3.2 Origin of shear thickening . . . 74
3.2.1 Experimental . . . 75
3.2.1.1 Tuning repulsive steric interaction . . . 75
3.2.1.2 Rheology . . . 76
3.2.1.3 Substrates . . . 76
3.2.1.4 Quartz-tuning fork based Atomic Force Microscope (AFM) . . . 78
3.2.2 Results . . . 79
3.2.2.1 Nanoscale force profile . . . 79
3.2.2.2 Critical Load Friction . . . 81
3.2.3 Discussion . . . 82
3.2.4 Conclusion . . . 83
3.3 Maximum packing fraction . . . 84
3.3.1 Viscosity VS volume fraction ϕ . . . 84
3.3.2 Comparison with plasticizer absorption test . . . 85
3.3.3 Conclusion . . . 86
3.4 Discussion . . . 87
3.4.1 Impact of PVC granulometry . . . 87
3.4.2 Shear thinning region . . . 88
3.5 Ageing . . . 90
3.5.1 Quantification of viscosity increase . . . 91
3.5.2 Tuning shear thickening with swelling . . . 93
3.6 How does a shear-thickening fluid flow? . . . 94
3.6.1 Introduction . . . 94
3.6.2 Impact of gap on viscosity . . . 95
3.6.2.1 Protocol . . . 95
3.6.2.2 Results . . . 95
3.6.3 Checking slip at the wall . . . 96
3.6.4 Shear-induced particle migration? . . . 98
3.6.4.1 Materials . . . 98

3.6.4.2 Rheometry . . . 98
3.6.4.3 D1 60% in a Couette cell geometry . . . 98
3.6.4.4 D1 60% in a capillary flow . . . 100
3.6.5 Discussion . . . 101
3.6.5.1 Particle migration . . . 101
3.6.5.2 Gap dependence on viscosity . . . 104
3.7 Chapter conclusion . . . 107
3.8 Summary . . . 109

4 Impact of formulation 111
4.1 PVC suspensions . . . 111
4.1.1 Impact of different surfactants . . . 111
4.1.1.1 Experiments . . . 111
4.1.1.2 Discussion: surfactant effect . . . 115
4.1.2 Impact of water... . . . 116
4.1.2.1 ...on raw PVC powders . . . 116
4.1.2.2 ...depending on surfactant nature . . . 117
4.1.2.3 Importance of water repartition in the system . . . 118
4.1.2.4 Discussion: water effect . . . 119
4.2 Filler suspension . . . 120
4.2.1 Impact of granulometry on maximum packing fraction . . . 120
4.2.2 Rheological behaviour . . . 121
4.2.3 Impact of surfactants on rheological behaviour . . . 122
4.2.4 Impact of water . . . 124
4.3 Dispersing together PVC and filler . . . 126
4.3.1 Variation of maximum packing fraction . . . 127
4.3.1.1 Experimental results . . . 127
4.3.1.2 Filler size dependance . . . 127
4.3.1.3 Packing model description . . . 128
4.3.1.4 Application: mixing one PVC and one filler . . . 130
4.3.1.5 Mixing one PVC and two fillers . . . 131
4.3.2 Rheological behaviour . . . 134
4.3.2.1 From PVC to filler suspensions . . . 134
4.3.2.2 Adding filler . . . 135
4.3.3 Modelling viscosity of a PVC-filler dispersion . . . 136
4.3.3.1 First Model: Description . . . 137
4.3.3.2 Validity and limitations . . . 138
4.3.3.3 Second model . . . 140
4.3.3.4 Back to first rheological experiments . . . 142
4.3.3.5 Practical application . . . 142
4.3.4 Impact of surfactant on filler surface . . . 144
4.3.4.1 Rheological curves . . . 144

4.3.4.2 Impact on packing fraction 145
4.3.5 Impact of residual water 147
4.4 Chapter conclusion 147
4.5 Summary 149

5 Flow instabilities during the coating process **151**
5.1 Industrial relevance 151
5.1.1 Defect presentation 151
5.1.2 State of the art 152
5.2 Lab-scale coating machine 154
5.2.1 Presentation 154
5.2.2 Qualitative behaviour 154
5.3 Ribbing induced by normal stress differences 156
5.3.1 Description 156
5.3.2 Comparison with a dilute polymer solution 158
5.3.3 Wavelength of ribbing 159
5.3.4 Toward deposit formation 160
5.4 Deposit formation 161
5.4.1 Influence of coating speed 162
5.4.2 Critical shear rate $\dot{\gamma}_c$ 163
5.4.3 Other formulations 163
5.4.4 Correlation with rheological properties of the suspension 163
5.5 Suggested mechanism 166
5.6 Practical solutions for defects reduction or elimination 167
5.6.1 Changing coating knife position 167
5.6.2 Roughness 168
5.7 Chapter conclusion 170
5.8 Summary 170

6 General conclusion and Perspectives **171**

List of abbreviations

— ϵ_r: dielectric constant (= relative permittivity)
— $\dot{\gamma}$: shear rate ($\dot{\gamma}$ s^{-1})
— $\dot{\gamma}_c$: minimum shear rate to get a deposit on knife
— $\dot{\gamma}_{DST}$: critical volume fraction upon which DST appears
— $\dot{\gamma}_{ribbing}$: minimum shear rate to get ribbing-like instability during knife coating
— $\dot{\gamma}_{sf}$: shift factor describing the shift of shear thickening at lower shear rate upon filler particles addition
— η: viscosity (Pa.s)
— η_f: viscosity of the interstitial liquid of a suspension
— $\eta_r = \frac{\eta}{\eta_f}$: relative viscosity (suspension viscosity divided by the viscosity of the liquid medium)
— η_{sf}: shift factor describing the rise in viscosity upon filler particles addition
— ϕ: particle volume fraction
— $\phi_{\text{absorption test}}$: maximum packing fraction measured according to plasticizer absorption test
— ϕ_{CST}: ϕ at which CST appears
— ϕ_{DST}: ϕ at which DST appears
— ϕ_{Filler}: volume fraction of filler particles
— ϕ_m: ϕ at which viscosity diverges when particles are frictional
— ϕ_{PVC}: volume fraction of PVC particles
— ϕ_{RCP}: Random Close Packing jamming density (divergence of viscosity in frictionless regime)
— ϕ_{tot}: total particle volume fraction $= \phi_{PVC} + \phi_{Filler}$
— σ: shear stress (Pa)
— σ_c: onset stress for shear-thickening
— ξ: correlation length used in the non-local approach
— ξ_{PVC}: PVC fraction of total powder =$\frac{\phi_{PVC}}{\phi_{PVC}+\phi_{filler}}$.
— $\xi_{PVC}^{boundary}$: maximum PVC fraction of total powder to achieve significant increase in compacity of a filled plastisol ($\geq$ a few %) when using decanoic acid
— $\xi_{PVC,c}$: theoretical maximum PVC fraction at which the surface of PVC particles is equal to the surface of filler particles
— a: loosening effect coefficient from De Larrard model
— AFM: Atomic Force Microscopy
— b: wall effect coefficient from De Larrard model
— C14: sodium myristate
— C16: sodium palmitate

— C^*: minimum concentration of surfactant to reach powder surface coverage.
— $CaCO_3$: calcium carbonate
— CST: Continuous Shear-Thickening
— D1: suspension of PVC 1 particles dispersed in plasticizer DINCH
— D2: suspension of PVC 2 particles dispersed in plasticizer DINCH
— D50: median diameter of of a particle size distribution
— $D_{[4,3]}$: Volume or mass moment mean of a particle size distribution
— $D_{[3,2]}$: Surface area moment mean (Sauter mean diameter) of a particle size distribution
— DINCH: 1,2-Cyclohexane dicarboxylic acid diisononyl ester (plasticizer)
— DINP: DiIsoNonyl Phthalate (plasticizer)
— DOSS: Di-Octyl SulfoSuccinate
— DST: Discontinuous Shear-Thickening
— K: compaction index from De Larrard model
— L/D: length over diameter ratio for a capillary
— MRI: Magnetic Resonance Imaging
— N_1: first normal stress difference
— N_2: second normal stress difference
— NMR: Nuclear Magnetic Resonance
— PMMA: Poly(Methyl MethAcrylate)
— Pe: Peclet number
— PVC: Poly-Vinyl Chloride
— Re: Reynolds number
— RMS: Root Mean Square
— SDBS: Sodium Dodecyl Benzene Sulfonate
— SDS: Sodium Dodecyl Sulfate
— *s.e.m.*: standard error of the mean
— SEM: Scanning Electron Microscopy
— T_g: glass transition temperature

Introduction

This thesis was carried out within a partnership between the company Tarkett and SIMM lab. Tarkett is a worldwide leader of flooring and sports surface solutions. The company develops, manufactures and sells a large portfolio with products as diverse as vinyl, linoleum, wood, laminate, rubber, carpet, artificial turf and sports tracks (see Fig. 1). Their flooring solutions are widely used in many market segments like Healthcare, Education, Housing, Retail & Hospitality, Offices and Sports.

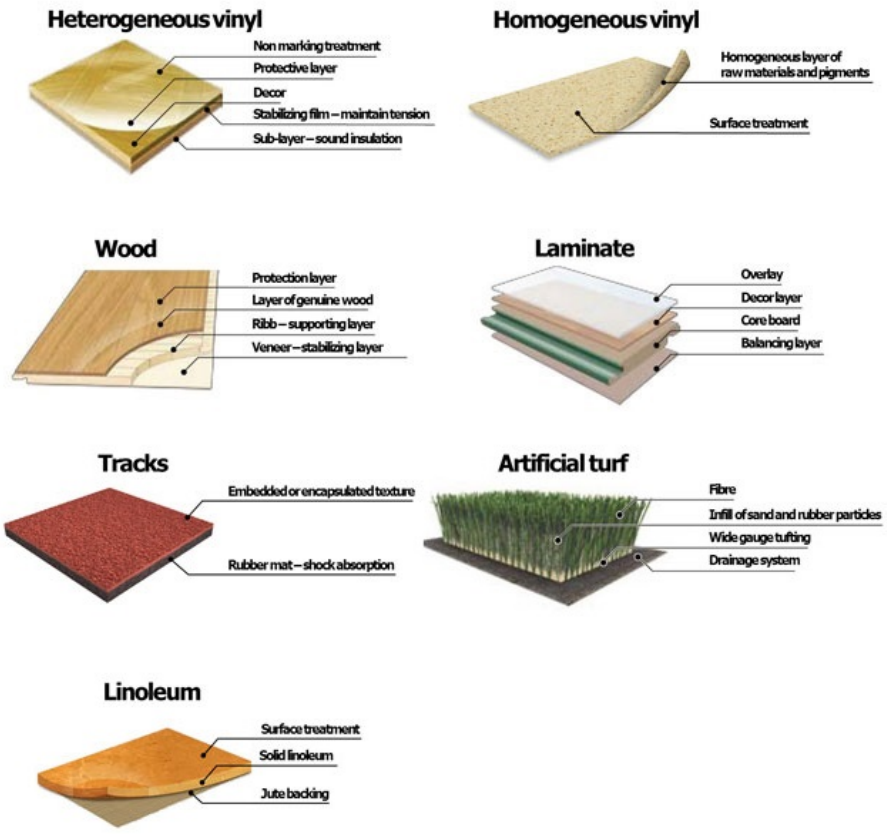

Figure 1: Portfolio of products developed and manufactured by Tarkett.

In particular, Tarkett is the worldwide leader in vinyl products. Most of them are called "heterogeneous", meaning that they are made of multiple layers. All core layers of such products are made of plastified PVC (Poly-Vinyl-Chloride) (see Fig. 2). They are obtained by coating a plastisol on a glass veil substrate. **A plastisol is the name for a concentrated suspension** basically made of:

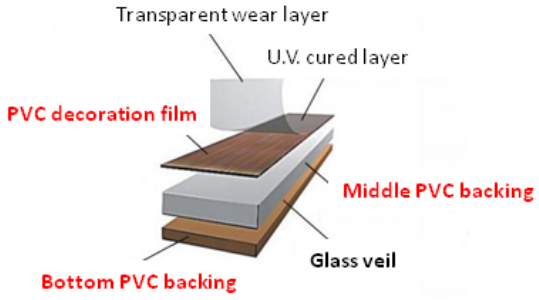

Figure 2: Different layer composing a vinyl product. Layers made from plastified PVC are core of the product.

— PVC powder (solid particles)
— Plasticizer (liquid phase with very low volatility)
— Filler powder (calcium carbonate) for some specific layers
— Some additives (stabilizers, foaming agents, surfactants...)

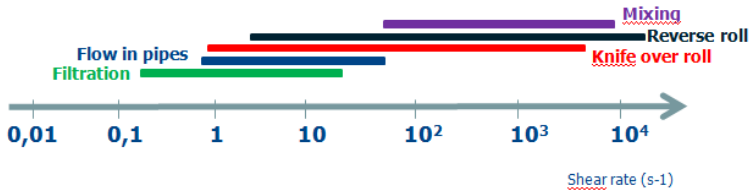

Figure 3: Ranges of shear rate encountered in different steps from the industrial process

Plastisol is industrially produced by dispersion of all components. It is usually a white viscous paste (beige color with filler) with a solid volume fraction $\phi = Vol._{solid}/Vol._{total}$ around ϕ = 60-70 %. ϕ represents the ratio between the volume of particles ($Vol._{solid}$) over the total volume of the suspension ($Vol._{total}$) . This PhD thesis is centred on the plastisol and more precisely its rheological behaviour.

Once prepared, the plastisol is in a liquid state in order to be coated on a substrate (glass veil on Fig. 2). Here, mainly knife-over-roll coating process is used. Rheological measurements of the plastisol is thus critical at each step of the process: coating (implying largest shear rates) but also mixing, filtering, pumping... (cf. Fig. 3).

After being coated on a substrate, plastisol is heated in an infra-red oven at a temperature between 140 ˚C and 180 ˚C for the gelation and fusion steps. During this high-temperature step, the plasticizer diffuses in the resin PVC causing, first, the swelling of the grains, then, their percolation and finally the interpenetration of the grains of PVC during the fusion step. After the process, the homogeneous soft material used in layers of vinyl floors is obtained (cf. Fig. 4).

We focus in this work only on the plastisol at liquid state (before heating). The system under scope is thus a concentrated suspension (paste) of PVC particles (solid phase) dispersed in a plasticizer (liquid phase). Formulation of the system can however be more complex. Surfactants are present on the surface of commercial PVC particles (residue from PVC synthesis process); Those

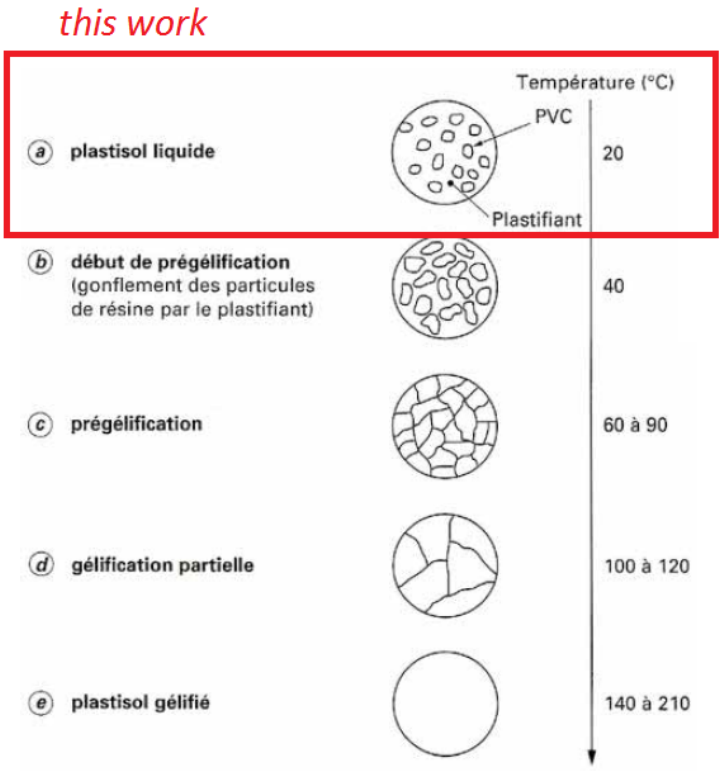

Figure 4: Gelation process: increasing temperature favours diffusion of plasticizer into the grains. At the end, a homogeneous and soft (=plasticized) material is obtained [1].

surfactants can modify interparticle interactions and their role in the rheological behaviour is not clear. Moisture content is also empirically known to influence paste rheological properties. Furthermore, filler particles ($CaCO_3$) with completely different size and shape than PVC particles can in some cases be added to the formulation, changing also dramatically paste rheological behaviour. Finally, even if the rheological behaviour is critical for the process, **there was up to now no clear understanding of the link between the formulation of the plastisol (PVC particles concentration, role of surfactant, filler content) and its rheological behaviour**. Understanding the rheological behaviour of the plastisol (and the link with the microstructure) could thus open new ways to reduce plasticizer content or to increase filler particles content while keeping a good processability.

The state of the art on the rheology of concentrated suspension is first reviewed in the first chapter (**Chapter 1**). We then focus on the literature for our specific system, namely a plastisol. **Chapter 2** deals with experimental details and information about raw materials, but also on the use of capillary rheometer in addition to standard rotational rheometry to reliably characterize viscosity up to $10^4 s^{-1}$.

In **Chapter 3**, we study a concentrated rather "simple" suspension by considering only PVC particles in plasticizer. As many concentrated suspensions, plastisol often exhibit shear-thickening behaviour. Even well characterized at the macroscale, there is still debate about its microscopic root cause. We then achieve to correlate microscopic particle interaction measurements with macroscopic rheological measurements. We further investigate possible particle migration under shear and appearance of normal stress differences. Moreover, we underline new non-local phenomena which would explain the observed influence of flow geometry on the suspension viscosity.

Given these new insights on a suspension of PVC particles in plasticizer, we focus on the impact of formulation on rheological properties in **Chapter 4**. We propose to dissociate viscosity contribution from the surfactant and viscosity contribution from PVC powder itself (role of granulometry). We then investigate the impact of filler particles on the rheological properties.

A last question arises when the coating of such a suspension is carried out at high shear rate. Flow instabilities can occur, leading to macroscopic defects. A lab-scale prototype mimicking the industrial coating step is built for studying these defects encountered in industrial processes and especially their root cause (**Chapter 5**). By varying both coating speed and gap and studying different formulations, critical parameters are highlighted.

Chapter 1

Rheology of concentrated suspensions

The system under scope, a plastisol, is a viscous concentrated suspension of PVC particles (possibly also $CaCO_3$ filler particles) dispersed in a liquid. As we focus in this thesis on its rheology and the link with formulation, we first review in the beginning of the chapter the state of the art for the rheology of concentrated suspension. The second part of the part is devoted to the literature on the specific suspension studied here: the plastisol.

1.1 Non-dimensional numbers

Suspensions cover a wide range of systems depending on the particle size, nature, shape, concentration but also on the liquid properties (viscosity, Newtonian or Non-Newtonian behaviour, chemical nature...). We focus in this work on particles dispersed in a Newtonian liquid phase. This Newtonian behaviour of plasticizer will be checked later in chapter 2.

Dynamics of particles in the liquid phase imply some hydrodynamic. Thus inertia could be a relevant parameter depending on the size and density of particles but also on liquid phase viscosity. Its role can be checked by calculating the dimensionless Reynolds number which expresses the ratio of inertia to viscous forces:

$$Re = \frac{\text{inertia forces}}{\text{viscous forces}} = \frac{\dot{\gamma} a^2 \rho}{\eta_f} \tag{1.1}$$

with a the typical radius of particle, ρ the fluid density and η_f the viscosity of interstitial fluid. In our case of PVC concentrated suspension, for a shear rate of $\dot{\gamma}$ = 1000 s^{-1}, a typical size of 1 μm and a liquid viscosity of 0.05 Pa.s (plasticizer viscosity), the Reynolds number is found to be around 10^{-8} which is far smaller than 1, corresponding to the case of Stokes flow (or laminar flow). Even with filler with largest particle size (100 μm in this work), Reynolds number would still be far smaller than 1. Thus, we neglect in the following particle inertia

Furthermore, suspensions are traditionally divided into non-Brownian suspensions and Brownian suspensions. Importance of Brownian motion can be assessed by another non-dimensional number: the Peclet number. It is the ratio of the typical time of shear flow to the typical time for Brownian motion.

$$Pe = \frac{\text{typical time of shear flow}}{\text{typical time for Brownian motion}} = \frac{6\pi\eta a^3 \dot{\gamma}}{k_b T} \tag{1.2}$$

For Pe « 1 (Brownian suspensions), the regime is dominated by Brownian motion which can largely restore equilibrium microstructure at the time scale of shear flow. For Pe » 1 (non-Brownian suspensions), the regime is dominated by hydrodynamical interactions. For non-Brownian particles, the Peclet number tends to the infinite.

In our case, $Pe \approx 250\dot{\gamma}$ (a = 1 μm, η = 0.05 Pa.s). For studied shear rate range (from $10^{-1}s^{-1}$ to $10^{4}s^{-1}$), the Peclet number is always higher than 1. Brownian motion is thus throughout this work neglected. We focus in the following on non-Brownian concentrated suspension with no inertia. It is interesting to note than our system of PVC suspension lies in the industrially ubiquitous intermediate size regime between Brownian suspensions and granular suspension.

1.2 Simple scaling?

We consider a simple suspension made of hard spheres with no interaction (except no overlapping in space). Like our suspensions, Brownian motion and inertia are neglected. Based on a recently developed framework which unveils universal laws for dense granular flow [2, 3, 4], Boyer et. al [5] shows the system can be fully described by one dimensionless viscous number I_v:

$$I_v = \frac{\eta_f \dot{\gamma}}{P^p} \tag{1.3}$$

where η_f is the fluid viscosity, $\dot{\gamma}$ the shear rate and P^p the confining pressure applied on suspension. This number is the ratio between two typical times of the system: the viscous time scale η_f/P^p and the typical time of shear $1/\dot{\gamma}$. Contacts between particles can occur especially at high volume fraction. Friction between particle is taken into account with a solid friction coefficient μ. Shear stress τ and normal pressure can be related using $\tau = \mu(I_v)P^p$.

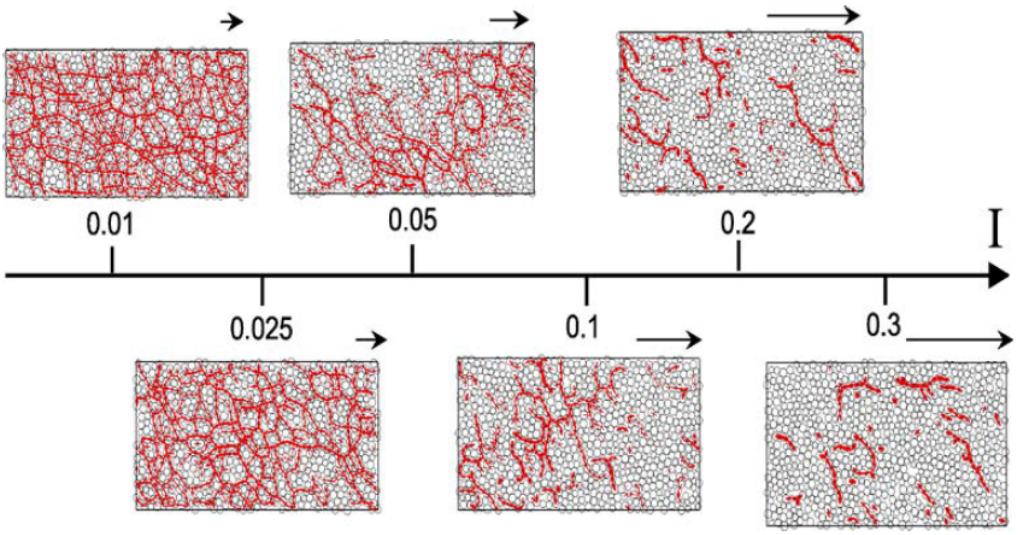

Figure 1.1: In a granular, stress can be dominated either by the contact network, i.e when particles touch and scrape (red paths), or by viscous dissipation (particles still separated by a fluid layer) [6]

I_v « 1 means that the stress is dominated by frictional contacts whereas I_v » 1 means that stresses are dominated by viscous dissipation (cf. fig 1.1). As the system is fully described by I_v, all parameters can be expressed as a function of I_v. In particular, ϕ = $\phi(I_v)$. Inverting this relation gives that I_v depends only on ϕ : $I_v = g(\phi)$.

$$\sigma = \mu(I_v)P^p = \mu(g(\phi)).\frac{\eta_f\dot{\gamma}}{I_v} = \frac{\mu(g(\phi))}{g(\phi)}.\eta_f.\dot{\gamma} \tag{1.4}$$

But, shear stress σ and shear rate $\dot{\gamma}$ are related by the following equation (η_r is the relative viscosity):

$$\sigma = \eta_r.\eta_f.\dot{\gamma} \tag{1.5}$$

Thus, identifying eq. 1.4 with eq 1.5,

$$\eta_r = \frac{\mu(g(\phi))}{g(\phi)} \tag{1.6}$$

In conclusion, one shows that for a simple suspension made of hard spheres with no interaction, viscosity depends only on ϕ and not on shear rate $\dot{\gamma}$. In particular, Boyer and collaborators [5] are able to find a description for the volume fraction dependence of viscosity:

$$\eta_s(\phi) = 1 + \frac{5}{2}\phi(1 - \frac{\phi}{\phi_{max}})^{-1} + \mu_c(\phi(\frac{\phi}{\phi_m - \phi})^2) \tag{1.7}$$

The first term comes from solvent. The second term stems from hydrodynamical interactions and the last one is due to solid contacts. The hydrodynamical contribution tends to Einstein viscosity law at low volume fraction ϕ: $\eta_r = 1 + 2.5\phi$. The contact contribution predicts the divergence of the viscosity when the volume fraction tends to the maximum volume fraction ϕ_{max} (i.e in a concentrated suspension). Einstein law is indeed limited to low volume fraction and has been extended only to semi dilute regime ($\phi \sim$ 0.1-0.15) with a quadratic term : $\eta_r = 1 + 2.5\phi + 5.2\phi^2$ [7].

Other empirical models describing $\eta = f(\phi)$ are used for concentrated suspensions like Quemada's model [8]:

$$\eta_r = (1 - \frac{\phi}{\phi_{max}})^{-2} \tag{1.8}$$

or the Krieger-Dougherty one [9]:

$$\eta_r = (1 - \frac{\phi}{\phi_{max}})^{-[\eta].\phi_{max}} \tag{1.9}$$

with $[\eta]$ is the intrinsic viscosity and is dependent on particle shape (for example, $[\eta]$ = 2.5 for spheres). ϕ_{max} is the maximum packing fraction which is experimentally determined. For monodisperse spheres, $\phi_{max} \leq 0.74$. Random close packing (RCP) gives ϕ_{max} = 0.64. Indeed ϕ_{max} can be higher using polydisperse spheres (for example,value of 0.87 for bimodal systems with large size gap [10]). All these empirical models reduce to Einstein viscosity law for ϕ/ϕ_{max} « 1.

The simple framework of an assembly of spheres without interaction leads to a constant viscosity with no shear rate dependence even at high particle concentration (Newtonian behaviour). In this

case, viscosity depends only on the ratio ϕ/ϕ_{max}.This description holds pretty well for granular suspensions, i.e. when particle size is higher than $\sim 50\ \mu m$. Nevertheless, suspensions with typical size around 1-10 μm often display a non-Newtonian behaviour, i.e. viscosity does depends on shear rate: $\eta = \eta(\phi, \dot{\gamma})$. As the range of size is in this case smaller than the granular one (close to colloidal domain), intermolecular or surface forces cannot be ignored. In the following, we consider both repulsive and attractive interactions encountered in concentrated suspensions and detail their effects on rheology.

1.3 Role of repulsive forces

Repulsive interactions are required to counterbalance inevitable attractive Van der Waals forces and obtain a stable (= well dispersed) suspension. Repulsive forces have also a role in more complex phenomena like shear-thickening.

1.3.1 Suspension stabilization

Ubiquitous Van der Waals forces are attractive interactions due to fluctuating polarization. The value depends on inter-particle distance as well as on the suspending medium characteristics and particle material (via the Hamaker constant). Such attractive interactions mean that a dispersion is naturally unstable and will be agglomerated. As for industrial applications, a stable suspension (=flowable suspension) is needed, the two main mechanisms of suspension stabilization, steric and electrostatic, will be discussed here.

1.3.1.1 Electrostatic stabilization

Suspending particles in water are often charged either due to acid/bases functions on their surfaces or adsorption of free ions (clays for example), surfactants or polyelectrolytes (cement). This charged surface leads to a double layer of counter ions to fulfil electro-neutrality (Stern layer and Debye layer). Stability comes then from the mutual repulsion of these double layers surrounding particles. This type of stabilization is basically restricted to aqueous systems as a high dielectric constant is needed to allow sufficient charge dissociation. DLVO theory enables quantification of the resulting balance between attractive Van der Waals interactions and electrostatic repulsion.

By suitably defining a effective diameter which includes the double charged layer, rheology of such electro-statically stabilized suspensions can be rationalized on that of hard spheres [12]. The thickness of this layer depends on the ionic strength which affects the suspension rheology (cf. Fig. 1.2). Adding salt decreases the Debye layer by screening charges on surfaces, resulting in less repulsion but also on lower effective volume fraction. As particle concentration is pretty high, this drop of effective volume overcomes the loss of electrostatic repulsion, explaining the drop in viscosity on Fig. 1.2. It is nonetheless a matter of balance: adding too much salt would lower again the effective volume fraction but repulsive force will be so screened that the suspension flocculates: resulting viscosity will be higher. Minimum viscosity position is highly dependant on physico-chemical characteristics of the system.

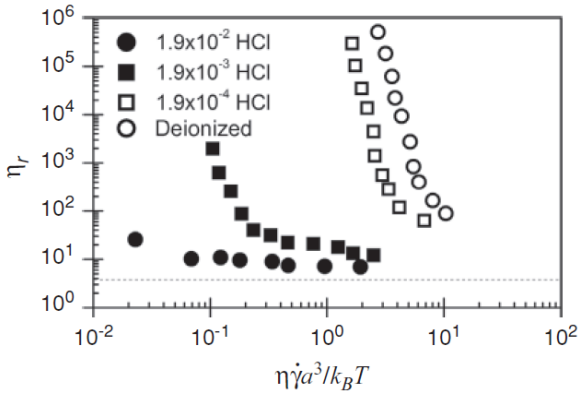

Figure 1.2: Effect of electrolyte (HCl) concentration on the relative viscosity of an electrostatically stabilized latex suspension (ϕ = 0.40, d = 110 nm), [11].

1.3.1.2 Steric stabilization

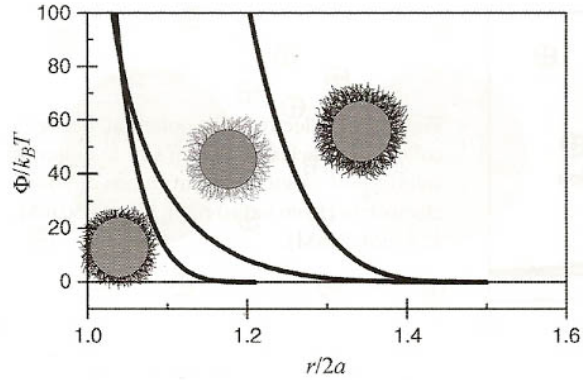

Figure 1.3: Potential of interaction due to steric repulsion between grafted polymer brushes of varying length and graft density. The thicker the layer, the more repulsive the potential of interaction [13].

Polymers or molecules can also induce inter-particle repulsion and suspension stability when they are grafted or adsorbed onto the particles. For grafted polymer brushes, the repulsive potential is more efficient if the grafting density or the length of polymer are higher (cf. Fig. 1.3) [13]. So sufficiently thick and dense brushes of polymers should be achieved for efficient stabilizing. To a first approximation, adsorbed layer of polymer can be taken in account by considering an extension of the particle volume due to the polymer layer. This scaling works for the zero shear viscosity [14] but not for the high shear limiting viscosity [15] because polymer layer may deform under stress. Thus, as for electrostatic stabilization, an optimum thickness exists because very high thickness causes too large effective volume fraction increase counterbalancing the viscosity loss by stabilization [16]. Steric repulsion potential is in most cases steeper (short range behaviour) than electrostatic[10]. It implies two mechanisms : the first is the decrease of entropy if chains begin to overlap (distance between δ and 2 δ, where δ is the thickness of the layer) ; the second is the interpenetrationnal plus compressional domain (distance between 0 and δ) [16].

For the specific case of particles dispersed in organic media (low dielectric constant), steric stabilization is of prior importance. For example, high loadings of ceramic can be easily dispersed in alcane oils thanks to efficient steric repulsion induced by polymers or surfactants at particle surface [16, 17].

1.3.1.3 Combining steric and electrostatic stability

Cementitious pastes are highly concentrated aqueous suspensions made of cement and some mineral additives (silica fume, ultrafine fly ash [18]) of many different sizes from several tens of nm to 100 μm. It is an intermediate between concentrated colloids suspension and coarse granular media. Current cementitious pastes display a yield stress which is due to flocculation induced by Van der Waals interactions that create an inter-particle contact network. To improve workability, superplasticizers are used. They achieved stabilization both by steric (side chains) and electrostatic repulsion (backbone). This electrosteric stabilization turns a flocculent state into a dispersed one and decreasing drastically low-shear viscosity and yield stress. Nowadays, the most effective superplasticizers are comb-type copolymers which consist of an anionic backbone (often polycarboxylate) and uncharged side chains. [19, 20, 18, 21, 22, 23]. Indeed, as for electrostatic stabilization, it is a matter of optimum concentration. An excess of polymer or fine colloidal particles can promote attractive depletion forces, i.e destabilizing such concentrated suspensions [19, 20]. Same trends have also been found on aqueous carbonate calcium [24, 25], aqueous kaolinite suspensions [26, 27, 28] or aqueous ceramic suspensions [29, 30].

1.3.2 Shear-thickening

Among the rich non-Newtonian rheology of concentrated suspensions, dense suspensions often exhibit shear-thickening behaviour [31], i.e. the viscosity increases with applied shear stress (cf. Fig. 1.4). Firstly observed by Freundlich and Roder [32], this phenomenon of shear-thickening has been now reported in both colloidal suspensions [33, 34, 35, 36, 37] and in non-Brownian suspensions [38, 39, 40, 41]. The phenomenon has been first reviewed by Barnes [31] and more recently by Brown and Jaeger [42].

1.3.2.1 Description

In industry, shear-thickening leads to large processing issues such as pipe fouling or clogging of spraying equipment. On the contrary, its enhanced energy dissipation makes it ideal for damping and shock-absorption applications like armours and protective clothing [43].

Depending on its intensity, a distinction is made between Continuous Shear-Thickening (CST) with a continuous viscosity increase at increasing shear rate or Discontinuous Shear-Thickening (DST) with an abrupt increase in the viscosity of the suspension at a critical shear rate (cf. Fig. 1.5). CST and DST can be observed for the same system but at different solid volume fraction: CST at moderate ϕ and DST at high ϕ. Shear thickening can be found at volume fraction as low as ϕ = 0.3 or 0.4 [5] but the higher the solid volume fraction, the steeper the shear thickening (cf. Fig. 1.4). This shear-thickening behaviour is completely reversible; once the stress is removed, the suspensions can relax and flow like any other liquid [42, 45]. A hysteresis is nevertheless in most cases observed [46, 44].

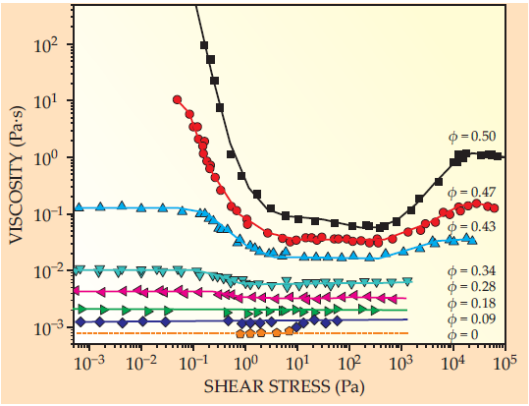

Figure 1.4: Experimental data of the viscosity of colloidal latex dispersions, as a function of applied shear stress. Shear thickening is visible for volume fraction upon 0,43.[44]

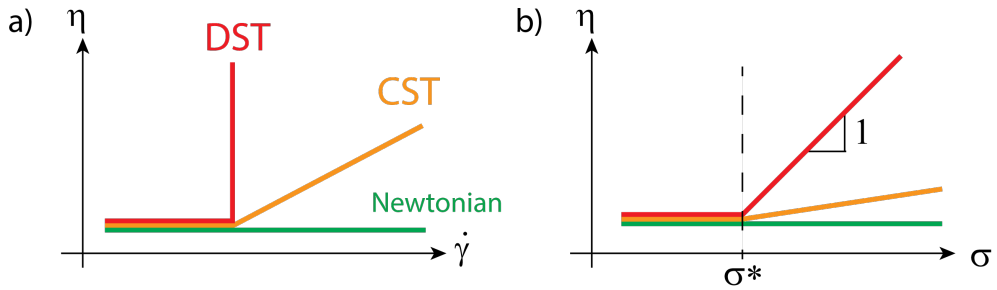

Figure 1.5: Difference between Newtonian, Continuous shear thickening (CST) and Discontinuous shear thickening (DST) when viscosity is plotted versus (a) shear rate $\dot{\gamma}$; (b) stress σ.

Different mechanisms have been suggested over time to explain experimental results: order-disorder transition at the particle scale, formation of hydroclusters upon shearing... Recently, a new framework based on friction is a promising way for underlying microscopic explanation of shear thickening. All these mechanisms are detailed below. As inertia is neglected throughout the work, shear thickening which could be induced by inertia [47] at high shear rate is not tackled here.

1.3.2.2 Order-disorder transition

This is the oldest proposed mechanism to explain shear thickening. It was first identified and developed by Hoffman [48] while he was working on suspensions of monodisperse spherical PVC particles exhibiting DST. He found that in some cases a transition to DST coincides with a transition in the microstructure from ordered layers at lower shear rates to a disordered state at higher shear rates. Nevertheless, it has been definitely shown that DST can occur without an order-disorder transition [49, 45]. Thus, this is not a required mechanism of shear-thickening but an order-disorder transition may indeed accompany shear thickening according to experimental work from Kalman and Wagner [50].

1.3.2.3 Dilatancy

Granular media have the well-known tendency to expand under flow. This behaviour is referred as dilatancy. The phenomenon is often reported along shear-thickening [51, 52] but there are two different

phenomena which have been for a long time mixed up in the literature [42]. However, dilatancy can be for example observed without any shear-thickening (in the absence of inertia) as for the case of perfectly hard spheres [5] (detailed in part 1.2). Thus the argument of dilatancy to explain DST [40, 53, 42] appears to be too general. Both dilation and shear thickening are separate consequences of frictional interactions [54]. Dilatancy requires the span of whole sample to get volume expansion whereas shear thickening can occur with only non system-spanning frictional contacts.

1.3.2.4 Hydroclustering

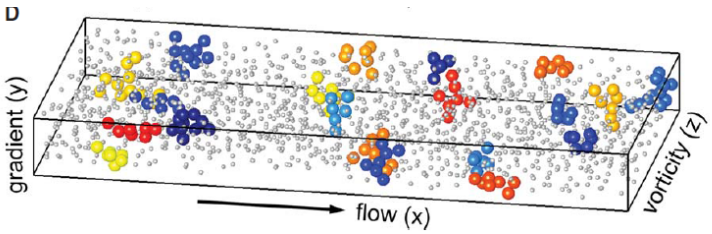

Figure 1.6: Image of a flowing concentrated suspension visualized by high-speed confocal microscope. Dynamic particle clusters (>6 particles) are represented with colors. The boundary box is 31.2 by 15.4 by 3.1 μm^3[35]

This interpretation is more recent (1990's and 2000's). During shear flow, particles are pushed against each other but a thin layer of fluid remains between them. At high shear rate, particles can be so close that lubrication forces cannot be overcome and particles stay grouped together and form particles clusters (often referred as hydroclusters, typically 2-3 particle diameters[50]). Those clusters become larger as the shear rate increases [42] and produce unwanted flow structures that increase the viscosity : the suspension shear-thickens. Besides, hydroclusters are not aggregated or coalesced particles, but rather local transient fluctuations in particle density (dynamic hydroclustering with perpetually created and destroyed clusters) organized in the compressive axis of flow. Evidences supporting this theory include rheo-optical measurements : dichroism [45], confocal microscopy [35] (cf. Fig. 1.6) and neutron scattering [50].

This mechanism describes quite well only some moderate CST (increase of viscosity 2-3 times). When normal elastohydrodynamic contact forces (cf. part 1.7) are taken into account (without solid friction) [55], model predicts steeper shear thickening but is unable to really capture DST and leads to a shear rate independent rheology for non-Brownian systems. Moreover, despite lubrication forces diverge as interparticle distance vanishes, solid contacts between particles could exist as particles are in reality not totally flat with always some roughness. There is also generally a finite slip length rather than a true no-slip boundary condition at a fluid/solid surface [56] which cuts off the divergence and enables contact to form. Eventually, experimental proves showing clusters of particles upon shearing cannot really assert if particles are really separated by a thin liquid film or if there are some contacts between them. In particular, those contacts would create friction between particles; a dissipation mechanism which is not addressed within hydroclustering theory.

1.3.2.5 Stress-induced friction scenario

Unlike hydroclusters theory, some recent works [57, 58] propose a new picture which incorporates both the role of repulsive and frictional forces into the hydrodynamic description. Shear thickening is then seen as a transition from lubricated contacts to frictional contacts. It is different from the simple description (cf. part 1.2). Here, the repulsive force between particles ensuring suspension stability is taken into account. Its strength sets a characteristic scale σ_c of stress σ . Removing repulsion in this stress-induced friction allows recovering the simple scaling detailed in part 1.2 in which contacts are present in dense granular formulation.

At low particle pressure, i.e for $\sigma < \sigma_c$ the particles do not touch, the contacts are lubricated (frictionless state), and the viscosity of the suspension diverges at random close packing ϕ_{rcp}. At high pressure i.e for $\sigma > \sigma_c$, the repulsive interactions that prevent the contact are overcome, the particles are now in frictional interaction. The viscosity of the suspension now diverges at a jamming density $\phi_{\text{m}} < \phi_{\text{rcp}}$ due to frictional contacts. Jamming density is indeed sensitive to interparticle friction coefficient: the higher the friction coefficient μ between particles, the lower ϕ_{m}.

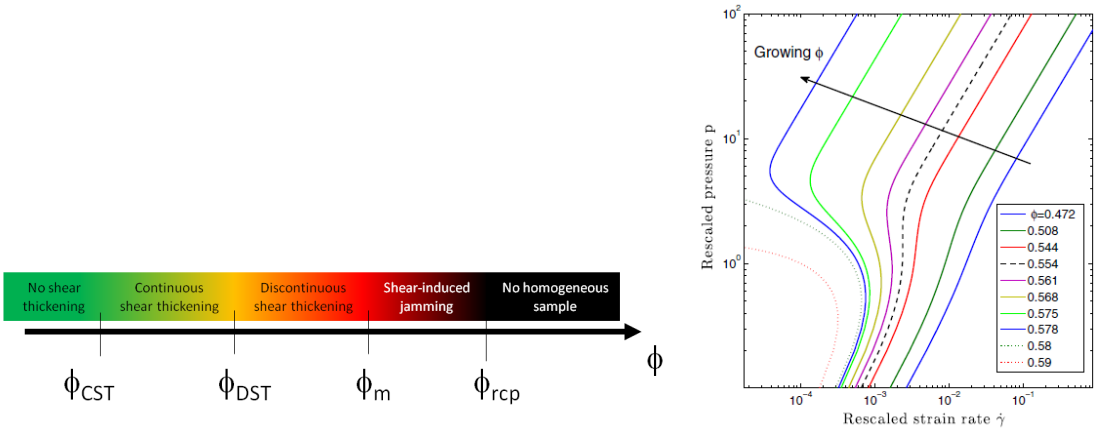

(a) (b)

Figure 1.7: (a) Phenomenology of shear thickening depending on volume fraction ϕ. (b) Associated flow curves computed from the model. For $\phi <$ ϕ_{CST} , the behaviour is near Newtonian. As ϕ increases, CST becomes pronounced. For $\phi_{DST} < \phi < \phi_m$, DST occurs (cf. dashed line on b) and is predicted with hysteresis between two flowing (unjammed) states. For $\phi > \phi_m$ (dotted lines), homogeneous flow can only occur at small strain rates (thickened state is not a liquid state) [57].

Small values of ϕ correspond to a Newtonian behaviour. For intermediate values of ϕ, the viscosity of the system increases smoothly with the shear rate, a regime referred to as *continuous* shear thickening (**CST**). For higher values of ϕ, $\phi_{\text{DST}} < \phi < \phi_{\text{m}}$, a *discontinuous* shear thickening (**DST**) transition is observed between a low-viscosity non-frictional state and a high-viscosity frictional but flowable state (because $\phi < \phi_{\text{m}}$). Finally, for $\phi > \phi_{\text{m}}$, flow can only occur in the frictionless state, thus for very small shear rates. The thickened state is not a liquid state and is expected to flow inhomogeneously or exhibit fracture or edge instability

ϕ_{rcp} is experimentally determined by fitting low-shear viscosity (no friction) with a Krieger-Dougherty law (or similar) while ϕ_m is retrieved while fitting high-shear viscosity (on top of shear thickening where friction is maximum). Difference between ϕ_{rcp} and ϕ_m can be as high as around

10 %. For instance, Guy et. al. found ϕ_{rcp} = 0.64 and ϕ_m = 0.55 (3.7 μm PMMA particles in a density-matching mixture of cyclohexylbromide and decalin) [59] while Royer et. al. reported ϕ_{rcp} = 0.71 and ϕ_m = 0.592 (1.5 μm silica spheres suspended in a glycerol-water mixture) [54].

Shear thickening is now viewed as a stress controlled phenomena with a transition between a low-viscosity non-frictional state to a high-viscosity frictional state. Within this picture, the onset stress σ_c is intrinsic of the system (i.e. set by repulsion force) and depend slightly on volume fraction. This feature is experimentally observed for different systems [59, 60, 39]. Onset stress scales with particle diameter with a power law of exponent -2 [59, 31, 61, 62].

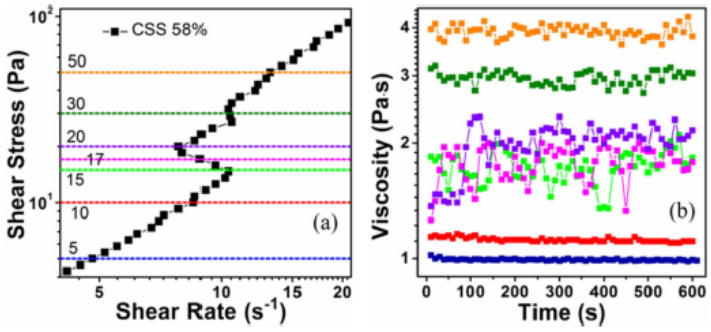

Figure 1.8: Experimental S-shaped flow curve on which the different constant stress levels are indicated: 5, 10 Pa for the Newtonian state; 15, 17, 20 Pa for the intermediate state; and 30, 50 Pa for the thickened state. The corresponding viscosities are shown aside as a function of time [63]

Furthermore, measuring experimentally discontinuous shear thickening (DST) can lead to a non-monotonic flow curve, often referred as sigmoidal or S-shape flow curves as displayed in Fig. 1.8a (a value of shear rate is associated with two values of viscosity) [64, 63]. Precise shape is found to depend upon experimental conditions as stress ramp characteristics for instance. Such experimental features can be explained within the stress-induced friction picture (cf. Fig. 1.7b) as shown also by Wyart and Cates [57]. Furthermore, a recent simulation work taking into account both hydrodynamic and interparticle friction also captures the phenomena [65]. Flow in the S-shape region and more generally in the DST region is found to be very unstable under stress-control conditions (fig 1.8b) but without steady-state shear bands [63, 60]. These fluctuations are likely due to the dynamic building and release of the percolating frictional network leading to local stress fluctuations. However, explanation for the precise nature of fluctuations (periodic, intermittent and chaotic upon increasing stress) is not really clear yet [60]. Fluctuations can even be very huge under strain-controlled conditions with jumps between low viscous lower branch and high viscous upper branch [66, 67].

This new framework for explaining shear thickening has been validated by simulations which are able to reproduce shear thickening (cf. Fig. 1.9b) both for non-Brownian suspensions [70, 69, 71] and colloidal suspensions [72]. Especially the transition from continuous at moderate ϕ to discontinuous shear thickening at high ϕ is retrieved. Simulations show also that contact contribution is the most important dissipation source in the shear thickening transition. Indirect experiments using shear reversal procedures [68] demonstrate experimentally also that contact contributions are dominant (cf. Fig. 1.9a) compared to hydrodynamic ones in the shear thickening transition (even for continuous shear thickening). In their work, Clavaud et. al. [73] proves the frictionless state at low stress with rotating

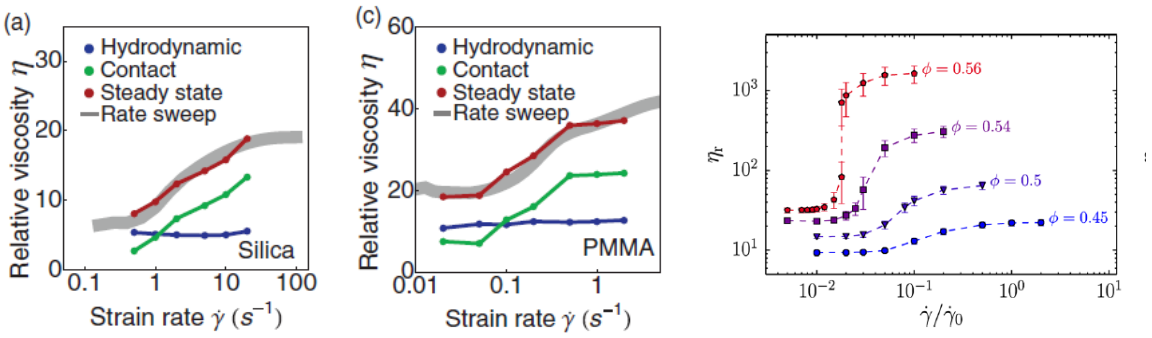

(a) (b)

Figure 1.9: (a) Experimental relative viscosity η vs strain rate $\dot{\gamma}$ for the silica (left) and PMMA (right) suspensions. Shown are rate-sweep measurements (thick gray line), steady-state relative viscosities from flow reversal (red) decomposed into contributions from hydrodynamic (blue) and contact (green) interactions [68]. (b) Simulated shear rate dependence of the relative viscosity η_r of a concentrated suspension while taking into account the transition from frictionless to frictional rheology (friction coefficient $\mu = 1$) [69].

drums experiments and are able to transit from frictionless to frictional rheology when decreasing interparticle repulsion force. All these results add further weight to the scenario in which shear thickening is driven primarily by the formation of frictional contacts.

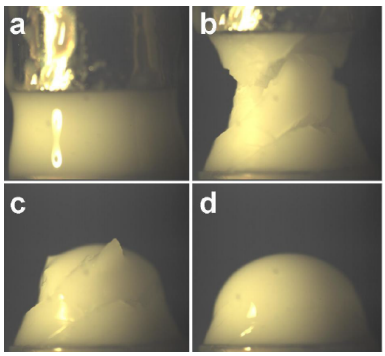

Figure 1.10: Under rapid extension, the glossy surface seen at equilibrium (a) becomes matt with solid-like rough interface (b). The suspension then slowly relaxes back into the equilibrium phase (c, d). [74]

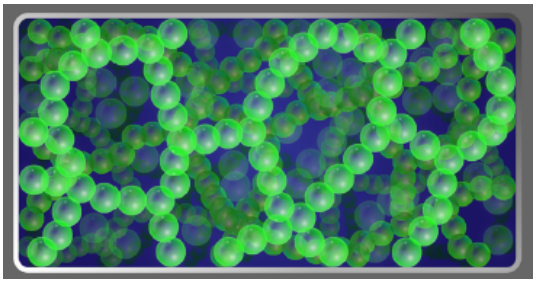

Figure 1.11: Illustration of the particle contact networks that dynamically form during the shear thickening transition. These networks support frictional forces that are transmitted across the system, producing the solid-like properties of discontinuous shear thickening fluids [75]

At sufficient volume fraction, concentrated suspension exhibiting DST can even also turn into a solid-like sample for example with sudden impact on their surface [76, 77] or rapid extension (cf. Fig.

1.10) [74, 78]. This effect is also seen when a person can run across a dense cornstarch suspension without sinking. This solid-like state is created by transient shear-jamming fronts experimentally pointed out [79, 80]. According to the authors, the DST regime is just a precursor to the shear-jamming transition (for a given ϕ, DST occurs a moderate stress and shear jamming at high stress). Shear jamming (real solid-like behaviour) would appear beyond DST (highly viscous state still flowable) when the network of touching particles becomes so dense than a fully shear-jammed state is reached (cf. Fig. 1.11). This picture is quite different to the theory of Wyart and Cates previously described [57]. According to the latter, shear jamming and DST are two well separated states: shear jamming occurs with $\phi > \phi_{\mathrm{m}}$ whereas DST occurs at lower concentration $\phi_{\mathrm{DST}} < \phi < \phi_{\mathrm{m}}$. For very fast impact-activated solidification, no volume fraction changes are observed (contrary to a former hypothesis of jamming via densification). It contrasts with findings of Fall et. al. on the same system [81] where they observe a intense stationary particle migration (phase separation in a Couette cell) in the DST regime attributed to shear-jamming occurrence.

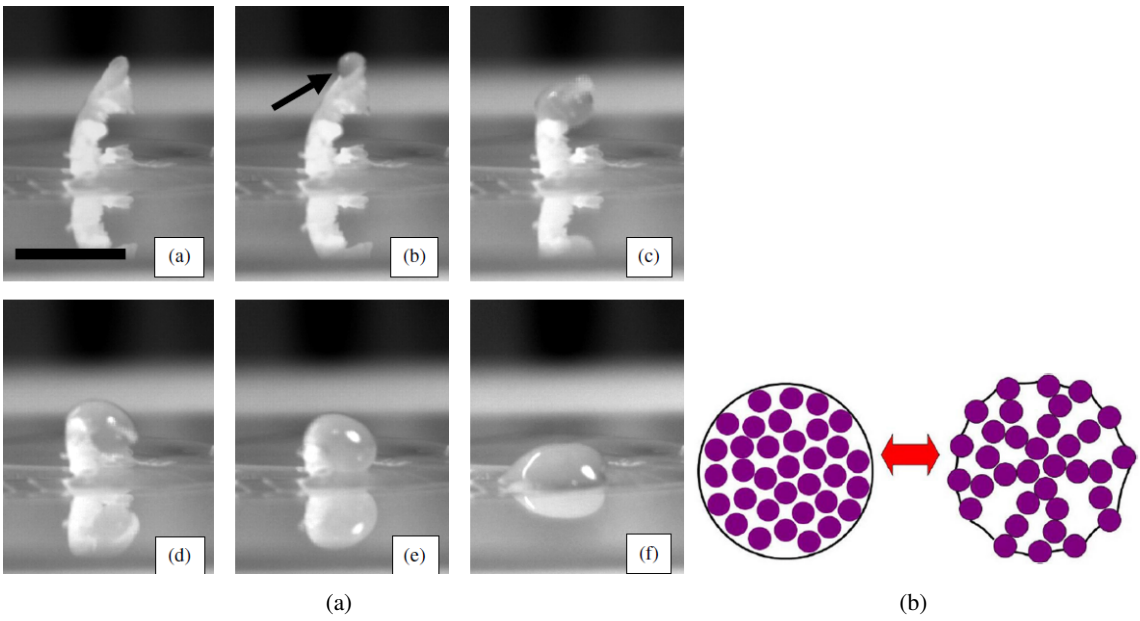

Figure 1.12: (a) A sample PMMA hard-sphere suspension at ϕ = 0.61, partly granulated by pushing a spatula through a droplet. The granulated, opaque, solid piece of the sample can be seen; this persists indefinitely if left undisturbed. Melting of the granulated sample is achieved by contact with a droplet of a more dilute solution. The scale bar in (a) is 5 mm. [82] (b) Schematic of a fluid droplet (shiny surface) and a solid granule with rough surface (particles pokes out of the surface). [83].

Another consequence of frictional contacts upon shearing can be observed within the granulation phenomenon (cf. Fig. 1.12a). A sufficiently dense suspension turns into discrete lumpy granules upon shearing. The surface changes from shiny to rough (solid-like sample which persists indefinitely if left undisturbed). This change can be explained with the stress-induced friction scenario. As explained before, at a sufficient concentration, shearing creates more and more frictional contacts. The suspension initially liquid at low stress turns into a jammed sample. Particles appear to poke out as the confining capillary stress keep them in this high stress jammed state (cf. Fig. 1.12b) [83]. This confining capillary stress (maximum $\sim \frac{\gamma}{r}$ with γ the surface tension and r the particle radius) provides in fact a maximum stress value for shear thickening (remember, minimum stress value was given by onset stress linked to

particle repulsion). If particle pressure becomes higher than capillary stress, the sample will undergo fracture [52, 42]

1.3.2.6 Tuning shear thickening

As detailed above, shear thickening is now viewed as a transition from a low-viscosity frictionless state to a high-viscosity frictional state upon shearing. Transition occurs when shear stress exceeds the critical stress keeping particles apart from each other (stemming from microscopic repulsion forces). One can easily understand that surface properties (roughness, adsorbed molecule, charge...) will then modifying value of this critical stress, giving a way to modify macroscopic shear thickening behaviour

Role of short-range repulsive force Fifteen years ago, Bergenholtz and collaborators [84] reported that adding an extra additional short range repulsive force (which acts to prevent particles from being into close proximity) has a major impact on shear thickening of a concentrated suspension and can even suppress it. Same trend was found with Shenoy and Wagner where they prevented "hydroclusters formation" with electrostatic field. This resulted in postponing the shear thickening at higher stresses [85]. Considering the new picture of stress induced friction, it shows than hindering particles from touching each other can notably postpone the shear thickening. In a recent simulation work, Mari et al. [72] shows exactly the same: increasing repulsion force (i.e increasing σ_c) between particles shifts shear thickening to higher shear rates (cf. Fig. 1.13a).

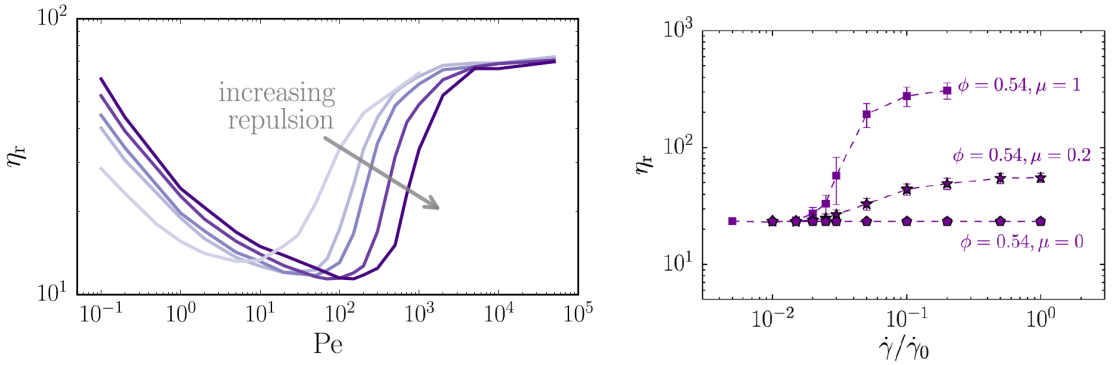

Figure 1.13: (a) Delaying shear thickening by increasing short-term repulsive force between particles. Simulation work from [72] (b) Increasing shear-thickening intensity by increasing interparticle friction coefficient. Simulation work from [69]

Impact of particle surface roughness Lootens et.al. have described the effect of roughness of silica particles on rheological properties [39]. After having chemically eroded the particles (i.e. higher roughness), the critical shear rate before DST becomes significantly lower (cf. Fig. 1.14). The higher roughness certainly means a lower stress needed for frictional contact and a higher dissipative friction between particles. In another work based on simulation, Mari et. al. [69] reported that increasing the interparticle friction dramatically amplify shear thickening (cf. Fig. 1.13b). The two results are in line with the theory of Wyart and Cates described above.

Beyond shear thickening, an increase of whole viscosity curve is measured when rougher particles are used [86, 87], certainly due to an increase of interparticle friction coefficient. Indeed, a simulation with increasing roughness of frictionless particles shows a slight viscosity drop [88].

Adsorbed species at particle interfaces Apart roughness, surface property of particles can be widely modified by adsorbing/grafting some chemicals leading to major changes in the shear thickening behaviour of concentrated suspension.

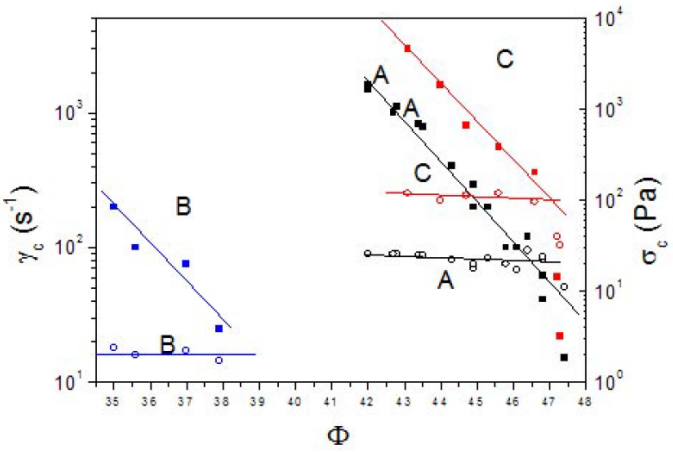

Figure 1.14: Role of particle surface on shear thickening for a suspension of 1 μm silica particle. Critical shear rate (left axis) and critical shear stress (right axis) are reported for (A) particle as synthesized; (B) rougher surface after chemical erosion (C) particle as synthesized but adsorbed surfactant on surface [89].

Some studies on shear thickening behaviour of cement based suspensions have been done [90, 91, 21, 92]. Shear-thickening appears when using a superplasticizer which enables a well dispersed suspension [93]. Toussaint found admixtures (certainly polymers) that play only on rheological behaviour at high shear rates by reducing shear-thickening (lubrication thanks to polymer layer) [21]. On a more simple system (silica spheres), Lootens reported a shift in shear-thickening behaviour at higher shear rate when particles surface was covered with a bilayer of surfactant (cf fig 1.14) [89]. Similarly, similar results [94, 95] were found for colloidal suspensions where the longer the polymer adsorbed on particles, the more shifted shear thickening is. However, a long polymer enhances low-shear viscosity. Grafting directly onto particle surface can achieve similar results [96].

This influence on shear thickening can be explained by two mechanisms. Adsorbing or grafting a surfactant or a polymer can (i) rise the repulsion force needed to enter shear-thickening regime and/or (ii) reducing dissipation in the frictional regime (i.e tempering shear-thickening) by some lubrication due to species on surface (especially with bilayers). Indeed, fundamental studies between two surfaces shows that lubrication [97, 98, 99] exist with adsorbed species. It is more efficient with long carbon chain , with bottle-brush polymers (compared to linear ones) and with charged polymers (compared to uncharged ones).

Surfactant can sometimes have an inverse effect; i.e. lowering critical shear for shear thickening occurrence [100] which could be interesting for some specific applications (as for example for body armors, dampers...). Same trend is achieved by a neutralization of surface charge [101, 102, 103] where increasing the salt concentrations leads to lower electrostatic repulsion and lower critical shear rate. A

large amount of salt can even suppress shear thickening but creates infinite low shear viscosity (yield stress) [73].

Active suppressing of shear-thickening Recently, a new strategy for tuning shear thickening on demand has been developed by Lin et al. [104]. They achieved a shear thickening reduction (up to 2 decades, starting from DST) by superimposing a high-frequency and low-amplitude shear perturbation orthogonal to the global shear rate. Their results are interpreted in light of stress induced friction scenario recently suggested to explain shear thickening microscopic origin. During DST, numerous frictional contacts are created leading to particle chain forces (large and dynamic network of frictionally-contacting of particles). The orthogonal shear perturbation will dynamically break these chains forces, reducing frictional contacts, thus macroscopic shear-thickening. To the best of our knowledge, this is the first method allowing in-situ dynamic modification of shear thickening behaviour during shear itself.

Up to now, only repulsive forces and their implications have been reported. However, attractive forces are also always present: at least London-van der Waals forces but others source of attraction can exist in suspensions. The microstructure of the dispersion will be impacted by those interactions, modifying a a consequence their rheology. Likewise for repulsive interactions, origins and implications for rheology of attractive forces are detailed in the next part.

1.4 Role of attraction

Van der Waals or dispersion forces are a ubiquitous source of attraction. A stable dispersion can only be prepared by counterbalancing them with some repulsions stabilization forces as detailed in part 1.3.1. Attractive interactions are responsible for particle aggregation: both reversible (flocculation) and irreversible (coagulation).

1.4.1 Different attractive interactions

There are different ways to induce more attractive interactions between particles so as to control the dispersion state. A way is about reducing the suspension stability to tune the flocculation state. For instance, electro-statically stabilized suspensions can be destabilized by adding salt or components which neutralize surface charge. Both reduce electrostatic repulsion. On the other hand, sterically stabilized suspensions can be flocculated by chemical or physico-chemical procedures: changing the solvent, adjusting the temperature, modifying coating nature... Here below are detailed some examples.

But attractive forces can stem from specific interactions as hydrophobic or H-bonding or from capillary bridges (see below). Adding a non-adsorbing polymer can also induce depletion forces between particles. This force is attractive with a range of attraction close to radius of gyration of the polymer in solution. Similar results can be achieved using micelles or nano particles. Depletion occurs when an excess of adsorbing polymer is in solution. Attractive interaction can also result form simultaneous adsorption of a polymer molecule onto two particles, a phenomena called bridging

flocculation. For example, amphiphilic polyelectrolytes are often used for flocculation in water clarification. Associative block copolymer are also used to thicken water-borne suspensions.

1.4.2 Tuning attractive interactions with formulation

Changing dispersing medium This has already been tried in PVC dispersion. As it deals with our system, it will detailed in the last part of the chapter.

Adjusting temperature A typical example is in the photographic industry. Here, adsorbed gelatin stabilizes dispersions but only at a temperature above the solidifying temperature. Decreasing the temperature induces gelatin solidification, suppressing particles stabilization [105]. Mewis et al. [94] reported also that changing the temperature modifies greatly the viscosity. The change in rheology can be explained by shrink or expansion of the polymer coated on particles upon temperature variations.

Changing coating nature A well dispersed suspension can be turned into a flocculated one by modifying chemical nature of particle surface. For example, Yang et. al. [96] report a huge increase of viscosity (30 times) if they graft a hydrophobic alkyl group (octadecyl) on surface of their silica nano-particles dispersed in hydrophilic medium. No more electrostatic stabilization prevents attractive Van der Waals forces. Moreover, particles interact via hydrophobic interactions between alkyl chains. Attraction winning over repulsion, the rheology will be characterized by a yield stress.

Conversely, Brown et al [53] suppresses the yield stress of their hydrophobically treated (silane) glass sphere dispersed in water by adding a surfactant. The new surfactant coating has an affinity both with particle hydrophobic surface and aqueous liquid phase. Attractive interaction between particles are then far lowered: dispersion is enhanced (cf. Fig. 1.15a).

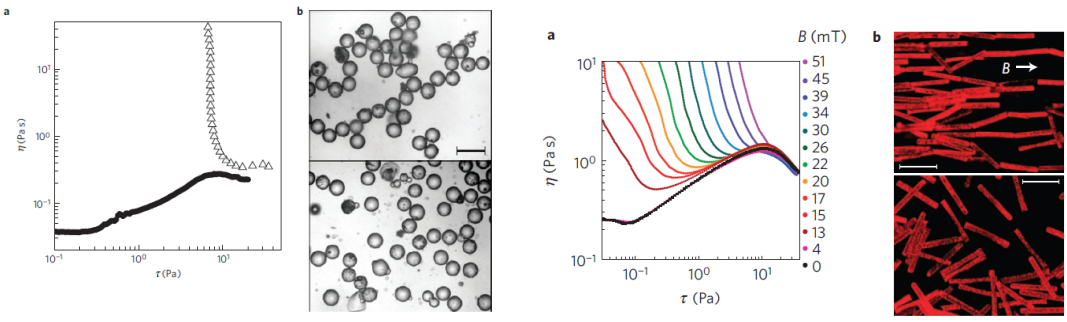

(a) (b)

Figure 1.15: (a) Flow curves of glass spheres (mean diameter 90 μm) with a hydrophobic silane coating suspended in water (ϕ = 0.52) without (open symbols) and with surfactant (closed symbols) (b) Flow curves for a suspension of ferromagnetic rods (254x32x25 μm) for different values of applied magnetic field B [53].

Another example of using a surfactant for facilitating the processing of non-aqueous suspensions can be found in the food industry. Melted chocolate is a suspension with cocoa butter as the liquid phase and sugar as particles. A surfactant, lecithin, which will be adsorbed on polar sugar grains, is used to reduce apparent viscosity (even at high shear rate, typically 30 % at 1000 s^{-1}) and yield

stress [106, 107]. By measuring interactions at the particle scale with AFM, authors show that lecithin reduces adhesion between sugar particles.

Magnetic field Brown et. al. [53] are able to tune attractive interactions in a suspension of magnetite rods. The higher interparticle attractive interactions are, the higher low-shear viscosity is (cf. Fig. 1.15b). For sufficient flocculation, a yield stress even appears (infinite low-shear viscosity). In their study, Bossis et.al. [108] can also add an extra attractive interaction with magnetic field, resulting in shear thickening transition at lower shear rate.

Concerning shear thickening, increase of low shear viscosity due to attractive interactions is able to hide completely shear thickening of previous well dispersed suspension. This effect on additional attractive interaction on a shear thickening system was seen on Fig. 1.15 on two systems. Same trend was reported when tuning attractive interaction with depletion forces [109]. Such flow curves were recently successfully captured by simulation [110].

1.4.3 Capillary bridges

Capillary bridges are a particular type of attractive interactions. They occur when a second immiscible fluid that wets particles is added in small amount (typically 1 % water in oil) to a suspension, capillary bridges (cf. Fig. 1.16a) are operative and change drastically the rheological properties. For example, Koos and Willenbacher [111] showed that the addition of small amounts of a secondary fluid, immiscible with the continuous phase of the suspension, causes agglomeration due to capillary forces and creates particle networks (yield stress, cf. Fig. 1.16b). It was for example observed for hydrophobic calcium carbonate particles in DINP (phtalate) or in oil. They distinguish two states: one where the second immiscible fluid does not preferentially wet the particles (capillar state) and the other where the secondary fluid preferentially wets the particles (pendular bridges). This phenomenon is completely reversible by evaporating the second fluid. Besides, using fluorescence, they can track the aqueous phase in the suspension.

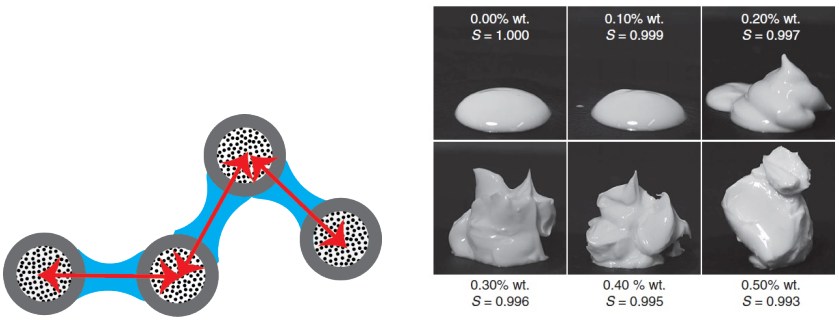

(a) (b)

Figure 1.16: (a) Schematic view of interparticular interactions by capillary bridges (b) Transition from weakly elastic, fluid-like behaviour to highly elastic, gel-like behaviour is visible by increasing the amount of water to a suspension of hydrophobically modified calcium carbonate in plasticizer DINP [111]

K. Cavalier and F. Larche [112] have also noticed the great impact of water on yield stress of carbonate calcium (0.85 μm) suspensions in DOP (di-octyl phtalate) even for low volume fraction (10.8 %). In an other paper, Koos et. al. [113] proposed to tune the rheological properties at low shear rate (particle interactions) through changes in the particle size, temperature induced changes to the interfacial tension, and through the addition of surfactants. They use nonionic surfactants as Tween 20, Tween 85 and Span 80. In addition to the nonionic surfactants, the ionic surfactant dioctyl sulfosuccinate sodium salt (DOSS) was also used. They found that the yield stress was reduced by two orders of magnitude when using surfactant. Decrease in the particle size leads to a strengthening of the network. On the contrary, increasing temperature causes a decrease of interfacial tension and yield stress.

1.4.4 Thixotropy and microstructure

Attractive interactions between particles can lead to macroscopic thixotropy. It is a reversible flow induced change in viscosity which takes a significant amount of time. More precisely it consists in a continuous decrease of viscosity with time when constant flow is applied to a sample that has been previously at rest and the subsequent recovery of viscosity when flow is stopped. Main suspensions encountered in daily life (paints, biological fluids, cement, filled polymers, printing inks...) exhibit some thixotropy. It is most often the result of relatively weak attractive forces between the particles.

This behaviour can be linked with suspension micro-structure. At rest, attractive interactions leads to flocs organizing themselves in a percolation network. The inter-particle bonds are, however, weak enough to be broken by the mechanical stresses that occur during flow. Thus, upon shearing, network evolves in separate flocs which decrease further in size when the shear rate is further increased. This change in micro-structure induces significant viscosity change. On the other hand, reducing the shear rate can cause a growth of the flocs; arresting the flow will allow the particulate network to rebuild [114]. Detailed flow-induced structural changes can be quite complex as reviewed by Vermant and Solomon [115]. In fact, a specific degree of thixotropy is often desirable for a product formulation. Objective could be for example to obtain a rapid recovery of the viscosity after a sudden decrease in shear rate or shear stress.

As a conclusion, interactions in concentrated suspensions are of prior importance for understanding their rich non-Newtonian rheology. Relevant interactions depends also on considered shear rate and are mainly imposed by formulation. At low shear rate, repulsion is very important to ensure best possible stabilization. Any attractive interactions will induce viscosity increase even including a yield stress. At high shear rate, some attraction interactions are no longer relevant as flow energy is enough to break them. Repulsion will still be critical to maintain as long as possible a fully dispersed state before contacts cannot be prevented anymore. Friction is there a major dissipation source macroscopically visible with shear thickening. A few tools remain to decrease dissipation in this regime as lubricating contacts with surfactants or having smooth particles. However, formulation is always a trade off: for

example, using long polymers will delay thickening (i.e. lowering high-shear viscosity) but creating inter-particles interactions (i.e increasing low-shear viscosity)

1.5 Normal stress differences

Contrary to simple viscous fluids but like polymers (cf. Weissenberg effect), concentrated suspensions can exhibit normal stresses anisotropy upon shearing. They are associated with microscopic anisotropy in the microstructure upon shearing (breakdown of fore-aft symmetry).

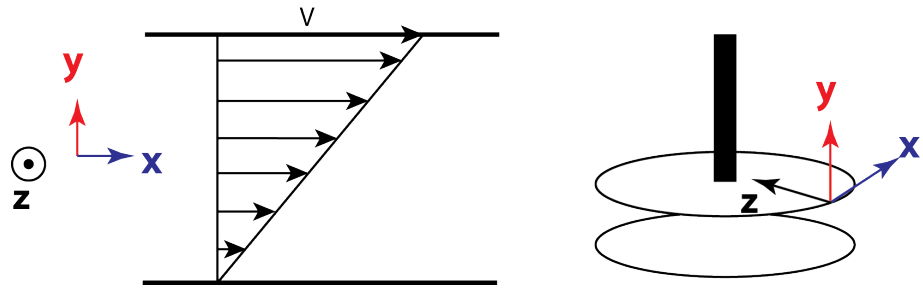

Figure 1.17: Definition of axes: x, y and z refer to the direction of velocity, velocity gradient and vorticity respectively.

In order to study this anisotropy, one can define the first normal stress difference N_1 and the second normal stress difference N_2 as following:

$$N_1 = \sigma_{xx} - \sigma_{yy} \text{ and } N_2 = \sigma_{yy} - \sigma_{zz} \tag{1.10}$$

with σ_{xx}, σ_{yy} and σ_{zz} the normal stresses (shear stress = $\sigma = \sigma_{xy}$) where x, y and z refer to the direction of velocity, velocity gradient and vorticity respectively (cf. Fig. 1.17).

At low volume fractions, those normal force differences are much smaller than the shear stress. On the contrary, in concentrated suspensions, same order of magnitude can be achieved at high shear rate. Measurements of normal forces are not an easy task. Early measurements of normal stress differences of spherical particles in Newtonian fluids were performed by Gadala-Maria [116] who observed a linear dependence of N_1 - N_2 versus the shear rate.

Zarraga and coworkers [117] used both parallel plate and cone-and-plate geometries, as well as laser profilometry measurements of the suspension surface deflection in a rotating rod geometry (access to N_2 +1/2 N_1). They observed negative values for N_1 and N_2 for volume fractions between 0.31 and 0.56 (also linear with shear rate), with $|N_2/N_1|$ around 3-4 in most cases ($|N_2| > |N_1|$). Similar results were found both in experiments by Singh et Nott [118] (parallel plates and Couette cell with a force transducer on the outside cylinder) and in simulation by Gallier et. al. [88]. This dominance of N_2 over N_1 observed in concentrated suspensions is different from flexible polymer where N_1 is generally dominant. N_2 was found to be negative also by Boyer et. al. who used rotating rod geometry [119], by Dbouk et. al. with a controlled stress rheometer equipped with plate plate geometry with extra transducers [120] or by Gamonpilas et. al. with classical plate/plate and cone/plate measurements [121]. However, the experimental value of N_1 for non Brownian suspensions is still under debate as some study found it negative [117] [122], around zero within experimental incertitude [123] or slightly

positive [120, 121]. Volume fraction dependence of normal stresses difference is often described using the scaling suggested by Morris and Boulay [124]:

$$\gamma_1, \gamma_2 \sim (\frac{\phi}{\phi_{max}})^2 (1 - \frac{\phi}{\phi_{max}})^{-2} \tag{1.11}$$

where $\gamma_i = \frac{-N_i}{\eta_f \dot{\gamma}}$ with i = 1 or 2.

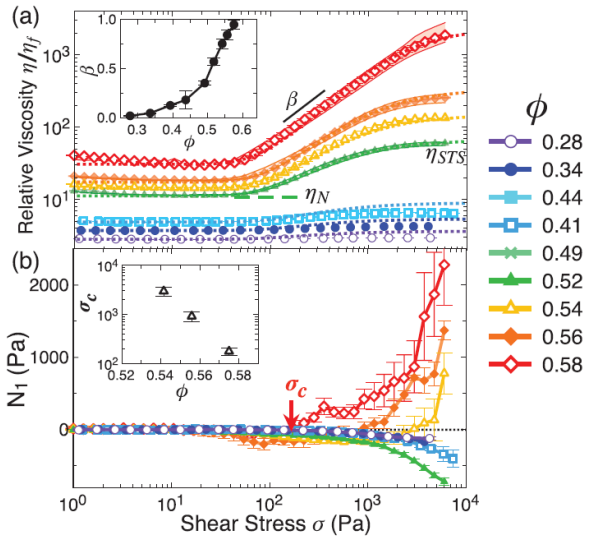

Figure 1.18: Relative viscosity η_r and first normal stress difference N_1 for silica spheres concentrated suspensions (diameter = 1.5 μm)[54]

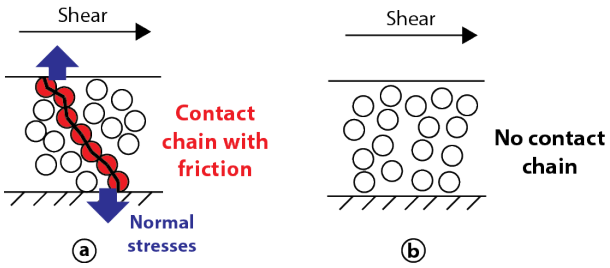

Figure 1.19: (a) Transient forces chains of frictional particles resulting in a high normal stresses (b) No major positive normal stresses without frictional contact network of particles.

All above cited work deals with moderate concentration (<50%). In particular, the shear-thickening effect is not significant. On the contrary, a recent work from Royer and coworkers [54] report measurements of N_1 as function of stress σ and volume fraction ϕ (28-58 %) for a continuous shear thickening system (DST occurs at 59 %). They found N_1 to be around zero for low volume fraction (< 40 %), negative at high stress for intermediate volume fraction (< 52 %) and positive at high stress for high volume fraction (> 52 %) (figure 1.18). This change of sign of N_1 upon increasing solid loadings was also reported by Lootens et. al. [39]. As a remark, for Brownian suspensions, reported values are negative in the shear thickening region [37, 125, 36, 126]. Sign of N_1 can give interesting insight in the underlying physics of the system. Indeed, simulations based on hydrodynamic interactions show that shear-induced distortions of the suspension microstructure and short ranged lubrication forces drive $N_1 < 0$ [10, 127, 84]. These simulations show also that increasing particle concentration is expected

to make N_1 increasingly negative. Including repulsive interactions or elastic particle deformations to these hydrodynamic models does not change the sign of N_1 [128, 129, 55]. On the contrary, one expects frictional networks to lead to dilatancy, a well-known feature of dense frictional granular materials, giving $N_1 > 0$ due to anisotropic nature of chain force [130]. Royer et. al. [54] suggests a picture which makes up hydroclusters and friction based shear thickening. At moderate volume fraction, clusters of particles are formed. Friction inside these clusters will increase viscosity but normal stress will be dominated by hydrodynamic lubrication films (leading to N_1 negative). Thus, viscosity increase driven by frictional contacts and a negative N_1 are not contradictory. Increasing volume fraction leads to bigger clusters, higher friction and less hydrodynamic lubrication explaining N_1 sign reversal. Finally, frictional clusters can dynamically span the whole system when DST occurs. The fluctuating spanning between the shear plates would explain for example positive large normal forces fluctuations in a system which exhibits DST [67].

Another very recent paper [131] explores the effect of particle size and gap in the measurements of second normal stress difference. They found a large effect of both parameters on the value of N_2, resulting from a balance between the positive contribution of the particle stress and the negative contribution of the liquid stress.

Numerical simulations [132, 133] without friction leads to N_1 et N_2 negatives with N_1 approximately equal to N_2. Taking into account friction in simulations [88][132] increases the relative viscosity and N_2 but decreases N_1. Wall bounding can also greatly affect N_1 and make it positive [134]. However, such simulations are done at moderate volume fraction (0.1-0.5%) and simulating polydisperse systems is still a challenge. Experimental work [86, 87] shows an increase of N_1-N_2 with increasing roughness for vol. fraction up to 50 % (probably linked with increased friction). Recent simulation from Mari and co-workers [69, 72] are able by taking into account friction to reproduce a transition from weaker negative N_1 to a positive one when increasing solid volume fraction. However their predictions hold for Brownian suspensions whereas experimental values for those suspensions are always negative [37, 125, 36, 126].

1.6 Shear-induced particle migration

Up to now, no deviation from an homogeneous concentrated suspension was considered. Unfortunately, it is not always the case and some local particle concentration heterogeneities can occurs. As viscosity depends widely on particle concentration, even small variation (few percent) can have important effects when studying flow properties of these suspensions.

First detailed studies were published in the eighties [135, 136]. They show a slow decrease of viscosity when sheared at a given shear rate in different Couette cell geometries (cf. Fig. 1.20). Same behaviour was observed by Mehri et. al. [137]. They interpret their results by suggesting that particles migrate over time towards regions with lowest shear rates (outer cylinder). Local volume fraction measurements by NMR [138, 139, 81] have pointed out these high-concentrated regions and low concentrated regions (see for example Fig. 1.21)

Migration was also reported in channels (rectangular or cylindrical) where particles migrate toward the center where shear rate is the lowest. Again, this was confirmed by local volume fraction measurements using NMR [140, 141, 142] or modified Doppler velocimetry [143, 144]. This kind of

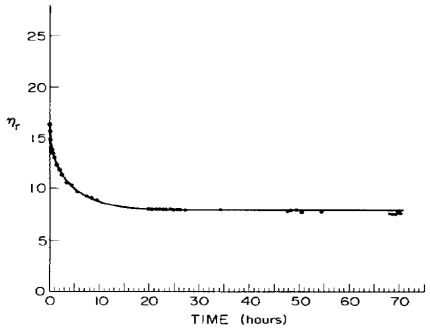

Figure 1.20: Relative viscosity of a ϕ = 0.45 suspension as a function of the time it was sheared in the Couette device at $\dot{\gamma}$ = 24 s^{-1}. Polystyrene spheres, 40-50 μm in diameter, in a mixture of silicone oils [135]

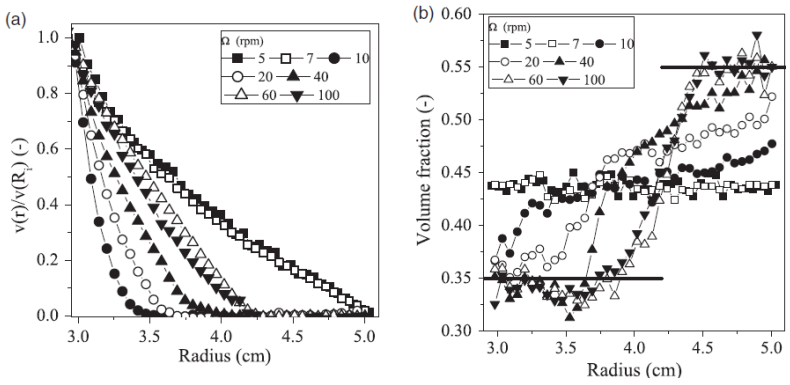

Figure 1.21: Steady MRI data for a ϕ = 43.9% cornstarch suspension and different rotational velocities Ω. (a) Velocity profiles within the Couette cell. (b) Related density profiles. Solid lines indicate ϕ_{RLP} and ϕ_{RCP} [81]

migration can have dramatic effect by creating high concentrated plugs at center of the pipe, leading sometimes to a complete flow stop and pipe damage [145].

Contacts are also thought to be important for shear-induced migration of particles [120]. Different models have been suggested to capture experimental results. The first one is the diffusive flux model (kinematic model) [136]. The higher the shear rate, the higher the number of collisions between particles. Slight difference in local shear rate implies different collision rates creating a diffusive flux from high-collision regions (=high shear rate) to low-collision regions. This flux is not compensated by reverse flux from particle concentration gradient and viscosity gradient. This model successfully explains many results but failed to explain why Chow et al. [146] observed an outward migration in cone plate geometry (constant shear rate in this geometry). Other unusual results showing migration towards high shear rate region were reported [137] in a plate-plate geometry.

The second model is more recent and called suspension balance model [124, 147, 148, 119]. This model is based on normal stresses and aims at linking rheological properties with migration features. It describes the migration flux of particles as the divergence of the particle stress tensor. By considering mass and momentum balance both for particles and for liquid phase alone, they suggested a prediction for local volume fraction over time. It gives a good agreement on F. Boyer data [149] and relative

agreement on A. Machado data [150]. Dbouk [151] reported also correct modelling of data from Philips [138] and Lyon and Leal [143].

However, the migration phenomena is not totally solved as discrepancy still exist between some experimental results and prediction [152]. Besides cornstarch dispersed in water shows a rapid and intense stationary particle migration [81]) in particular in the DST regime (phase separation). According to their authors, macroscopic DST in this system would rather corresponds to shear-jamming, explaining the fast migration observed. On the contrary, some systems (PMMA particles in water/NaI) seem to exhibit no visible particle migration even during the shear-thickening transition [63].

Particle migration is a complex phenomena occurring in suspensions, in particular the concentrated ones. It adds to other complex phenomena reported for rheology of concentrated suspensions: shear thinning due to particle attractive interactions, shear thickening certainly due to interparticle friction. One has to be careful about particle migration because it induces an heterogeneous sample. Thus, macroscopic rheological measurements can be not related to intrinsic flow curve and really dependant on real particle concentration mapping. Local measurements coupled to rheometry are encouraged to fully describe the rheological response of concentrated suspensions.

1.7 Beyond shear-thickening: rheology at high shear rate

Recent explanations for shear-thickening behaviour are linked with particle-particle friction when flowing at high stress. In their theory, Wyart and Cates describe a transition between a frictionless and a frictional state (see part 1.3.2.5). In particular, depending on considered volume fraction, the frictional state is considered either as a Newtonian flowing state (upper branch of high viscosity) or as a jammed state.

However, experimental results beyond shear thickening show that the upper branch is seldom a Newtonian state. Shear thinning is often measured for different systems: PMMA in poly(ethylene glycol)[153]; fumed silica in poly(propylene glycol) [154, 155, 156], cornstarch in water [81], glass spheres in mineral oil [40], cementitious pastes [22], carbon black particles in tetradecane [157], PS particles dispersed in polyethylene glycol [158]. However, experimental measurements in this high shear rate region have to be carefully done as sample ejection (due to high normal stresses difference during shear thickening) can occur and hinder reliable measurements.

Wall slip cannot explain this feature as same behaviour is retrieved when using roughened plates [153]. The explanation for this specific regime is still controversial and few works focuses on this topic. One possibility is the elastohydrodynamic limit [153, 10]. Particles in the suspension have a finite modulus. In this theory, lubrication high stresses during shear thickening might be enough to induce particles elastic deformation and then creating an upper bound for shear thickening. More precisely, the stress resulting from the the lubrication forces acting between an elastically deformable particle of radius a, moving with velocity V relative to a neighbouring wall scales as [153]:

$$\sigma \sim (\frac{\eta_f V G_p}{a})^{1/2} \tag{1.12}$$

where η_f is the intersticial liquid viscosity, a the particle radius and G_p the shear modulus of the particles themselves [10]

Replacing the relative velocity and particle size by shear rate gives:

$$\sigma \sim (\frac{V}{a})^{1/2}(\eta_f G_p)^{1/2} = (\dot{\gamma})^{1/2}.(\eta_f G_p)^{1/2} \tag{1.13}$$

This also can be written in term of a limiting suspension viscosity:

$$\eta = (\eta_f G_p)^{1/2}\dot{\gamma}^{-1/2} \tag{1.14}$$

The model predicts a shear thinning behaviour with an exponent -0.5 when plotting η=f($\dot{\gamma}$). As their experimental data deals only with rotational rheometry (limited to moderate shear rate), predicted exponent is difficult to compare to available experimental data. Nevertheless, this simple scaling model provides a expression for the upper bound of the suspension shear thickening. Adjustment of this upper bound on experimental data from polymer colloid dispersions is well achieved with a pre-factor depending on ϕ (ranging from 0.005 to 1 in their fitted data). The model would explain why polymer colloid dispersions show significant post-thickening shear thinning and why suspensions of mineral particles not. The high shear modulus of the latter prevents from reaching sufficient stresses within the measurement range of conventional rheometers.

Of course, if this critical stress is higher than confining capillary stress (maximum $\sim \frac{\gamma}{a}$ with γ the surface tension and a the particle radius), upper bound of shear thickening will be fixed by this capillary stress and elastohydrodynamic regime will not be accessible.

1.8 Focus on plastisol suspensions

The system under scope in this thesis is a particular case of concentrated suspension: PVC particles dispersed in a plasticizer, called plastisol. Formulation can be complexified by adding another powder (filler) with or by presence of additives (thermal stabilizer, various additives,...). As attention is paid only to the rheology before gelation, literature review is limited to these aspects. Many parallels with features from concentrated suspensions will be underlined.

1.8.1 Formulation

1.8.1.1 Poly-Vinyl-Chloride (PVC) powder

Unlike PVC manufactured by suspension polymerization which produces particles with typical size 50 -200 μm, PVC powder used in flooring industry is produced by emulsion or micro-suspension polymerization ($\sim$ 5-10% of PVC market) [159, 160]. Both routes produce an aqueous latex. The process consists in dispersing hydrophobic monomer in a water batch using a surfactant. The latter stabilizes fine droplets of Vinyl Chloride monomer and growing latex particles in the continuous phase. Final latex have a typical range size 0.2 - 2 μm and are spherical. Seeding may also be used, for example to obtain higher particle sizes and bidispersity. Once synthesized, latex goes through an spray-atomizer to be dried. Depending of the atomizer parameters, small elementary particles of PVC can sometimes be stuck together to create aggregates of a few tens micrometers. Dried PVC powder still contains on its surface surfactants from the synthesis.

Molecular weighs of PVC chains in the particles are industrially characterized using number called K-value. Chain length depends on synthesis conditions and will impact the fusing temperature, the melt viscosity and the final mechanical properties. Most of the PVC inside particles is in an amorphous state even if there is a small part of crystalline domains [161, 162].

1.8.1.2 Filler

Some formulations are filled with calcium carbonate ($CaCO_3$) powder. In fact, filler replaces part of the PVC, typically up to half of PVC powder (in volume) for both economic reasons and modifying some properties of final product (flame resistance, mechanical properties...). Used calcium carbonate is natural (ground calcium carbonate, or GCC) coming from chalk, coral limestone or marble quarry as all of these rocks contains nearly pure $CaCO_3$ (>98 %) . A grinding step allows to obtain desired particle size.

1.8.1.3 Plasticizer

A plasticizer is defined as a molecule with very low volatility (technical standard ISO 472 (1988)). It facilitates the forming process of PVC and increases flexibility and extensibility of a plastic material [163]. This is often macro-molecules which form an oily liquid. Traditionally, widely used plasticizers are phtalates molecules (cf. Fig. 1.22a) like DINP for example. Because of their toxicity, they are now more and more replaced by non-phtalate plasticizer as for instance DINCH for example,used throughout this work (cf. Fig. 1.22b).

Plasticizer has a good chemical affinity with PVC grains and is in fact a solvent of PVC but only at high temperature. When T > T_g(PVC) = 80 °C, plasticizer fast enters particles and solvates PVC within less than one minute (gelation process, cf. introduction). But at room temperature, the process is much slower. Plasticizer enters only on a small depth as penetration is very slow. It creates a brush of solvated PVC around particles. This brush explains the stability of our suspensions by a steric mechanism [164] [165]. As plasticizer is a non-aqueous liquid with low dielectric strength ($\epsilon_r \approx$ 5 -8 [166]), steric stabilization is largely predominant over electrostatic one.

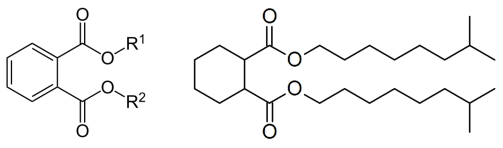

(a) (b)

Figure 1.22: (a) Chemical formula of a phtalate (typically R1 and R2 are alkyl chains with 12 carbon atoms). (b) DINCH (1,2-Cyclohexane dicarboxylic acid diisononyl ester), the non-phtalate plasticizer used as liquid in all suspensions studied here.

After gelation, plasticizer allows to get a soft PVC piece by decreasing the glass transition temperature under room temperature (typically -30 °C). But what happens exactly at the microscopic scale during plasticization is not really clear and several theories have been suggested based on PVC-plasticizer interactions [167, 168] :

— **Lubricating theory** : this old theory (in the forties) developed by Kirk, Clark and Houwink explains that the plasticizer diffuses into polymer grains and weaken the polymer-polymer interactions (no rigid network). This allows to reduce intermolecular friction between polymer molecules. Gidvani criticized Houwing work by assuming that plasticizer did not always involve swelling of the polymer and that lubrication effect of the plasticizer was the most important effect.

— **Gel theory**: this is also a theory developed in the forties (by Aiken, Manfred, Obrist) in which the plasticized polymer is seen as loose 3D network (state between solid and liquid). Interactions between plasticizer and PVC are weak. That is why, there is a dynamical exchange process. Here, rigidity is due to resistance of 3D network (microcrystallites are acting as the crosslinks). The role of plasticizer is here to reduce the number of polymer-polymer contacts of the network letting more deformation (desaggregation of the polymer).

— **Free volume theory**: This theory was developed in the fifties and is the one giving more precise explanations. It was first postulated by Fox and Flory. Plasticizer is here thought to increase the free volume of polymer, i.e. the space for chain movement.

A good plasticizer consists of one polar part and one apolar part (in some manner like a surfactant). The polar moiety (e.g. carbonyl group) can interact with PVC polymer (aligned dipoles forming attraction points between plasticizer and polymer) and the non polar moiety controls the interaction by preventing a full solvatation, adds a free volume and provides lubrication. So, both polar and non polar group are necessary for a plasticizer. This equilibrium between polar and apolar part can be calculated using solubility parameters [167]. The difference in plasticizing yield are explained by the difference in the strength of interactions.

No more mechanistical models were reported in the literature since the free volume one. All three theories give a good picture of fundamental principles of plasticization but none of them explains all facts related to plasticization. Some mathematical models were although proposed trying to model experimental data. Quantitative data were obtained also with molecular modelling : for instance structure property relationship for the system PVC plasticizer. They found that plasticization of PVC is explained by the solvation of polymer chains by plasticizer molecules as well as the increase in the free volume. [169].

1.8.1.4 Surfactants

Surfactant used during PVC synthesis are commonly anionic ones [160]. For microsuspension polymerisation, a co-surfactant (highly water insoluble component) such as a C18 alcohol is used. Surfactants will have an impact on air release, VOC, odour, clarity, gloss... [159] but also on rheology as detailed hereafter.

1.8.2 Ageing

Ageing in plastisol corresponds to a viscosity increase over days when sample is stored at a temperature far smaller than glass temperature T_g = 80˚C (room temperature for example). It is related to the microscopic diffusion of plasticizer into PVC particles which is slow at such temperatures (PVC

is in its glassy state) but does exist. Apart slow particle swelling, the plasticizer diffusion into particles promotes also desagglomeration which is found to be the main contribution to ageing. The viscosity increases faster in the beginning but slowly continues to increase over time [170, 171, 172]. Ageing is accelerated when increasing the temperature [171]. Intensity depends also naturally on plastisol formulation:

— The higher the particle concentration, the higher the viscosity uptake [173, 174]
— Plasticizer has an impact through its dielectric constant and molecular weight [172]
— Size distribution of PVC has an impact, in particular aggregates and small PVC particles. The latter favours ageing due to their high specific surface. Furthermore, a lower molecular weight of PVC chains enhances ageing as plasticizer penetration is eased. [173, 174, 175, 176]
— Additive like surfactants and thermal stabilizers have some effect but real impact and origin is not clear [177, 172, 173]

All studies are mainly empirical and no modelling and/or quantitative predictions have been developed so far contrary to the gelation process [178, 179].

1.8.3 Rheological behaviour

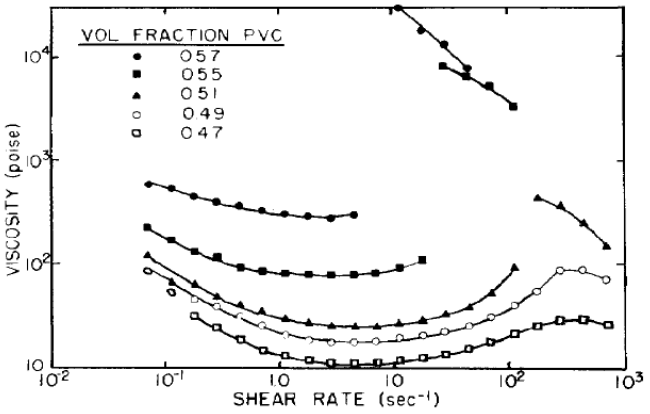

Figure 1.23: Effect of volume fraction of monodisperse 1.25 μm PVC in dioctyl phthalate upon viscosity discontinuity. CST is visible at moderate ϕ while DST occurs at large ϕ [180]

Some of first detailed reports of shear-thickening were performed by Hoffman who studied very monodisperse ($D_{[4,3]}/D_{[3,2]}$=1.01) dense suspensions of PVC in plasticizer [180, 48]. He observed CST and DST at large volume fraction (cf. figure 1.23) Same behaviour was observed also for other polymer particles (like polystyrene in PEG). His light scattering experiments show an ordering of monodisperse spheres before shear thickening, ordering which is broken during the shear thickening transition. Thus, he developed his theory of an order-disorder transition to explain its rheological results. As detailed in part 1.3.2.2, order/disorder transition is not always necessary et could be due to its very low polydispersity of the powder. Moreover, the word "dilatancy" is often used instead of shear thickening as concepts were not clearly defined and separated at that time.

Nakajima and Harrell developed their own model for explaining the results from Hoffman [181, 182]. Along them, the first shear-thinning behaviour was interpreted as the result of the stress-induced phase separation into an immobilized layer and a mobile phase. The immobilized layer grows with the

increase of shear rate. Consequently, the particle concentration of the mobile phase decreases, resulting in the decrease of viscosity. The dilatant behaviour was explained as the result of the dilatation of the immobilized layer. However, their theory was never confirmed by any local direct experiments showing this stress induced separation

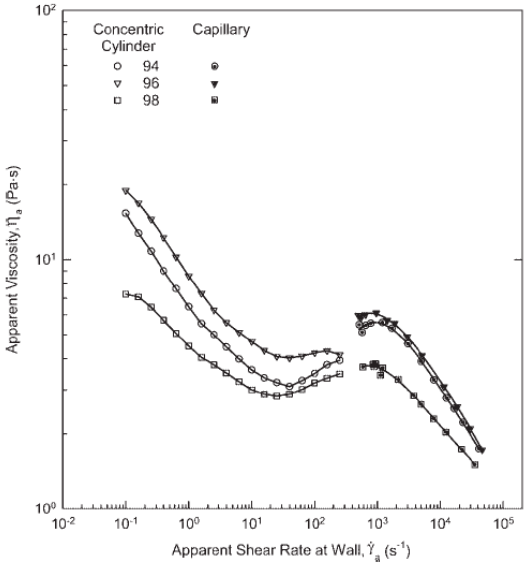

Figure 1.24: Complex rheological behaviour for a plastisol with shear thinning at low and very high shear rate and shear-thickening in-between. Experiments are carried out by combining rotational rheometer (low and moderate shear rate) and capillary rheometer (high shear rate) [183]

Other steady state viscosity measurements were performed on plastisols made of more widely used powder (i.e more polydisperse and closer to industrially used powder). Similarly to literature on concentrated reviewed until now, they report a shear thinning flow behaviour at low shear rate and a continuous shear thickening at high shear rate (cf. Fig. 1.24). These studies on plastisol also describe a shear thinning flow at very high shear beyond shear thickening [184, 185, 183, 186]. Measurements performed with capillary rheometer avoid sample ejection at high shear rate encountered with rotational rheometer. Shear-thinning over shear-thickening was also observed by Hoffman on its monodisperse suspensions exhibiting DST [180]. Besides, some thixotropy has been observed in PVC plastisols. The higher the volume fraction, the greater the thixotropy [173].

Unlike steady state flow displayed by Hoffman's experiments, some dynamic measurements has been carried out [173, 187]. Behaviours can be very different depending on powder granulometry: either elastic (G' > G") or viscous (G"> G') can be encountered. In particularly, ratio of coarse and fine particles can change [188]. They report an increase of both modulii with frequency. On the other hand, complex viscosity is found to decrease with frequency.

1.8.4 Impact of formulation on rheology

1.8.4.1 Surfactant

The effect of surfactant on rheology of PVC particles suspensions (unfilled plastisols) has not extensively been studied. For instance, Nakajima ad collaborators [185] used PVC powder with an

excess of surfactant for its plastisol (adding more surfactant than normal amount). They noticed that this excess of surfactant leads to a slight increase of viscosity at low shear rate (< 100 s^{-1}) and does not modify viscosity at high shear rate (> 1000 s^{-1}). Origin is not really detail even through authors think that excess of surfactant "influences the interparticle interaction". Collins et. al. [176] reported also that using a PVC with a linear sodium alkyl sulphate (A) results in a much high viscosity at low shear rate than a branched sodium alkyl sulphate (B). There is few difference at high shear rate. In their opinion, this change is induced by enhanced interparticle repulsion in presence of B.

According to Tomas et. al. [177], some SPAN 20 (another surfactant) added after the polymerization promotes aggregation of suspension and reduces ageing. The experiments were done however only on a shear thinning formulation. This is also the case in Marcilla's work [175] where some PVC powder are washed with methanol to remove surfactant (~ 0.8 % of sodium lauryl sulfate). They obtained a lower zero shear rate viscosity without surfactant. The study was done on again on a shear-thinning formulation, thus it is hard to conclude something at high shear rate. A last paper [174] uses PVC with either Sodium Dodecyl Benzene Sulphonate (SDBS) or Sodium Dodecyl Sulfate (SDS) but no real comparison was investigated.

Impact on rheology of covering filler particles (in filled formulations) with a surfactant have been less investigated and is controversial. One old paper about calcium carbonate in plastisol describes the advantage of using a filler covered with stearic acid [189]. In particular, the mixing process is found to be easier with such treated filler. In contrast, inverse effect is reported [190] where stearic acid coated filler increases plastisol viscosity. One last work [191] reports that covering filler with stearic acid does not modify significantly the viscosity but only limited amount of filler are investigated.

1.8.4.2 PVC granulometry

As expected, powder granulometry is critical in the rheological behaviour of plastisol, especially possible aggregates [173]. Smaller particles (range 100 - 1000 nm) leads to higher viscosity at low shear rate (100 times higher when using particles of 200 nm instead of 1 μm) by enhancing interparticle attractive interactions [164, 175]. It can even create a yield stress with only shear thinning rheology [190, 175].

Conversely, viscosity can be decreased by replacing some PVC micrometric particles by bigger ones ($\sim$ 30 μm), called extenders [187, 192, 193]. These non-porous and large particles have less specific surface and allow an increase of polydispersity. Generally, polydispersity of the PVC powder is a good way to decrease both its viscosity and its shear thickening amplitude [194, 176, 186, 191].

1.8.4.3 Water

Adding water in suspensions made of PVC dispersed in plasticizer is described in some papers [111][195]. Adding a small amount of water (immiscible liquid in plasticizer) increases viscosity (up to 10 times) and leads to a yield stress (non flowing suspension) most probably by creating water capillary bridges. Upon a critical amount adding more water does not change anything. This phenomenon is more generally reported when adding a second immiscible fluid in small amounts in a dispersion (cf. part 1.4.3).

1.8.4.4 Dispersing liquid

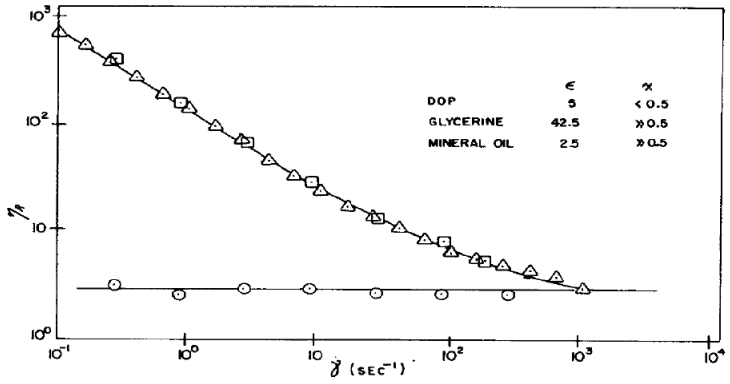

Figure 1.25: Relative viscosity of a PVC suspension (ϕ = 0.2) in different suspending fluids: plasticizer DOP (circle), glycerine (triangle) and mineral oil (square) [165]

Willey et. al. [164, 165] reported a transition from a stable state in plasticizer to a strongly flocculated state in aliphatic hydrocarbons or glycerine (yield stress) as displayed Fig. 1.25 . In plasticizer, suspension is sterically stabilized thanks to the solvated PVC brush on particle surface (slow diffusion of plasticizer). On the contrary, lower compatibility between PVC and glycerine or mineral oil does not allow such a brush formation (liquid does not enter PVC particles as affinity is not good). The suspension is thus not stabilized in those dispersing liquids, resulting in a flocculated (high low shear viscosity) state. Authors give quantitative results for the affinity between PVC and dispersing liquid using the Flory-Huggins theory. The Flory parameter χ is found to be between 0 and 0.5 for different plasticizers but > 2 for mineral oil. As reminder, the limit is 0.5 between a good solvent resulting in a polymer brush on surface (χ < 0.5) and a bad solvent where dispersing liquid does not diffuse into particle surface (χ > 0.5).

1.8.4.5 Filler effect

Even thought often used in industrial applications, there are very few studies on filled plastisols. In these suspensions, an important part (up to 50 % in vol.) of PVC is replaced by filler. The latter has completely different characteristics comparing to PVC: higher size (> 10 μm), not spherical and composed of $CaCO_3$.

One PhD thesis [191] partly focuses on studying viscosity of filled plastisols. However, the study is limited to low filler content (up to 18 vol% of the total powder). Moreover, filler size is limited to around 1-5 μm, smaller than typical sizes currently used $\sim$ 20 μm. Substituting PVC by filler increases the viscosity especially the low shear one. The smaller the filler, the higher the viscosity increase. Moreover, shear-thickening has in some cases a weaker intensity

While studying much higher filler content (up to 50 % in vol.), a recent paper [186] reports also a weak shear-thickening behaviour compared to suspensions with pure PVC, similarly to observations in cement when adding fillers [196]. Abdesselam et. al noticed also that viscosity at low shear rate can be more important when substituting PVC by filler. More generally, the whole flow curve is dependant on filler size distribution but no detailed mechanisms or quantitative modelling are given to explain those observations.

1.8.5 Normal stresses difference

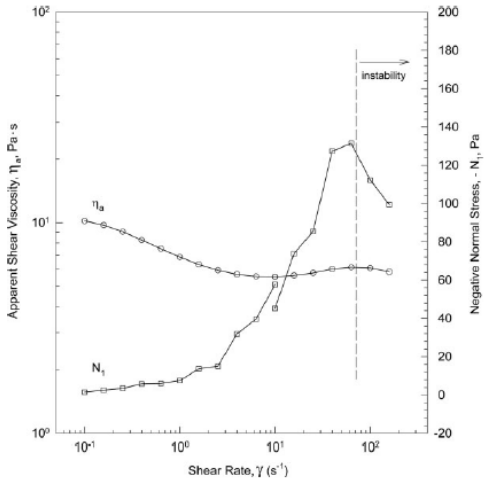

Figure 1.26: Apparent viscosity and normal stress difference, as function of shear rate. A rise of normal stress is visible before appearance of shear thickening on viscosity curve. Instability is assumed to occur above 100 s^{-1} [197].

A very few studies have been performed on normal forces studying the plastisol system. Nakajima report negative values of the first normal stress difference N_1 (cf. Fig. 1.26) for a plastisol exhibiting continuous shear-thickening [197]. The drop at high shear rate is due to flow instabilities (ejection). On a contrary, Willey reported a N_1 positive and a linear scaling of $\dot{\gamma}$ for N_1 but on plastisol exhibiting DST [164]. These results are very similar to the ones found by Lootens et. al. [39] for example (cf part 1.5) where highly shear thickening (DST) is linked with positive normal stresses, reminiscent from dilatancy and chains of solid-solid contacts. On the contrary, moderate CST is linked with negative normal stresses as there are no large spanning particle chains even if friction is not negligible

The rise in normal forces before the viscosity is already see as the preliminary step of shear thickening behaviour. Moreover, linear scaling between 1^{st} normal stress difference N_1 and shear stress in the case of DST was observed by Nakajima [198], a few months after Lootens et. al. noticed the same on its data [39]. These kind of measurements showing a equivalent macroscopic friction coefficient reinforce the idea of a large but dynamic network of particles in frictional interactions causing the DST.

1.9 Conclusion

Suspension viscosity is highly dependant on the volume fraction ϕ of solid particles dispersed in the liquid. A closer look to regime of high particle loading shows that dense suspensions exhibit also a rich non-Newtonian rheology due to numerous interparticle interactions, either attractive or repulsive.

The system under scope, called a plastisol, is a concentrated suspension of PVC particles which does exhibit non-Newtonian effects: shear thinning at low and very high shear rate; shear thickening in-between. Well dispersed state is achieved here by steric stabilization due to slight swelling of particle

at the surface by plasticizer, creating a brush of solvated PVC. The latter prevents particles from being completely flocculated

Even through hydrodynamic interactions (lubrication films between particles) are dominant at low and moderate volume fractions, friction between particles appears to be critical at high volume fraction. Shear-thickening, the rise in viscosity upon shearing observed in many dense suspensions, is now viewed as a transition from a low-viscous state with lubricated contacts to a high-viscous state with many frictional contacts between particles. Transition would occur when shearing forces overcome interparticle repulsion forces. Thus, surface properties have a key role. The new picture has been validated by number of indirect proves like simulations and indirect experiments. Direct experiments showing this transition at the microscopic level and making the link with macroscopic rheological change is still lacking. Specific literature on plastisol, especially the rheology, does not answer the question and it is quite old. Most of results have indeed been interpreted according to Hoffman's theory which was created in the 1980's and is not really up to date now. It is then interesting to study this shear thickening regarding the recent picture of shear-thickening driven by stress-induced friction.

In industrial process, suspensions are sheared up to a few thousands of s^{-1}. For plastisol under those conditions, no inertial effect has to be considered. However, as for many concentrated suspensions, normal stress difference have been measured at high shear rate during the shear thickening transition. These results for plastisol are rare; in particular impact of concentration or powder granulometry are not reported. Moreover, these features complicates measurements at high shear rates they promote sample ejection and other edge instability. Difficulty is overcome by using capillary rheometer which unveils a new shear-thinning regime upon shear-thickening. Even if observed for different systems, this regime is not well understood. Some invokes the deformability of particle at high stresses. Moreover, stress inhomogeneities can induce shear-induced particle migration, leading to spatial inhomogeneities. This features is not completely understood especially for shear-thickening systems.

Impact of formulation on the rheology of plastisol has been partially explored. In particular, review on different concentrated suspension show that physico-chemistry of particle surface is critical in the rheological response of the suspension. For example, some surfactant can delay shear thickening by enhancing the repulsion force stabilizing particles. But for plastisol, no quantitative and extensive study on the role of surfactant exist up to now. The few studies report some effect but rather at low shear rate before shear thickening. They focus on one or two surfactants, but commonly used surfactant in PVC synthesis are more numerous. Besides, moisture content is empirically known to impact rheology but again few studies on the subject are incomplete, especially the coupling between surfactant and moisture effect is unexplored.

Concerning the particle size distribution, granulometry of PVC are been rather well explored and is naturally found to be critical in the resulting paste viscosity. In particular, the wider the size distribution, the less shear thickening observed. However, filled plastisol are also extensively used. In these suspensions, some PVC powder (up to half in volume) is replaced by a filler with completely different characteristics (shape, size, surface chemical nature...). Surprisingly, impact of adding filler in the PVC paste has not been extensively studied. In particular, changes on the viscosity are mainly known empirically. No predictive model allows to a priori predict the effect of filling the plastisol.

At this stage, many questions remain unanswered. In this PhD dissertation, by studying a plastisol, we will address the following questions:

— **The link between the transition into frictional regime at the particle scale and the transition of shear thickening at the macroscopic scale will be experimentally shown in chapter 3.**
— **The way a shear-thickening flows depending on the concentration and the flow geometry will be also explored in chapter 3.**
— **The variation rheological properties (both viscosity and maximum packing fraction) when dispersing filler and PVC together is investigated in chapter 4**
— **The influence of surfactant and moisture content on rheological properties of a plastisol is studied in chapter 4 too.**
— **Instabilities of coating a concentrated suspension in chapter 5.**

1.10 Summary

— Interactions are primordial in concentrated suspensions and explain non-Newtonian behaviour
— Shear thickening is recently thought to be the consequence of microscopic breakdown of lubrication film
— Suspensions exhibit normal stress differences at high shear rate
— Stress inhomogeneities can induce local particle inhomogeneities
— A plastisol as a concentrated suspension exhibits such features: shear thickening, normal stress difference...
— Literature on plastisol is mainly empirical. No quantitative model predict rheology when adding a filler which is the case in some pratical applications

Chapter 2

Materials and experimental methods

2.1 Characterisation of the raw materials

2.1.1 PVC powders

For this work, two different PVC powders were used, both synthetized from a micro-suspension polymerization. B7021 from Vestolit GmbH, is often used in industrial processes. However, this powder is highly polydisperse and contains some surfactants (see below). Thus, another PVC powder has been studied : P70 from Vinnolit. Its size distribution is narrower and it contains nearly no surfactant but has almost no use in industrial processes due to its high shear-thickening behaviour. This powder is considered as a "model" system for our study even if a lot of experiments were done also on B7021 due to its industrial relevance. **In the following, the P70 powder is called PVC 1 and the B7021 (more polydisperse) is called PVC 2**.

Different characterisations were done on the PVC powder (density of 1.4). First, the powder was imaged using a scanning electronic microscope. Pictures for PVC 1 and for PVC 2 are presented on Fig. 2.1. In both cases, the particles exhibit a round shape even if they are not perfectly spherical. PVC 2 shows a lot more small particles (under 1 μm) and is more polydisperse than PVC 1 as detailed below in granulometry measurements. However even PVC 1 shows a level of polydispersity. A closer look on the surface of particles is presented on fig 2.2. Nanometric rugosity can clearly be seen.

Figure 2.3 compares the granulometry of PVC 1 and PVC 2 directly in the plasticizer. For the PVC 1, the mean particle diameter is 2 μm. The size distribution is lognormal and the standard deviation estimated using the volume distribution is 45%. No aggregates are present. For PVC 2, the particle size histogram using a volume distribution is bimodal with lognormal peaks around 700 nm (standard deviation of 25%) and 6.6 μm (standard deviation of 55%). Again, this powder contains nearly no aggregate (typical size of tens of μm). Specific surface of PVC 1 and PVC 2 are respectively 2.13 and 1.57 m^2/g.

2.1.2 Surfactant on PVC 2 powder

Due to its synthesis process, surfactant remains on the surface of PVC particles purchased from supplier [199]. There are few powders on the market where surfactant is industrially removed from the powder. PVC 1 is one of them. This feature can simply be observed by putting a water droplet

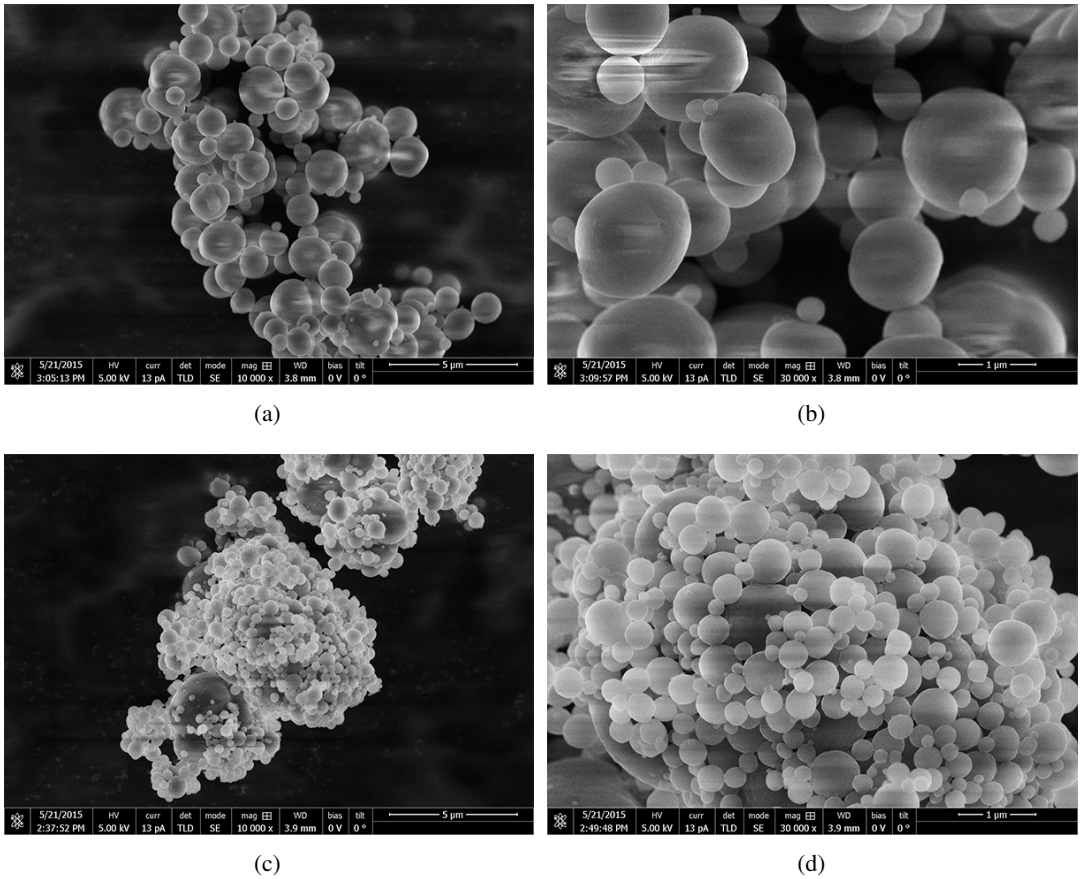

Figure 2.1: SEM image of PVC 1 (dry powder) at a zoom of (a) 10 000 x and (b) 30 000 x. Same for PVC 2 at (c) 10 000 x and (d) 30 000 x. In both cases, the particles are roughly spherical. PVC 2 shows a lot more small particles (under 1 μm) and is more polydisperse than PVC 1 as detailed below in granulometry measurements. However even PVC 1 shows a level of polydispersity.

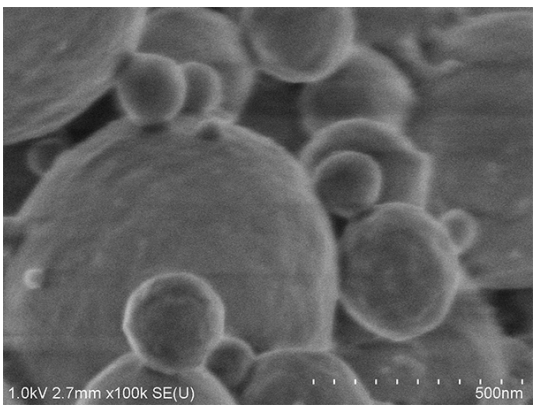

Figure 2.2: Zoom on surface of PVC particles (PVC 2). Surface is not really smooth and exhibits some nanometric roughness.

on a PVC powder bed. Water stays on the powder until evaporation and do not wet the PVC powder (cf. Fig. 2.4) as pure PVC is hydrophobic. Doing the same on PVC 2 (which does contain surfactant) results in a nearly instantaneous wetting of the powder by the water droplet.

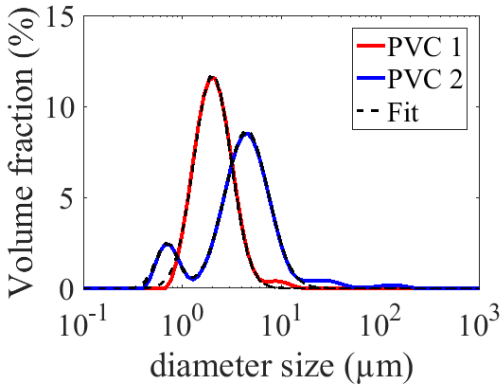

Figure 2.3: Comparison of particle size distribution of PVC 1 (one log normal peak) and PVC 2. For the PVC 1, the mean particle diameter is 2 μm. The size distribution is lognormal and the standard deviation estimated using the volume distribution is 45%. For the PVC 2, the particle size histogram using a volume distribution is bimodal with lognormal peaks around 700 nm (standard deviation of 25%) and 6.6 μm (standard deviation of 55%).

Figure 2.4: Picture of a water droplet which does not wet PVC 1 (PVC powder without any surfactant on its particle surface).

On the contrary, PVC 2 contains surfactant. A water droplet wets very fast (less than 1 s) the powder when deposed on it. Identification and quantification using elementary analysis have been done.

2.1.2.1 Identification

15 g of PVC was mixed overnight in water (100 mL). Suspension was filtered on a sintered filter equipped with vacuum pump . Supernatant was retrieved and further purified from finest particle on a 220 nm filter. Remaining solution was dried using a freeze-drier. Freeze-dried solid was analysed by NMR spectroscopy in solvent D_2O (cf. Fig. 2.5).

A comparative NMR analysis of Sodium Dodecyl Benzene Sulfonate (SDBS) was done : a good match between spectra was obtained. Hydrogen atoms from the benzene group are found at a displacement of 7.11 (b) and 7.69 ppm (a). Hydrogen atoms from different alkyl chains (mix of isomers, cf. fig 2.5 where R1 and R2 can be different) are responsible for the broad peak (c) between 0.5 and 1.5 ppm. The most important peak at 4.8 ppm is due to deuterated water, the solvent used for NMR (hydrogen peak from H_2O. It was experimentally found that SDBS is not soluble in platicizer (DINCH) but is completely solubilized in water.

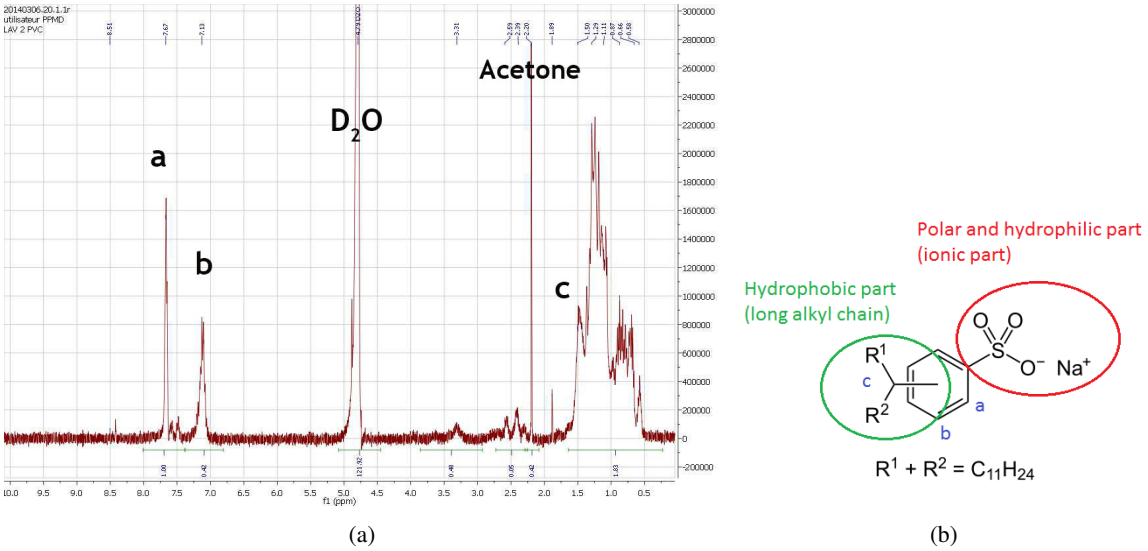

(a) (b)

Figure 2.5: (a) NMR spectroscopy on concentrated supernatant (b) Chemical formula of SDBS (Sodium Dodecyl Benzene Sulfonate, M = 348.5 g/mol) with its hydrophilic and its hydrophobic part.

2.1.2.2 Quantification

Once the surfactant has been identified, it is relevant to assess the total amount of SDBS in the PVC powder. An elementary analysis was carried out on PVC powder especially for sulphur atom (sulphur atom is found only in the surfactant and not in pure PVC). The results are presented in the table 2.1.

Element	Cl	C	O	H	N	**S**
Content (wt %)	56	39.1	0.47	5.0	<0.1	**0.1**

Table 2.1: Results of elementary analysis for commercial PVC powder.

An amount of 0.1 wt % of sulphur is found, which correspond to **1.1 wt %** of surfactant in the powder. This surfactant is spread on all the surface of elementary sub-particles and not only on the apparent surface of agglomerated biggest particles.

2.1.3 Plasticizer

Only one plasticizer of PVC has been used in this study: 1,2-Cyclohexane dicarboxylic acid diisononyl ester produced by BASF under the tradename of Hexamoll DINCH (called DINCH in this work). It is an aliphatic ester but is not a phtalate due to the hydrogenated aromatic ring. Density is 0.95. The DINCH slightly dissolves the outer part of the particles and creates a swelled polymer brush at particle surface as described in the literature (cf. part 1.8.1.3). This layer enables stabilization of the suspension due to steric repulsion [164]. At high temperature ($T \geq 100°C$), DINCH can dissolve the PVC particles [1]. At room temperature, this process is much slower and takes more than one year.

Viscosity of this plasticizer has been measured over a wide range of shear rate (cf. Fig. 2.6). Newtonian behaviour has been found with a viscosity of 41 mPa.s. Capillary measurements were carried out on the air-pressurized home-made capillary. Precise calibration of diameter was done using a oil with a known viscosity of 12.64 Pa.s at 25 ˚C. A diameter of 0.388 mm was found (0.400 mm

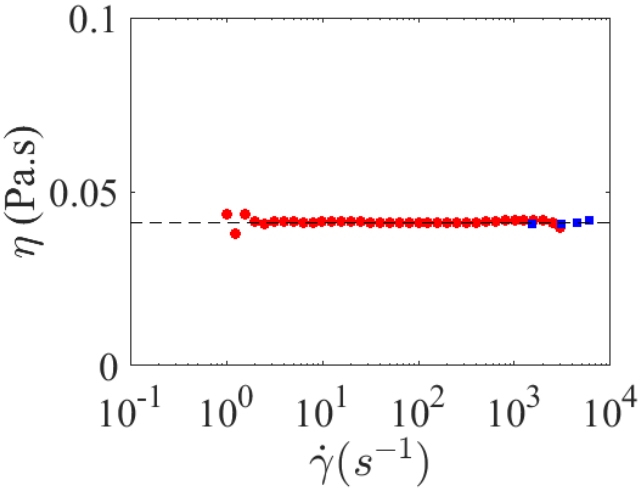

Figure 2.6: Viscosity of plasticizer DINCH at 25 ˚C measured in a Couette cell (●) and in a capillary (■). The dotted line stands for 41 mPa.s.

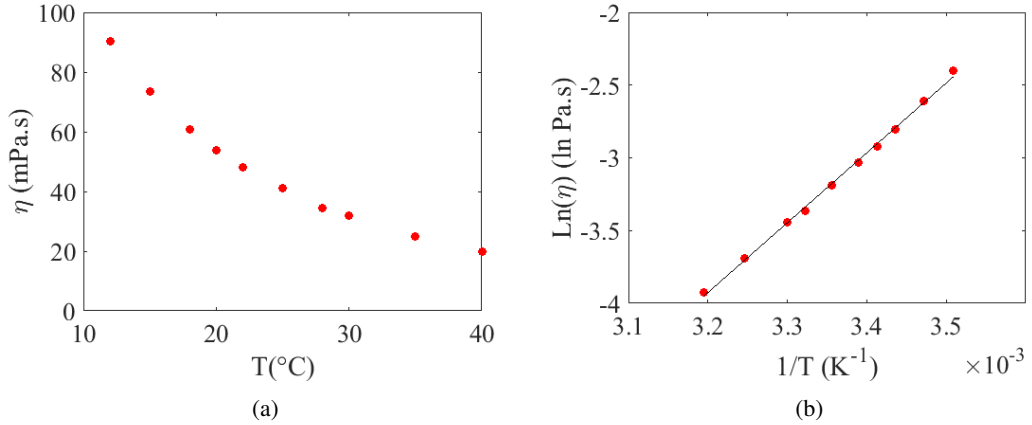

Figure 2.7: (a) Viscosity of plasticizer VS temperature (b) Same curve plotted following Arrhenius scaling. Solid line represent fit using Arrhenius law.

on datasheet). These small differences in diameter are important in the calculation as the shear rate is proportional to the radius power -3. The calibration step allows a good match between Couette Cell measurements and capillary measurements.

DINCH viscosity was also measured for different temperatures. Plasticizer viscosity follows an Arrhenius law:

$$\eta(T) = Ae^{-\frac{E}{RT}} \tag{2.1}$$

Obtained parameters (figure 2.7) are for the pre-exponential factor A =$4.15.10^{-9}$ Pa.s and for the activation energy E = 39.9 kJ/mol. In this study, rheological experiments performed in a rheometer on concentrated suspension were always done at a temperature of 25 ˚C (viscosity of interstitial fluid: 41 mPa.s).

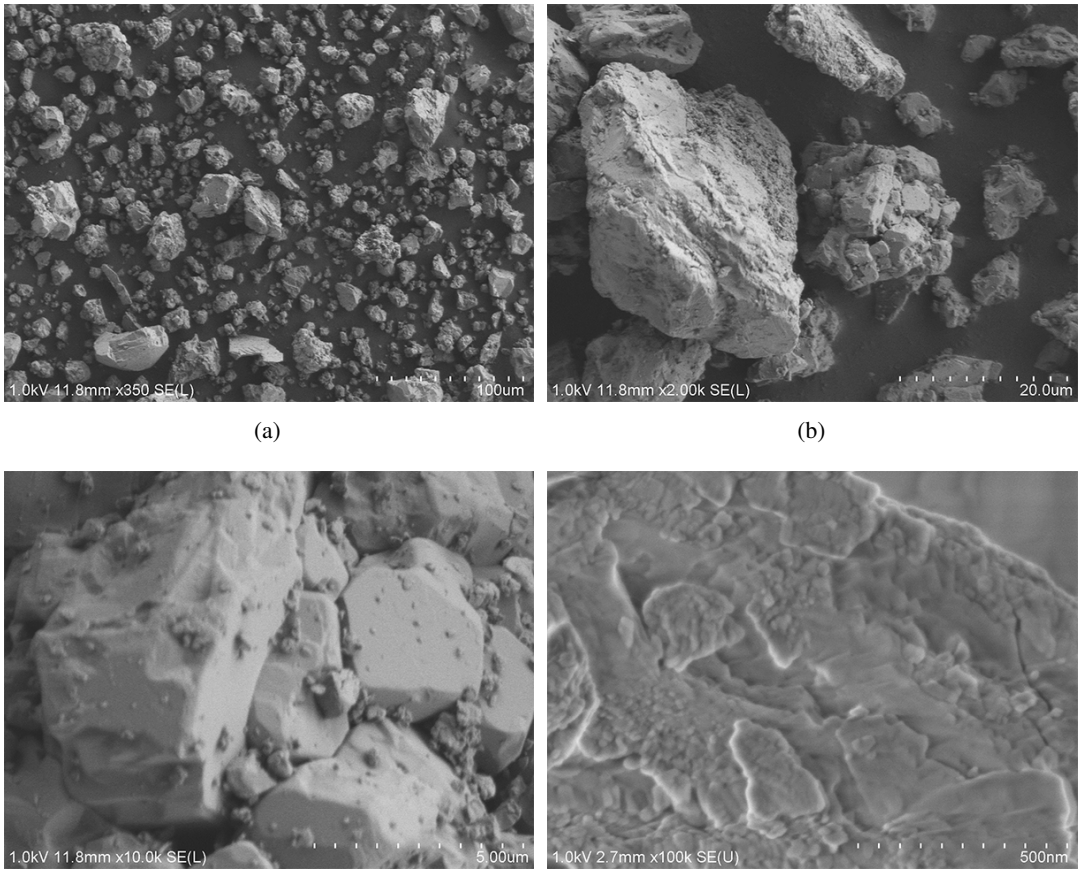

(a) (b)

(c) (d)

Figure 2.8: SEM pictures of calcium carbonate filler M (reference filler in this work). Crushing process leads to high polydispersity (D50= 22.6 μm) and irregular shapes with many ridges and edges (contrary to PVC which was quite spherical). Moreover, surface exhibits some roughness with very small particles stuck on it (cf. picture (d)).

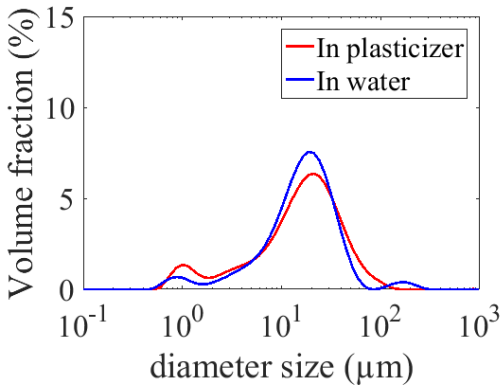

Figure 2.9: Particle size distribution of reference filler M measured in water and in DINCH. The measure depends here slightly on the dispersion medium.

2.1.4 Fillers

Reference filler used in this work is Omya BL20 which is a ground calcium carbonate (GCC) made of coral limestone with a D50 of 22.6 μm. It will be denoted filler M in the following. It

consists mainly in $CaCO_3$, especially the polymorph calcite (refractive index 1.57). Its density is 2.7. Electronic microscopy has been done on filler (see Fig. 2.8). Particles have very irregular shapes in link with the crushing process. Particle size distribution has been measured using laser diffraction apparatus Mastersizer 3000 both in water and in plasticizer (cf. Fig. 2.9). Unlike PVC, the liquid phase has nearly no impact on filler size distribution.Size distribution is pretty wide with a main peak around 20 μm.

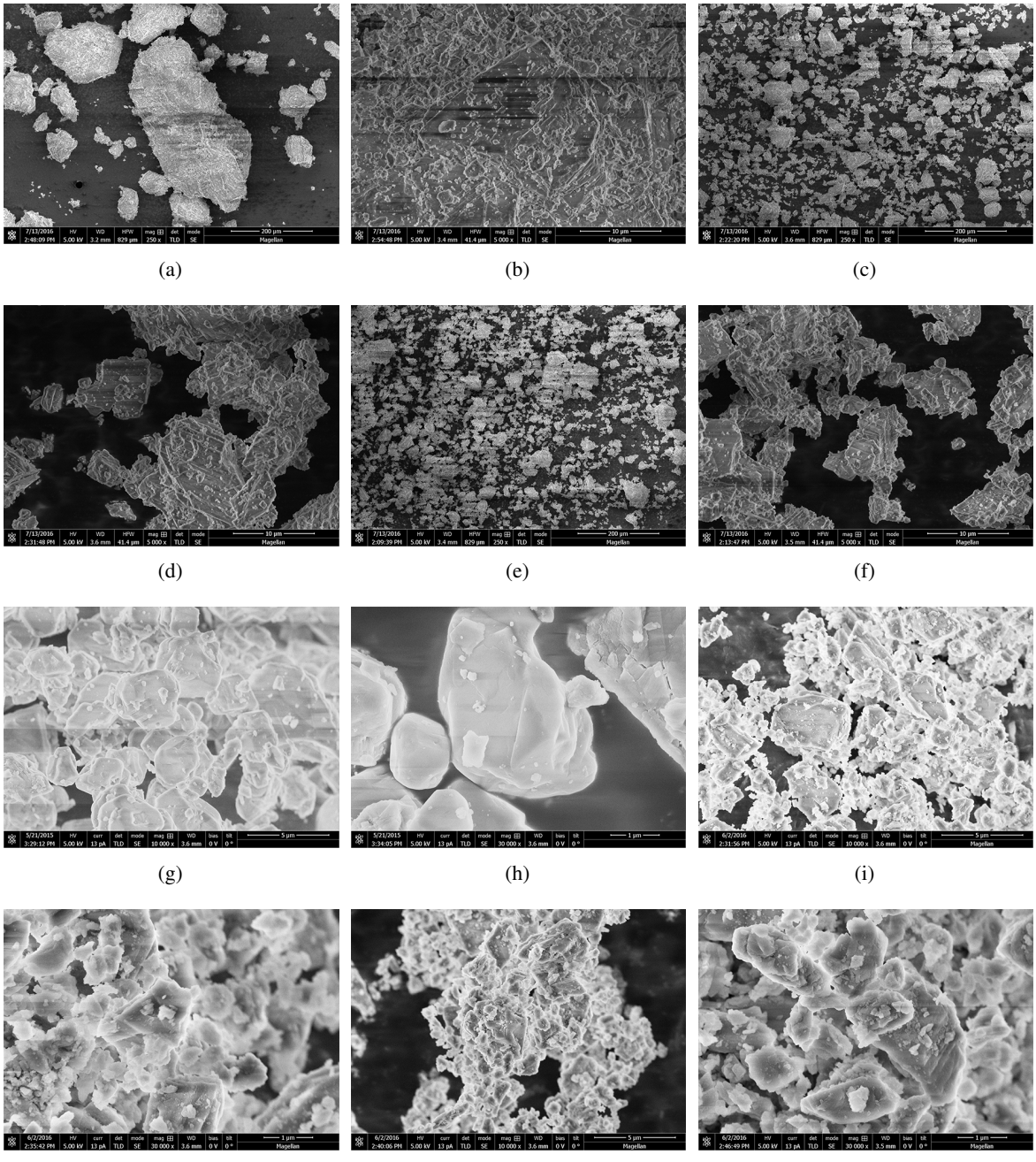

(a) (b) (c)

(d) (e) (f)

(g) (h) (i)

(j) (k) (l)

Figure 2.10: SEM pictures of other fillers than reference Filler M: (a)(b) XXL with D50 = 251 μm (c)(d) XL with D50 = 159 μm (e)(f) L with D50 = 68.3 μm (g)(h) S with D50 = 6.9 μm (i)(j) XS with D50 = 2.7 μm and (k)(l) XS-treated with D50 = 2.4 μm. As for reference filler, shape is very irregular and surface rough.

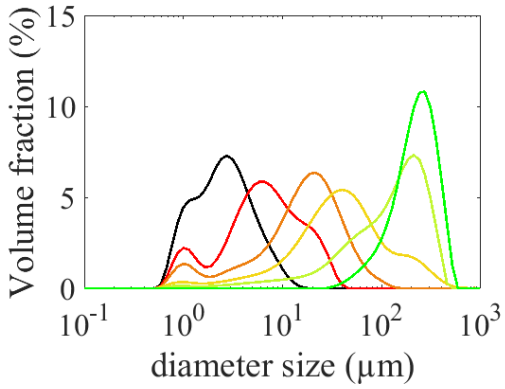

Figure 2.11: Comparison of filler particle size distribution: XS (■), S (■); M (■); L (■); XL (■) and XXL (■)

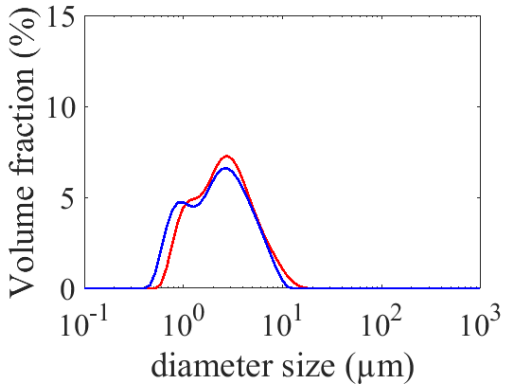

Figure 2.12: Comparison of particle size distribution of smallest filler XS between untreated surface (blue) and hydrophocally-treated one (noted XS-treated, red line). Both are very similar. Surface modification does not modify granulometry.

Name in with work	Commercial name	Specific surface (m^2/kg)
XXL	Durcal 130	11.5
XL	Durcal 65	59.7
L	Durcal 40	142
Medium M	BL20	327
S	BL200	552
XS	Hydrocarb OG	1034
XS-treated	Hydrocarb 75 T	1238

Table 2.2: Name, trade name and specific surface (estimated from granulometry measurements) of different fillers used in this work.

In order to study influence of filler size, different calcium carbonate filler size were used. To simplify commercial names, reference filler is written M in the following (medium) and other filler are noted XS (extra small), S (small), L (large), XL (extralarge), XXL. All names and specific surface of fillers used in this work are reported in table 2.2. Size distributions are on Fig. 2.11. All fillers exhibit the same irregular shapes than filler M (cf. electronic microscopy images on fig 2.10)

For XS filler, which is the filler with the smallest mean size (D50= 1.8 μm), the same product but with an hydrophobic treatment (fatty acid) is also available and used here (tradename Hydrocarb 75T). It is written "XS-treated" in the following. Granulometry is nearly not modified by the treatment (cf. Fig. 2.12).

2.1.5 Cornstarch

Cornstarch dispersed in water is a well-known shear thickening system [81, 60]. Even if it is not the main system of the PhD, the comparison between the two systems is of interest from a number of perspectives: shear thickening, particle migration... Cornstarch was supplied by Sigma Aldrich and used without further modification. It contains approx. 73% amylopectin and 27% amylose with particle diameter around 14 μm (polydispersity 40% from static light scattering) [60].

2.2 Sample naming

All solid loading are expressed in volume. We prepare our dispersions by weighting a given amount of PVC particles and a given amount of DINCH. The solid fractions are then calculated knowing the density of PVC $\rho_{\text{PVC}} = 1.38$ g.cm^{-3}, the density of DINCH $\rho_{\text{DINCH}} = 0.95$ g.cm^{-3}. The solid volume fraction of the suspension is defined as the volume of particles divided by the total volume: $\phi = \frac{m_{\text{PVC}}/\rho_{\text{PVC}}}{m_{\text{PVC}}/\rho_{\text{PVC}}+m_{\text{DINCH}}/\rho_{\text{DINCH}}}$. **In this work, a suspension made of PVC 1 (respectively PVC 2) dispersed in plasticizer will be denoted D1 (respectively D2)**. For example, a suspension made of PVC 1 dispersed at 60 vol% will be denoted as D1 60%. In the last chapters, more complex suspensions are studied: PVC powder and filler powder are dispersed together in the plasticizer liquid phase. For example, a suspension made of 33 vol.% of PVC 1, 30 vol.% of filler Medium (so 37 vol.% liquid) will be denoted as "PVC 1 33% - Filler M 30%".

2.3 Dispersion protocole

(a) (b)

Figure 2.13: (a) Mixing device *Dispermat LC55* used for sample preparation. (b) Used impellers geometry which ensure high shear rate and a well dispersed sample.

As granulometry and dispersion quality are critical for rheological properties, a well-defined protocol of dispersion was set up. Complete dispersion is achieved using a *Dispermat LC55* ® from *VGA Getzmann* (cf. Fig.2.13). The volume of the batch was always 25 mL (diameter of container = 50 mm). Protocols depends on sample type:

— **Unfilled plastisol**: Add plasticizer and PVC powder in a plastic container. Mix with spatula to get a complete wetting of powder. Use mixer 5 min at 1000 rpm (diameter of the impeller = 30 mm)

— **Filled plastisol**: Due to their different rheological behaviour, protocol has been slightly modified. First add PVC and filler powders in a plastic container (order does not matter). Mix them with spatula. Add the plasticizer. Mix with spatula to get a complete wetting of powders. Use mixer 5 min at 750 rpm for PVC-filler-plasticizer sample (diameter of the impeller = 40 mm).

The stirring time was optimized in order to ensure reproducibility of rheological experiments. Moreover,the parameters (diameter of impeller, size of the container...) were chosen to ensure a good mixing ("doughnut" shape of the sample during mixing) following advices from the supplier of Dispermat® mixing system. Reproducibility of the protocol was checked by comparing the viscosity obtained with these protocols and the ones usually mixed at Tarkett $R\&I$ center on larger scale (a few kilos) as displayed on Fig. 2.14.

The temperature was followed during the mixing and, if needed, the dispersion were done in several steps to keep a temperature of the sample below 35 ˚C in order to avoid plasticizer diffusion into PVC particles which can affect viscosity (promote ageing). Samples were freshly mixed before each experiment.

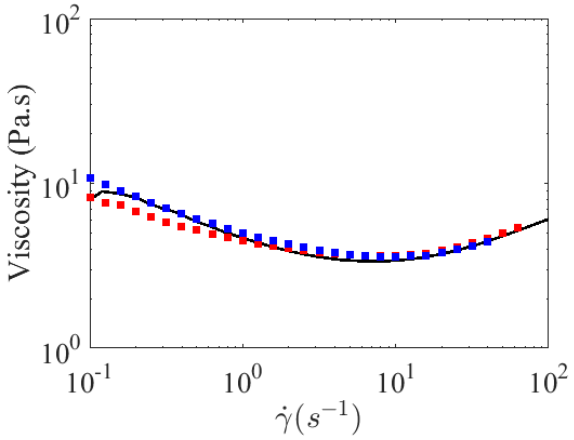

Figure 2.14: Comparison between results on a 3-litres batch prepared at Tarkett R& D center (black solid line, no degassing) and results on a 25 mL sample made in the lab without degassing (■) and with degassing (■).

Besides, the presence of surfactant in PVC 2 and absence in PVC 1 can be noticed when observing both suspensions just after preparation under vacuum. Suspension D2 exhibits white foam formation while, for D1, nearly no foam appears. The high-speed dispersing process includes air in the sample. Small bubbles are more stabilized in D2, certainly due to its surfactant content. A long time under vacuum can achieve total bubble removal (degassing). Impact of these small bubbles on rheological properties was assessed (cf. Fig. 2.14). In fact, these bubbles do not really affect rheology except a little bit at low shear rate. Then, unless otherwise specified, samples were prepared according to the protocol detailed above.

Behaviour is little bit different for a filled formulation where degassing has a non-negligible impact on rheology up to 1 s^{-1} (cf. figure 2.15). Even if, in industrial process, no degassing is done on this

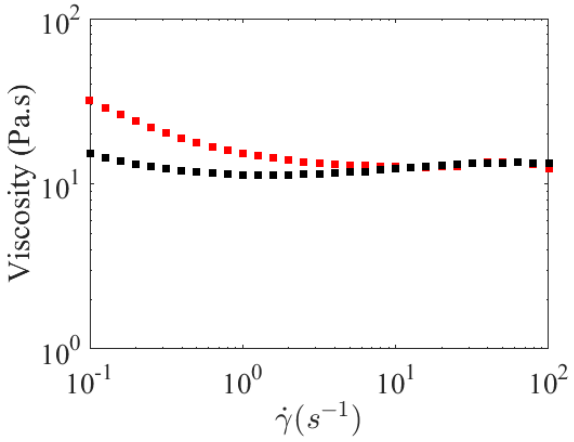

Figure 2.15: Viscosity of a suspension made of 25.6% PVC and 38.5% Filler (size M) without degasing (■) and with degasing (■).

kind of filled formulations, degassing was always (unlike specified) performed on filled formulations to remove air contribution to the rheology.

2.4 Surfactant-modified PVC

To investigate the role of surfactant in PVC concentrated suspensions, modified PVC powder has been prepared. PVC 1 was used as a convenient source of PVC sold without surfactant at particle surface. To modify surface, surfactant, 100 mL water and 50 g of PVC were mixed all together overnight. The dispersion was dried with a freeze-drier and modified dried PVC was retrieved. Surfactant-containing powder was thus used for suspension preparation following the protocol described in 2.3.

2.5 Granulometry

Granulometry measurements were done on a Mastersizer 3000 which is a laser diffraction apparatus. The cell was a Hydro SV small volume ($\sim$ 6 mL) wet sample dispersion unit. It consists in two parallel glass plates where the sample is in between. The Hydro SV enables measurements in all kinds of liquids without cleaning of long plastic pipes. This device uses the technique of laser diffraction to measure particle size distributions from 10 nm to 3.5 mm. During measurements, the laser goes through the cell and the liquid is stirred with a small magnetic agitator. The scattered intensity is then analysed for different scattering angles to calculate the size of the particles .

Samples for granulometry were always dispersed prepared at high volume fraction (typically 60 %) following the protocol described in 2.3. They were then diluted (one droplet in 100 mL of plasticizer) and added droplet by droplet in the Mastersizer cell to reach optimum absorbency needed by the apparatus.

2.6 Plasticizer absorption value

This test is inspired from oil absorption test which is often used in industry especially for pigments (for example ISO 787-5:1980 or ASTM D281). The plasticizer absorption value $\phi_{\text{absorption test}}$ is the maximum packing fraction determined by measuring the minimum amount of liquid needed to wet a known amount of dry powder. It is measured following this protocol:

— Weight a fixed amount of powder in a plastic vial (make the reference weight with the spatula, see Fig. 2.16a)

— Add the plasticizer drop by drop to the powder. After the addition of each drop, thoroughly incorporate the plasticizer by rubbing up with the spatula. Powder is progressively wet and looks like a "crumble" (Fig. 2.16b-c-d)

— Do this until reaching a very stiff, putty-like paste that is homogeneous (Fig. 2.16e) and does not break or separate (neither cracking nor crumbling) . Weight thus the total powder to know the added amount of plasticizer.

— Compute the volume fraction of the powder $\phi_{\text{absorption test}}$ thanks to weight of powder and plasticizer.

This test is reproducible and a precision of one droplet can be achieved. As it will be detailed later, this test does not give exactly the random close packing (ϕ_{rcp}) but a slightly lower value (see detailed part 3.3). Then it can be used for screening different formulations. It has also the great advantage of being fast (10-15 min), uses a few grams of products and does not require extensive rheological

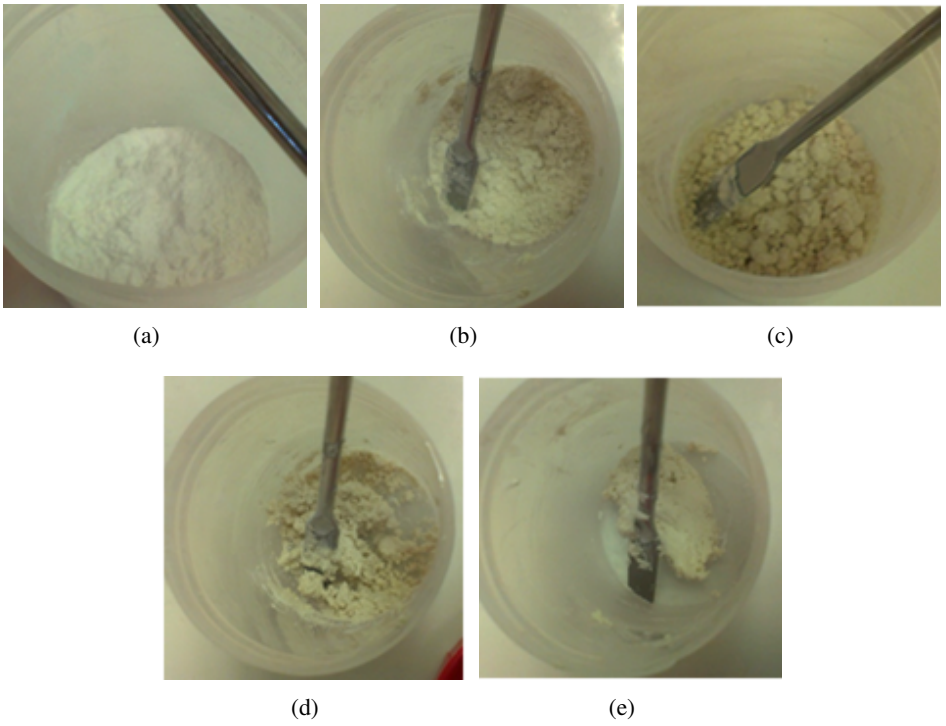

Figure 2.16: Plasticizer absorption test: (a) initial state with dry powder (b)(c)(d) with adding more and more plasticizer but not enough to obtain an homogeneous paste (e) with the right amount of plasticizer to wet all the powder.

measurements. Such tests have been already performed for some PVC powders or some fillers in plasticizer especially for comparing different powders [200, 191] but such measurements are also extended in this work for mixes of PVC and filler.

2.7 Rotational rheometer

2.7.1 Used rheometers

Different rheometers were used in this study: a controlled strain ARES, a controlled stress DHR3 or a controlled stress ARG2, all from *TA instruments*. For logistic reasons, experiments from chapter 3 were mostly carried out on the controlled strain ARES rheometer. Cone/plate, plate/plate and Couette cell geometries were used for measurements. When specified, cross-hatched geometries were used to prevent slip at the wall.

For the stress-controlled rheometer, the lower part is fixed and the upper part contains the motor and the sensor. For the strain-controlled rheometer, the lower part imposes the deformation and the upper part contains the sensor.

Here are the characteristics of geometries for controlled stress DHR3:

— Smooth cone (diameter D = 40 mm, angle = 2 $^\circ$, truncation gap = 54 μm).

— Couette cell (inner radius R_i= 14 mm, outer radius R_o= 15 mm, bob length = 42 mm)

— Cross-hatched plate/plate (diameter D = 40 mm)

For the controlled strain ARES, it was used at the beginning of the PhD for PVC suspensions mainly in cone and plate geometry:

— Smooth cone (diameter 25 mm, angle = 2.3 °, truncation gap = 43 μm)

— Smooth cone (diameter 50 mm, angle = 2.3 °, truncation gap = 50 μm)

2.7.2 Basic of rheometry

We give only important results, all details from calculation can be found in textbooks [201]. In the following, η is the viscosity (Pa.s), $\dot{\gamma}$ the shear rate (s^{-1}) and σ the shear stress (Pa).

$$\eta = \frac{\sigma}{\dot{\gamma}} \tag{2.2}$$

Torque from the rheometer is noted Γ and Ω is the rotation speed (rpm)

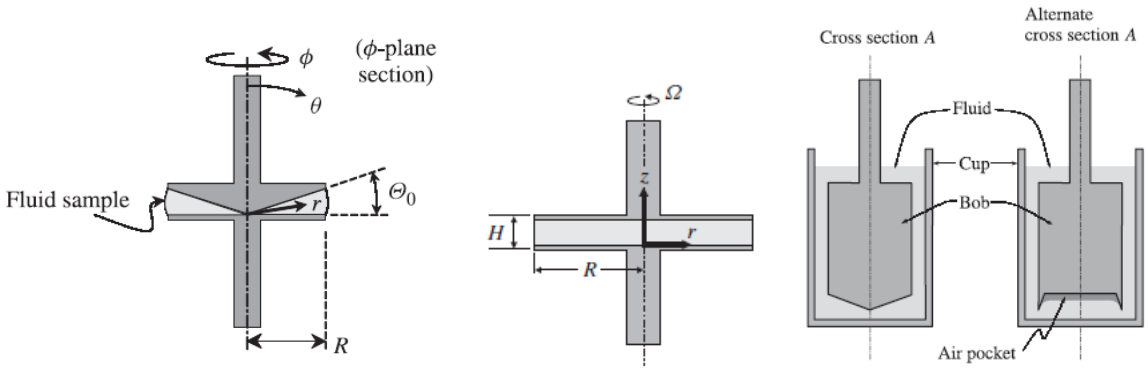

Figure 2.17: Details of different geometries used in this thesis : (a) Cone and plate (b) Plate-Plate (c) Couette cell with the two main designs for the bottom. [201]

2.7.2.1 Cone and plate

Flow is induced by rotation (speed Ω). The cone (radius R and angle α) is fixed on top of a plate surface at a distance h (h= truncature gap $\sim$ 50 μm). A schematic is on fig 2.17a. If α « 1, shear rate and shear stress are homogeneous is the geometry:

$$\dot{\gamma} = \frac{\Omega}{tan\alpha} \tag{2.3}$$

$$\sigma = \frac{3.\Gamma}{2\pi R^3} \tag{2.4}$$

Homogeneous strain in the sample is the main advantage of this geometry which is however limited to small size of particle (avoid any blocking at the center). Cone and plate geometry allows measurements of the first normal stress difference N_1 using axial force F sensor:

$$N_1 = \frac{2F_z}{\pi R^2} \tag{2.5}$$

2.7.2.2 Plate and plate

Flow is induced by rotation (speed Ω). The plate (radius R) is on top of a similar plate at a gap h. A schematic is on fig 2.17b. Here, shear rate and shear stress are not spatially homogeneous. Assuming a Newtonian fluid, shear rate $\dot{\gamma}$ and stress σ are given by:

$$\dot{\gamma}(r) = \frac{\Omega r}{h} \tag{2.6}$$

$$\sigma(r) = \frac{2\Gamma}{2\pi r^3} \tag{2.7}$$

Here are reported values at the rim for r = R

$$\dot{\gamma}(R) = \frac{\Omega R}{h} \tag{2.8}$$

$$\sigma(R) = \frac{2\Gamma}{2\pi R^3} \tag{2.9}$$

Measuring axial force F with this geometry gives access to the second normal stress difference N_2:

$$N_1 - N_2(\dot{\gamma}(R)) = \frac{F}{\pi R^2}(2 + \frac{d(ln(F))}{d(ln(\dot{\gamma}(R)))}) \tag{2.10}$$

2.7.2.3 Couette cell

The geometry consists of two coaxial cylinders (radii R_1, R_2 with $R_1 < R_2$, height H). The rotation speed is denoted Ω.

The fluid in the bottom of the cup is assumed to transfer a small stress compared to the one from the fluid in the narrow gap. In fact, bob are designed along two ways: (i) bottom has a cone geometry. Gap is adjusted to truncature gap and cone/plate contribution is subtracted or (ii) bottom is drilled so as to a bubble is trapped when loading the bob. No stress stems from the bottom (slip condition at the air/sample interface). A schematic is on fig 2.17c.

In this geometry, stress and shear rate are not spatially homogeneous. Stress is given by (r^2 decay)

$$\sigma(r) = \frac{\Gamma}{2\pi H r^2} \tag{2.11}$$

Assuming a small gap, i.e $R_2 - R_1 \ll 1$ which is often the case for commercial geometries:

$$\sigma \approx \frac{\Gamma}{2\pi H R_1^2} \tag{2.12}$$

$$\dot{\gamma} \approx \frac{2\pi\Omega R_2}{R_2 - R_1} \tag{2.13}$$

2.8 Capillary rheometer

In the framework of this project, measurements with a cone and plate geometry on a rotational rheometer is quite limited to shear rate $\sim 100\ s^{-1}$ owing to sample ejection (normal stress differences). However, a robust characterisation of viscosity is needed for shear rates up to $10^4 s^{-1}$.

2.8.1 Need for capillary rheometer

First idea was to change rheometer geometry and use a Couette cell geometry. In such a geometry, sample ejection is delayed (at higher shear rate). Figure 2.18 shows the measurements done in Couette VS Cone and plate for D2 at 60%. Results are almost similar in the range $10^{-1} - 100 s^{-1}$. However,

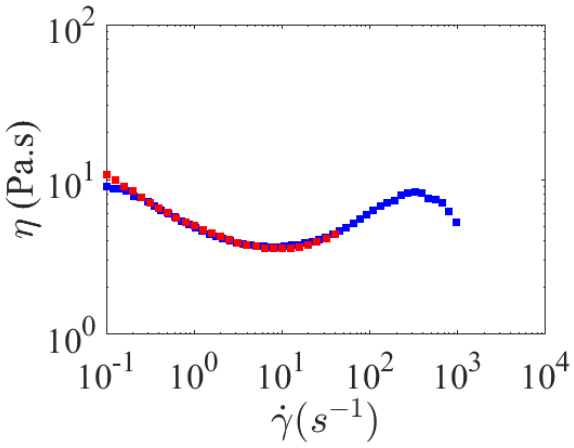

Figure 2.18: Measure of viscosity for D2 at 60% in a Couette cell geometry (■) compared to a measure using a cone and plate geometry (■).

the Couette measure allows to at higher shear rate, thus measuring the shear thickening transition (viscosity increase up to 300-400 s^{-1}). A shear thinning regime is measured in this case upon 500 s^{-1}. Sample ejection was observed upon 1000 s^{-1}.

One is however far away for the maximum value of $10^4 s^{-1}$. We use now capillary rheometer which is the most effective instrument for measuring shear viscosity at high shear rate (cf. figure 2.19)

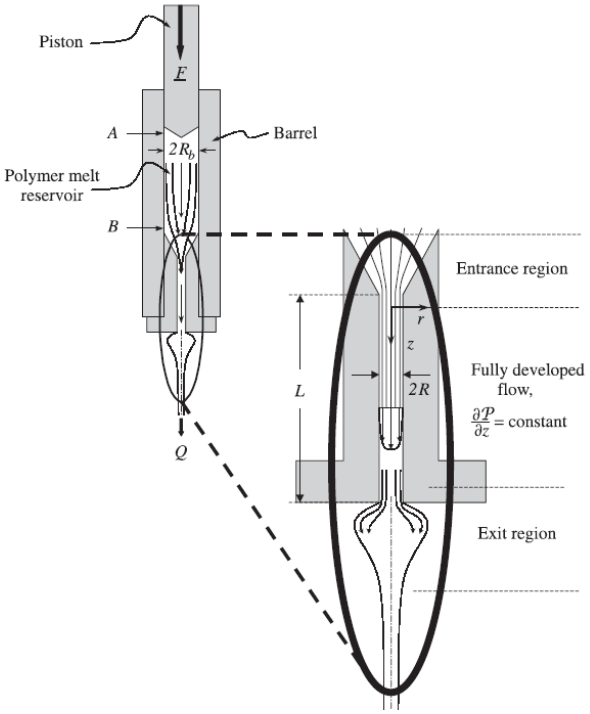

Figure 2.19: Geometry used in one type of commercial capillary rheometer. The bulk of the sample being tested resides in the upstream reservoir. A piston pushes the fluid through a small capillary of radius R, and the material exits at the bottom at a flow rate Q. The figure is not drawn to scale; the ratio of the capillary radius R to the barrel radius R_b is typically 10 to 1. [201]

2.8.2 Basics of capillary rheometry

We study the flow of a fluid through a capillary (radius R, length L). We give here only important results. All details can be found in textbooks (for example [201]) .

In this geometry, the stress is not spatially homogeneous and its value at the wall is given by:

$$\sigma_R = \frac{\Delta P R}{2L} \tag{2.14}$$

For the shear rate, assumptions are needed as the velocity profile is a priori unknown. For a Newtonian fluid, the value at the wall is equal to

$$\dot{\gamma}_{newtonian} = \frac{4Q}{\pi R^3} \tag{2.15}$$

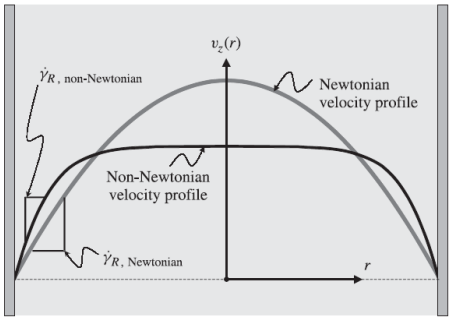

Figure 2.20: Schematic of the effect of material properties on the shear rate at the wall: Newtonian fluid VS shear thinning fluid. In the latter case, the shear rate at the wall is higher than in a Newtonian fluid with the same average velocity. [201]

For a non-Newtonian fluid, the velocity profile is different from a simple Poiseuille flow (cf. fig 2.20). Thus, the real shear rate at the wall is slightly different and given by the Weissenberg and Rabinowitsch correction [202]

$$\dot{\gamma} = \dot{\gamma}_{newtonian}(\frac{1}{4}[3 + \frac{dln(\dot{\gamma}_{newtonian})}{dln\sigma_R}]) \tag{2.16}$$

Two other corrections have to be taken into account: the Bagley correction (entrance pressure loss) and the Mooney analysis (slip at the wall).

Bagley correction (entrance pressure loss)

Up to now, we assumed that all the pressure drop was coming from the flow in the capillary over a length L. However, the flow takes some time to develop at the inlet (and may be disturbed at the exit for polymeric material). Then, a proportion of the pressure drop does not contribute to the flow in the capillary and can be estimated by carrying out measurements of pressure for various L/D [203]. When plotting the pressure versus L/D, y-intercept gives the pressure correction. Indeed, without entrance pressure loss, pressure drop would be directly proportional to L/D.

Slip at the wall (Mooney analysis)

To calculate a viscosity in a situation where slip is occurring, one must calculate the true shear rate near the wall; this analysis is due to Mooney [204]).

From equation 2.15,

$$\dot{\gamma}_{newtonian} = \frac{4Q}{\pi R^3} = \frac{4v_{av}}{R} \tag{2.17}$$

where v_{av} is the average fluid velocity in the tube. Nevertheless in case of wall slip, a corrected value for $\dot{\gamma}_{newtonian}$ may be obtained by substituting $v_{av} - v_{slip}$ for v_{av} in this expression, where v_slip is the wall slip velocity.

$$\dot{\gamma}_{newtonian,slip-corrected} = \frac{4v_{av}}{R} - \frac{4v_{slip}}{R} \tag{2.18}$$

Plotting $\frac{4v_{av}}{R} = \frac{4Q}{\pi R^3}$ versus 1/R at constant σ_R (Mooney plot) would give straight lines with a slope of $4v_{slip}$ and an y-intercept of $\dot{\gamma}_{newtonian,slip-corrected}$.

2.8.3 Commercial capillary rheometer

Figure 2.21: Göttfert capillary rheometer used in this work.

Measurements were performed in Sophia Antipolis at CEMEF (Centre de Mise en Forme des Matériaux) laboratory using a rheometer Göttfert Rheotester. Flow rate is imposed when choosing a piston velocity. A pressure sensor is positioned near the exit to measure wall pressure. Different formulations were measured : D2 at 60 and 64 %; D1 at 55% and 60%. **Details of calculations and approximations are described below only for D2 at 60%**. Then results for other formulations will be presented without all details.

Most data were obtained with a 0.5 mm die using different lengths: length over diameter ratio (noted L/D) of 4,8 and 16. Three different lengths allow to do Bagley pressure entrance correction. A die with a diameter of 0.3 mm was also used for Mooney analysis (L/D =4 and 8 in this case). Here, piston speed is imposed and is varied from 0.1 to 1 mm/s (0.1; 0.2; 0.4; 0.6; 0.8; 1 mm/s). As piston speed is proportional to shear rate, this device is a shear rate imposed rheometer. Speed range was chosen to achieve a range of shear rate from 920 to 9200 s^{-1} with a 0.5 mm die. Pressure is recorded with a pressure sensor of 100 bar (10 MPa) full scale. A trial uses around 20 mL of product. The pressure at rest, before imposing a piston speed, was always subtracted to the measured pressure (value

typically between 0 and 1 bar). As $\dot{\gamma} \sim D^{-3}$, die diameter was carefully checked using a optical microscope.

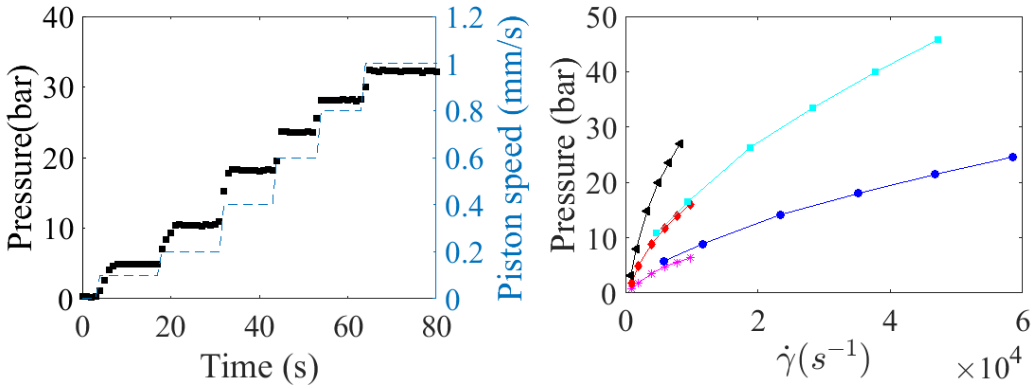

(a) (b)

Figure 2.22: (a) Typical graph of pressure from the sensor (■) versus time for all piston speeds. Blue dotted line reports piston speed (right y-scale). Here, the sample is D2 at 60% with 0.5 mm die and L/D=8. (b) Pressures from the plateau versus corresponding shear rate for all experiments on D2 at 60%: die diameter 0.5 mm with L/D=4 (∗), L/D=8 (◇), L/D=16 (◀)and die diameter 0.3 mm with L/D=4 (●)and L/D=8 (■).

A typical pressure diagrammed recorded during one experiment with D2 60 % is displayed on Fig. 2.22a. The pressure reaches steady state equilibrium fast (a few seconds) for each imposed speed. Values reported on Fig. 2.22b are steady state pressures for each plateau after subtracting reference pressure (pressure at zero speed). It is worthy to note that pressure do not increase linearly with the shear rate, implying a shear thinning behaviour of our sample in the range of studied shear rate. A more quantitative analysis will be done in the next paragraphs.

2.8.3.1 Bagley pressure correction

The Bagley diagram described theoretically in 2.8.2 and plotted on Fig. 2.23a for out suspension D2 60 % shows that pressure measurements are quite linear with capillary length. Bagley corrections can then be applied to get rid of entrance pressure losses. Ratios between pressure entrance loss and measured pressure are plotted on Fig. 2.23b. The correction is logically more important for the smallest ratio aspect (L/D = 4). For the longest one (L/D = 16), correction is relatively small with around 10-15 %.

To minimize error, we used now data from L/D=16. Figure 2.24 shows experimental points found with capillary rheometer superposed with data from rotational rheometer. As expected, a shear thinning behaviour is found (except first point which is discarded because of too low pressure for sensor) and follows shear thickening observed by conventional rheometry. Nevertheless, data are slightly shifted compared to data from rotational measurements. After Bagley correction, one needs to check wall slip and compute correction for non-Newtonian fluids.

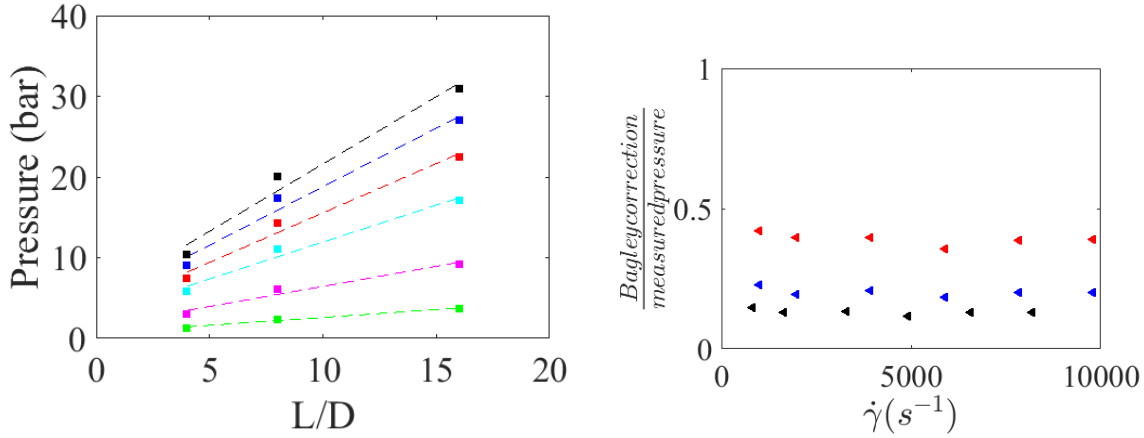

(a) (b)

Figure 2.23: (a) Bagley plot for D2 at 60% : pressure versus L/D for different shear rate: 925 s-1 (■), 1852 s-1 (■), 3703 s-1 (■), 5555 s-1 (■), 7407 s-1 (■), 9258s-1 (■). Dotted lines are linear fits. Their intercepts with y-axis represent entrance pressure losses for each shear rate. (b) Ratio between pressure entrance loss and measured pressure for L/D=4 (■), L/D=8 (■) and L/D=16 (■).

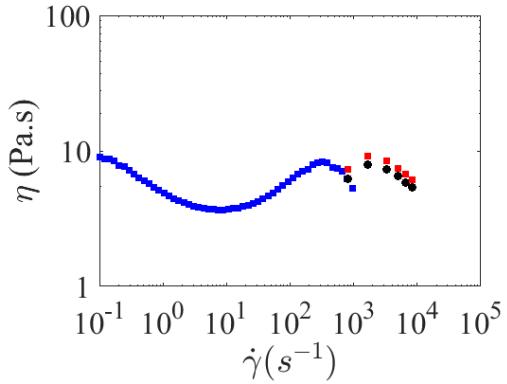

Figure 2.24: Viscosity measured on D2 60 % from capillary data with the Bagley correction (■) and without (■) for L/D=16. As a reference, measurements from the Couette cell geometry are also plotted (■)

2.8.3.2 Mooney analysis: slip at the wall

Slip at the wall can hinder reliable measurements. To quantify possible slip, measurements using a 0.3 mm diameter die are carried out. Figure 2.25a shows the results for the 0.3 mm die after Bagley corrections. Data are coherent with the ones found with the 0.5 mm. The viscosity decreases with the same slope upon $10^4 s^{-1}$. Measuring with another diameter allows for Mooney analysis (cf. part 2.8.2) to check for a possible slip at the wall. Mooney plot is on Fig. 2.25b. In this kind of graph, slope is proportional to slip velocity. However, the slope is here negative and would mean a negative velocity speed, which makes no sense. Thus, no wall slip in assume here. This choice will be more justified later when a master curve will be built. For other samples: Mooney analysis has been performed. Slightly negative slope is also obtained for D2 more concentrated (64 %). For D1 55 %, a slope of 0 is found (no wall slip) but not enough data is available for D1 60 %. To sum up, no wall slip is found for D2 (60 % and 64 %) and for D1 55 %. There is no conclusion for D1 60 %.

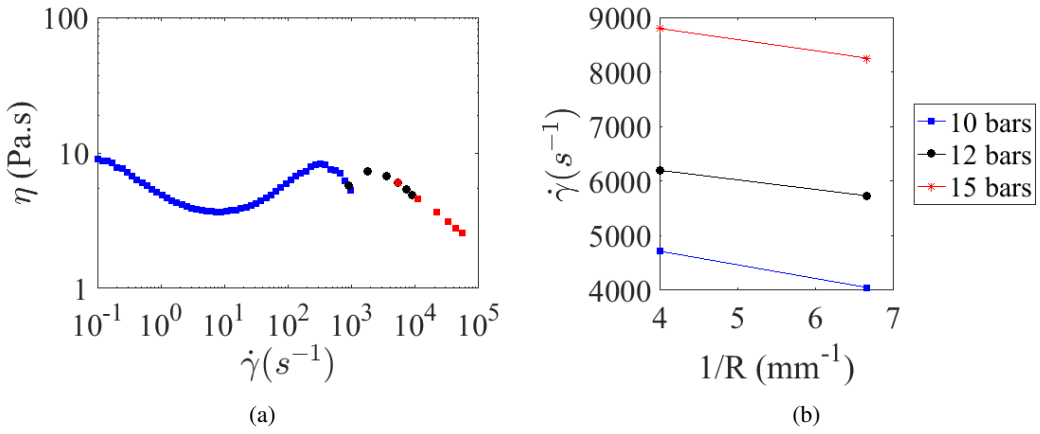

Figure 2.25: (a) New measurements with a die with a smaller capillary of 0.3 mm diameter (■) compared to ones with 0.5 mm diameter die (■) and Couette cell data (■) (b) Mooney diagram plotting shear rate versus inverse radius for three different pressures.

2.8.3.3 Weissenberg-Rabinowitsch correction for non-Newtonian fluids

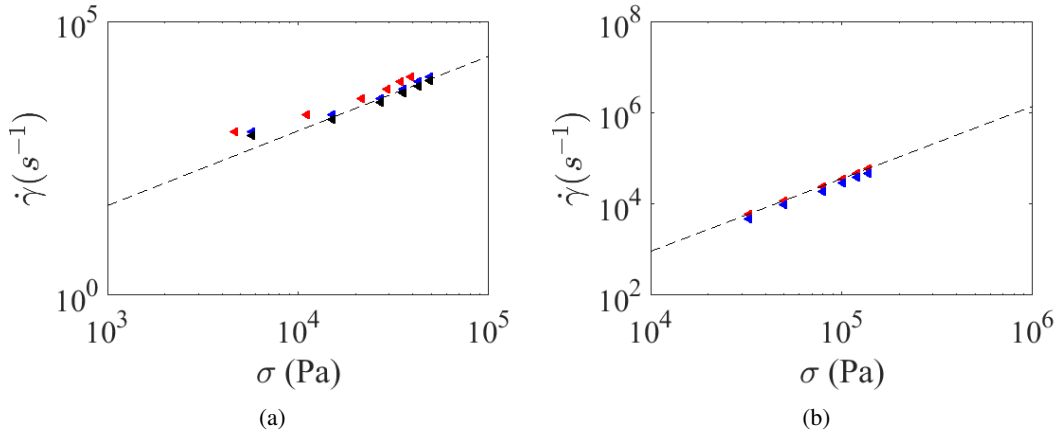

Figure 2.26: Logarithmic plot of shear rate versus stress for all measurements respectively with 0.5 diameter (a) and 0.3 mm diameter (b) for L/D = 4 (■); 8 (■) and 16 (■). Slope of dotted line gives the Weissenberg-Rabinowitsch correction for each die (respectively 1.36 and 1.59).

The Weissenberg-Rabinowitsch correction is needed for all non-Newtonian fluids. It allows to compute the real shear rate at the wall as velocity profiles for non-Newtonian fluids in capillary flow are non parabolic. Figure 2.26 shows the Weissenberg-Rabinowitsch plot for the 0.5 mm die (a) and the 0.3 mm die (b), namely shear rate versus stress, both in logarithmic plot. Data are fitted linearly (on data with L/D=16) and slopes (cf. black dotted lines: slope of 1.36 for left graph and 1.59 for right graph) are used to calculate real shear rate at the wall. For the 0.5 mm die, the first point is not fitted as it is very inaccurate if we compared the measured pressure (3.7 bar) to the full scale of the sensor (100 bar). Measurements with home-made capillary rheometer (see next section) will confirm the inaccuracy of this point.

The real shear rate at the wall is recalculated following eq. 2.16. By dividing the stress at the wall calculated from the corrected pressure by the real shear rate calculated here, the viscosity is now computed.

2.8.3.4 Conclusion

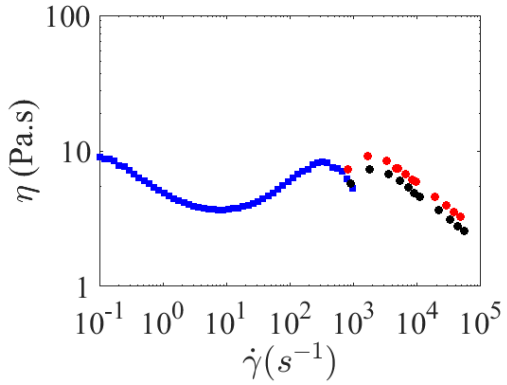

Figure 2.27: Data for viscosity of D2 at 60% using rheometer with a Couette cell (■) and a commercial Gottfert capillary rheometer: (■) without Bagley correction and Weissenberg-Rabinowitsch correction and (■) with the two corrections)

With the measurements done in a Couette cell and with a commercial Gottfert capillary rheometer, a quite continuous curve is obtained (cf. figure 2.27). The suspension is shear thickening at intermediate shear rate while shear thinning at high shear rate. Intermediate region for shear rate between 200 and 2000 s^{-1} is not clearly measured. A more sensitive sensor for the Gottfert rheometer (10 bars for example) could have been a good option to probe the shear rate range around 1000 s^{-1}. However, this sensor was not available at CEMEF lab. Then, an in-house-built capillary rheometer with compressed air was developed.

2.8.4 In-house-built capillary rheometer

2.8.4.1 Device presentation

Device is presented on fig 2.28. It consists in a a syringe with a piston and a capillary firmly plugged to the syringe. Pressure is obtained by plugging the syringe on compressed air network through a manometer (pressure range 0-8 bars). Capillary used are made of PEEK (Polyether ether ketone) polymer which ensure a good rigidity. The real diameter was measured with an optical microscope and found to be 1.55 mm which is the announced diameter. Capillary length used varies along experiments but is always between 12 and 25 mm. On the contrary to commercial capillary rheometer described before (choice of piston velocity), this one works on a stress controlled mode (choice of pressure). Stress is imposed and computed from air pressure. Shear rate is computed from flow rate which is measured by weighting the sample collected from the nozzle of the capillary in a cup during the known time of an experiment.

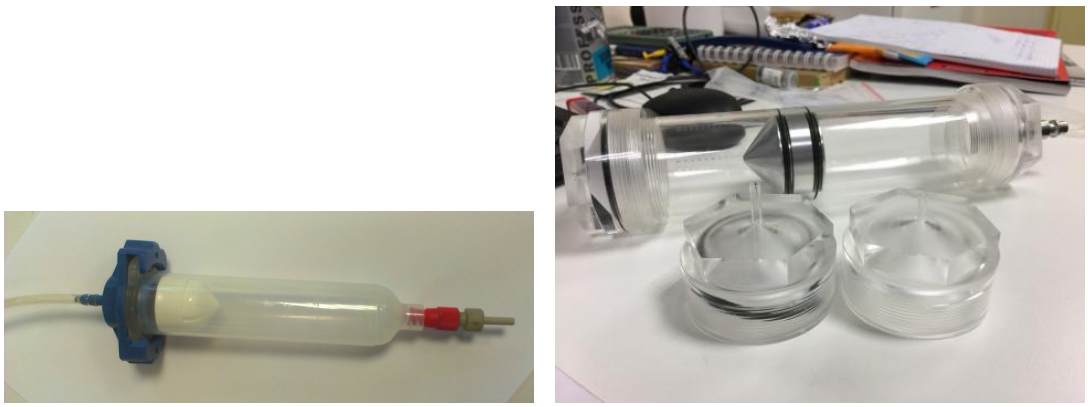

(a) (b)

Figure 2.28: Home-made device for capillary measurements consisting in a manometer branched on compressed air network (pressure range 0-8 bars), a syringe with a piston and a capillary at the exit of the syringe. Pressure is imposed and flow rate is measured by weighting. (a) purchased syringe (V = 30 mL , σ_{max}= 20 kPa) (b) home-made syringe (V = 500 mL, σ_{max}= 50 kPa)

2.8.4.2 Results for D2 at 60%

Figure 2.29 shows results from capillary device without Bagley and Rabinovitsch correction and with these two corrections. First, viscosity found with this device is very coherent with measurements from rotational rheometer and Gottfert capillary rheometer. Corrections result in very small deviations. In the following, no correction will be done with this capillary to spare time. It can be also concluded that the shear-thinning behaviour observed in Couette at high shear rate is just artefact and measurements are only reliable up to 400-500 s^{-1}. Only capillary measurements allow access to reliable viscosity measurements at high shear rate

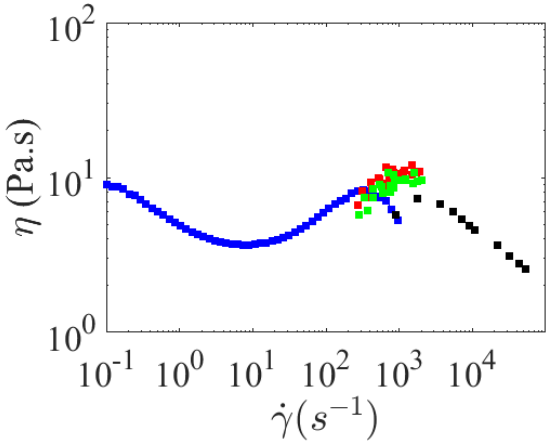

Figure 2.29: Viscosity measurements with air pressurized capillary rheometer: with Bagley and Rabinovitsch correction (■) and without correction (■). Measurements in a Couette cell (■) and with commercial capillary rheometer (■) are displayed for comparison.

2.8.4.3 Results for D1 at 60%

Same was applied on D1 at 60%. Figure 2.30 shows that measurements from rotational rheometer in high shear rate regime (shear thickened state) are not accurate. This is due to some sample ejection at geometry edges (cf. high normal stress difference during DST transition). As for D2, only capillary measurements allow access to reliable viscosity measurements at high shear rate

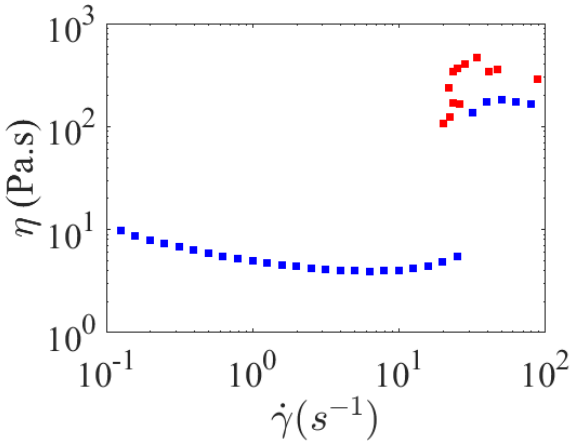

Figure 2.30: Viscosity for D1 60 % found with cone/plate on a rotational rheometer (■) and points a at high stress found with home made capillary rheometer (■).

2.9 Ultrasonic velocimetry

In chapter 3, we couple rheometry (in a Couette cell) with in-situ ultrasonic velocimetry (USV) to access local velocity profile along the gap. These experiments were done at the "Laboratoire de Physique" of ENS Lyon with Sébastien Manneville. We briefly detail here the principle of the measurements which was extensively described elsewhere [205].

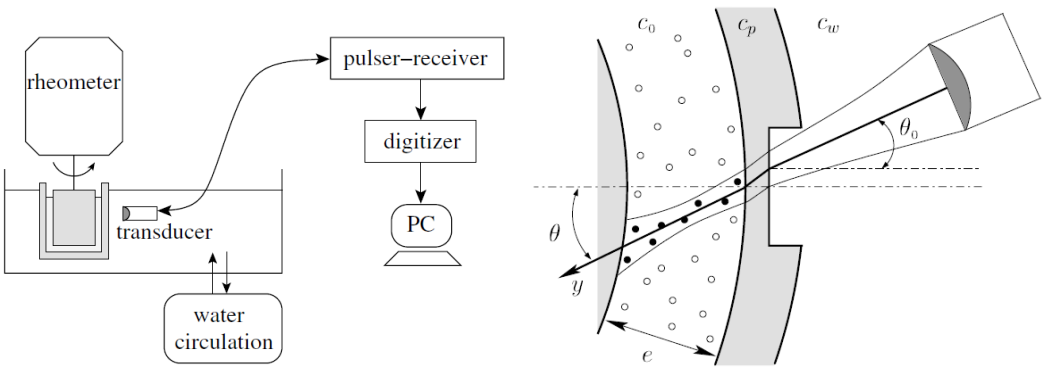

Figure 2.31: (a) Electronic system used for high-frequency USV. Transducer and Couette cell are surrounded by water whose temperature is kept constant to within $\pm$ 0.1 ˚C. (b) Experimental setup for USV in complex fluids sheared in the Couette geometry. c_0, c_p, and c_w stand for the speed of sound in the complex fluid, in Plexiglas, and in water respectively [205].

We use an ARG2 rheometer from *TA instruments* with a transparent Couette cell (smooth Plexiglas) to impose a stress on the sample. The Couette cell is surrounded by water whose temperature is kept constant to within $\pm$ 0.1 $^{\circ}$C. Simultaneously, a PVDF piezo-polymer transducer (Panametrics PI 50-2) immersed in the water in front of the stator generates focussed pulses (of frequency 36 MHz and wavelength 40 μm). These pulses are incident on the stator with a given angle $\theta_0 \approx 20$ $^{\circ}$relative to the normal to the window in the stator as sketched in Fig. 2.31. θ_0 is carefully calibrated to minimize reflections on water–Plexiglas or Plexiglas–fluid interfaces.

We directly track the backscattered (BS) signals in the time domain. This backscattered signal stems from inhomogeneities that can be either naturally present or artificially introduced to enhance the acoustic contrast. In our case, both dispersions D1 and D2 contain a few "large" particles or bubbles (of typical diameter $\sim$ 10 μm) that scatter the incoming ultrasonic pulses efficiently. Therefore, in spite of a strong attenuation of the scattered signal due to the large particle volume fraction, ultrasonic velocimetry can be directly used as described in [205] on both dispersions without tuning their acoustic properties, even though multiple scattering becomes an issue in D2 for the largest gap width (see chapter 3).

Sound speed in the dispersion is carefully measured using a classical transmission setup consisting of two immersed transducers facing each other (one fixed and one moving). θ_0 is determined by carefully calibrating velocity profiles on a Newtonian fluid (water or plasticizer).

The BS signal results from the interferences of all the backscattered waves and appears as complex (speckle). However, between two successive pulses, echoes will move along with the flow. Under the assumption of single scattering, the speckle signal received between times T and T + ΔT can be interpreted as interferences coming from scatterers located between y and y + Δy, where y = $c_0 T/2$, $\Delta y = c_0 \Delta T/2$. Following this idea, Δt for different positions y_k in the gap can be determined using a time cross-correlation of the back-scattered signal. Thus, velocity along the acoustic axis (v_y) at time T is retrieved for different positions y_k in the gap and basically corresponds to:

$$v_y(y_k, T) = \frac{c\Delta t(y_k, T) f_p}{2} \tag{2.19}$$

with f_p is the pulse frequency. Knowing the angle enable to access the real velocity v_θ. Finally, the technique allows the measurements of velocity profiles in a Couette cell with a resolution close to ultrasonic wavelength (40 μm).

2.10 X-ray tomography

In chapter 3, we couple rheometry with in situ X-ray tomograph (phoenix v|tome|x) from *General Electric* which is able to do 2D X-ray inspection or 3D computed tomography. Here we use it only in a 2D mode by making radiography of spatial X-ray absorption and then monitor real time spatial particle repartition upon flow. All X-ray absorption experiments were done at the scientific platform *Placamat* in Bordeaux with Nicolas Lenoir (*Placamat*) and Guillaume Ovarlez (*Laboratory Of the Future*). Principles and calculations have already been detailed elsewhere [206] and are reproduced hereafter.

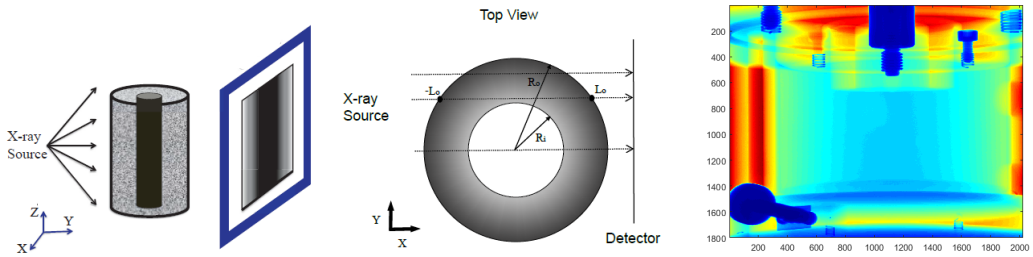

Figure 2.32: (a) Scheme of the radiography: X-rays go through the sheared sample. A 2D map of X-ray absorption is measured with a detector (scheme from [206]). (b) Image of the Couette cell produced by X-ray radiography. Sample is located between stator and rotor (thin ....).

Fig. 2.32 is a scheme that shows the X-ray penetrating the object in a linear path, in which the X-ray is absorbed by the various media in the beam (here, the PMMA Couette cell, the PVC beads and the interstitial liquid). In the experiments, the camera's response is first calibrated to provide a homogeneous intensity response I_0 over all pixels when there is no object between the X-ray source and the detector. When an object is studied by radiography, the detector then provides a field $I(y,z)$ of measured intensity, which follows the Beer-Lambert law [207, 208]:

$$I(y,z) = I_0 \ \exp\Big(-\sum_i L_i(y,z)\nu_i\Big), \tag{2.20}$$

where μ_i is the attenuation coefficient of the material i, $L_i(y,z)$ is length of the material i crossed by the beam at position (y,z).

For the problem under study, we can replace the subscripts $i = 1,2,3$ by 'cell', 'beads', and 'fluid'. When the particle volume fraction field $\phi(r,z,t)$ evolves in time, the lengths $L_{\text{fluid}}(y,z,t)$ and $L_{\text{beads}}(y,z,t)$ measured at a given position (y,z) do not vary independently: they can be written as

$$L_{\text{beads}}(y,z,t) = \Phi(y,z,t)L_{gap}(y,z) \tag{2.21}$$

$$L_{\text{fluid}}(y,z,t) = (1-\Phi(y,z,t))L_{gap}(y,z) \tag{2.22}$$

where $L_{gap}(y,z)$ is the size of the sheared gap crossed by the beam at (y,z), and $\Phi(y,z,t)$ **is the averaged particle volume fraction seen by the beam along its path at this position**. Finally, the intensity field $I(y,z,t)$ that we measure during an experiments is:

$$I(y,z,t) = I_0 \ \exp\Big(-L_{\text{cell}}(y,z)\nu_{\text{cell}} - L_{\text{gap}}(y,z)\Big(\Phi(y,z,t)\nu_{\text{beads}}(y,z) + (1-\Phi(y,z,t))\nu_{\text{fluid}}(y,z)\Big)\Big). \tag{2.23}$$

Of course, geometrical functions $L_{\text{cell}}(y,z)$ and $L_{gap}(y,z)$ can in principle be computed, and all absorption coefficients can either be computed from the knowledge of the material properties or measured independently, which would allow us to extract directly $\Phi(y,z,t)$ from $I(y,z,t)$. In order to be as accurate as possible we have instead chosen to rely on measurements performed directly within our system in order to remove all parameters from (2.23) and finally get $\Phi(y,z,t)$. The first

step consists in measuring the intensity field $I_{\text{fluid}}(y,z)$ when the Couette cell is filled with the pure background fluid only (i.e., $\Phi(y,z)=\phi(r,z)=0$). From (2.23):

$$I_{\text{fluid}}(y,z) = I_0\ \exp\Big(-L_{\text{cell}}(y,z)\nu_{\text{cell}} - L_{gap}(y,z)\nu_{\text{fluid}}\Big), \tag{2.24}$$

Then for the suspension, we can write:

$$I(y,z,t) = I_{\text{fluid}}(y,z)\ \exp\Big(-\Phi(y,z,t)\Big(\nu_{\text{beads}}-\nu_{\text{fluid}}\Big)L_{gap}(y,z)\Big), \tag{2.25}$$

The next step is to use the information that the material is initially homogeneous, and was prepared at a known volume fraction $\Phi(y,z)=\phi(r,z)=\phi_0$. The initial intensity field is

$$I(y,z,0) = I_{\text{fluid}}(y,z)\ \exp\Big(-\phi_0\Big(\nu_{\text{beads}}-\nu_{\text{fluid}}\Big)L_{gap}(y,z)\Big), \tag{2.26}$$

From (2.25) and (2.26), we are finally able to calculate $\Phi(y,z,t)$ for each experiment:

$$\Phi(y,z,t) = \frac{\ln\Big(I(y,z,t)/I_{\text{fluid}}(y,z)\Big)}{\ln\Big(I(y,z,0)/I_{\text{fluid}}(y,z)\Big)}\phi_0. \tag{2.27}$$

Finally, note that: (i) in the experiments $I_{\text{fluid}}(y,z)$ and $I(y,z,0)$ are averaged over 10 seconds to minimize their contribution to the noise in the analysis; (ii) for long experiments, the source intensity may slowly drift (i.e., I_0 might slightly change in time), which is compensated at each time by normalizing the intensity field by its current value in a zone of the image where the X-ray source has crossed no object.

For the results presented in this PhD thesis, we plot $\Phi(y,z,t)/\phi_0$ which is the relative variation of the averaged particle volume fraction seen by the beam along its path at this position. One has to be aware that we do not compute here the local solid volume fraction $\phi(y,z,t)$ but only variations of absorption intensity. Please also note that we checked initial homogeneity of the suspension by measuring the intensity for an empty Couette cell

$$I_{cell}(y,z) = I_0\ \exp\Big(-L_{\text{cell}}(y,z)\nu_{\text{cell}}\Big),$$

then, the ratio

$$\frac{\ln\Big(I(y,z,0)/I_{\text{cell}}(y,z)\Big)}{\ln\Big(I_{\text{fluid}}(y,z)/I_{\text{cell}}(y,z)\Big)} = \Phi(y,z,0)\frac{\nu_{\text{beads}}-\nu_{\text{fluid}}}{\nu_{\text{fluid}}}.$$

has to be constant for all beam paths crossing the suspension if the material is indeed initially homogeneous [206].

2.11 Summary

— Two PVC powders used in this work: 1 (monomodal) and 2 (bimodal).
— Reference filler ($CaCO_3$) is filler M (D50 $\sim$ 20 μm). Other sizes are used to control the effect of filler size.
— The liquid is always DINCH (plasticizer).
— Maximum packing fraction are experimentally determined from plasticizer absorption test.
— Capillary rheometer enables reliable viscosity measurements up to $10^5 s^{-1}$
— Rheometry can be coupled to X-ray absorption and ultrasonic velocimetry to respectively follow local solid volume fraction changes and local velocities.

Chapter 3

Suspension of PVC particles in a plasticizer

We study the flow of concentrated suspensions of PVC particles in a plasticizer. Formulation (filler, additive) is not tackled here and will be addressed in the next chapter. In this chapter, the leverage in formulation remains the nature of the PVC powder (1 for monomodal or 2 for bimodal) and the volume fraction ϕ. The rheological properties over a wide range of shear rates (0.1 to $10^4 s^{-1}$) are characterized for both powders and different solid volume fractions. Attention is paid to shear thickening, and especially to the discontinuous one. Thanks to a collaboration with a team at ENS Ulm, we are able to experimentally unveil its microscopic origin. Extended rheological characterization of the system enables us to draw a phase diagram versus particle volume fraction ϕ. The final part deals with the flow of a shear thickening formulation: in particular, the influence of the gap geometry on measured viscosity and possible shear-induced particle migration are investigated. As a reminder, D1 and D2 correspond respectively to suspensions made of PVC 1 + plasticizer and PVC 2 + plasticizer.

3.1 Rheological characterization of the system

3.1.1 Linear rheology

Prior to steady-state shear flow, viscoelastic linear properties of D1 and D2 has been probed with small amplitude oscillatory measurements. Figure 3.1 show the moduli of D1 and D2 at 60% versus the frequency. The experiments are performed in the linear regime. In dispersion D1, the elastic modulus is larger than the loss modulus at low frequency. This behaviour has already been encountered in cornstarch suspensions [38]. In dispersion D2, G' and G" remain close to each other over the whole investigated frequency range. The sample is not simply viscous but exhibits significant elasticity. In both situations, the elastic behaviour at low frequency may be attributed to colloidal forces between particles.

3.1.2 Flow curves

We now turn to steady-state viscosity measurements. Flow curves of both D1 and D2 are respectively displayed on Fig.3.2 for different volume fractions ϕ. These flow curves were obtained on a

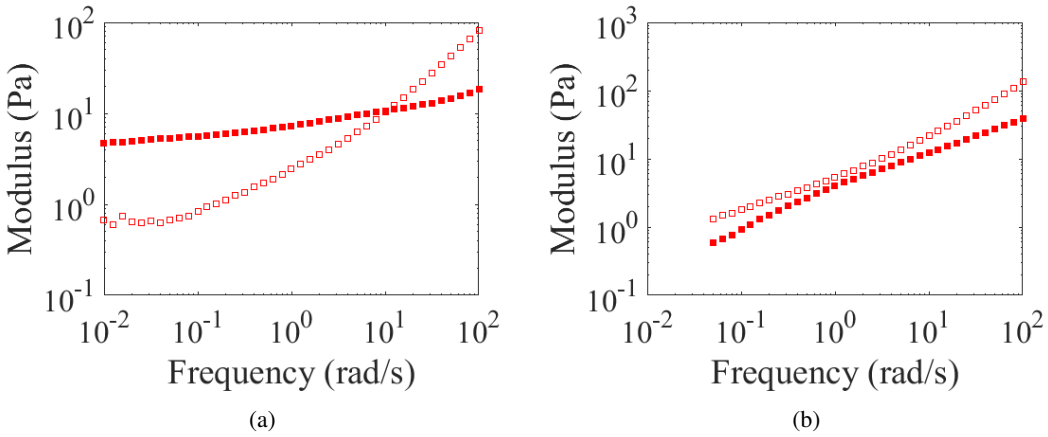

Figure 3.1: (a) Evolution of the elastic modulus (filled symbols) and the loss modulus (open symbols) as a function of frequency in the linear regime for dispersion D1. The geometry is a cone-and-plate with a radius of 25 mm, an angle of 0.04 rad and a truncation distance of 43 μm. The applied strain amplitude is equal to 0.02 and lies within the linear regime. (b) Same for D2. The geometry is a Couette cell with a gap of 1 mm. The applied strain amplitude is equal to 0.008 and lies within the linear regime.

strain-imposed rheometer with a cone/plate geometry (except for $\phi < 50$ %). Measurements at high shear rate are limited by sample ejection and we discard data upon sample ejection.

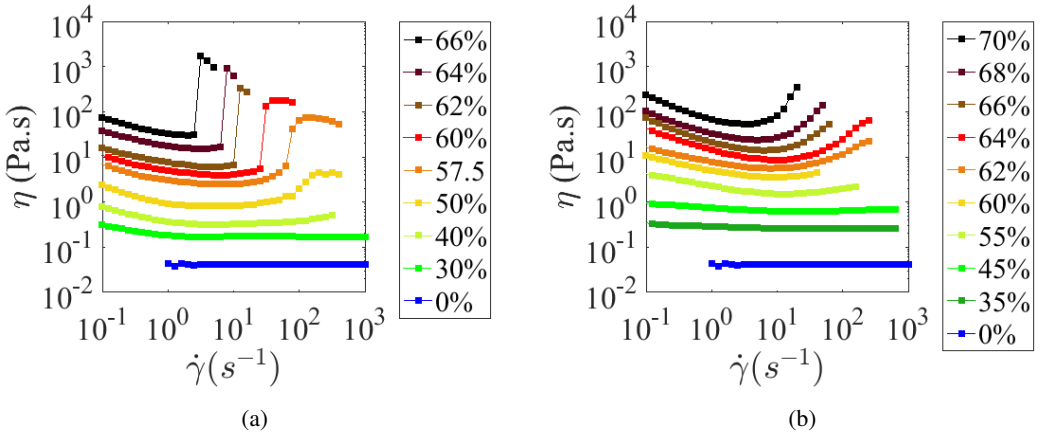

Figure 3.2: Strain-controlled flow curves for different ϕ (a) for D1 ;(b) for D2. For both D1 and D2 here, curves were obtained on a strain-imposed rheometer with a cone/plate geometry (except for $\phi < 50$ % which are done in a Couette cell with a gap 1 mm).

For D1 (cf. Fig.3.2a), the behaviour is Newtonian for ϕ up to 30 %. Above 30 %, slight shear thinning at low shear rate is observed and much stronger shear thickening appears. As reviewed in chapter 1, the shear thickening is continuous at moderate volume fraction ($40 < \phi < 56\%$) and discontinuous for higher ϕ. On the contrary, D2 is Newtonian for ϕ up to around 40 % and exhibits a continuous shear thickening at higher volume fraction (Fig. 3.2b). But, unlike to D1, shear thickening stays continuous in the explored range of shear rates and concentrations.

3.1.3 Normal stresses differences

Measurements of the first normal stress difference N_1 was achieved by measuring viscosity in a cone and plate geometry. To access the second normal stress difference N_2, a plate/plate was used to measure $N_1 - N_2$. Mathematical relationships are detailed in part 2.7.2.

For all measurements, a bit of sample at the edge is ejected simultaneously to the normal stresses burst. The loss of sample can be quantified by comparing the measured viscosity (lower than expected) with a measure without significant loss of sample, for example in a Couette cell (artefacts are found to appears at higher shear rate in such geometry, cf. Fig. 2.18). In the following, all normal stress differences measurements were offset following this way to compensate partial sample ejection. Offsetting the normal stress differences was done linearly with the viscosity loss.

Figure 3.3a and 3.3b shows first normal stress difference (N_1) for respectively D1 and D2 for different ϕ. Associated flow curves are displayed on Fig. 3.3e and 3.3f. For D1, N_1 becomes positive at high shear rate, both for continuous shear thickening (here at 55 %) and discontinuous shear thickening (for example at 60 % and above). For D2, the lowest measured volume fraction (55 %), N_1 is slightly negative at intermediate shear rate, then slightly positive. The zone slightly negative is in fact visible for all plotted volume fraction but its intensity does not depend much on it. On the contrary, at high shear rate and for higher ϕ ($\geq$ 60 %) high positive N_1(comparable to shear stress) are achieved. Increasing the volume fraction shifts the onset of positive N_1 to lower shear rates. Those results show that the suspension D1 become dilatant ($N_1 > 0$) at high shear rate for all tested ϕ. The feature is striking for discontinuous shear thickening. This signature of positive N_1 is related to interparticle friction at high shear giving multiple force chains which completely span the system. A direct measure of frictional interaction between particles at the shear-thickening transition will be detailed later.

Even for the polydisperse PVC with continuous shear thickening, the dilatant behaviour (N_1) is observed at high shear rate, particularly for $\phi >$ 60 %; meaning that contact contribution is also important in the continuous shear thickening of D2, similarly to findings of Royer et. al [54]. Like Lootens et. al. [39], Royer et. al. observed at intermediate ϕ purely negative normal stress (between nearly zero normal stresses at low volume fraction and purely positive at high ϕ). Here, we just however observe a transition from nearly zero value to positive values at high ϕ. Several hypothesis can be drawn: (i) the transition zone in ϕ might be very thin and not probed here. (ii) the zone of N_1 < 0 could be at higher shear rate than the probed range here. Moreover, the range of shear rate with slightly negative N_1 might be reminiscent of this transition. The slightly negative value of N_1 appears concomitantly to the beginning of shear thickening. Following the findings of Royer. et al. [54], this zone may be interpreted as the presence of some frictional clusters which are not enough to span the system (but enough to increase viscosity), leading to N_1 <0 due to major hydrodynamic contribution. It is worthy to note that a viscosity increase driven by frictional contacts and a negative N_1 are not contradictory as underlined recently by Royer et. al [54].

N_2 for both D1 and D2 are plotted on fig 3.3c and 3.3d. For D2, N_2 is found to be around zero for volume fraction up to 55 %. At higher ϕ, N_2 becomes negative at high shear rate. As for N_1, the onset of N_2 is shifted to lower shear rate when increasing the volume fraction. The sign of N_2 is in agreement with other available measurements [121, 131]. Its absolute value is found to be higher than

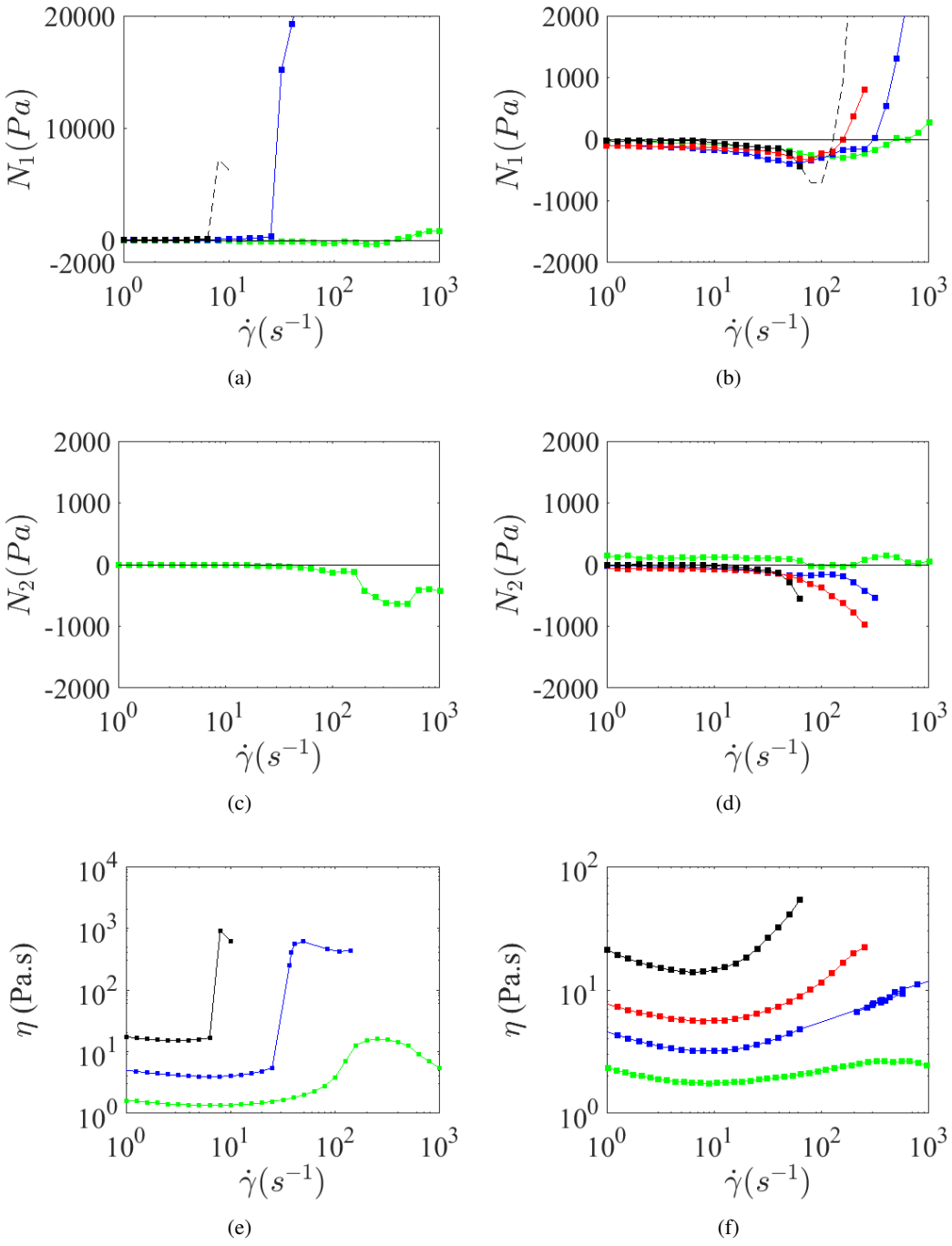

Figure 3.3: Normal stress differences for various concentrations. Left side corresponds to D1: (a) N_1 (c) N_2 and (e) associated flowcurves: 55% (■), 60% (■), 64% (■). Right side corresponds to D2: (b) N_1 (d) N_2 and (f) associated flowcurves: 55% (■), 60% (■), 64% (■) and 66% (■). Dotted lines represent data where sample ejection could not have been offset, thus such data represent a lower bound of real values Horizontal solid lines represent the zero.

N_1 for a given shear rate with for example a ratio of 4-5 for ϕ = 0.62, close to values of 3-4 from literature [209].

As a conclusion, positive N_1 and negative N_2 are reported for both suspensions. Higher values are found for the DST. Offsetting data with a reference flow curve (done in Couette) allow a gain in

the maximum shear rate achievable but it can hinder accuracy especially in plate/plate where shear rate is not homogeneous whereas we assume a linear contribution of the surface. Better accuracy could have been achieved using more advanced experimental setups like for example surface deflection profilometry in a Couette cell [119] or tilted-trough setup [123].

3.1.4 Discontinuous shear thickening (DST)

We focus here on D1 at $\phi > \phi_{DST} = 56\%$ where discontinuous shear thickening (DST) occurs.

3.1.4.1 Stress-control sweep

Curves for D1 shown before (Fig. 3.2) were done on a strain-controlled rheometer (ARES). Thus, the discontinuous jump in viscosity cannot be fully measured due to the discontinuity. Measuring the flow curve with a stress controlled rheometer (DHR3) enables a full characterisation of the DST. Figure 3.4 shows comparison between two protocols for three volume fractions: 60 %, 64 % and 66 %. First, the stress-controlled protocol allows to well measure the vertical jump of viscosity, characteristic of DST. But the shear rate in the shear-thickening jump is found to be lower with a stress-control sweep. This effect is more visible at very high ϕ. It is worthy to note that our measurements on stress-controlled rheometer are limited by the maximum torque for the sensor (200 mN.m) which is lower than the one on the strain-controlled rheometer. For the three probed concentrations, a S-shaped curve is observed with a decrease of the shear rate when entering the shear thickening regime. The amplitude of the S-curve depends upon the details of the protocol: a faster procedure induces a direct jump with no incursion at high shear rate on the low viscosity branch. This effect cannot be observed with strain-controlled rheometer as shear rate is forced to monotonically increase. Such shapes for the flow curves are currently observed for DST systems [60, 63]. Nevertheless, the shear rate in the DST (corresponding to the vertical increase of viscosity) does not depend on the details of the protocol.

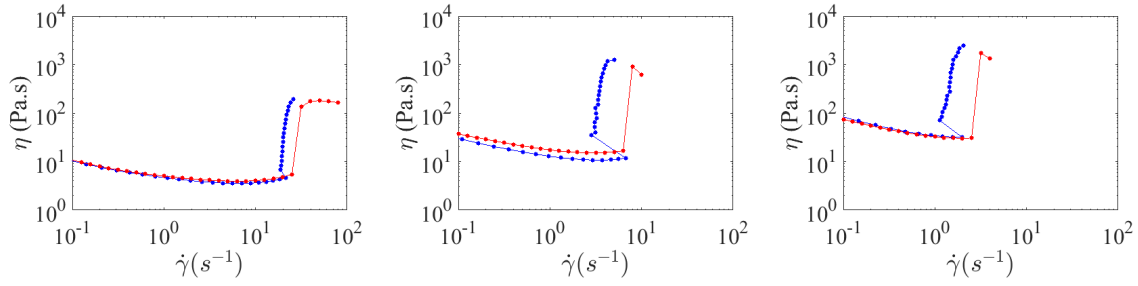

Figure 3.4: Flow curve of D1 at ϕ = (a) 60 %, (b) 64 % and (c) 66 % measured with a stress sweep (blue) versus shear rate sweep (red). Measurements are performed using a cone/plate geometry.

3.1.4.2 Onset stress for shear thickening

DST is found to appear at a critical stress which depends slightly on volume fraction as displayed on Fig. 3.5 in line with others shear-thickening systems [59, 60, 39]. For our system, a critical stress of σ_c = 75 Pa $\pm$ 5 is measured. Such results are interpreted within the stress-induced friction scenario of

shear thickening. The macroscopic critical shear stress is linked to the microscopic stress needed to overcome interparticle repulsion and enter the frictional regime.

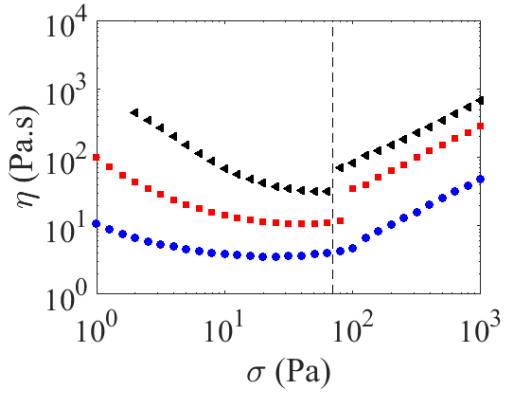

Figure 3.5: Flow curves of D1 in a Couette cell (gap 1 mm) for ϕ = 66% (▲), 64% (■) and 60% (●) allowing the characterization of the critical shear stress σ_c. The vertical dashed line corresponds to the critical shear stress σ_c = 75 Pa $\pm$ 5.

3.1.4.3 Time-resolved data

Figures 3.6 and 3.7 show the full shear rate responses $\dot{\gamma}$(t) recorded during the various steps where a constant stress value is imposed for at least 150 s. A steady state is reached in less than 2 s for dispersion D2 (see Fig. 3.7). In dispersion D1, a steady state is reached in less than 15 s for low shear stresses (see Fig. 3.6). The signals $\dot{\gamma}$(t) become intermittent for shear stresses larger than 150 Pa. The oscillations are rather periodicals, similarly to intermittent flow observed in the discontinuous shear thickening in a cornstarch suspension [60]. For all flow curves presented in this PhD thesis, only values from the steady state are reported.

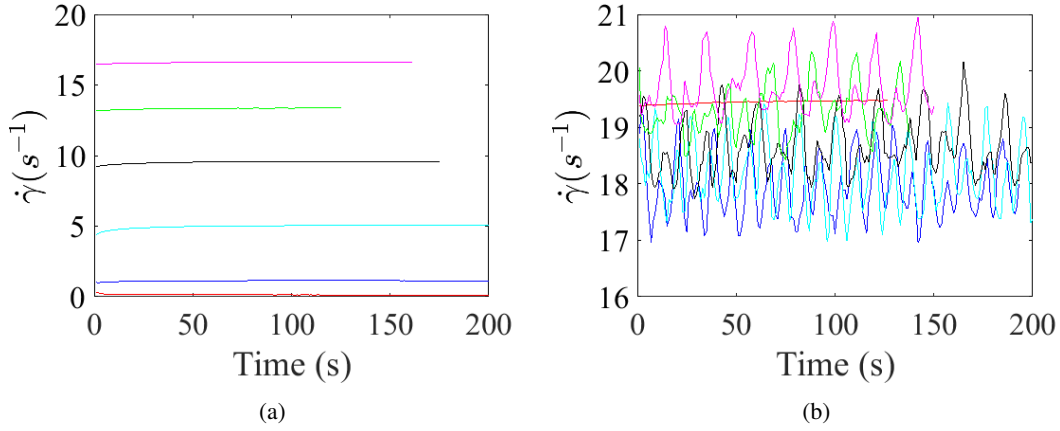

Figure 3.6: Shear rate response as a function of time for various applied shear stresses σ for dispersion D1 (a) from top to bottom σ = 80, 60, 40, 20, 5, 1 Pa and (b) from top to bottom σ = 800, 600, 300, 200, 150, 100 Pa. Measurements are done in a Couette cell (gap 1 mm).

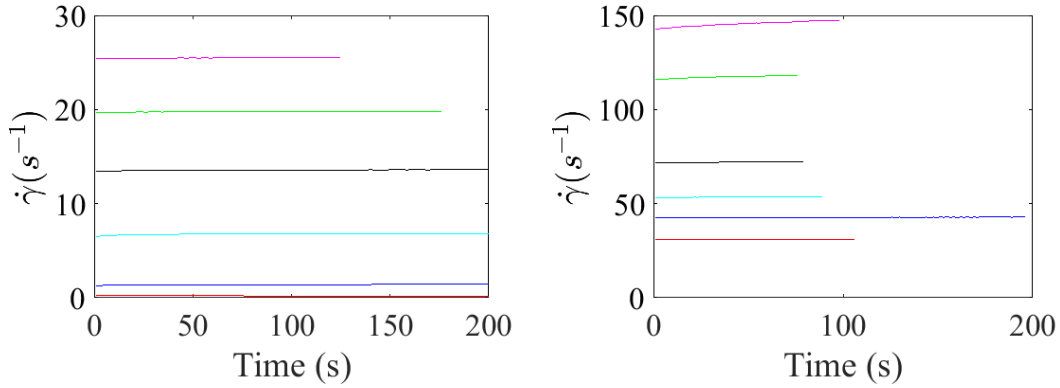

(a) (b)

Figure 3.7: Shear rate response as a function of time for various applied shear stresses σ for dispersion D2 (a) from top to bottom σ = 80, 60, 40, 20, 5, 1 Pa and (b) from top to bottom σ = 800, 600, 300, 200, 150, 100 Pa. Measurements are done in a Couette cell (gap 1 mm).

3.1.5 Capillary rheometer

As described in the introduction of the manuscript, characterizing the viscosity of a PVC suspension at shear rate up to $10^4 s^{-1}$ is relevant because of some industrials steps (for e.g high speed coating at small gap). Measurements presented previously with rotational rheometer cannot access high shear rate viscosity (typically > 200-500 s^{-1} for D2) because of sample ejection (cf. high normal stresses differences at high shear rate). Here, capillary rheometer is used to complete rotational rheometer data with reliable viscosity measurement at high shear rate (up to $10^4 - 10^5 s^{-1}$).

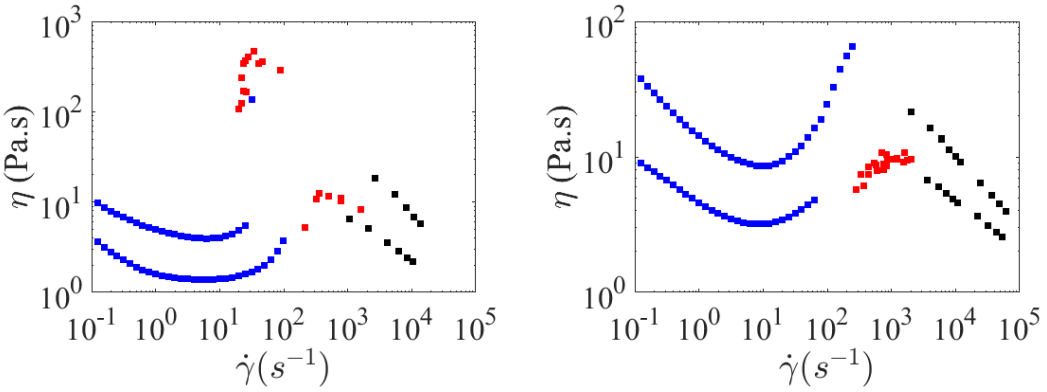

(a) (b)

Figure 3.8: Rheological curve overs six decades of shear rate obtained both with rotational rheometer (■), air pressurized capillary rheometer (■) and commercial capillary rheometer (■) for (a) D1 (55 and 60%) and (b) D2 (60 and 64%).

Full-viscosity curves of D1 and D2 for different volume fractions Results for D1 (ϕ = 55 and 60%) and D2 (ϕ = 60 ad 64 %) are on Fig. 3.8. The combination of different rheological tools gives coherent results as a quite continuous viscosity curve is found. Capillary rheometer allowed us to investigate the end of the shear thickening regime which is followed by a shear thinning regime as

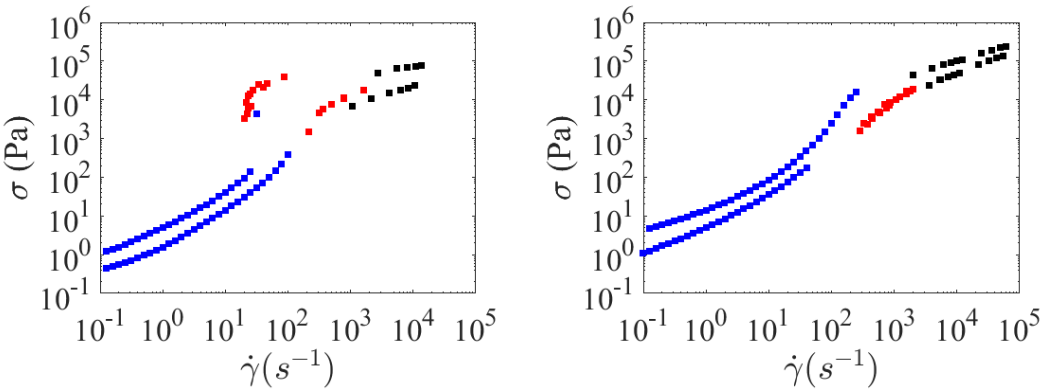

Figure 3.9: Same graph as 3.8 but plotted against shear stress.

reported by previous works [184, 185, 183, 186]. We underline that this regime over shear thickening is measured with increasing stress (cf. Fig. 3.9) and is not related to sample ejection. Moreover, the viscosity of the suspension exiting from the capillary was measured without specifically re-dispersing the suspension. Viscosity was found to be the same than the batch suspension and not modified by its flow into the capillary. More specifically, no self filtration seems to occur and suspensions stay spatially homogeneous during the capillary flow. This point will be confirmed at the end of this chapter by real-time volume fraction mapping using X-ray radiography.

We also check for a possible slip at the wall which was found to be absent for all samples (cf. part 2.8.3.2) except D1 60% where no conclusion is drawn due to a lack of data. These checks confirm that the shear thinning following the shear-thickening is not an artefact or rheological slip but an intrinsic behaviour of the suspension. Analysis of this regime and comparison between D1 and D2 will be discussed a little bit later in the chapter.

3.2 Origin of shear thickening

This work is the outcome of a collaboration with the team of Lydéric Bocquet and Alessandro Siria at the lab LPS (Laboratoire de Physique Statistique) in ENS Ulm who have a quartz-tuning fork based Atomic Force Microscope with subnanonewton resolution. It has been recently published in Nature Communications [210].

Despite an extensive characterization of discontinuous shear thickening transitions at the macroscale, there is still no clear understanding of the microscopic mechanisms at play in this transition, principally owing to the challenges associated with quantitative frictional measurements at the nanoscale [211], especially for pairs of particles [212].

A long standing view is that thickening is driven by hydrodynamic and Brownian forces [44]. At large shear rate, these forces create highly dissipative transient clusters of particles, due to the singular lubrication flows between the particles. When normal elastohydrodynamic contact forces are taken into account (without solid friction), these simulations capture continuous shear thickening and large

increase in suspension viscosity [55]. However, this model predicts shear rate independent rheology for non-Brownian systems and broader transition that observed experimentally.

In order to get around this issue, recent works [57, 70] propose a new picture that neglects thermal fluctuations and put forward the role of (nanoscale) repulsive and frictional forces. At low pressure, neighboring particles are separated by a gap filled with solvent and interact via hydrodynamic forces. At high pressures, repulsive forces are overcome, leading to frictional contacts and shear thickening. At this stage, this picture and the role played by frictional forces have been validated through numerical simulations but only indirectly through experiments at the level of the suspension [59, 54, 68].

In the present work, we bridge this gap between nano and macro-scales. Taking advantage of their quartz-tuning fork based Atomic Force Microscope with subnanonewton resolution, we build upon state of the art procedures [213, 210] to measure the pairwise force profile and the frictional interactions between pairs of particles, and correlate these measurements to the macroscale rheology of suspensions. We study two well known shear thickening systems: polyvinyl chloride (PVC) suspended in various solvents [164, 165] and cornstarch particles suspended in water [81, 60].

3.2.1 Experimental

3.2.1.1 Tuning repulsive steric interaction

As detailed in part 2.1.3, DINCH slightly dissolves the outer part of the particles and creates a polymer brush around them, sterically stabilizing the suspensions [164]. Using physico-chemistry leverage, we are able to play with this suspension stability. For example, dispersing high volume fractions of PVC particles in mineral oil results in a non-flowing pasty material (cf. picture 3.10) as PVC is particles are in a bad solvent, so no stabilizing brushes are created [165]. By mixing mineral oil and plasticizer, we are able to tune the stabilizing brush. For example, a dispersing liquid richer in oil diminishes the stabilizing force between particles, thus shear-thickening should appear at lower stress as it is easier to enter frictional regime according to Wyart and Cates theory.

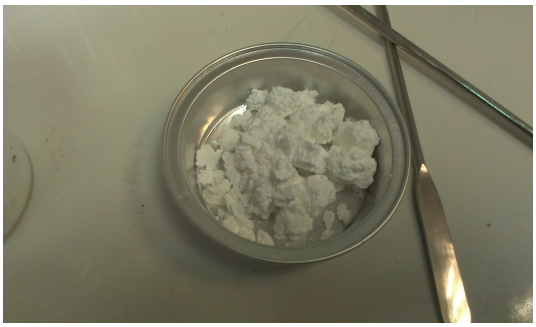

Figure 3.10: Non-flowable paste obtained when dispersing a high volume fraction of PVC particles (ϕ = 60 %) in a bad solvant (mineral oil). Critical stress for entering shear thickening regime is reduced to 0 as particles are already in contact

Mineral oil viscosity standards were provided by *Paragon Scientific Ltd*. Same viscosity as DINCH (41.1 mPa.s at 25°C) was achieved by mixing two different viscosity standards (55.7 mPa.s and 29.0 mPa.s). Resulting viscosity was checked in a shear rate range from 1 to 100 s^{-1} for different temperatures. Same viscosity at 25°C and same temperature dependence of viscosity (range 20-25°C)

were found between plasticizer and mineral oil. Concerning PVC, we report results (both AFM and rheological experiments) for three different plasticizing liquids: (1) 100 vol.% plasticizer; (2) 90 vol.% plasticizer + 10 vol.% mineral oil; (3) 67 vol.% plasticizer and 33 vol.% mineral oil.

In addition to PVC, we study another well known shear thickening system: cornstarch in water. Due to very low volume used and evaporation related problems, AFM measurements for cornstarch were done in pure water as a suspending liquid. Rheological measurements were then also carried out in pure water for the cornstarch suspensions.

3.2.1.2 Rheology

Rheology was measured using a stress controlled DHR-3 rheometer (TA Instruments). For PVC suspension, a stainless steel smooth cone (diameter D = 40 mm, angle = 2°, truncation gap = 54 μm) was used. A logarithmic stress sweep (50 s per point) between 1 and 1000 Pa (10 points/decade) was performed to measure the flow curve. Steady-state flow curve obtained matches the viscosity found using "peak holds" of shear rate (flow steady state is reached within 10 seconds). No wall slip was measured in these experiments. This was checked indirectly by measuring velocity profiles using ultrasounds in Couette cells. Cross-hatched plates were used for cornstarch suspensions (diameter D = 40 mm) to avoid wall slip like in previous works [60]. Flow curves were obtained with a logarithmic stress sweep from 0.1 to 100 Pa (10 points/decade). Each point was measured during 10 s which was long enough to ensure equilibrium while avoiding water evaporation and/or particles sedimentation.

Ah high stresses (see Fig. 3.11), both PVC and cornstarch suspensions exhibit Discontinuous Shear Thickening (DST) where the gradient d(log η)/d(log σ) reaches 1 (vertical flow curve when plotting $\eta = f(\dot{\gamma})$). Within experimental uncertainty, shear thickening begins at a fixed onset stress which depends only on the studied system and not on the volume fraction ϕ [59] (see dotted lines on Fig. 3.11). As expected, the richer in oil the dispersing liquid is, the lower the critical stress for shear-thickening is (cf. Table 3.1).

System	σ_c (Pa)
PVC dispersed in 100 vol.% plasticizer	75$\pm$5
PVC dispersed in 90 vol.% plasticizer	38 $\pm$5
PVC dispersed in 67 vol.% plasticizer	8$\pm$2Pa
Cornstarch in pure water	3-4 Pa

Table 3.1: Critical stress σ_c at which shear-thickening appears in each studied system.

3.2.1.3 Substrates

To elaborate the PVC substrate, a given amount of PVC powder is introduced into a metallic mold laying on a glass slide. A counter-mold is used on top. The mold and counter-mold are then transferred into a hot press and compressed 5 min at 150°C and 20 bars. Then, the sample is cooled down, resulting in a compact and transparent piece of PVC. Even if the pressing temperature is higher than the PVC glass transition temperature (T_g = 80°C), the original shape and surface topography of the particles is preserved (see Fig. 3.12). RMS of measured roughness is $\approx$ 2.2 nm.

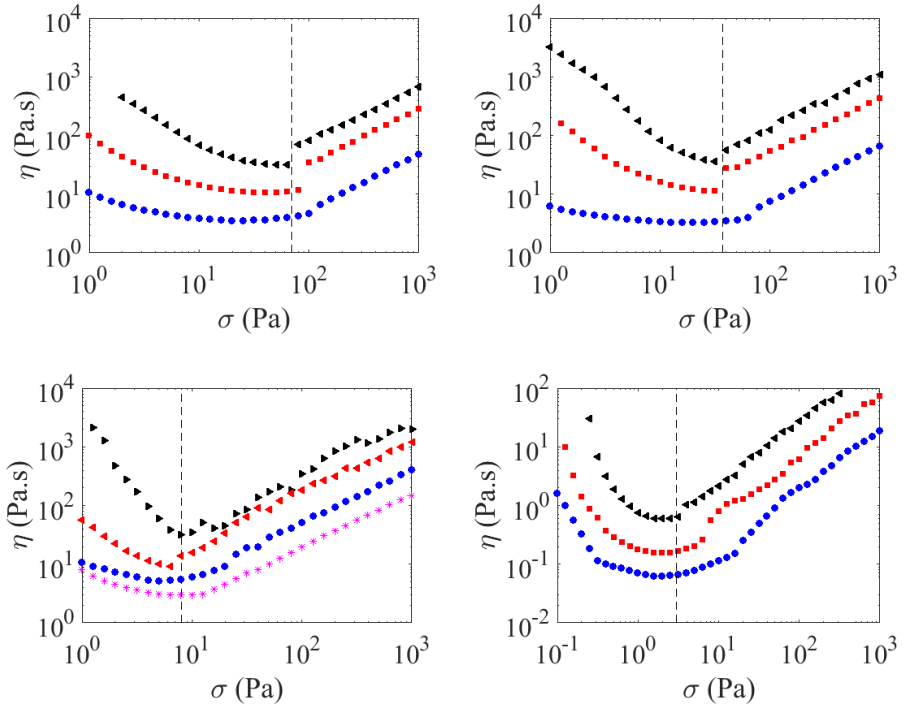

Figure 3.11: Measurements of the viscosity as a function of the shear stress for various solid volume fractions. Top left: PVC, 100% Dinch, from top to bottom the volume fractions correspond to 66%, 64%, 60%. The dotted line corresponds to the shear stress σ_c above which discontinuous shear thickening occurs. Top right: PVC, 90% Dinch; from top to bottom the solid fractions correspond to 66%, 64%, 60%. Bottom left: 67% Dinch, from top to bottom the solid fractions correspond to 63%, 62%, 60% 58%. Bottom right: Cornstarch suspension in water, from top to bottom the solid fractions correspond to 44%, 42%, 40%.

Substrates of cornstarch were made by gluing cornstarch particles on a flat silicon substrate using cyanoacrylate glue (see Fig. 3.12). RMS of measured roughness is 14 nm for the cornstarch particles.

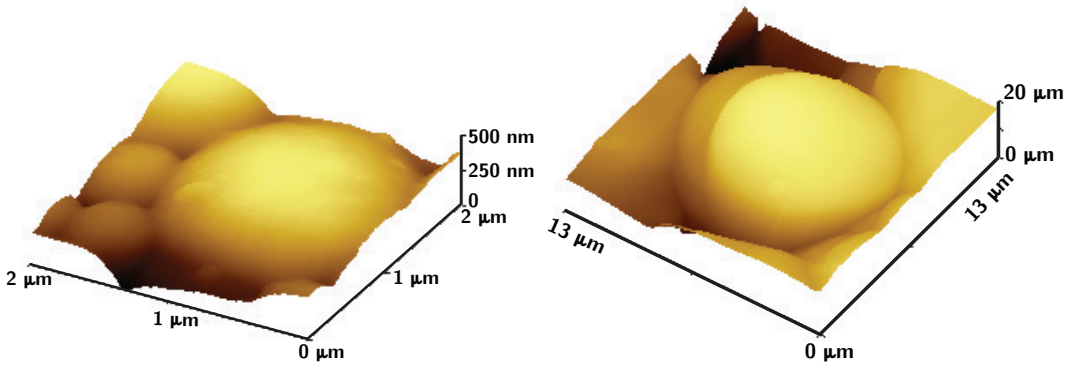

(a) (b)

Figure 3.12: AFM image of (left) one casted PVC particle at the surface of the substrate. RMS roughness is ≈ 2.2 nm on the upper part of the particle. (right) one cornstarch particle at the surface of the substrate. RMS roughness is ≈ 14 nm on the upper part of the particle.

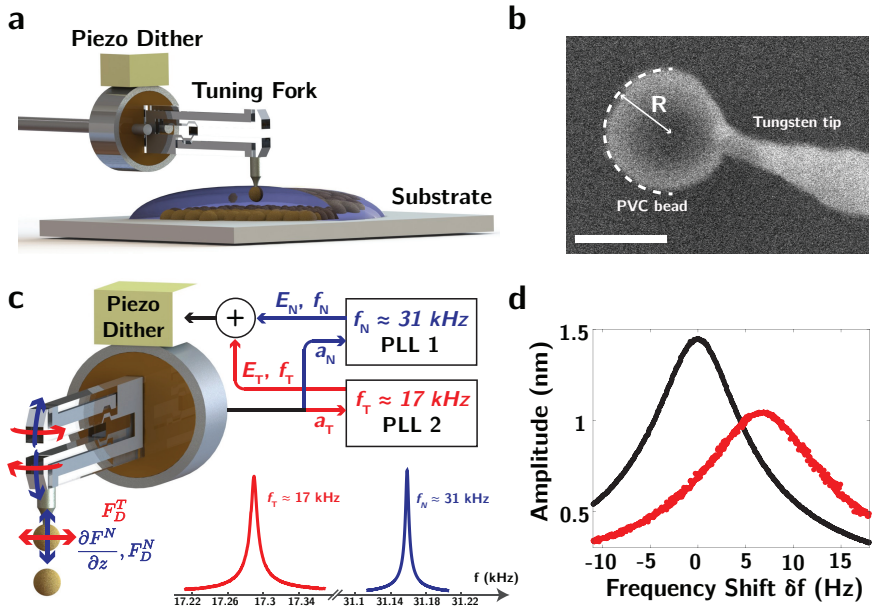

Figure 3.13: Experimental set-up. **(a)** Schematic of the set-up. A particle is glued to the quartz-tuning fork based AFM, immersed in the liquid and approached to the substrate, made of casted particles. **(b)** SEM image of a 0.6 μm radius PVC bead glued to the tungsten tip. Scale bar is 1 μm. **(c)** During the experiment, the tuning fork is excited at two distinct frequencies, corresponding to mechanical oscillation of both normal (N, blue) and tangential/shear (T, red) modes. Two Phase Locked Loops (PLL) track the frequency of the resonance peaks, allowing characterization of normal and tangential force gradients $\nabla\mathbf{F}$ (Eq. 1) and dissipative frictional forces $\mathbf{F_D}$ (Eq. 2). **(d)** Typical resonance curve of the normal mode, for a bead in liquid (black) and in contact to another bead on the substrate (red).

3.2.1.4 Quartz-tuning fork based Atomic Force Microscope (AFM)

The setup was developed in LPS (Laboratoire de Physique Statistique) lab within the team of Lydéric Bocquet and Alessandro Siria. Experiments and data analysis dealing with AFM experiments were done by Jean Comtet in LPS lab. Setup is briefly described here. More information, especially the detailed movement equation can be found here [210].

Briefly, they glue an electrochemically etched tungsten tip of approximately 50 nm end radius to a millimetric quartz tuning fork, which serves as force sensor. Using an in-house-built nano-manipulator in a scanning electron microscope (SEM), they then glue one individual particle to the end of the tungsten tip (cf. Fig. 3.13b).

During a typical experiment, the attached particle is immersed in solvent and brought into contact to another bead fixed on the substrate, while monitoring the force profile (Fig.1a). To measure simultaneously normal and tangential force profiles between the two approaching particles, they simultaneously excite the tuning fork via the piezo-dither at two distinct resonance frequencies $f_\mathrm{N} \approx 31$ kHz and $f_\mathrm{T} \approx 17$ kHz, corresponding to the excitation of both normal (blue arrows) and shear modes of the tuning fork (red arrows), as shown in Fig. 1c. Both modes correspond to symmetric excitation of the prongs, leading to negligible motion of the center of mass and high quality factor of the oscillator [214]. Owing to the very large differences in resonance frequency, the two modes are uncoupled. Monitoring changes in the resonance of each modes (cf. Fig. 3.13d) allows us to measure respectively the normal and tangential force profile between the two objects.

We now detail how to obtain force profile for each normal (N) and tangential (T) modes (cf. Fig. 3.13d). When excited close to a resonance frequency, the system can be modelled as a mass-spring resonator [215], whose resonance profile will be modified by the interacting forces. First, position dependent forces $\mathbf{F}(x,z)$ will lead to shifts in the resonance frequency of the oscillator (comparing black and red resonance curves in Fig. 3.13d). Hence, the spatial force gradient $\nabla\mathbf{F}$ [N.m^{-1}] is proportional to the shift in the resonance frequency δf^i [Hz] according to [215]:

$$\nabla F_i = \nabla\mathbf{F}.\mathbf{e_i} = -2k^i_{\mathrm{TF}}\left(\frac{\delta f^i}{f^i_0}\right) \text{ with } i \in \{N,T\} \tag{3.1}$$

where f^i_0 [Hz] and k^i_{TF} [N.m^{-1}] are the spring constants respectively associated with normal (N) and tangential (T) oscillation modes, $\mathbf{e_i}$ corresponds to the unit vector along direction i.

We can then express the frictional forces applied on the bead as the sum of viscous-like friction force (proportional to speed) and solid friction force (independent of speed and corresponding to sliding friction for tangential motion, $i = T$):

$$F^i_{\mathrm{D}} = \gamma_i \cdot v_i + F^i_{\mathrm{s}} \cdot \frac{v_i}{||v_i||} \text{ with } i \in \{N,T\} \tag{3.2}$$

where v [m.s^{-1}] is the oscillating speed, γ [kg.s^{-1}] is a viscous-like friction coefficient, and the second term F_{s} [N] characterizes the solid friction force, only dependent on the sliding direction $v_i/||v_i||$. The tangential friction forces F_{s} are assumed to be velocity independent as experimentally confirmed a posteriori. Over one oscillation period, all friction forces in eq. 3.2 have zero mean, only leading to changes in the height and broadening of the resonance peak (comparing black and red resonance in Fig. 1d). Note that we can not measure static friction forces with our set-up. However, we expect static friction to appear concurrently to sliding dynamic friction.

Keeping a constant oscillation amplitude a_i at resonance requires the external excitation force F_{ext} (due to the piezo dither) to be equal to the sum of all dissipative forces F_{D}. As the external force F_{ext} is directly proportional to the excitation voltage E_{ext}, the sum of all dissipative forces F_{D} is directly measured by tracking the excitation voltage necessary to keep a constant oscillation amplitude (see [210] for further details).

3.2.2 Results

3.2.2.1 Nanoscale force profile

We show in Fig. 3.14 the typical force profile measured between two approaching PVC beads in good solvent. Monitoring changes in the resonance (Fig. 3.13d) for the two oscillating modes (Fig. 3.13c) allows us to characterize pairwise interparticles interactions through the normal dissipation $F^{\mathrm{N}}_{\mathrm{D}}$ (Fig. 3.14b), the projection of the normal force gradient along the normal direction - $\partial F_{\mathrm{N}}/\partial z$ (Fig. 3.14c) and the tangential friction force $F^{\mathrm{T}}_{\mathrm{D}}$ (Fig. 3.14d).

We first show in Fig. 3.14b the inverse of the normal dissipative force $1/F^{\mathrm{N}}_{\mathrm{D}}$. The red line is a linear fit of the inverse dissipation, showing that normal dissipation $F^{\mathrm{N}}_{\mathrm{D}}$ is characterized by hydrodynamic

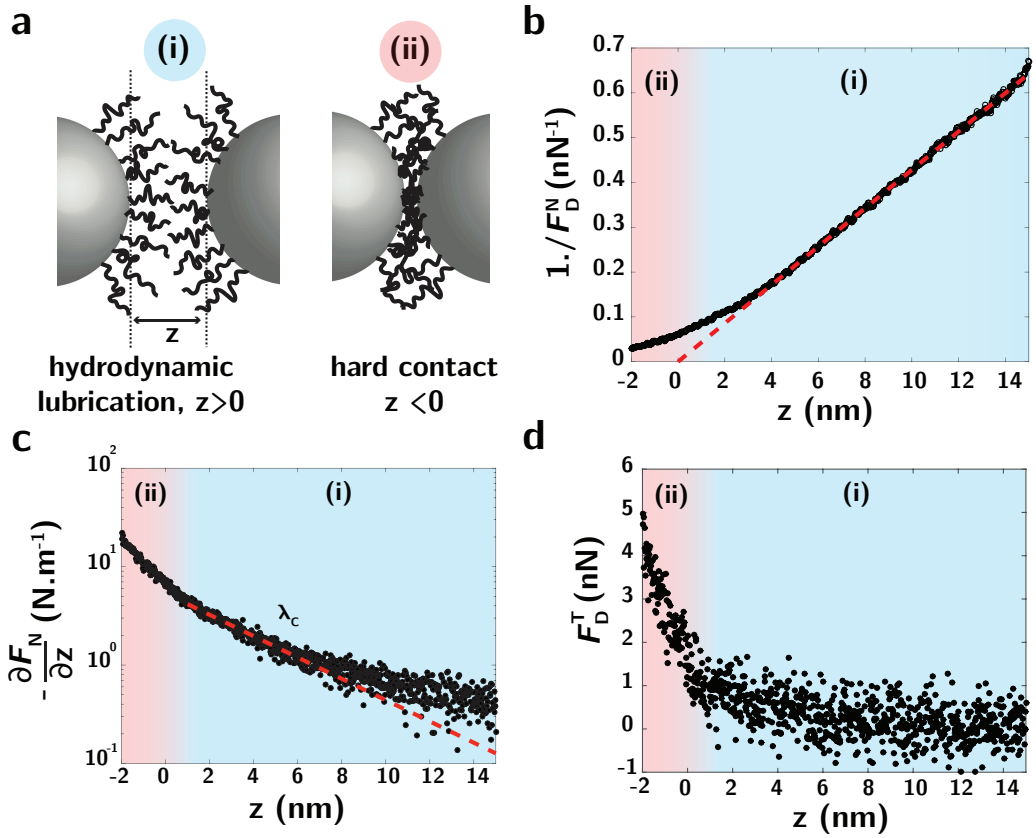

Figure 3.14: Characterization of nanoscale force profile. **(a)** When immersed in Dinch a good solvent, polymer brush form at the surface of PVC particles. Distance between bead's no shear plane is written z, where $z = 0$ correspond to hard contact. *(i)* $z > 0$ Entropic repulsion between polymer brushes. *(ii)* $z < 0$ hard contact. **(b)** Inverse of the normal friction force $1/F_{\mathrm{D}}^{\mathrm{N}}$. **(c)** Projection of the normal force gradient along the normal direction $-\partial F_{\mathrm{N}}/\partial z$. **(d)** Tangential friction force $F_{\mathrm{D}}^{\mathrm{T}}$. The radius of the attached bead is 0.6 μm and beads are immersed in pure Dinch.

drainage and Stokes law as the beads are separated from each other:

$$F_{\mathrm{D}}^{\mathrm{N}} \sim \frac{\eta R^2 v}{z} \tag{3.3}$$

where $\eta \approx 40$ mPa.s is solvent viscosity, $v = a\omega$ [m.s^{-1}] is the typical speed of the oscillating particle, z [m] is the distance between the two no-shear planes and R [m] is an equivalent bead radius. The intersection of the red line with the horizontal axis defines the hydrodynamic zero ($z = 0$), which defines the absolute position of the no-shear planes between the two objects (vertical dotted lines Fig. 2a). This zero defines two domains, corresponding to (i) $z > 0$, hydrodynamic lubrication (light blue) and (ii) $z < 0$ hard contact (light red). Note that for confinement below ≈ 3 nm, we observe a deviation from Stokes hydrodynamics with a regularization of the hydrodynamic divergence, possibly stemming from elastohydrodynamic interactions [216, 217, 55]. The dissipative normal forces measured for $z < 0$ may be due to viscoelasticity of the PVC particles.

We now turn to the normal force gradient $-\partial F_{\mathrm{N}}/\partial z$ [N.m^{-1}] shown in Fig. 3.14c. For the two approaching particles, we observe an increasing repulsive normal force gradient ($-\partial F_{\mathrm{N}}/\partial z > 0$) before contact between the two particles ($z > 0$, blue zone). These repulsive forces vary steadily and

smoothly with distance, while normal dissipation is dominated by hydrodynamics during the approach (Fig. 3.14b). We thus interpret these repulsive forces as a signature of the entropic repulsion between polymer brushes forming at the surface of the PVC beads, due to the effect of the plasticizing solvent [218, 164] (Fig. 3.14a). We can characterize the steepness of this repulsive profile right before contact by an exponential-like law $F \approx \exp(-z/\lambda)$ with $\lambda \approx 4$ nm (Fig. 3.14c, red dotted line) [219]. Upon contact, the steepness of the repulsive profile increases slightly.

We show in Fig. 3.14d the tangential dissipative friction force $F_{\mathrm{D}}^{\mathrm{T}}$ (tangential mode T, Fig. 3.14c). Before contact (blue zone (i)), tangential forces are below 1 nN, consistently smaller that the normal hydrodynamic dissipative forces which are of the order of 5 to 10 nN. Upon contact (red zone, (ii)), we observe a clear increase of frictional forces. We note that, depending on the respective surface states of the beads, contact can also occur before the hydrodynamic zero (for $z > 0$), due to the presence of asperities on one of the bead surface (see figure 3.12). Finally, we note that the fact that we recover solvent viscosity η in the dissipative normal force and that there is low tangential lubrication forces before contact are a signature of the absence of brush interpenetration in the probed experimental conditions [220].

3.2.2.2 Critical Load Friction

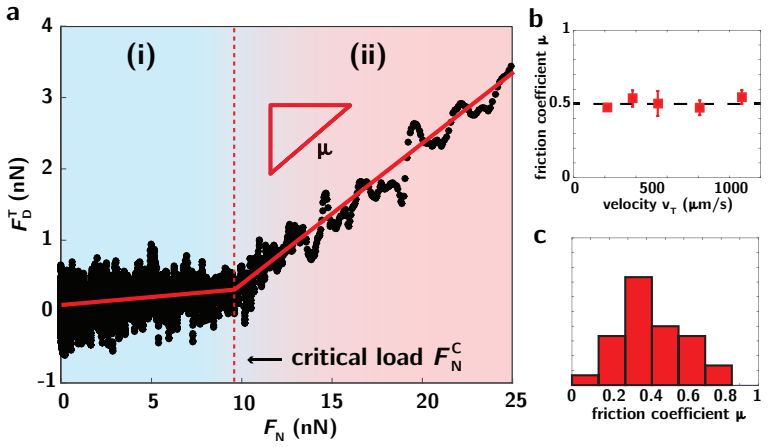

Figure 3.15: Critical load frictional profile. (a) Tangential friction forces versus normal load, showing a transition between (i) a hydrodynamically lubricated low friction regime, to (ii) a solid-like high friction regime. **(b)** Variation of the friction coefficient μ with sliding velocity v for one pair of beads. Error bars are *s.e.m.* (standard error of the mean) for $N > 2$. **(c)** Distribution of the friction coefficient found on 30 different pairs of beads. The radius of the attached bead is 0.5 μm and the solvent between the two beads is pure DINCH.

We now turn to the nature of the frictional profile (cf. Fig.3.15), as uncovered by the two regimes shown in Fig.3.14. We plot in Fig. 3.15a the typical form of the tangential dissipative force $F_{\mathrm{D}}^{\mathrm{T}}$ as a function of the normal load F_{N}, obtained by integrating the normal force gradient [221]. In the first regime of hydrodynamic lubrication (blue zone, (i)), tangential frictional forces are small, and arise purely from hydrodynamic interactions while a normal load F_{N} can be sustained due to entropic repulsion of the brushes. This situation results in a friction coefficient as low as $\mu \approx 0.02$, as observed in previous friction studies on polymer brushes in SFA [222, 223, 220, 224, 225].

Upon a critical normal load F_N^C corresponding to the force necessary to completely compress the polymer layers and reach hard contact, the system switches to a second state characterized by a sharp increase in friction (Fig.3.14d, red zone (ii)). This second regime is well characterized by Amontons-Coulomb laws, with a proportionality between tangential frictional forces and normal load: $F_D^T = \mu(F_N - F_N^C) + F_V^C$, where F_V^C is the tangential viscous dissipation right before contact. Moreover, as shown in Fig.3.15b, the friction coefficient between two beads is independent of the sliding speed for tangential speeds above 200 μm.s^{-1}, a clear characteristic of solid-like friction (relative speed is changed here through the oscillation amplitude a_0). The independence of sliding friction with speed validates a posteriori our choice for the form of Eq. 3.2.

Finally, we show in Fig.3.15c the distribution of friction coefficient obtained over 30 different pairs of beads. As characterized in Fig. 3.15b, the friction coefficient is a well defined properties of each particle interactions (Fig. 3.15b) but also depends on the local physicochemical, geometrical, mechanical and roughness surface state of the two sliding beads. We find a mean interparticle friction coefficient $\mu = 0.45 \pm 0.2$, in very good agreement with the macroscopic friction coefficient of PVC on PVC [226].

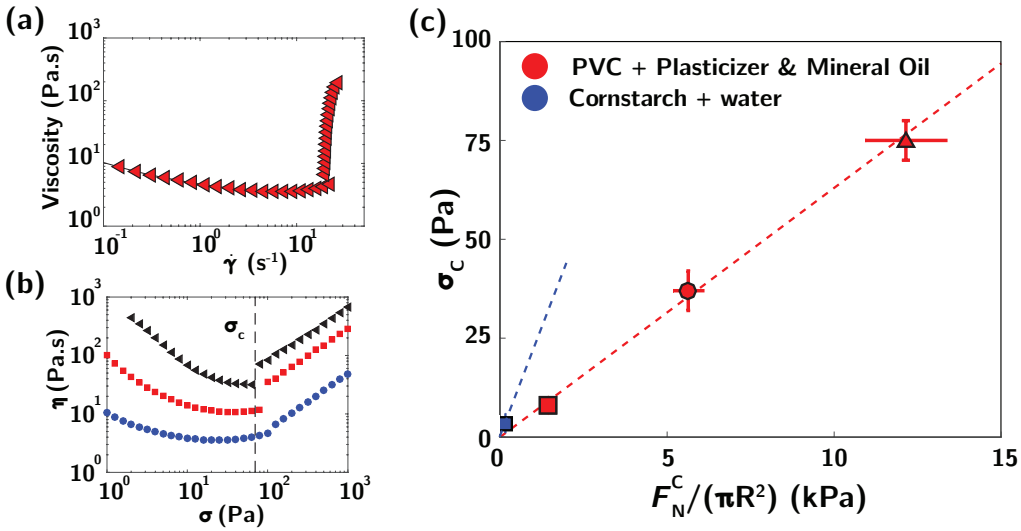

Figure 3.16: Nanoscale critical load determines macroscale critical shear stress. **(a)** Shear viscosity as a function of the shear rate for suspensions of PVC in pure Dinch and a volumic solid fraction equal to 60%. **(b)** Flow curves for PVC in pure Dinch, for volumic solid fractions equal to 66%, 64% and 60% (from top to bottom) allowing the characterization of the critical shear stress σ_C. The vertical dashed line corresponds to the critical shear stress $\sigma_C = 75$ Pa ± 5. **(c)** Correlation between the critical normal stress F_N^C and macroscopic critical shear stress σ_C for PVC in 100% (red triangle), 90% (red circle) and 67% (red square) plasticizer and cornstarch in water (blue square). Horizontal error bars are *s.e.m.* for PVC, with $N > 15$ and standard deviation for Cornstarch ($N = 4$). Red and blue dotted lines are respectively linear fit to the PVC and cornstarch systems.

3.2.3 Discussion

Following recent models, σ_C corresponds to the shear stress required to obtain a particle normal stress high enough to overcome the repulsive forces and to transit from lubricated to frictional contacts [69, 70]. If the shear thickened state is characterized by frictional interactions between the particles,

there should be a correlation between the macroscale critical shear stress σ_C and the critical load F_N^C uncovered in Fig. 3.15. To verify this correlation, they measured the microscopic critical load F_N^C for each of the systems of Fig. 3.16a.

We report in Fig. 3.16c the macroscale shear stress σ_C, versus the nanoscale critical force F_N^C for each discontinuous shear thickening systems. For both PVC and cornstarch systems, we see a clear correlation between those two nanometric and macroscopic quantities, with the critical stress at the macroscale varying proportionally to the critical force needed to enter into frictional contact at the nanoscale:

$$\sigma_C = \beta \cdot \frac{F_N^C}{\pi R^2} \tag{3.4}$$

We find here a proportionality coefficient $\beta_{PVC} \approx 0.006$ and $\beta_{Cornstarch} \approx 0.02$, in relatively good agreement with predictions from simulations performed on smooth particles ($\beta_{simu} \approx 0.05$ for a friction coefficient $\mu = 1$ [69]). Those coefficients characterize stress transmission from the suspension to the particles level and depend on the microscopic friction coefficient [69] for both static and sliding friction, as well as particle shape and roughness. Note that in the simulations, the values of the static and dynamic friction are assumed to be the same, which may not be the case in our situation. Macroscopic roughness may also block the particles and affect the value of β found by numerical simulations.

Let us underline that F_N^C does not depend upon the relative tangential velocities between particles in the range of experimental data. Moreover both F_N^C and σ_C are measured for approximatively the same range of relative velocities between the two particles. In the macroscopic experiments, the relative velocity between two particles can be approximated as $v \approx \dot{\gamma}_C R$ at the onset of the shear thickening transition and varies between 4 μm.s^{-1} and 200 μm.s^{-1}. In the AFM experiments, the normal RMS speed is approximately $30 - 200$ μmm.s^{-1} and the tangential RMS speed $150 - 800$ μmm.s^{-1}.

3.2.4 Conclusion

The unique experimental set-up allowed for the first time to characterize frictional interactions between pairs of particles from discontinuous shear thickening suspensions. We explain unambiguously discontinuous shear thickening transition as stemming from the breakdown of lubrication between particles and the onset of hard frictional contacts. Even though normal elastohydrodynamic forces appear for very small separation distances (Fig. 3.14b, $z < 2$ nm), they do not contribute to the observed shear thickening transition. Indeed, we find that the critical shear stress σ_C at the shear thickening transition varies as a function the contact forces (Fig. 3.16c). This is opposite to predictions of numerical simulations proposed by Jamali [55], for which the shear thickening transition is found to be independent of particle elastic modulus if stemming from elastohydrodynamic forces. We also experimentally measure the thickness of the stabilizing PVC brush and found it to be around 4 nm.

Our measurements pave the road for direct simulation of the rheological properties of dispersions. In particular, the distribution of friction coefficients, contact forces and size distribution of the dispersion should be taken into account in future numerical simulations to capture at which solid fraction the dispersion evolves to a continuous or discontinuous shear thickening transition.

3.3 Maximum packing fraction

Following the model proposed by Wyart and Cates (detailed in section 1.3.2.5), the phenomenology of shear thickening can be summed up depending on the volume fraction of particles:

— $\phi < \phi_{CST}$: The rheology is Newtonian.

— $\phi_{CST} < \phi < \phi_{DST}$: Continuous Shear Thickening.

— $\phi_{DST} < \phi < \phi_m$: Discontinuous Shear Thickening. The thickened state (frictional) is highly viscous but still a flow state.

— $\phi_m < \phi < \phi_{rcp}$: Flow can only occur in the frictionless state, thus for very small shear rates. The thickened state is not in a liquid state and is completely jammed.

— $\phi > \phi_{rcp}$: Impossible as sample is not homogeneous (crumble).

Such regimes are summarized in Fig. 3.17. In the following, we address the experimental determination of critical volume fractions which delimit the different regimes for both PVC 1 and PVC 2.

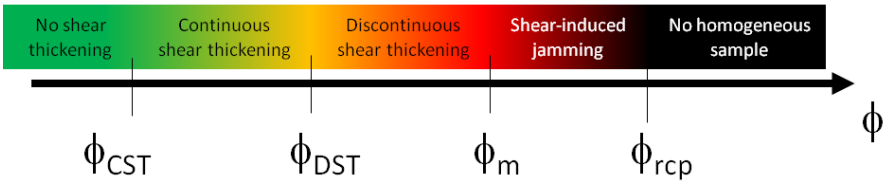

Figure 3.17: Schematic diagram of different regimes of a shear thickening system when particle concentration is increased according to the model proposed by Wyart and Cates. Shear thickening is firstly continuous a moderate volume fraction (green) and turn into a discontinuous one at higher concentration (orange). The system becomes shear-jammed and jammed is the particle concentration is again increased (red, black).

3.3.1 Viscosity VS volume fraction ϕ

Following the model proposed by Wyart and Cates (detailed in section 1.3.2.5), the value of ϕ_{rcp} corresponds to the value of ϕ at which the viscosity diverges at low shear rate. Therefore, to estimate ϕ_{rcp}, we measure the value of the viscosity at the minimum (around 5-10 s^{-1} for most of cases). We do not take the zero-shear limit of the viscosity to get rid of the interparticle interactions which impact viscosity at low shear rates [52]. On the contrary, the value of ϕ_m can be measured at high shear rate and corresponds to the value of ϕ at which the viscosity diverges at high shear rate. We measured the viscosity at the maximum of the shear thickening (highest viscosity before the shear-thinning regime at high shear rate) as a function of ϕ. For the high-shear viscosity of highest volume fractions (especially for DST of D1), we use data obtained from capillary rheometer which are more reliable than data from rotational rheometer due to sample ejection at high shear rate (cf. Fig. 3.19).

The data and fits are plotted on figure 3.18. For D1, ϕ_{rcp} is found to be 69.4 % and ϕ_m = 61.9 %. For D2, ϕ_{rcp} is found to be 77.1 % and ϕ_m = 68.2 %. Such results show that maximum packing fraction is highly dependant on shear rate and are in line with the frictional transition in the shear-thickening regime. Indeed, higher interparticle friction tend to decrease the maximum packing fraction. Moreover, quantitative shifts between ϕ_{rcp} and ϕ_m are coherent with previous studies where shifts as high as 13 % are reported [59, 54].

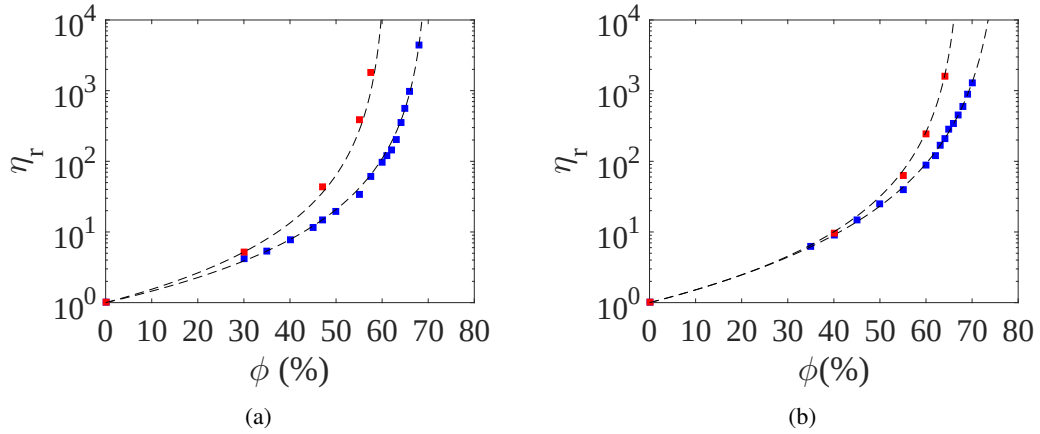

(a) (b)

Figure 3.18: (a) Variation for the D1 dispersion of the low shear viscosity η_{low} measured at the minimum of viscosity (around 10 s^{-1}) (■) and maximum viscosity η_{high} measured at the maximum of the shear thickening (■). Fitted parameters are ϕ_{max} = 69.4% and $[\eta]$ = 2.9 for low-shear viscosity and ϕ_{max} = 61.9% and $[\eta]$ = 4.3 for high-shear viscosity (b) Same for the D2 dispersion. Fitted parameters are ϕ_{max} = 77.1% and $[\eta]$ = 3.9 for low-shear viscosity and ϕ_{max} = 68.2% and $[\eta]$ = 3.8 for high-shear viscosity

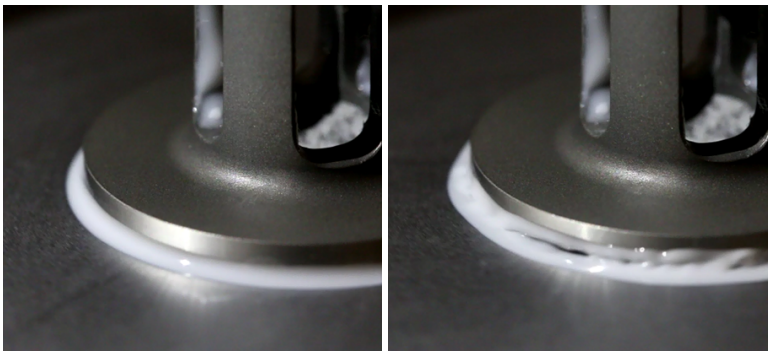

(a) (b)

Figure 3.19: Side view of a typical flow test in a cone and plate (diameter 25 mm) of dispersion D1 at 60%: (a) in the low-shear state and (b) in the high-shear thickened state. In the latter, flow instabilities lead to deposit on the side of the cone and air entrance under the cone. Thus precise and reliable measurements on the upper frictional state are impossible

3.3.2 Comparison with plasticizer absorption test

Following the protocol described in section 2.6, plasticizer absorption test were carried out on the two PVC powders. Values for PVC 1 and PVC 2 are respectively $\phi_{\text{absorption test, PVC 1}}$ = 68.0 % ± 0.5 % and $\phi_{\text{absorption test, PVC 2}}$ = 72.5 % ± 0.5 %. These results are in line with those expected from the size distribution displayed in part 2.1.1: PVC 2 has a broader size distribution (bimodal) which explains the higher maximum packing fraction measured by the plasticizer absorption value. Values are slightly lower than ϕ_{rcp} from fitting rheological curves. Similarly, water absorption test has been also performed on cornstarch powder which results in a value of $\phi_{\text{absorption test, cornstarch}}$ = 52.5 %, compared to the ϕ_{rcp} = 55 % found in literature [81].

The value found with this test lies in each case $\sim$ 2-3 % under the value of ϕ_{rcp} deduced from the extrapolation of data outside of measurable limits (fitting low-shear viscosity versus ϕ). The

difference could stem from two possibilities. First, one can reasonably presumes that when liquid is experimentally added, it is very difficult to be exactly at ϕ_{rcp} where viscosity diverges and a little bit too much liquid more is added. Secondly, ϕ_{rcp} refers to a value at zero shear rate whereas plasticizer absorption test is performed by mixing the liquid and the powder at a non zero shear rate (hand stirring). Even if it is difficult to access an accurate value, it is logic to find a value which lies between ϕ_{rcp} (zero shear) and ϕ_m (high shear). For example, for suspension D2, a value of 72.5 % can be achieved by fitting viscosity at 30 s^{-1} which lies between the low shear rate region (taken at the minimum viscosity around 5- 10s^{-1}) and the high shear rate region (100 s^{-1} in our case).

The plasticizer absorption test thus gives a unique value comprised ϕ_{rcp} and ϕ_m. However, its big advantage is its speed ($\sim$ 15 min) compared to the exact determination of ϕ_{rcp} and ϕ_m obtained by a much longer process (rheological experiments done at various ϕ). In particular, it could be useful and sufficient for powder comparison or follow the evolution of maximum packing fraction when filler is mixed with PVC as detailed in next chapter

3.3.3 Conclusion

Critical volume fractions extracted from the data can be plotted on a single graph (see Fig. 3.20). It gives an overview of the different regimes versus ϕ for both PVC 1 and 2.

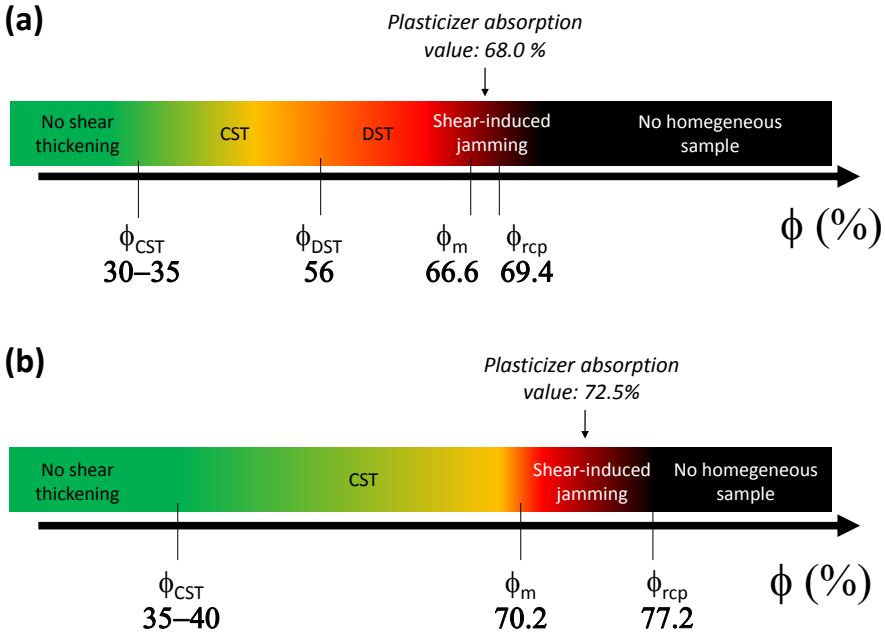

Figure 3.20: Characterization of the different rheological behaviours for the two dispersions D1 and D2. For D1, we observe a shear thickening for volume fraction higher than 45 %. Upon 56 %, sample exhibit discontinuous shear thickening at a critical shear which is smaller and smaller when ϕ is increased. Upon 66.6 %, the sample flows only for very low shear rate near to zero and shear-thickened state is expected to flow inhomogeneously or exhibit fracture. Random close packing which corresponds to the most concentrated obtainable sample is 69.4 %. For D2, the behaviour is almost the same except that DST is absent even at high concentration. Transitions between regimes occur at higher volume fraction than for D1.

For PVC 1, we observe a shear thickening for volume fraction higher than 45 %. Upon ϕ_{DST}56 %, the suspension exhibits discontinuous shear thickening at a critical shear which is smaller and smaller when ϕ is increased. DST occurs at $\phi/\phi_{\text{absorption test}}$= 0.82, comparable to value from the literature (0.84 [180] or 0.87 [200] . In particular, the thickened state is a flowable state as evidenced by the capillary flow beyond shear thickening. According to the picture developed by Wyart and Cates [57], this holds for ϕ up to ϕ_m = 66.6 % (extrapolated concentration at which DST occurs at zero shear). At higher concentration, the thickened state is expected to be completely jammed and be unable to flow without inhomogeneity or fracture. The random close packing is very difficult to access experimentally, in particular the plasticizer absorption test reaches a value of 68 % whereas random close packing from fit of viscosity curves is estimated to 69.4 %.

Transitions between regimes which occur at higher values for D2 than D1 are explained by the polydispersity of the powder (better packing possible). Besides, the latter lessens shear-thickening so much that no DST is found for PVC 2, explaining why such a powder is widely used in industrial production compared to PVC 1. Again, random close packing is difficult to experimentally access and result from plasticizer absorption test is below the ϕ_{rcp} obtained from fitting low-shear viscosity.

3.4 Discussion

3.4.1 Impact of PVC granulometry

Flowcurves of D1 and D2 are first compared at a fixed volume fraction 60 % with also data from capillary rheometer. Viscosity at low shear rate is very similar (shear-thinning) but the shear thickening behaviour is completely different: moderate for D2 and abrupt for D1. Viscosity at high shear rate tends to be similar. The lower viscosity peak of D2 during shear thickening is explained by its extended size distribution (two distinct populations instead of one). Such shear thickening reduction using more polydisperse powder has been observed by several works on PVC suspensions [176, 194] as well as on other suspensions [227].

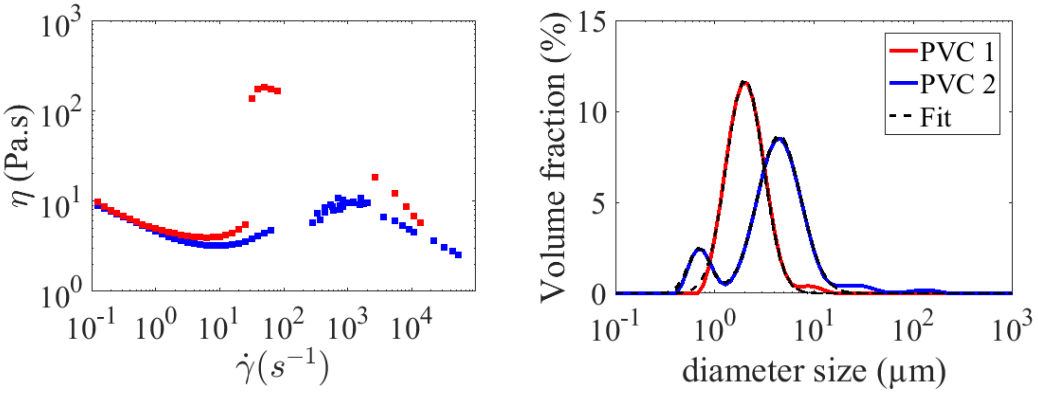

(a) (b)

Figure 3.21: (a) Flow curves of D1 (■) and D2 (■) at a fixed volume fraction 60 % (b) PVC size distribution of D1 (red) and D2 (blue) measured directly in plasticizer.

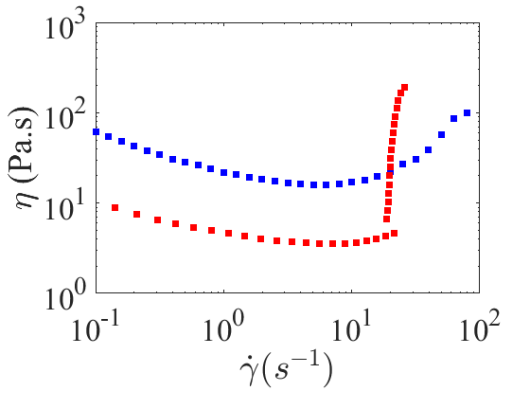

Figure 3.22: Flow curves of D1 (■) at 60.3% and D2 (■) at 67%. Both chosen volume fraction correspond to ϕ/ϕ_{max} = 0.87. Measurements were performed in a cone/plate geometry.

Rather than a fixed ϕ, flow curves are plotted at a fixed distance from jamming (ϕ/ϕ_{max}=0.87) on Fig. 3.22. ϕ_{max} refers here to ϕ_{rcp} obtained by fitting low shear viscosity versus ϕ. The trend is opposite before and after the shear thickening. As previously, ever normalized by the maximum packing fraction, shear thickening is still lower for polydisperse powder. More generally, no DST is observed for D2 made of polydipserse PVC 2. However, at low shear rate, viscosity of D1 is lower (factor 7). This is probably due to small attractive interactions between particles which are numerous in the case of PVC 2 due to a peak under than 1 μm (cf. SEM pictures in part 2.1.1). Even if plasticizer well disperses PVC, there is some residual attraction especially for this range of small sizes: perfectly hard particles with no interaction are not encountered in real life! As small particles are quite numerous (in numbers but not in volume), their interactions contribute to the higher low-shear viscosity observed for D2.

3.4.2 Shear thinning region

Capillary measurements show a shear thinning region upon the shear thickening one with no wall slip encountered. This behaviour is completely out of the scope of the picture for stress-induced shear thickening: shear thickening is described as a transition from a low viscous Newtonian state to a high viscous Newtonian state. Even if reported in several works (cf. part 1.7), such shear thinning has not been studied in great details.

Our data of the viscosity beyond shear thickening can be fitted versus shear rate by a power law scaling (linear in log-log graph). All fits have a R^2 over 0.99. Slopes giving viscosity scaling (versus shear rate) in the 2^{nd} shear thinning region are plotted on fig 3.23. Horizontal axe corresponds to ϕ renormalized by ϕ_{rcp} of each powder (69.4 and 77.2 % for respectively PVC 1 and PVC 2) in order to ease comparison of data between PVC 1 and PVC 2. First, exponent is found to depend on the volume fraction. The higher the volume fraction, the higher the absolute value of the exponent. Surprisingly, data from PVC 1 and PVC 2 collapse roughly on the same straight line. The point close to -0.7 (ϕ/ϕ_{rcp} = 0.87) is the only case where absence of wall slip has not been checked.

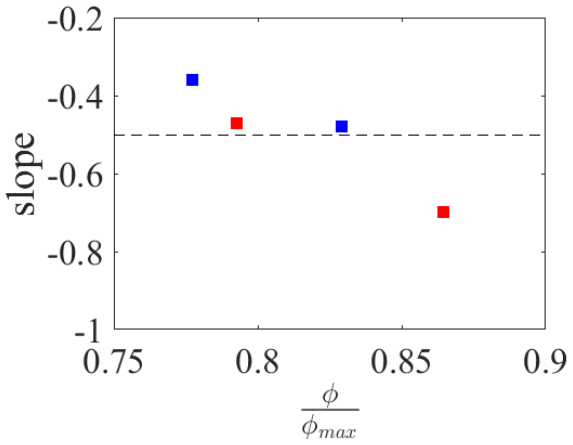

Figure 3.23: Slopes extracted from a power law fit on the viscosity of the second shear thinning region (above shear thickening) plotted versus the normalized volume fraction for PVC 1 (■) and PVC 2 (■).

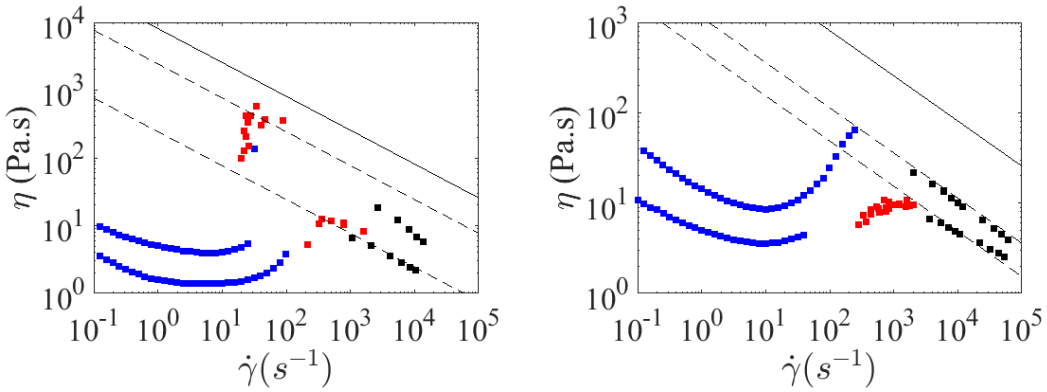

Figure 3.24: Elastohydrodynamic model compared to our rheology data of (a) D1 at 55 and 60 % or (b) D2 at 60 and 64 %. The solid line indicates the model with f(ϕ)= 1 (G_p = 1.6 GPa [153] and η_f = 0.041 Pa.s); the dotted line indicates the model with f(ϕ) = 0.03 and 0.3 for D1 55 and 60 % respectively and with f(ϕ) = 0.06 and 0.14 for D2 60 and 64 % respectively

Main works in the literature deal with an elastohydrodynamic model [153]. This simple model give a scaling (exponent -1/2) for the viscosity in this shear thinning regime:

$$\eta = (\eta_f G_p)^{1/2} \dot{\gamma}^{-1/2} f(\phi) \tag{3.5}$$

where η_f is the medium viscosity, G_p is the shear modulus of the particles and f(ϕ)a prefactor depending on particles concentration. Further details can be found in the first chapter (cf. part 1.7). Looking at our data, the exponent -0.5 is only correct at intermediate volume fraction ($\phi/\phi_{max} \sim$ 0.79-0.84, cf. dotted line on Fig. 3.23). If such a model is applied onto our viscosity curves (cf. Fig. 3.24), a prefactor very small compared to 1 should be taken for $f(\phi)$ (from 0.03 to 0.14). Such small prefactors were also used in [153]. However, this discrepancy of one decade should call the elastohydrodynamic model into question. The main drawback of this simple scaling is the hypothesis of lubrication: beyond the shear-thickening, a lubrication film would be present between particles. For our system, this

hypothesis would be in contradiction with experimental work done previously showing that shear-thickening corresponds to an interparticle solid frictional regime (i.e. no lubrication film, cf. part 3.2). Furthermore, we can have an estimation of the particle deformation. In the 2^{nd} shear thinning region, the shear stress is $\sim 10^5$ Pa. The particle deformation scales as $\sigma a/G$ with a the initial particle radius and G the particle young modulus. Taking $\sim 3.10^9$ Pa for the modulus and a $\sim 10^{-6}$ m for the radius, one gets a deformation of 1/3 Å, which is negligible. It is worthy to note that we perform some Hertzian contacts with quartz-tuning fork based AFM on particles immersed in DINCH and that a bulk modulus of 3 GPa in line with values of bulk PVC.

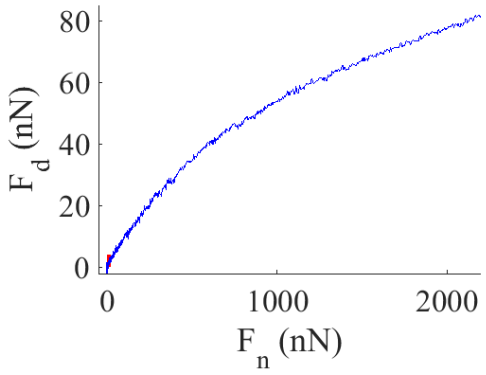

Figure 3.25: Tangential friction forces F_d versus conservative normal forces F_n for high normal load. Previous data concerned a normal load up to 25 nN (red rectangle near the origin). The friction coefficient corresponds to the local slope and decreases for increasing normal load.

Instead, we suggest two hypothesis:

— **the friction coefficient is less important at high stress**, resulting in less dissipation, thus a decreasing viscosity. Following experiments with quartz-tuning fork based AFM (cf. part 3.2), such trend has been measured as displayed on Fig. 3.25. At high normal load, the friction coefficient (corresponding to local slope) is weaker. High value of microscopic normal load would correspond to the shear thickening regime in macroscopic suspensions where shear stresses are important but also normal stresses as shown previously.

— **Collision are too fast at high stress**. DST results from dynamic solid friction interactions between particles. However, to be in a frictional interaction, the interstitial liquid should have time to be squeezed from the brush area in the contact area, which might be not the case at high stress (high particle velocities)

These hypothesis are new and have not been ever reported to the best of our knowledge. Further work is however needed to discriminate these possible mechanisms.

3.5 Ageing

Plastisol are known to exhibit ageing, i.e a slow viscosity increases over days due to slow plasticizer diffusion into particles. Here we quantify ageing in the suspensions for different storage temperatures.

3.5.1 Quantification of viscosity increase

A suspension D2 at ϕ_0 = 62 % was freshly prepared. The suspension was divided into three parts, each one stored at different temperatures : 7, 25 (room temperature) and 40 ˚C. Viscosities were monitored for different ageing times (maximum 15 days). Each sample is re-dispersed one minute prior to viscosity measurements to avoid any sedimentation or inhomogeneity after days of storage. Fig. 3.26 presents the flow curves of D2 62% freshly prepared and after 14 days at 25 ˚C. For aged samples, higher viscosities are measured over the whole shear rate range. Owing to the quasi-absence of aggregates in PVC 2 (cf. part 2.1.1), viscosity is expected to come only from the slow swelling of particles, meaning that the real particles volume fraction ϕ_{real} increases over time. This is confirmed by granulometry measurements where the size distribution nearly does not change even for the toughest conditions probed here 40 ˚C.

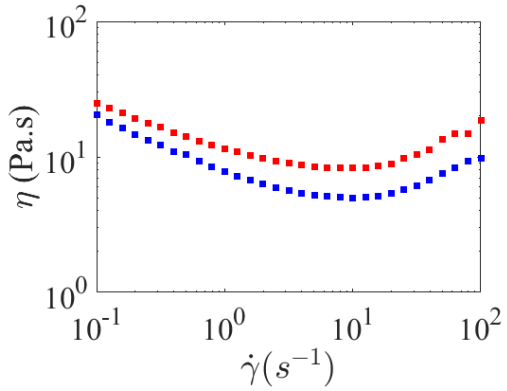

Figure 3.26: Flow curve of D2 62% freshly prepared (■) and after 14 days at 25 ˚C (■) using a cone/plate geometry.

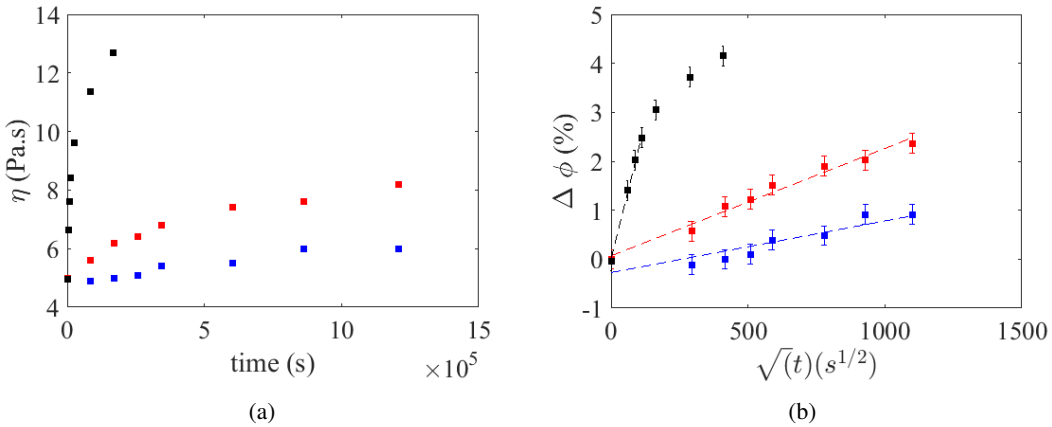

Figure 3.27: Variation of (a) viscosity versus time; and (b) real volume fraction versus square of time for three storage temperature: 7 ˚C (■); 25 ˚C (■) and 40 ˚C (■).

For each temperature, minimum viscosity (for $\dot{\gamma}$ = 10 s^{-1}) is reported versus time on fig 3.27a. We observe an increase of viscosity measurements which is non-linear. As ageing is attributed to a diffusive migration of plasticizer, we report the results versus the square root of time on Fig. 3.27b. η is converted to a real volume fraction ϕ_{real} using the curve $\eta = f(\phi)$ from section 3.3.1 which provides

a calibration curve for D2. We then define $\Delta\phi$ = ϕ_{real} - ϕ_0. A linear increase of volume fraction is observed suggesting a diffusive model. An exception is found for the highest temperature at large time and will be discussed later.

We can calculate a diffusive coefficient using a rough model. We assume a single size corresponding to the $D_{[3,2]}$ diameter of the PVC under scrutiny. The initial particle radius is written R (=$D_{[3,2]}/2$ = 1.2 μm) while the apparent radius of particle at time t is written R + Δ h(t) where Δ h(t) is the size of the polymer brush (thickness in which plasticizer is entered). One can write:

$$\Delta h = \sqrt{(Dt)} \tag{3.6}$$

with D the diffusion coefficient

A simple geometric consideration gives:

$$\frac{\phi_{real}}{\phi} = \frac{(R+\Delta h)^3}{R^3} \tag{3.7}$$

where ϕ_{real} is the actual volume fraction and ϕ the initial volume fraction.

Then, one deduces:

$$\frac{\Delta\phi}{\phi} = \frac{(R+\Delta h)^3 - R^3}{R^3} \approx \frac{3\Delta h}{R} \tag{3.8}$$

where $\Delta\phi = \phi_{real} - \phi$ and considering a slight increase of radius (Δh « R).

Combining Eq. 3.6 and 3.8, one finds:

$$\Delta\phi = \frac{3\phi\sqrt{(Dt)}}{R} \tag{3.9}$$

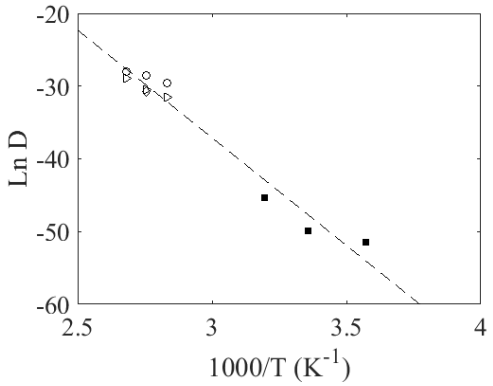

Figure 3.28: Logarithm of diffusive coefficient (D in m^2/s) for particle swelling versus inverse of temperature (closed symbols). For comparison, open symbols corresponds to data from Storey et. al for diffusion of similar plasticizers into PVC (open symbols): di-n-decyl phtalate (right triangles), di-n-nonyl phtalate (circles) and diisodecyl phtalate (diamond) [228].

From experimental values of $\Delta\phi$ versus $\sqrt{(t)}$ (cf. Fig. 3.27b) , one can calculate a diffusion coefficient D. Values at T = 7 , 25 and 40 ˚C are respectively D = 4.10^{-23}, 2.10^{-22} and 2.10^{-20} m^2/s. An Arrhenius plot showing temperature dependance is on fig 3.28. To the best of our knowledge, there is no measurement of the diffusion coefficient of plasticizer in PVC at temperature under 60

˚C. Some data exist for higher temperatures (around and above PVC glass transition temperature T_g = 80 ˚C) [228]. In the latter, they studied diffusion in disks of bulk PVC and find values of D $\sim 10^{-14} m^2/s$ in the temperature range 80-100 ˚C. Besides they showed that the scaling of the diffusion coefficient of plasticizer into PVC follows an Arrhenius law $D = Ae^{-\frac{E}{RT}}$ versus the temperature. Our indirectly-obtained values and their data can roughly be linked using this temperature scaling.

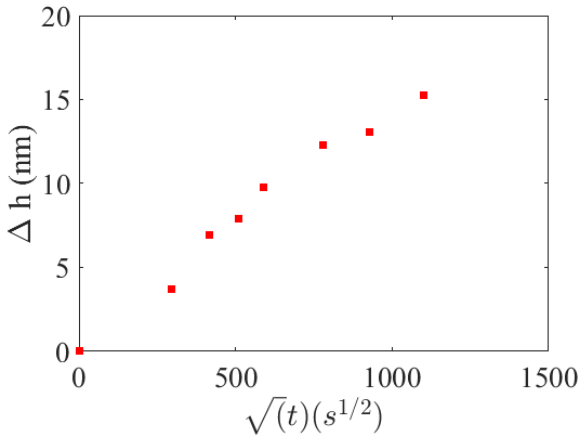

Figure 3.29: Evolution of the size of the brush of polymer Δh(t) as a function of time t at temperature T=25 ˚C.

Eq. 3.6 allows us to calculate an order of magnitude for the variation of mean radius of particles during ageing at room temperature (cf. Fig. 3.29). Variation within two weeks is around 15 nm which corresponds to 0.1 to 2 % of particle size depending on considered particle (dispersity of particle size from PVC 2). This value is coherent with the initial brush size estimated to 4 nm from AFM measurements (cf part. 3.2).

Our measurements are however limited to very small swelling ratio ($\sim$ 1-2 %). When swelling ratio is much high ($\sim$ 100 %), the regime of swelling can behave completely differently as for example the linear swell rate of grain microscopically observed by Boudhani et. al. [178]. The difference in scaling laws at high swelling ratio may also explain the deviation from a diffusive model when the swelling ratio exceed 2 % (temperature of 40 ˚C on figure 3.27).

As strong assumptions were used in the simple model, it gives only a rough value for diffusion coefficient and brush size calculation. Results could have been maybe more accurate with the less polydisperse powder (e.g PVC 1) or with a more complex modelling. Moreover, the measurements of diffusive motion is quite indirect from viscosity measurements. However, following the viscosity of concentrated suspensions is a way to measure very low diffusion coefficient ($\sim 10^{-21}$) with coherent results. In addition, those results confirm the need to prepare fresh suspensions for precise and reliable viscosity measurements

3.5.2 Tuning shear thickening with swelling

Ageing corresponds to a thickening of polymer brushes due to further plasticizer diffusion into particles. These brushes stabilize our suspensions by creating a repulsive steric interactions. As described in part 1.3.2.6, increasing the repulsive forces delay the shear thickening occurrence. We thus

may wonder if aged suspensions less shear-thicken than fresh ones. D1 is chosen for the experiment as PVC 1 granulometry is monomodal and shear thickening is more pronounced, which exacerbates any shear-thickening modification.

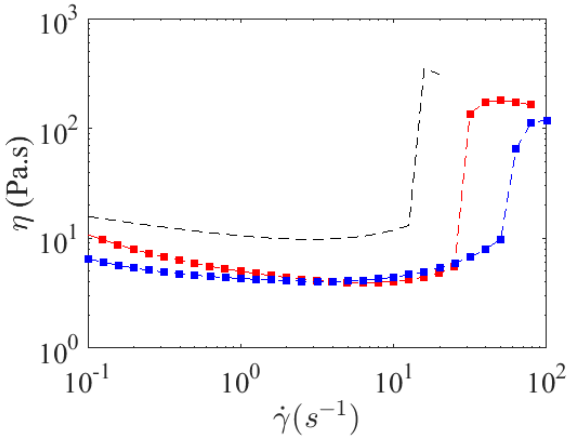

Figure 3.30: Aged sample (dotted black line) rediluted to initial volume fraction at ϕ = 60% (■) compared to fresh sample at ϕ = 60% (■). Measurements were performed in a cone/plate geometry.

Accelerated ageing was done on D1 at 60% at 50 ˚C. Viscosity of the aged suspension was naturally higher (cf. Fig. 3.30) due to plasticizer diffusion into PVC grains. Real volume fraction is consequently higher than the initial value. Initial volume fraction (60 %) is retrieved by adding a certain amount of plasticizer so as to match initial minimum viscosity (cf. Fig. 3.30). Discrepancy at low shear rate can be interpreted as modification in brushes leading to modified interparticular interactions which are critical at low shear rate. But the most important difference lies in the shear thickening regime. Aged suspension with corrected volume fraction exhibits a much less steep shear thickening instead of the discontinuous initial one. This result is interpreted at the light of the Wyart and Cates model (detailed in 1.3.2.5). Ageing produces a higher repulsive force via a thicker swelled PVC brush. A higher stress is thus needed to enter the frictional regime (shift from 80 to 500 Pa).

With experiments presented in previous sections, shear thickening origin in PVC suspensions in well understood: it stems from the breakage of lubrication film upon a critical stress. These new insights at the particle scale arise questions now at the global scale of the shear thickening system. In particular, impact of geometry in the flow behaviour and possible shear-induced particle migration are not well understood.

3.6 How does a shear-thickening fluid flow?

3.6.1 Introduction

Figure 3.31 shows an unusual viscosity dependence of geometry in the thickening transition. A Couette cell gives lower shear rates for the shear-thickened state than cone/plate. Underlined difference is more important at higher volume fraction. The amplitude of the S-curve depends upon the details of

the protocol: a faster procedure induces a direct jump with no incursion at high shear rate on the low viscosity branch. However, the critical value of the shear rate corresponding to the vertical part of the curve is not affected by the protocol. Geometry seems thus to play a role in the flow behaviour of our shear-thickening system. We better characterize this effect in the following by using Couette cells with different gaps.

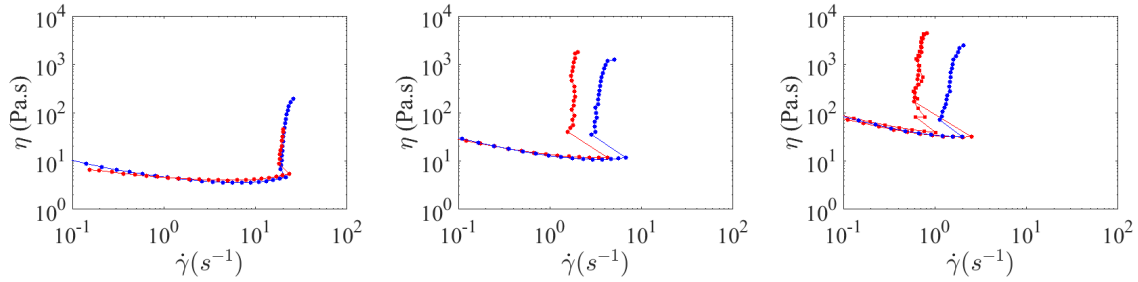

Figure 3.31: Flow curve of D1 at (a) ϕ = 60 %, (b) ϕ = 64 % and (c) ϕ = 66 % measured in a 1 mm Couette cell (red) or cone/plate (blue).

3.6.2 Impact of gap on viscosity

3.6.2.1 Protocol

We focus on both dispersion D1 and D2 at ϕ = 60 %. Rotational rheometry is performed on a stress-controlled ARGII rheometer from *TA instruments* in a Couette cell geometry. To investigate the influence of the geometry on shear thickening, three different Plexiglas cylindrical Couette cells are used with gap widths d = 1.0, 0.5 and 0.25 mm and the same outer radius of 25.0 mm and height of 30 mm. The stress is assumed to be homogeneous with a decreases only by 2%, 4% and 8% for d = 0.25, 0.5 and 1 mm respectively. We then apply successive steps of increasing shear stress σ for 500 s per step. Steady state is reached in less than 60 s as described in 3.1.4.3. The increment between two steps ranges from 5 to 300 Pa depending on σ.

3.6.2.2 Results

Figure 3.32 displays the flow curves of both systems for different gaps. Dispersion D1 exhibits a shear-thinning behaviour at low shear stress followed by a DST behaviour with a characteristic S-shaped flow curve. Dispersion D2 is also shear thinning at low shear stress but displays CST at higher shear stress due to the powder polydispersity. In both cases, the rheological behaviour depends upon the confinement: the smaller the gap, the smaller the viscosity and the higher the shear rate at which shear thickening sets in.

Such a behaviour has already been observed in dense suspensions: some have suggested that slip at the wall was at its origin [66, 101, 41] by calculating slip velocities using the Yoshimura and Prud'homme corrections [229]. One recent study observed the phenomenon [131] but did not discuss it and did not check for possible wall slip. Finally, two studies [47, 51] on cornstarch suspensions have however measured a gap dependence with roughened plate/plate geometry (no slip at the wall).

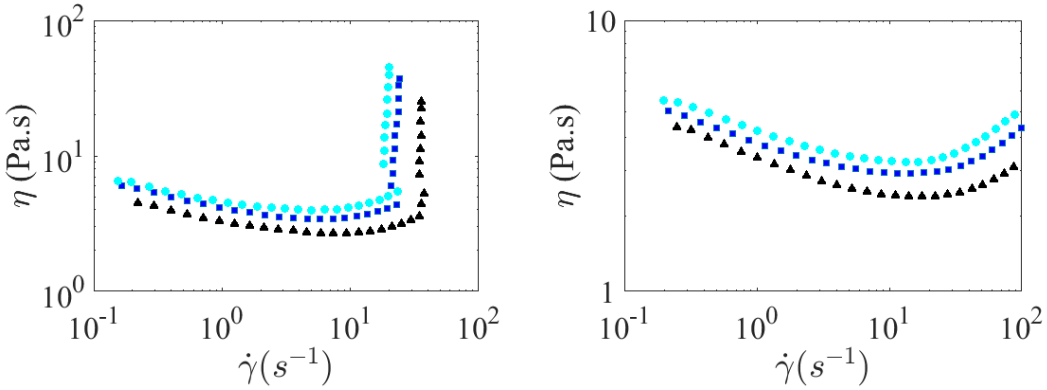

Figure 3.32: Flow curves, viscosity η vs shear rate $\dot{\gamma}$ of (a) dispersion D1 and (b) D2 in a Taylor-Couette cell of gap width d = 1.0 mm (●), d = 0.5 mm (■) and d = 0.25 mm (▲).

Strikingly, the trend was inverse to ours: in their system, a smaller gap results in a smaller critical shear rate. Nevertheless, the studied system, a cornstarch suspension, was found to migrate under shear especially during the shear thickening transition [47, 81]. Even if their experiments are carried out in a wide-gap Couette cell with a non homogeneous stress (d/R = 0.44 compared to d/R = 0.04, 0.02 and 0.01 in the present work where d is the gap and R the outer radius of the Couette cell), their migration is far faster than expected in such a geometry. To clarify this wall slip issue and to check for possible heterogeneous flows, we measure firstly the local velocity across the gap during the flow of our PVC-particles concentrated suspensions.

3.6.3 Checking slip at the wall

With ultrasonic velocimetry [205] combined simultaneously to rheometry, we measure the local velocity across the gap. Both dispersions D1 and D2 contain a few "large" particles (of typical diameter $\sim 10\ \mu m$) that scatter the incoming ultrasonic pulses (of frequency 35 MHz and wavelength 40 μm) efficiently. Therefore, in spite of a strong attenuation of the scattered signal due to the large particle volume fraction, ultrasonic velocimetry can be directly used as described in [205] on both dispersions without tuning their acoustic properties, even though multiple scattering becomes an issue in D2 for the largest gap width (see further).

The velocity profiles v(x) shown in Fig.3.33 for the D1 DST (D2 CST) dispersions are averaged over the last 200 s of the step (i.e. 5 to 100 profiles depending on the shear rate). The insets display the velocity of the fluid divided by the velocity of the rotor as a function of the position in the gap divided by the gap thickness.

For the D1 dispersion, no slip at the wall is evidenced in the 1 mm and 0.5 mm gap. The velocity of the fluid goes to zero at the stator and is equal to the velocity of the motor at the rotor (see the red diamonds). The inset shows that the flow is homogeneous. The data roughly collapse on the straight line of slope 1 showing without ambiguity that the sample is sheared homogeneously at the applied shear rate. In the 0.25 mm gap , we note the same behaviour for shear stress below 300 Pa. Some slip is noticed but only for 800 Pa. This cannot explain the global differences between the curves.

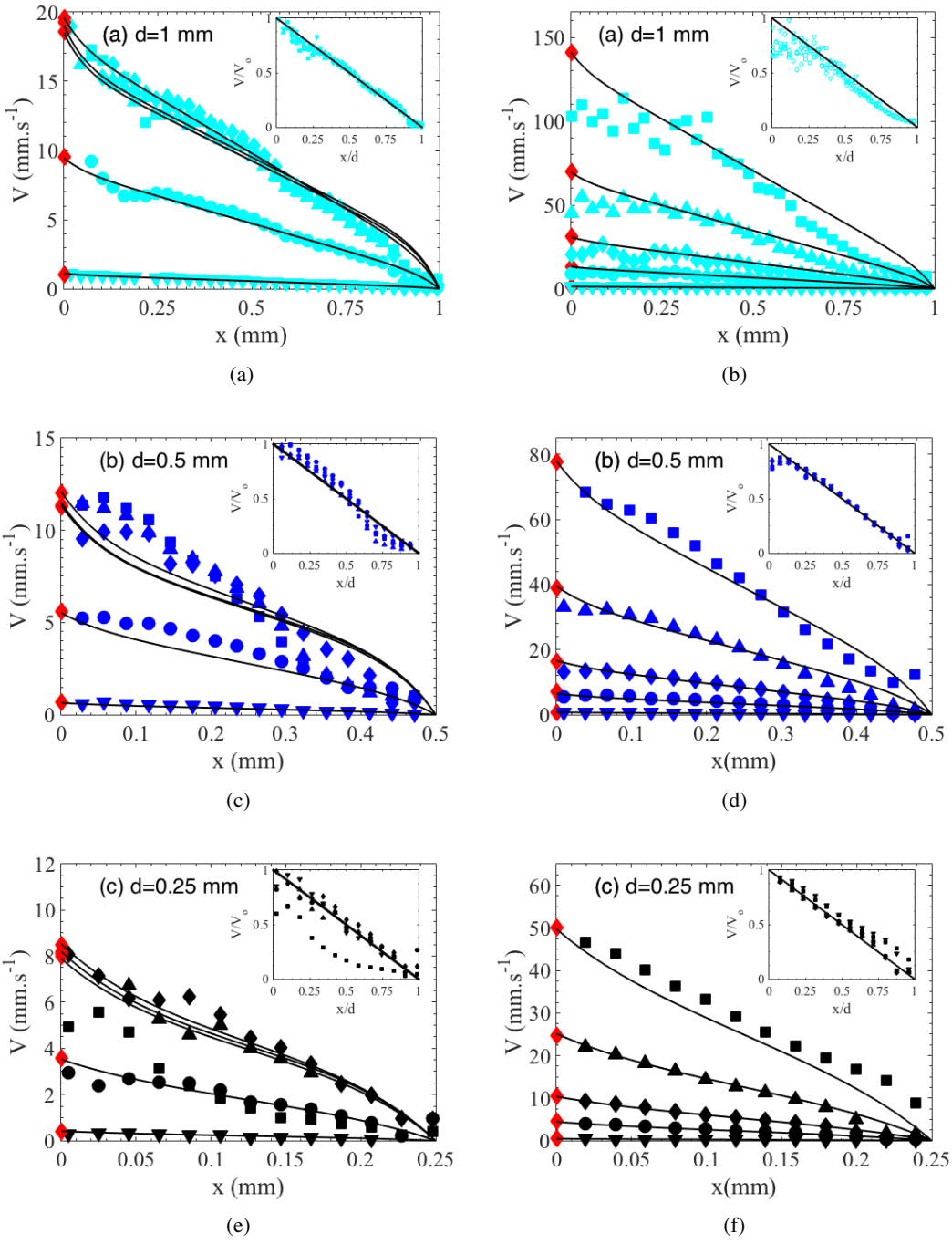

Figure 3.33: Velocity profiles $v(x)$ in dispersion D1 corresponding to the flow curves of Fig.3.41(a) in a Taylor-Couette cell of gap width (a) $d = 1$ mm, (c) $d = 0.5$ mm and (e) $d = 0.25$ mm. x denotes the distance to the rotor. The red diamonds (♦) indicate the rotor velocity v_0. The insets display the velocity of the fluid divided by v_0 as a function of the normalized position in the gap x/d. The applied shear stresses are $\sigma = 800$ (■), 300 (▲), 100 (♦), 40 (•) and 5 Pa (▼). Black solid lines correspond to Eqs. (3.18) and (3.19) with $\xi = 55$ μm. (b)(d)(f) Same for dispersion D2 with $\xi = 51$ μm.

For the D2 dispersion, no slip at the wall is evidenced in the 0.5 and 0.25 mm gap. In the 1 mm gap, the velocity of the rotor is not equal to the velocity of the sample at high shear stress. This deviation is due to multiple scattering that limits the resolution of our device for the 1 mm gap. We underline that

these low velocities close to the rotor are not realistic. We note that if they were realistic, they will increase the difference between the rheological curves obtained in the 1 mm and 0.5 mm gap.

The conclusions of our observations are twofold. First, the global differences between the flow curves of Fig. 3.32 are not due to wall slip: the samples are truly submitted to the applied shear rate. Secondly, those results suggest also that both DST and CST involve homogeneous flows in the shear gradient direction at least at the scale of the ultrasonic wavelength (i.e. 40 μm) as suggested by two recent works [63, 60]. We have measured velocity profiles as a function of the vertical position and found no variations so that flows are also homogeneous in the vorticity direction. This does not mean that there are no vorticity bands [24, 25]. Vorticity banding corresponds to structure banding and not to banded velocity profiles. Still direct observation of the present shear thickening suspension did not reveal any variation of the optical turbidity, suggesting either that no bands are present or that they are very thin. To confirm these findings, we use state-of-the-art method based on X-ray radiography.

3.6.4 Shear-induced particle migration?

Once slip at the wall hypothesis was ruled out by previously described experiments, we focus here on possible shear-induced migration. Real time spatial particles repartition upon flow is followed by X-ray radiography. All the following X-ray absorption experiments were done at the scientific platform *Placamat* in Bordeaux with Nicolas Lenoir (*Placamat*) and Guillaume Ovarlez (*Laboratory Of the Future*).

3.6.4.1 Materials

We focus here on suspension D1 at 60 % ($\phi_{DST} < \phi < \phi_m$). Suspensions were prepared just before used and degassed prior to experiments. Indeed, few remaining bubbles would be highly visible in X-ray absorption due to contrast difference and could hinder further image analysis.

3.6.4.2 Rheometry

Rotational rheometry is performed on a stress-controlled ARGII rheometer from *TA instruments* in a Couette cell geometry. Stator is cylindrical (inner diameter 50 mm) made of Poly Methyl Methacrylate (PMMA) to ensure as low X-ray absorption as possible. Stator has a diameter of 50 mm. Used rotors have various diameters ranging from 45.8 mm (2.1 mm gap) to 49 mm (0.5 mm gap) and are made of Delrin. In addition to rotational rheometry, capillary rheometry is performed with a home-made developed syringe. Flow is ensured by applying a pressure on the piston (0-8 bars). Die diameter is 2 mm. Two capillary lengths are used: 6.5 and 17 mm. Rheological measurements are carried out by recording pressure and flow rate during X-ray imaging.

3.6.4.3 D1 60% in a Couette cell geometry

2.1 mm gap As described in part 2.10, we follow in the gap $\Phi(r, z, t) / \phi_0$ which is the relative variation of the averaged particle volume fraction seen by the beam along its path at this position. One has to be aware that we do not compute here the local particle volume fraction $\phi(y, z, t)$ but only averaged particle volume fraction seen by the beam along its path at this position. All distances are

kept as pixels from the image analysis. Scale bar can however vary between experiments as it depends on the distance between the rheometer and the X-ray source. Figure 3.34 shows the relative variation of volume fraction (seen by the beam along its path) in the Couette cell gap versus the radial position for different applied stresses before and during the shear thickening transition (which occurs at $\sim$ 75 Pa). Measurements are averaged in the z-direction for each point in the radial direction r. Related snapshots of the gap corresponding to each stress step are displayed on Fig. 3.35.

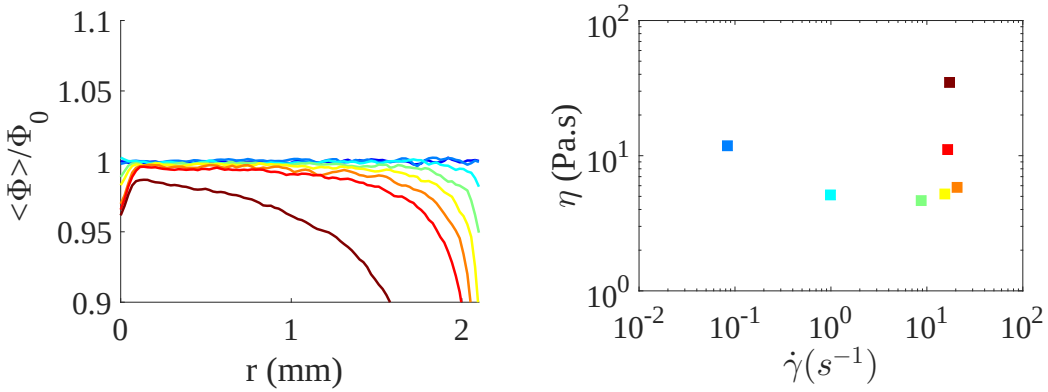

Figure 3.34: Flow of D1 (ϕ = 60 %) in a 2.1 mm Couette cell: (a) radial relative intensity variation for different applied stress steps (1 Pa; 20 Pa; 60 Pa; 100 Pa; 150 Pa; 200 Pa; 600 Pa). (b) Viscosity and shear rates corresponding to those stress steps.

At low stress (σ < 20 Pa), no significant particle migration is to be seen as the volume fraction stays homogeneous ($\Phi(r,z,t)/\phi_0 \sim 1$). At intermediate stress (20-200 Pa), a depletion zone appears at the outer cylinder but no over-concentrated zone is observed. This is likely due to air bubble inclusion, meaning that the interface is unstable in the shear thickening regime and let some bubble enters. The phenomenon is critical at 600 Pa where more than half of the gap is empty. It is worth noting that the scale bar on snapshots (Fig. 3.35) is constrained at 0.9-1.1 for sake of clarity, meaning than the blue zone (lower absorption compared to initial state) can represent relative volume fraction lower than 0.9 as it is the case for the last snapshots. We plotted the radial dependence as no global variation is observed in the z direction as seen on snapshots.

1 mm gap As for the previous 2.1 mm gap, figure 3.36 shows the relative variation of volume fraction (seen by the beam along its path) in the Couette cell (gap 1 mm) versus the radial position for different applied stresses before and during the shear thickening transition (which occurs at $\sim$ 75 Pa). Measurements are averaged in the z-direction for each point in the radial direction r. Related snapshots of the gap corresponding to each stress step are displayed on Fig. 3.37. Again, no experimentally measurable radial migration is observed during the experiment ($\Phi(r,z,t)/\phi_0 \sim 1$ in the gap for all stresses). As previously, the interface at the top moves during the experiment: it lowers (see expanding blue zone on top) but bubbles do not completely invade the gap as for the 2.1 mm gap. Again, no global variation of volume fraction is observed in the z direction.

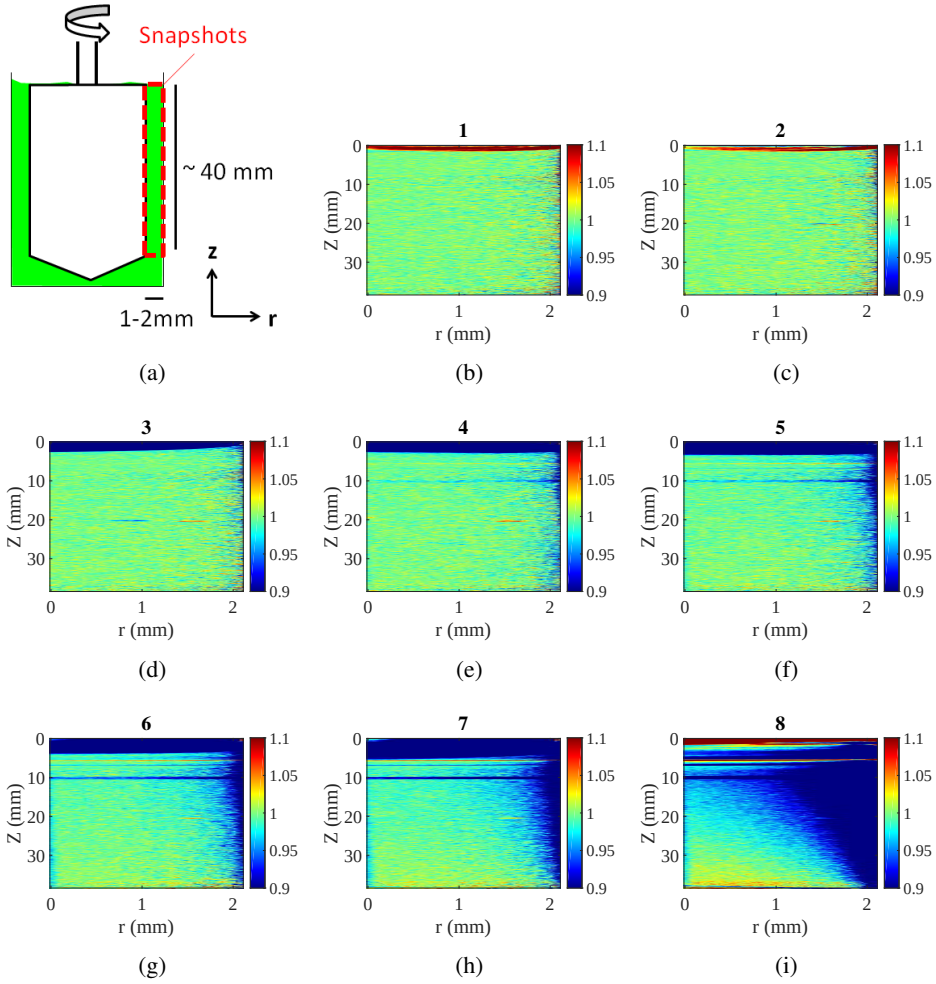

Figure 3.35: Flow of D1 (ϕ = 60 %) in a 2.1 mm Couette cell: (a) Scheme showing the gap zone under scrutiny. 2D map of the gap showing the relative variation of the particle volume fraction $\Phi(r,z,t)/\phi_0$ for increasing stress step σ = (b) 0 Pa (c) 1 Pa (d) 20 Pa (e) 60 Pa (f) 100 Pa (g) 150 Pa (h) 200 Pa (i)= 600 Pa. Scale bar for $\Phi(r,z,t)/\phi_0$ is constrained to 0.9-1.1 (green zones corresponds to a stable relative volume fraction; blue zones to a decrease and red ones to an increase). Left side of each picture corresponds to inner cylinder and the bottom corresponds to the bottom of the Couette Cell.

3.6.4.4 D1 60% in a capillary flow

We just showed that no particle migration happens in the previous experiments in Couette cell. However, the latter does not enable measurements of the upper bound of shear thickening and the 2^{nd} shear-thinning regime beyond (limitations in the torque and some artefacts as air inclusion or sample ejection). In order to probe local particles concentration at the end of shear-thickening and beginning of 2^{nd} shear-thinning regime, we perform a capillary flow of D1 at ϕ_0 = 60% under X ray radiography (cf. Fig. 3.38).

We detail here results for the shorter capillary (L = 6.5 mm) as it enables the highest stress (50 kPa). Same results were found for a higher length. Pressure range from 1 to 7 bars give access to the upper part of the shear thickening transition (see Fig. 3.39). Even in this region, the flowing sample does not show any segregation when going throughout the capillary ($\Phi(r,z,t)/\phi_0 \sim$1 for all stresses): neither in radial direction X nor in the flow direction Z (cf. Fig. 3.40). It is interesting to note that

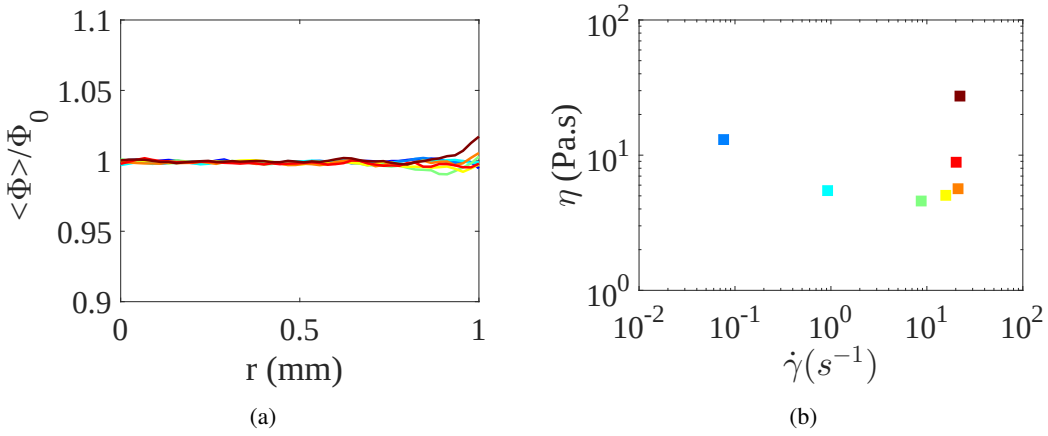

Figure 3.36: Flow of D1 (ϕ = 60 %) in a 1 mm Couette cell: (a) radial relative intensity variation for different applied stress steps (1 Pa; 20 Pa; 60 Pa; 100 Pa; 150 Pa; 200 Pa; 600 Pa). (b) Viscosity and shear rates corresponding to those stress steps.

flow stays homogeneous even in the shear-thinning region above shear-thickening (cf. highest stresses probed here).

3.6.5 Discussion

3.6.5.1 Particle migration

From X-ray radiography experiments, PVC suspensions flow homogeneously and do not show any measurable particles migration in the probed experimental conditions both before, during and after the shear thickening transition. As any particulate system, it should however be subjected to some migration. Thus, it could be too slow to probe it in standard rheological experiment ($\sim$ 15 min) or/and too weak (in term of amplitude $\Delta\phi$) to observe it. We thus attempt to calculate some orders of magnitude for both scalings (kinetics and amplitude of possible migration).

Two models have been developed (cf. part 1.6) to attempt a prediction of particle migration: (i) diffusive flux model where migration flux is induced by gradients in shear rate and (ii) the "suspension balance model" where particle flux is due to gradients in normal stresses. Such models allow to find a scaling for the diffusion coefficient of particles. They treat the suspension as an assembly of hard spheres with some contacts. Inertia is neglected and no repulsive forces is considered. The behaviour is then viscous (no shear rate dependence as detailed in part 1.2). For our case, in the shear thickening, particles are touching many others through frictional contacts particles (repulsion forces are overcome). So, we consider our suspension quite close to the model of an assembly of hard spheres. In such cases, the scaling for the diffusion coefficient is:

$$D = f(\phi)d^2\dot{\gamma} \tag{3.10}$$

where d is the particle diameter, f(ϕ) a pre-factor and $\dot{\gamma}$ the shear rate.

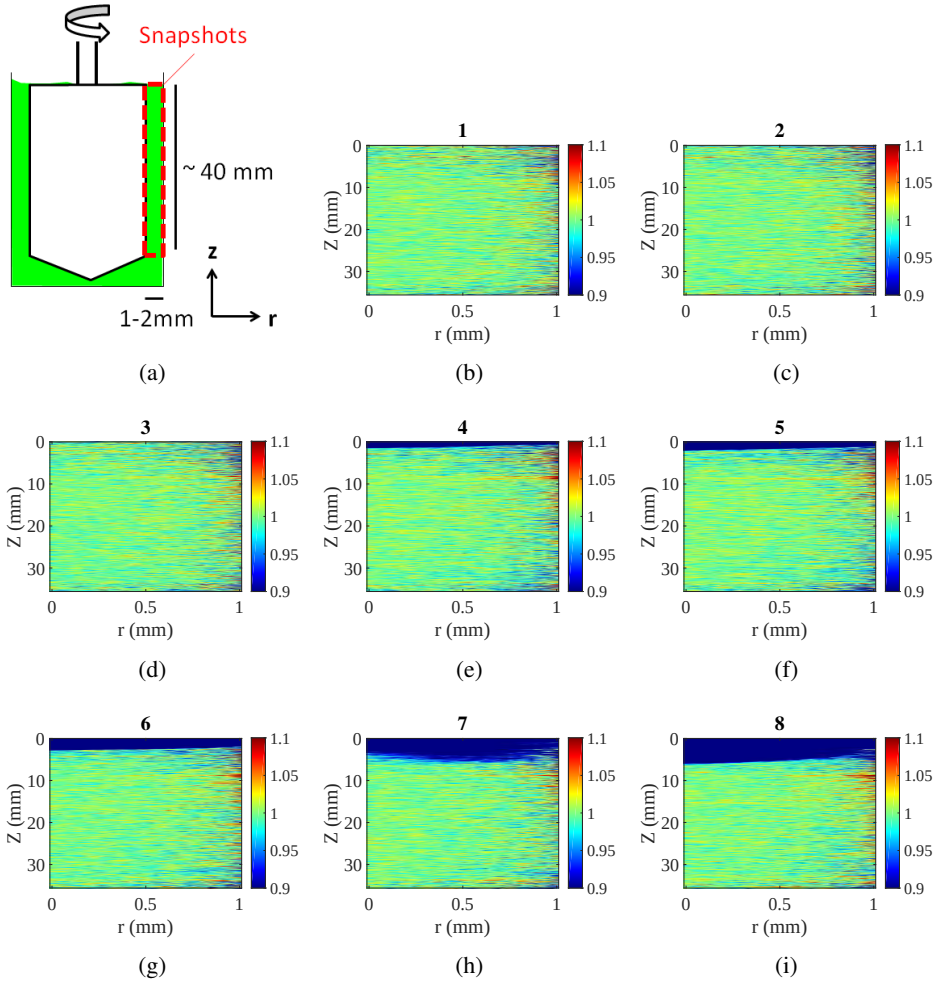

Figure 3.37: Flow of D1 (ϕ = 60 %) in a 1 mm Couette cell: (a) Scheme showing the gap zone under scrutiny. 2D map of the gap showing the relative variation of the particle volume fraction $\Phi(r,z,t)/\phi_0$ for increasing stress step σ = (b) 0 Pa (c) 1 Pa (d) 20 Pa (e) 60 Pa (f) 100 Pa (g) 150 Pa (h) 200 Pa (i) 600 Pa. Scale bar for $\Phi(r,z,t)/\phi_0$ is constrained to 0.9-1.1 (green zones corresponds to a stable particle volume fraction; blue zones to a decrease and red ones to an increase). Left side of each picture corresponds to inner cylinder and the bottom corresponds to the bottom of the Couette Cell.

Migration is significant when a particle has time to move on a distance of same order of magnitude than the gap h. Thus, we can write

$$h^2 = Dt = f(\phi)d^2\dot{\gamma}t = f(\phi)d^2\gamma \tag{3.11}$$

where gamma is the typical strain for migration to happen. it can rewritten

$$\gamma = f(\phi)\frac{h^2}{d^2} \tag{3.12}$$

We need a value for f(ϕ). In an extensive study with PS (Poly-Styrene) particles of 100 μm [230], Ovarlez and Guazzelli found f(ϕ) = 0.1 for similar relative concentration as in our case (ϕ/ϕ_m= 60/66.6 = 0.9). Using d = 2 μm, h = 1 mm, a typical strain of 25 000 is found. It corresponds to a typical time of 2500 s for a mean shear rate of 10 s^{-1}. The kinetics is thus quite slow as it will take around

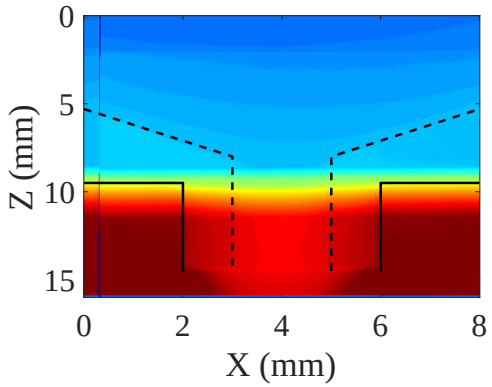

Figure 3.38: Image obtained by X-ray radiography. Blue zone on the upper part correspond to the reservoir of the syringe (see V-shape converging toward capillary). Capillary flow is visible in the middle of red region (capillary walls with flow in-between).

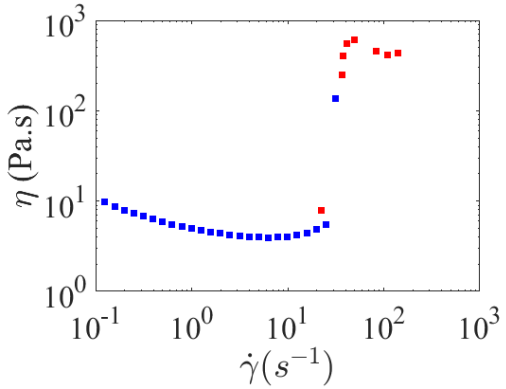

Figure 3.39: Red: Viscosity at high stress measured with capillary rheometer (R=1 mm, L = 6.5 mm). The red point in the low viscosity zone correspond to P = 0 bars (only gravity). Blue points correspond to flow curve obtained in a Couette cell.

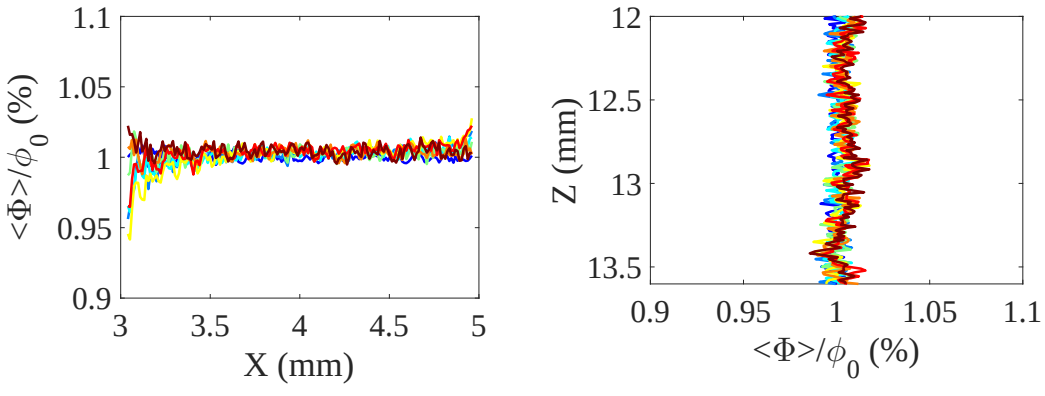

(a) (b)

Figure 3.40: Relative variation of the averaged particle volume fraction seen by the beam along (a) the flow direction Z or (b) the radial direction X for D1 60 %. Applied stresses range from 180 (electric blue) to 9.8 10^3 (blue), 1.5 10^4 (cyan blue), 2.3 10^4 (green), 3.0 10^4 (yellow), 3.9 10^4 (orange), 4.6 10^4 (red), 6.2 10^4 (brown) Pa and correspond to the ones obtained with the large PMMA syringe (from 0 to 8 bars) as shown in Fig. 3.39 (before, in and beyond the DST transition).

forty minutes to fully develop whereas our experiment in rotational rheometer last around 15 min. For capillary measurements, the time of shearing in the capillary is around 0.1-1 s. The small size of our particle compared to used Couette cell gap (ratio 1/500) explains the long time needed for a steady state in particle spatial repartition.

A scaling can also be calculated for the amplitude of migration (quantification of change in %). We note R_1 for the bob radius and R_2 for the outer cylinder radius. In the steady state regime, volume fraction in a Couette Cell can be written as [152]:

$$\phi(r) = \phi(R_1)(\frac{r}{R_1})^{\frac{1}{2}(\frac{\lambda_1}{\lambda 2}-1)} \tag{3.13}$$

where λ_1 and λ_2 are linked with particle normal stress. They are defined from the particle normal stress tensor $\Sigma_{ii} = \eta_0\eta_n(\phi)\dot{\gamma}\lambda i$ with i=1,2,3. 1, 2, and 3 denoting the flow, velocity gradient, and vorticity directions, respectively. It is worthy to note that the case of $\lambda_1 = \lambda_2$ refers to the case with no first normal stress difference. Recent measurements [152] suggests that $\lambda_2 \gg \lambda_1$ to correctly fit experimental data. Typical value of λ_1 =0.1 and λ_2 =3 are used in [152]

A second equation is necessary and comes from matter conservation. We write:

$$\phi_0 = \int_{R_1}^{R_2} \frac{\phi(r)}{R_2 - R_1}\,\mathrm{d}r \tag{3.14}$$

Using Eq. 3.13 and integrating,

$$\phi(R_1) = \phi_0(\alpha+1)(R_2 - R_1)\frac{R_1^\alpha}{R_2^{\alpha+1} - R_1^{\alpha+1}} \tag{3.15}$$

Using these equation with ϕ_0 = 60%, R_1= 48 mm, R_2= 50 mm, a variation of 0.3 % is found (59.7% at the inner cylinder, 60.3% at the outer one). This change in volume fraction is very low (ϕ/ϕ_0=0.995). This is explained by the small gap used compared to radius of the Couette cell (ratio 1/25).

At 60 %, the PVC suspensions exhibit DST ($\phi_{DST} < \phi < \phi_m$) which is seen as a transition between two viscous states according to Wyart and Cates framework. Here, our measures show that these suspensions do flow homogeneously before, during and beyond the shear-thickening transition. Using scaling laws, both a long-time scale and a small amplitude would be expected for possible particle migration. The absence of visible migration for PVC suspensions at 60 % in the probed experimental conditions then appears to be rationalized.

3.6.5.2 Gap dependence on viscosity

We show that viscosity was dependant on the gap in which the suspension flows (cf. part 3.6.2). More precisely the smaller the gap, the smaller the viscosity. As we measure a constant critical shear stress for shear thickening onset, shear thickening appears at higher shear rate in smaller gaps as the viscosity is lower. We also report that nor slip at the wall neither inhomogeneity in spatial particle concentration are measured along this gap dependence. To try to rationalize these results, we show in the following that a non-local approach inherited from previous models for flow cooperativity in soft glassy materials and granular systems accounts very well for our experimental results.

The finite-size effects reported here in a situation where the stress field is almost homogeneous point to the existence of extended spatial correlations. In granular media [231, 232] and more generally in soft glassy materials [233], flow occurs through a succession of elastic deformations and local irreversible plastic events. A localized zone of plastic grain rearrangement produces non-local elastic stress fluctuations extending on a distance ξ away from the rearrangement. These fluctuations superimpose with the stresses due to applied load and can cause a neighbouring material element to flow when it would not otherwise. We anticipate that the mean spatial value of these fluctuations is zero and that they do not correspond to the fluctuations of shear rate measured in the DST regime. This suggests that non-local effects affect the rearrangement rates and consequently the rheological properties.

Based on the statistics of such a kinetic-elasto plastic (KEP) mechanism, Bocquet *et al.* [234, 235, 236, 237] have derived a constitutive non-local equation for emulsions which has later been extended to granular materials [238, 239]. Here we propose to use an approach that builds upon these models to describe the flow of shear thickening suspension in terms of a generalized fluidity g. Note that other non-local models [240, 241] may also be relevant.

For the sake of clarity, we start with the description of the kinetic-elasto plastic mechanism. The sample is divided into elementary blocks of size a (typically the size of individual particles) carrying a scalar friction coefficient $\mu = \sigma / P$, where σ is the scalar shear stress and P the pressure. The system is described in terms of the block friction coefficient distribution $P(\mu, t)$. The evolution of the blocks follows simple rules. When submitted to a shear rate $\dot{\gamma}$, the friction coefficient of all the blocks increases with time interval dt by the quantity $\beta \dot{\gamma} dt$. If the absolute value of the friction coefficient μ of a given block is larger than a critical value μ_o, the block undergoes a plastic event, and the friction coefficient is set to zero after a time τ. This procedure modifies the value of μ throughout the whole sample. To relate the stress relaxed at a block i due to a localized plastic event in another block j, Bocquet [235] uses the stress-stress elastic propagator. Neglecting convection, assuming a full stress relaxation, a decoupling of the plastic-event dynamics, small μ, and returning to spatial variables , this leads Bocquet [235] and Kamrin [238, 239] to write :

$$\dot{\gamma} = g\mu \tag{3.16}$$

$$g = g_l + \xi^2 \Delta g \tag{3.17}$$

where $\mu = \sigma / P$. g and g_l both depend upon μ and P. μ is a function of ϕ [57]. g_l corresponds to the generalized fluidity in the absence of any finite-size effect. In an shear-thickening suspensions, it has to take into account the coupling between the structure and the flow and, more precisely, between the structure and the pressure. Its modelling is out the scope of this thesis. In the following, we will deduce g_l from the measurements.

Let us now discuss the solution of this rheological model in plane Couette flow. Non-local effects are expected when the size of the system d becomes comparable to a few times the correlation length ξ. The flow behaviour also requires boundary conditions for the fluidity at the confining walls, which we shall assume to be a given function g_w of μ and P at the walls in line with previous experimental results [234]. For a planar Couette cell made of two parallel walls separated by a distance d, the mean shear stress σ and the pressure P are spatially homogeneous and the resolution of the fluidity model is straightforward in this geometry. Using the boundary condition $g = g_w$ at both walls, we obtain the expression of $\dot{\gamma}(x)$ and $v(x)$:

$$v(x) = \frac{\sigma}{P}\left(g_l \cdot x + b(x)\right) \tag{3.18}$$

$$b(x) = (g_w - g_l) \cdot \xi \, \frac{\sinh\left(\frac{x-d/2}{\xi}\right) + \sinh\left(\frac{d/2}{\xi}\right)}{\cosh(d/2\xi)} \tag{3.19}$$

Thus, the spatially-averaged shear rate $\langle\dot{\gamma}\rangle$ measured by the rheometer is:

$$\langle\dot{\gamma}\rangle = \frac{v(d)}{d} = \frac{\sigma}{P}\left(g_l + (g_w - g_l)\frac{2\xi}{d}\,\tanh\left(\frac{d}{2\xi}\right)\right) \tag{3.20}$$

ξ, g_w/P and g_l/P are up to know unknown variables. We further simplify it by noticing that $d \gg 2\xi$ so that $\tanh(d/2\xi) \simeq 1$. ξ will be our fitting parameter for the above KEP model, So we need first to calculate g_w/P and g_l/P as a function of σ.

We use two out of three experimentally measured flow curves: in the 1-mm gap, σ vs $\langle\dot{\gamma}\rangle_{d=1\text{ mm}}$, and in the 0.5-mm gap, σ vs $\langle\dot{\gamma}\rangle_{d=0.5\text{ mm}}$.

Using Eq. (3.20) for d= 0.5 mm and d= 1mm leads to

$$g_l/P = (2\langle\dot{\gamma}\rangle_{d=1\text{ mm}} - \langle\dot{\gamma}\rangle_{d=0.5\text{ mm}})/\sigma \tag{3.21}$$

and

$$2\xi(g_w - g_l)/P = 10^{-3} \cdot (\langle\dot{\gamma}\rangle_{d=1\text{ mm}}/\sigma - g_l/P) \tag{3.22}$$

Then, using these expressions of g_l/P and $2\xi(g_w - g_l)/P$ gives us a expression for the velocity profile $v(x)$ with ξ as the only free parameter.

(3.23)

which allows us to fit the velocity profiles presented in figure 3.33. We find that $\xi = 55\ \mu$m $\pm$ 5 μm for D1 and $\xi = 51\ \mu \pm 5\ \mu$m for D2 allow us to accurately recover not only all velocity profiles measured in both dispersions but also the third flow curve in the 0.25-mm gap (see Fig. 3.41).

The length ξ corresponds to the spatial extension of the stress fluctuations due to a rearrangement. The obtained values are significantly larger than the ones found in emulsions but in agreement with correlation lengths already reported in granular materials [231]. We find similar values of ξ for both CST and DST systems. This might be a coincidence but this also echoes the results of Seto *et al.* [70] who report that the number of frictional contacts in the shear-induced network does not depend upon ϕ and is the same for CST and at the beginning of DST. The inverses of g_l/P and g_w/P are displayed in Fig. 3.41. For both DST and CST, they first increase and then decrease as a function of the shear rate in accordance with the picture discussed above and in contrast with emulsions where they show a monotonic increase [234]. g_w/P is always larger than g_l/P. This suggest that a smooth surface induces a fluidization of the sample. This may arise because the particles close to the walls have less neighbors and thus feel less friction than in the bulk. Note that this is not in contradiction with the absence of slip at the wall. Wall slip is caused by the presence of a solvent lubrication film while a lower viscosity at the wall derives from a larger number of rearrangement events than in the bulk [242]. In conclusion, a non-local approach accounts very well for our experimental results. The flow would

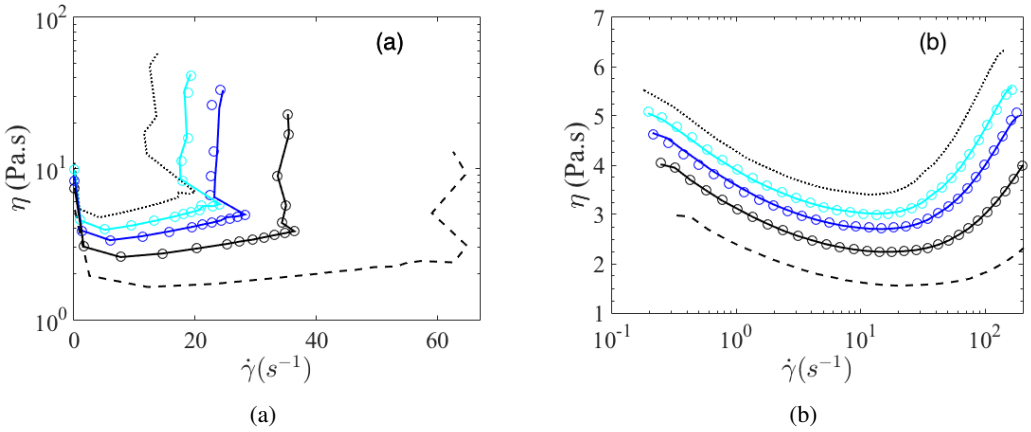

Figure 3.41: Flow curves, viscosity η vs shear rate $\dot{\gamma}$, of (a) dispersion D1 and (b) D2 in a Taylor-Couette cell of gap width $d = 1.0$ mm (○), $d = 0.5$ mm (○) and $d = 0.25$ mm (○). The solid lines show the flow curves predicted by the modified KEP model and based on the experimental data for $d = 1.0 and 0.5\ mm$ as discussed in the text. The dotted lines correspond to the viscosity in the limit of an infinitely wide geometry P/g_l and the dashed lines to the viscosity at the wall P/g_w extracted from the model.

involve an additional characteristic length that was at this stage never considered, namely the spatial extension ξ of the stress fluctuations induced by plastic events that rule the flow in the shear-induced structure. As a consequence, the flow curve of STS is not unique and depends upon the confinement, as also observed in soft jammed systems [233].

3.7 Chapter conclusion

Suspensions of PVC particles exhibit shear thickening at high concentrations. Its intensity depends also on the powder size distribution: a broader one diminishes the steepness of shear thickening. For the monomodal PVC powder, Discontinuous Shear thickening is observed at ϕ above 55%. Studying flow curves for different ϕ enables to find the jamming density. The latter is found to depend on the shear rate: lower at high shear rate than at low shear rate. These results follow the stress-induced friction scheme for shear thickening suggested a few years ago. Our PVC -particles suspensions share also other features from this picture. For example, shear thickening appears at a constant stress whatever the volume fraction, following the scheme of stress-induced friction scenario.

The nanoscale force profiles measurements performed at ENS bring t light a clear transition from a low-friction regime, where pairs of particles support a finite normal load, while interacting purely hydrodynamically, to a high-friction regime characterized by hard repulsive contact between the particles and solid friction. In particular, we show that the normal stress needed to enter the frictional regime at nanoscale matches the critical stress at which shear thickening occurs for macroscopic suspensions. Our experiments bridge nano- and macroscales and provide long needed demonstration of the role of frictional forces in discontinuous shear thickening.

Normal stress differences accompanying shear thickening occurrence have been measured combining cone/plate and plate measurements. N_1 is found to be around zero at moderate ϕ and positive at

high shear rate for the highest ϕ. On the contrary, N_2 is found to be negative. Same trends are found for both PVC, in relation with the major role of frictional interactions both for CST and DST.

An upper bound for shear thickening has been observed and measured with capillary rheometry. Beyond it, the viscosity decreases with shear rate even if suspension stays homogeneous and no slip at the wall is measured. As no lubrication film remains in the shear thickening and beyond, the simple elastohydrodynamic model cannot apply. We suggest that the friction coefficient between particles decreases at very high stress. Preliminary measurements are in this direction but further experiments are needed.

Ageing, corresponding to slow swelling of PVC particles by the plasticizer, has been characterized over days. A rough diffusive model captures our data and provides values for the very low diffusive coefficient ($\sim 10^{-20}\ m^2/s$). Swelling remains a surface phenomena (thickness of brush size after ageing $\sim$ 10 nm). As repulsive force is enhanced in this case, shear-thickening is shifted at higher shear rate.

Finally, the flow behaviour of shear thickening has been investigated. Strikingly, we show that the viscosity of the shear thickening suspension depends on the gap. Confinement promotes fluidization of the sample and shear thickening is pushed to higher shear rates as the gap size decreases. By using state of the art ultrasonic velocimetry, we confirm the absence of slip at the wall. Spatial concentration mapping is achieved using X-ray radiography combined with rheometry. No migration neither spatial heterogeneities develop during the flow both prior to, during and beyond shear-thickening. Using models developed for non-Brownian suspensions, we rationalize these last results by showing that possible migration would be minor and slow to set up. Finally, we show that a non-local approach inherited from previous models for flow cooperativity in soft glassy materials and granular systems which accounts well for our experimental results. As an outlook for this chapter, we notice that such behaviours are not universal and depends widely on the studied system.

3.8 Summary

— PVC concentrated suspensions exhibit shear thickening, continuous or discontinuous depending on ϕ and particle size distribution

— Macroscopic shear thickening appears simultaneously to the microscopic breakdown of lubrication film (onset of frictional interaction). The shear thickening regime corresponds to solid friction between particles.

— Both 1^{st} and 2^{nd} normal stresses differences are measured. N_1 is found positive and N_2 negative in probed experimental conditions.

— Concentration diagram in a good agreement with Wyart and Cates phenomenology. ϕ_{RCP}, ϕ_m, ϕ_{DST} are experimentally determined for both suspensions.

— Suspensions are shear-thinning beyond the shear thickening regime as measured with a capillary rheometer. Decrease of interparticle friction coefficient at high load would be an explanation.

— Geometry plays a huge role in the flow of concentrated suspensions. Confinement promotes fluidization of the sample. A non-local approach well suits for our experimental results.

— For $\phi_{DST} < \phi < \phi_m$, the system flows homogeneously and does not show any particle migration in typical rheological experiments (even at high stresses during and beyond shear-thickening).

Chapter 4

Impact of formulation

Once we got new insights on the flow behaviour of PVC concentrated suspensions, we tackle here challenges linked to the formulation. We first investigate a possible role of the surfactant at PVC particle surface (remaining from the synthesis) on the rheological properties. We then turn to the case of filled suspensions where a part of PVC particles is replaced by filler ($CaCO_3$) particles. Filler is investigated when dispersed alone in DINCH before studying suspensions composed of both PVC and filler. As a reminder, like in previous chapters, D1 and D2 correspond respectively to suspensions made of PVC 1 + plasticizer and PVC 2 + plasticizer. For PVC and filler together mixed in DINCH, we keep a detailed notation: for example, a suspension made of 33 vol.% of PVC 1, 30 vol.% of filler Medium (so 37 vol.% plasticizer) will be denoted as "PVC 1 33% - Filler M 30%".

4.1 PVC suspensions

4.1.1 Impact of different surfactants

4.1.1.1 Experiments

As described in part 2.1.2 , Sodium Dodecyl Benzene Sulfonate (SDBS) has been found on the surface of PVC 2 particles. However, there are different surfactants used in water-based PVC synthesis (emulsion or micro-suspension polymerisation) and which remain on the surface of raw PVC particles. Main chemical families [199] are listed below:

- a) Sodium Sulfosuccinate
- b) Sodium alkyl benzene sulfonate
- c) Fatty acid ammonium salt
- d) Alkyl sulfate
- e) Sodium alkyl sulfonate
- f) Fatty acid sodium salt
- g) Fatty alcohol ethoxylate

Such surfactant are rather charged as they are used during synthesis which is carried out in a water based medium (cf. part 1.8.1.1). To screen effects of these additives on the suspension rheology, modified PVC 1 powder (cf. protocol in 2.4) has been prepared with one representative molecule for each family, (see table 4.1). Detailed name, chemical formula and used abbreviations in the following

are also detailed in the table. Weight percents (ratio to PVC powder) were chosen to match a constant number of molecules per PVC surface area.

	Type	Surfactant molecule used in this work	Amount (wt%)
a	Sodium Sulfosuccinate	Dioctyl sulfosuccinate sodium salt (DOSS or AOT)	1
b	Sodium alkyl benzene sulfonate	Sodium Dodecyl Benzene Sulfonate (SDBS)	1
c	Fatty acid ammonium salt	Ammonium palmitate (C16)	0.85
d	Alkyl sulfate	Sodium Dodecyl Sulfate (SDS)	0.88
e	Sodium alkyl sulfonate	1-undecane sulfonate	1
f	Fatty acid sodium salt	Sodium palmitate (C16)	0.85
g	Fatty alcohol ethoxylates		

Table 4.1: Different surfactants used for assessing rheological impact on plastisol.

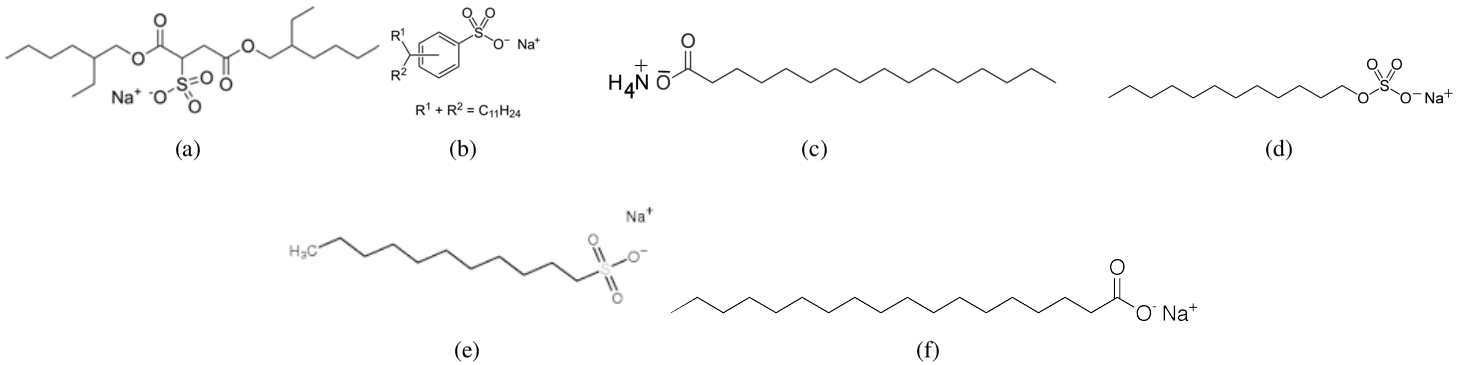

Figure 4.1: Chemical formula of surfactants used in this study (cf. table 4.1): (a) DiOctyl SulfoSuccinate sodium salt (DOSS or AOT);(b) Sodium Dodecyl BenzeneSsulfonate (SDBS); (c) Ammonium palmitate; (d) Sodium Dodecyl Sulfate (SDS); (e) 1-undecane sulfonate; (f) Sodium palmitate.

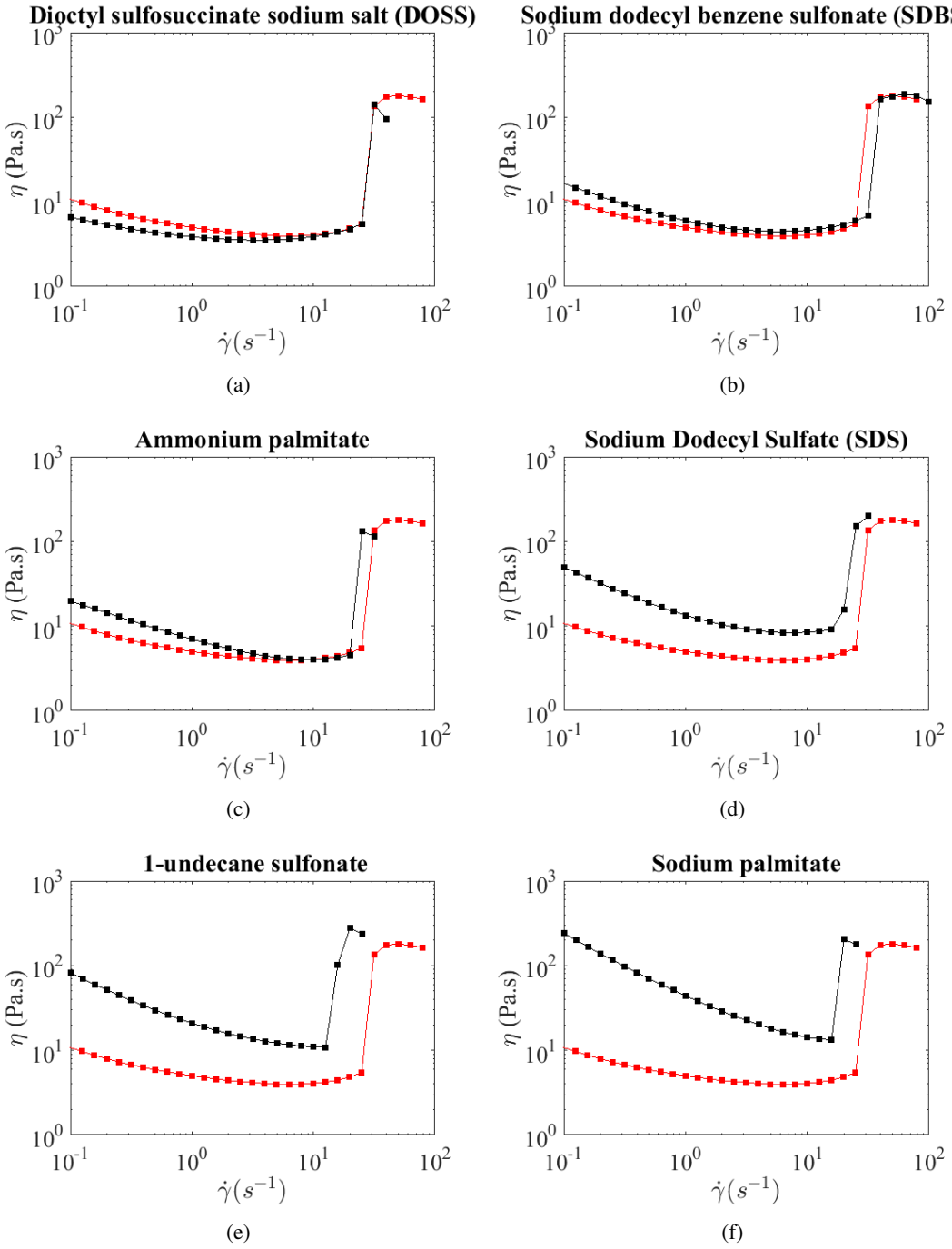

Figure 4.2: Viscosities of D1 with surfactant on PVC (■): (a) DiOctyl SulfoSuccinate sodium salt (DOSS or AOT); (b) Sodium Dodecyl Benzene Sulfonate (SDBS) (c) ammonium palmitate; (d) Sodium Dodecyl Sulfate (SDS); (e) 1-undecane sulfonate; (f) sodium palmitate (same trend with myristate or stearate). Reference of D1 without additive (■) in plotted on each graph. Measurements are performed in a cone/plate geometry.

Figure 4.2 shows viscosity versus shear rate for D1 60% without and with each surfactant. None of these surfactants manages a significant viscosity reduction or a shear-thickening postponing. Only a slight viscosity reduction is achieved with DiOctyl SulfoSuccinate sodium salt (DOSS) but is only limited to low shear rate. Other surfactants lead to a higher viscosity, especially at low shear rate.

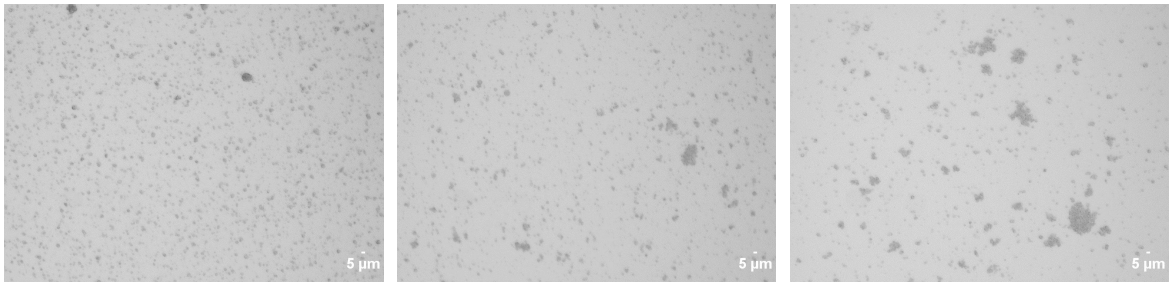

(a) (b) (c)

Figure 4.3: Optical microscopic image of D1 in dilute regime (ϕ = 0.006) with (a) no additive (b) SDBS and (c) sodium palmitate.

This is particularly striking for surfactants with long alkyl chains (SDS, 1-undecane sulfonate, sodium palmitate). Figure 4.3 shows optical microscopy pictures from studied suspension diluted at ϕ = 0.006. The suspension with no additive (Fig. 4.3a) has a well-dispersed microstructure. The suspension with SDBS (moderate viscosity at low shear rate) is a little bit more agglomerated but still quite well dispersed. On the contrary, the suspension with sodium palmitate (high viscosity at low shear rate) shows a strongly agglomerated microstructure.

1-undecane sulfonate was chosen as it is made of the alkyl chain of SDS while containing the sulfonate end group of SDBS. Its rheological curve (Fig. 4.2c) shows that suspension viscosity is more influenced by chemical structure rather than only terminal group nature itself.

Influence of counter-ion has been assessed by comparing sodium palmitate (Fig. 4.2e) to ammonium palmitate (Fig. 4.2f). Sodium counter-ion is found to promote higher viscosity at low shear rate compared to ammonium counter-ion.

4.1.1.2 Discussion: surfactant effect

The comparison between microstructure observed from the optical microscopy and the viscosity measurements shows that surfactant can induce attractive interactions between PVC particles, thus explaining the high low-shear viscosity observed for some surfactants. All surfactants do not destabilize particles with the same intensity. Long saturated alkyl chains (Fig. 4.2a and e) are found to highly destabilize the suspensions while surfactant like SDBS (Fig. 4.2b) or DOSS (Fig. 4.2d) does not affect much the dispersion. No particular dependence of balance HLB (hydrophilic Lipophilic Balance) is noticed. The case of DOSS is specific as it is the only one soluble in DINCH (side chains chemically similar to DINCH structure). Other are more polar and insoluble in DINCH.

From the literature of suspensions, we saw that the suspension viscosity at low shear rate is the lowest when attraction between particles are minimized (particles well dispersed). Moreover, shear thickening can only be delayed if interparticle microscopic repulsive forces are reinforced. Nevertheless, our system of PVC paste is stabilized at the particle scale by a layer of solvated PVC (slow plasticizer diffusion). Experiments from last chapter gave us a proof of its existence and a typical size (4 nm). This brush exists because plasticizer has a good chemical affinity with PVC. Thus, attractive interactions are minimized when PVC is dispersed in plasticizer. Adding a surfactant which is in most cases very polar (and water soluble because of aqueous-based PVC synthesis) could have nearly no impact (for example

DOSS because soluble in DINCH, SDBS) or perturb PVC/plasticizer interactions (for example fatty acid sodium salt). Similarly, the PVC brush is not enhanced with these surfactants insoluble in DINCH (except soluble DOSS), thus explaining why shear thickening is not shifted at higher shear rate.

Attractive interactions upon adding of surfactant might have different origins: depletion forces induced by micelles of surfactant (the solubility is never exactly zero), change of PVC surface polarity as insoluble surfactant stays on surface... Unfortunately, we do not have experimental data to choose among these hypothesis.

4.1.2 Impact of water...

4.1.2.1 ...on raw PVC powders

First, effect on water has been evaluated using directly PVC 1 and PVC 2 suspended in plasticizer. Figure 4.4 shows results for adding water at a ratio 0.01 g/g of PVC (noted 1 wt% in the following) in D1 and D2. Water was first introduced in DINCH and liquid phase was mixed a few second at high speed to ensure good dispersion of water in DINCH (emulsion). Then PVC powder was added and mixing was done following the usual protocol to prepare PVC concentrated suspensions.

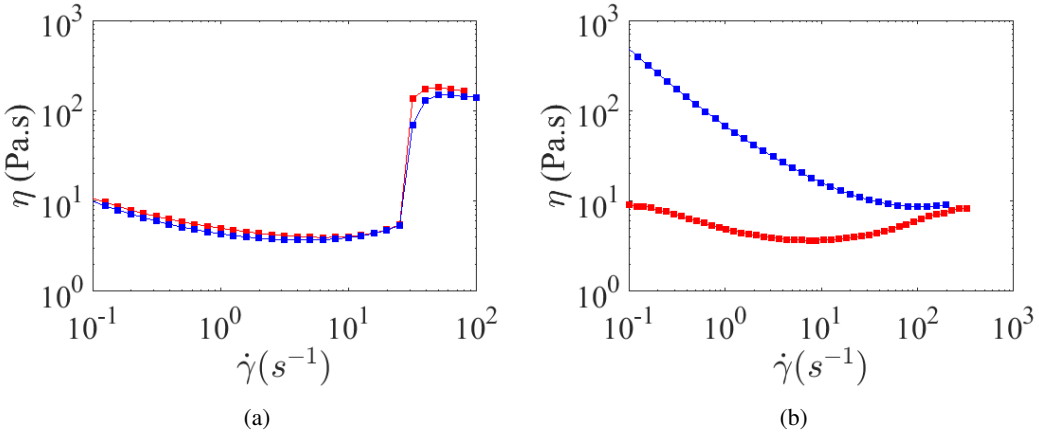

Figure 4.4: Flow curves with 1 wt% water (■) and without added water (■) for a PVC-plasticizer suspension at 60 vol% made from (a) PVC 1 and (b) PVC 2. Measurements are performed in a cone/plate geometry.

Results are totally different depending on the powder. No effect is observed in D1. Water in only dispersed in plasticizer phase (plasticizer and water are insoluble) and has no interaction with hydrophobic PVC (absence of surfactant on PVC particle surface). However, for PVC 2, adding water leads to a significant rise of low-shear viscosity. Viscosity does not change at high shear rate (> 100 s^{-1}). This increase of low-shear rate viscosity is linked with interparticle interactions, namely certainly capillary bridges between particles [195]. As PVC 2 has surfactant on its surface, water is able to wet PVC particles. Due to this wetting, capillary bridges between particles can be formed, leading to higher viscosity at rest. These attractive interactions are broken in case of high shear, explaining why high-shear viscosity remains unchanged with water.

4.1.2.2 ...depending on surfactant nature

We quantify here the effect of adding water in suspensions containing surfactant-modified PVC 1 powder (cf. part 4.1.1). Each time, 1 wt % water was added to suspension. Figure 4.5 shows the results with water and surfactant compared to only surfactant and with neither water nor surfactant.

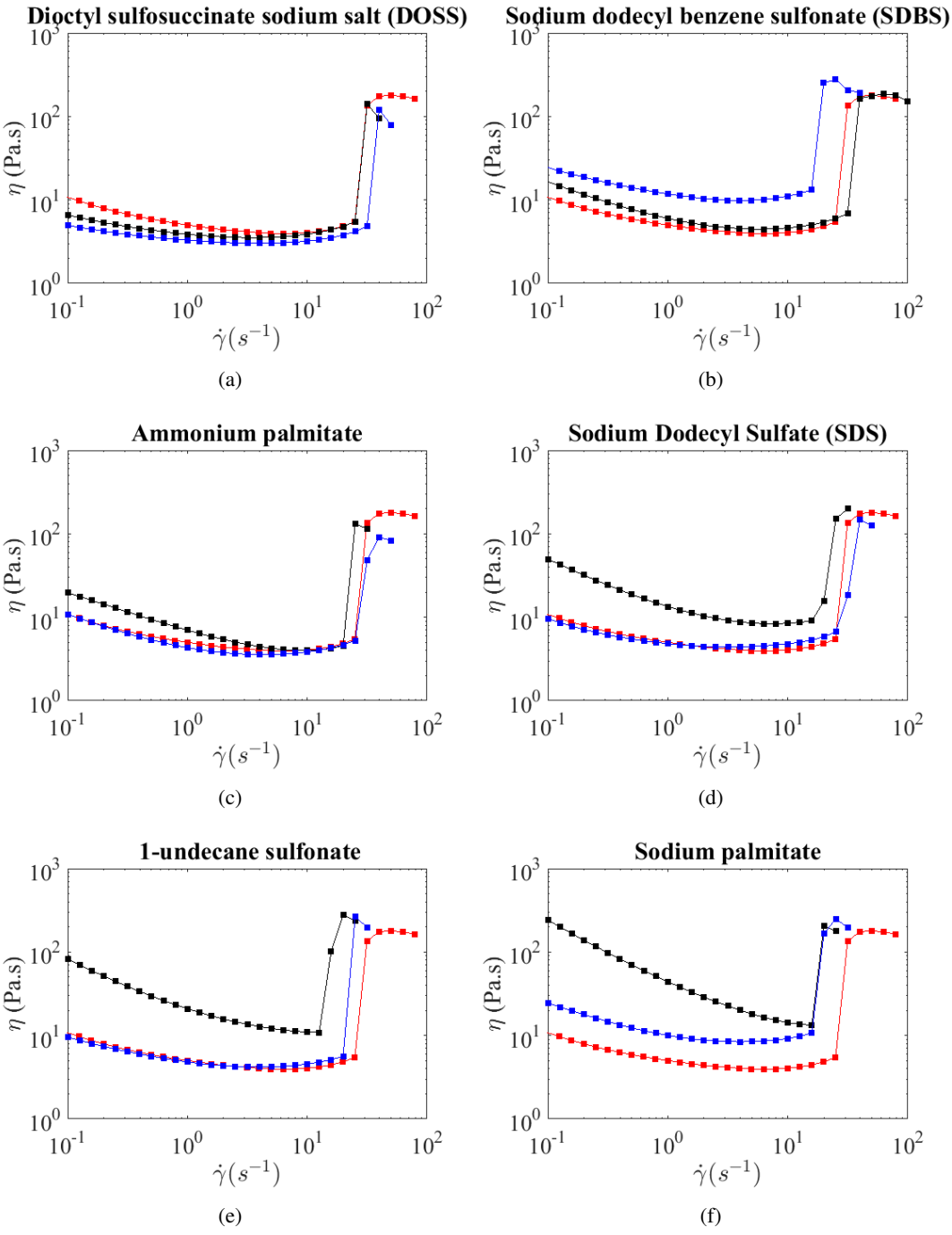

Figure 4.5: Impact of adding water + surfactant (■) in the suspensions compared to only surfactant (■) and no additive (■) for (a) Dioctyl sulfosuccinate sodium salt (DOSS or AOT); (b) Sodium dodecyl benzene sulfonate (SDBS); (c) Ammonium palmitate; (d) Sodium Dodecyl Sulfate (SDS); (e) 1-undecane sulfonate; (f) Sodium palmitate. Measurements are performed in a cone/plate geometry.

Effect of adding 1 wt % water in the suspensions appears to have different effects depending on the surfactant. For SDSB, water results in an increase of viscosity whereas for DOSS, the viscosity is nearly unchanged. For all other studied surfactants, added water decreases the viscosity. But in all cases, the discontinuous shear thickening (DST) remains and its intensity not modified. These results are discussed a little further.

4.1.2.3 Importance of water repartition in the system

We focus here on two close surfactants: sodium palmitate (noted C16) and sodium myristate (noted C14). Others surfactant were not tried with this specific protocol. We still focus PVC 1 with DST.

In the latter part, water was added in the plasticizer phase prior to surfactant-modified powder incorporation resulting in a water phase dispersed in DINCH. Here, we prepare surfactant-modified PVC 1 following the protocol from part 2.4 but the freeze-drying step is stopped just before complete drying, letting a moisture content in the powder between 0.5 - 1 wt% (of PVC powder) depending on the batch. This moisture content was assessed by thermogravimetric analysis (under dinitrogen atmosphere, ramp from room temperature to 120 ˚C). Hydrated powder is dispersed in DINCH at a volume fraction ϕ = 60 % and viscosity is measured (cf. Fig. 4.6)

Strikingly, the DST is lowered through this protocol whereas adding water droplets just before dispersing PVC (latter paragraph) did not show any reduction of shear thickening modification. It is worth noting that having same water content from one batch to another is difficult to achieve. The DST lowering is also visible on the 1^{st} normal stress difference N_1. Instead of an abrupt burst, the modified suspension exhibits a softer increase of N_1, showing that solid interparticle contact is modified. For the best case, values are divided by a decade.

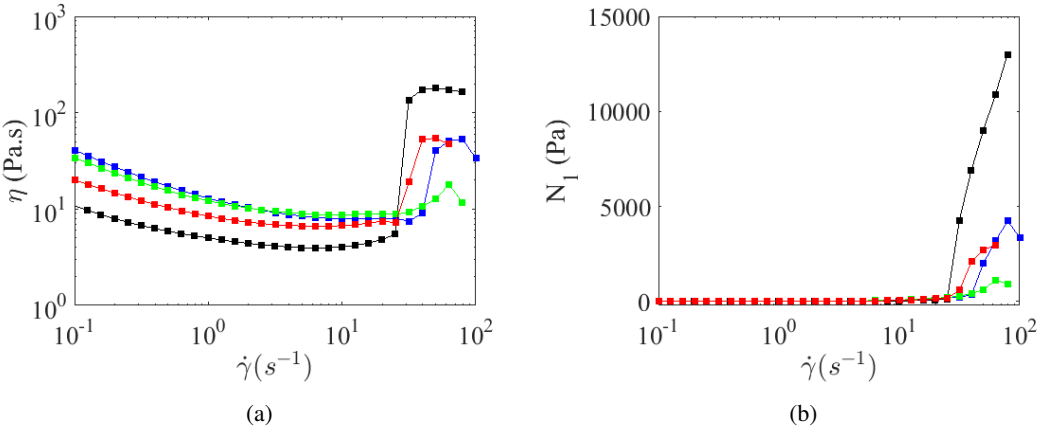

Figure 4.6: (a) Flowtest of D1 at ϕ = 60% without surfactant (■) and with surfactant and moisture content from the incomplete freeze drying: C14 + 0.50% water (■), C16 + 0.55% water (■) and C16 + 1.2% water (■). (b) Same graph for 1^{st} normal stress difference. Measurements are performed in a cone/plate geometry.

This specific protocol was applied to washed PVC 2 (washing removes most of the SDSB) with sodium palmitate but no reduction of shear thickening is observed. It may be due to higher polydispersity which makes the whole surface covering more difficult. Due to this inefficiency on PVC 2 (industrially relevant) combined with the fact that water cannot be used in the industrial process

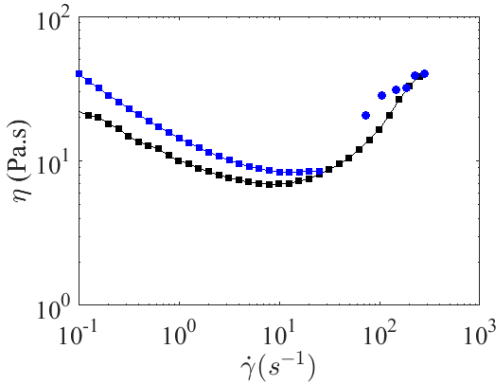

Figure 4.7: Effect of adding C16 and water with an unfinished freeze drying (0.85 % surfactant, 0.75 % water) on D2 63 % (■). Reference without additive (■). Circles are measurements from capillary rheometer.

(clogging/foaming during heating in the oven leading to rough surface), no further experiments were done.

4.1.2.4 Discussion: water effect

Concerning water added, the case of SDBS (increase of viscosity) can be explained by capillary bridges formation upon water addition. The increase of viscosity for the system PVC-SDBS-water is noticeably less important when using PVC 1 (here) compared to PVC 2 (cf. fig 4.4 in last part). We suggest that PVC 2 contains a high number of small particle under 1 μm which allows more capillary bridges to be formed. Such explanation is in line with figure 3.22 where it is shown that interparticles interactions are more numerous in the case of PVC 2.

For DOSS, as it is soluble in DINCH, it will not interact with PVC. Water will be also dispersed in DINCH and cannot wet PVC particles. Thus water does not interact with particles and do not modify the viscosity.

To explain the drop in viscosity with other surfactant, we postulate that adding water dispersed in DINCH phase mobilizes surfactant at DINCH/water interface. Less surfactant are thus interacting with PVC particles resulting in a lower destabilization of the suspension (i.e lower viscosity). Nevertheless, we do not have experimental proofs to confirm or infirm this hypothesis.

Getting a moisture content from incomplete drying gives however completely different results than adding droplets of water in DINCH. Thus water repartition in the system plays a crucial role in the rheology. To explain the last obtained results, we suggest that during incomplete freeze drying, remaining moisture content lies on PVC particle surface with surfactant. On the contrary, adding water droplets like in previous part (even with high speed mixing) does not manage to cover most of particles surface and results in dispersed water droplets. However, the exact structure or organisation at the particle surface is hard to predict in our case as surfactant used here are soluble neither in water nor in DINCH. But the surfactant could stabilize an hydrated layer on particle surface by helping the stabilization of PVC/water/DINCH interfaces. For example, bilayers of surfactants at particle surface are known to delays and reduce shear thickening intensity [89] by increasing repulsive force or diminishing interparticle friction.

Finally, surfactants remaining from the synthesis does not bring any viscosity reduction or shear thickening postponing in PVC concentration suspensions. On the contrary, they could destabilize the suspensions by creating attractive interparticles forces. We explain this by considering the physico-chemistry of the system. Plasticizer is a liquid optimized for the best compatibility with PVC. Adding non soluble compounds at PVC surface will disturb this compatibility. Moreover, shear thickening appears when the PVC brushes are no more sufficient for keeping particle from being frictional. Again, delaying shear thickening would imply a thicker or denser brush which cannot be achieved by surfactants. For water, the behaviour is very complex as it depends both on the water repartition in the system and also on the surfactant used. Water can decrease or increase the viscosity depending on the nature of the surfactant considered.

4.2 Filler suspension

In some industrial applications, some PVC particles are replaced by filler particles ($CaCO_3$) for both economic reason and modifying some properties of the final product (flame resistance, mechanical properties...). Amount of added filler changes the rheological profile as filler can replace as much as half of PVC powder (giving in volume one third PVC, one third filler, one third plasticizer).

In this part, we first study dispersion of filler in liquid plasticizer. Suspensions with mixed PVC and filler will be handled only in the last part of this chapter.

4.2.1 Impact of granulometry on maximum packing fraction

The main filled used in this work is filler M. For evaluating impact of filler size, different fillers will be used in some experiments: XS, S, M, L, XL, XXL where ranked from the smallest to the largest particle size. Respective particle size distribution is recalled on Fig. 4.8b.

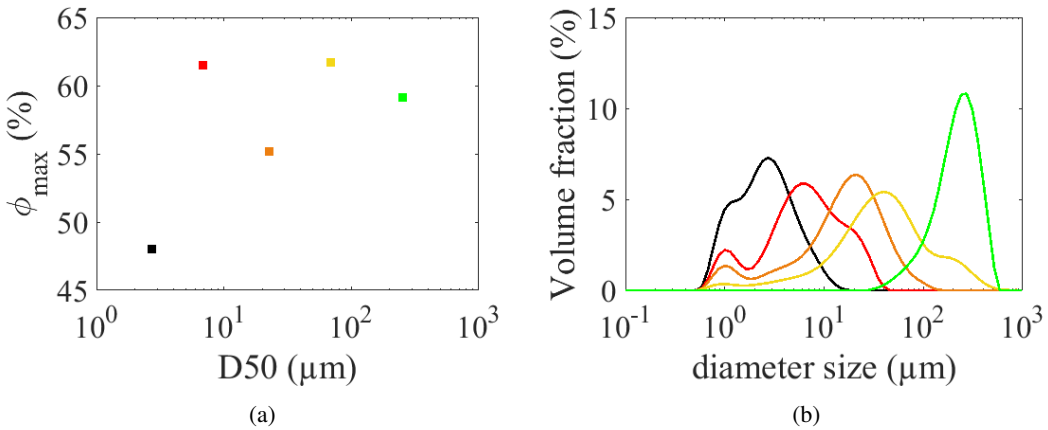

(a) (b)

Figure 4.8: (a) Variation of maximum packing fraction of different filler measured by plasticizer absorption value plotted against the typical diameter D50: XS (■); S (■); M (■); L (■) and XXL (■) (b) Reminder: associated particle size distribution.

Plasticizer absorption value tests were performed on all fillers (Fig. 4.8a). No clear trend in function of the mean particle size is observed. Globally, smaller size means smaller ϕ_{max} but the latter is also largely influenced by the particle size distribution which is not the same for each filler used in this work. For instance, filler S has a small mean diameter but relatively high maximum packing fraction due to its large polydispersity (three population about 1, 7 and 20 μm). On the contrary, filler XXL with a "narrow" particle size distribution has a relatively high maximum packing fraction.

4.2.2 Rheological behaviour

We focus on filler M which is widely used in industrial formulation and will be mainly used in the next part when mixing PVC and filler.

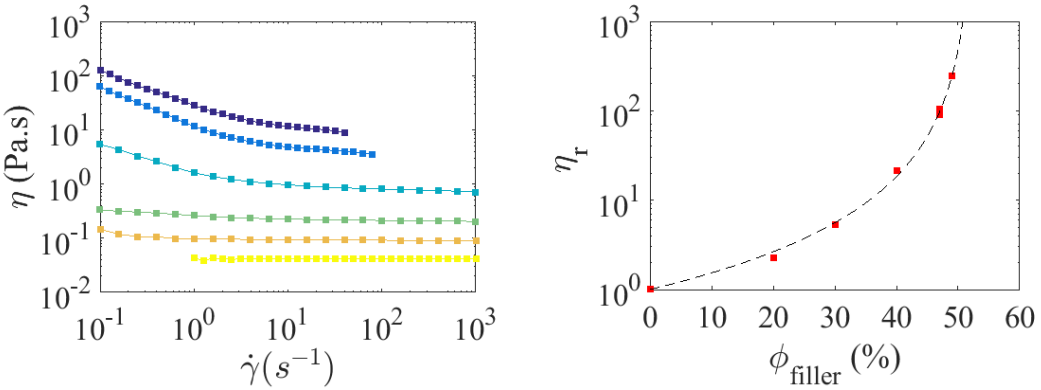

Figure 4.9: (a) Viscosity versus shear rate for filler M suspended in the plasticizer at different ϕ: 49% (■), 47% (■), 40% (■), 30% (■), 20% (■) and pure liquid (■). (b) Relative viscosity η_r at $\dot{\gamma}$ = 25 s^{-1} versus filler volume fraction ϕ. Dotted line represents a fit using a Krieger-Dougherty law $\eta_r = (1 - \frac{\phi}{\phi_{max}})^{-[\eta].\phi_{max}}$. Fitting parameters are ϕ_{max} = 52.5% and $[\eta]$=3.9.

Figure 4.9a displays flow curves for filler M particles suspended in plasticizer at different volume fractions ϕ. As for PVC, ϕ denotes here the volume fraction of filler. Measurements are done using a 40 mm cross-hatched plate-plate for highest ϕ ($\geq$ 47 %) as slip at the wall occurs at such concentrations (contrary to PVC suspensions which does not exhibit any slip at the wall). For lower concentration, a Couette cell (gap 1 mm) was used.

Suspensions at low ϕ are Newtonian on the whole shear rate range. Measurements at highest concentration (47, 49 %) are limited in shear rate by edge fracture. When ϕ increases, interparticle interactions become significant, samples exhibit shear thinning behaviour at low shear rate and rather Newtonian at higher shear rate (> 10 s^{-1}). In fact, calcium carbonate filler has a polar and hydrophilic surface and is not well dispersed in organic plasticizer. This bad compatibility results in attractive interactions between particles, explaining the shear thinning behaviour at low shear rate [243]. At high shear rate, hydrodynamic forces are enough to overcome those repulsive forces resulting in a Newtonian behaviour.

Unlike PVC, there is no shear-thickening behaviour at high shear rate. As explained previously (see. 1.3.2.5 and 3.2), repulsive forces between particles are needed for shear-thickening behaviour. For filler dispersed in DINCH, there are no such repulsive forces: neither electrostatic as DINCH

dielectric constant is low ($\epsilon_r \approx 5$ - 8 [166]) nor steric as the surface is bare (no organic brush around) and plasticizer does not enter filler particles as it does for PVC. This absence of microscopic repulsive forces explains why filler alone dispersed in plasticizer does not exhibit shear thickening. The state at rest implies already contacting particles.

Maximum packing fraction can be deduced from a fit using viscosity at 25 s^{-1}. Value of 25 s^{-1} is chosen as a trade-off between minimum inter-particle interaction and reliable viscosity measurements without sample ejection. A ϕ_{max} of 52.5% is found (cf. Fig. 4.9b). Contrary to PVC suspension, this value is slightly lower than the one experimentally found with the plasticizer absorption value (55.0%).

4.2.3 Impact of surfactants on rheological behaviour

Calcium carbonate filler has a hydrophilic and polar surface which is not really adapted to organic plasticizer. The idea here is to test of a surfactant which can compatibilize filler surface with plasticizer.

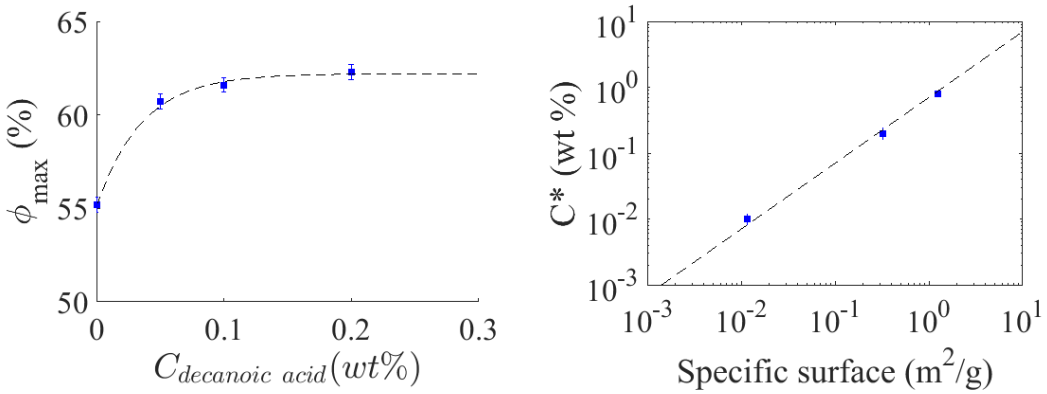

Figure 4.10: (a) Variation of maximum packing fraction of filler M (from plasticizer absorption test) when adding decanoic acid (concentration C in wt %). Optimum concentration C is found at 0.2%. (b) Scaling of C* for filler XS, M and XXL with their respective specific surface. Slope is 1.

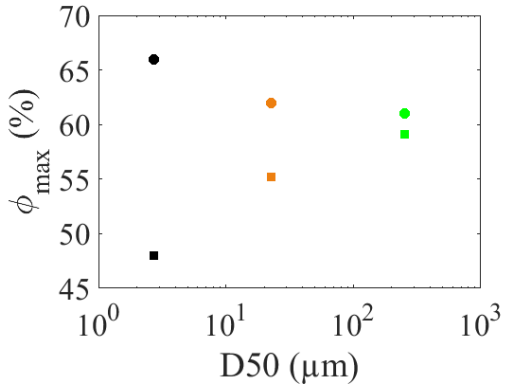

Figure 4.11: Variation of maximum packing fraction of different filler measured by plasticizer absorption value plotted against the typical diameter D50 without decanoic acid (squares) and with decanoic acid (circles) : filler XS (■); M (■) and XXL (■).

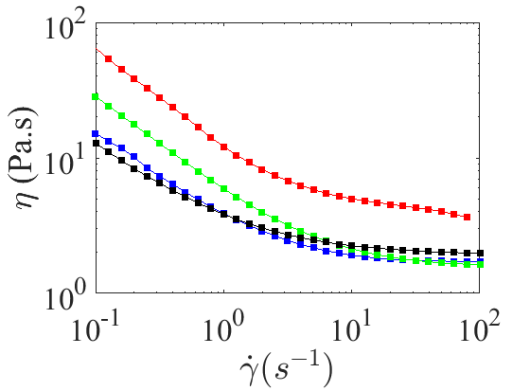

Figure 4.12: Viscosity of filler suspension at 47 % without additive (■) or with 0.2 % surfactant dispersed in DINCH: SDBS (■), decanoic acid (■) or stearic acid (■).

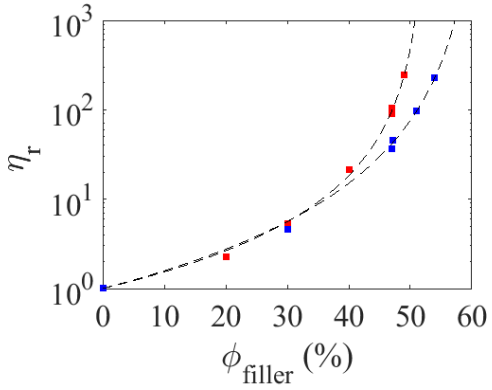

Figure 4.13: Effect of adding 0.2 wt% decanoic acid (■) on relative viscosity η_r at 25 s^{-1} of a filler suspension (■). With surfactant, maximum packing fraction is shifted from 52.5 to 61.5 % (+9%).

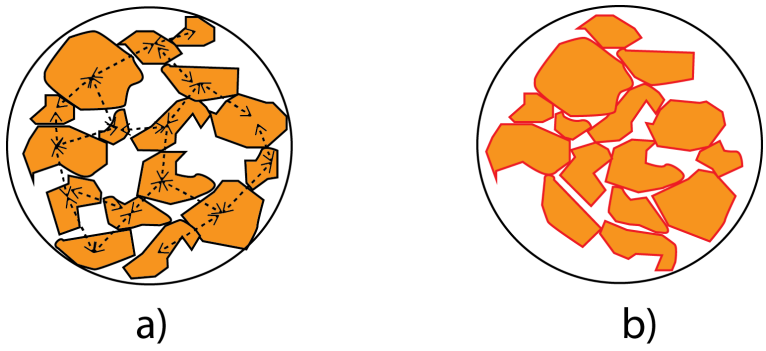

Figure 4.14: Schematic view for increase of maximum packing fraction with decanoic acid (right) compared to reference (left). Decanoic acid on filler surface is materialized in red. Without this surfactant, the attractive interactions (dotted arrows) result in a quite loose packing. Compatibilization (= decrease these attractive interactions) allows a better compacity.

We use decanoic acid as it is soluble in plasticizer (contrary to stearic acid for example). Maximum packing fraction of filler M measured using the plasticizer absorption value is displayed on Fig. 4.10a for different surfactant concentration. A increase of 7% (from 55 to 62 %) is achieved with decanoic acid. Optimum amount is assessed to be C* = 0.15-0.2 wt% (0.002g/g of filler, denoted 0.2 wt%). Same can be done with filler of different size: XS and XXL. Optimum amounts are respectively C* =

0.01 % and C* = 0.8 %. These optima scale linearly very well with filler specific surface (Fig. 4.10b). It implies that the optimum amount of surfactant is the needed amount for the whole surface coverage. The surfactant does allow compatibilization of filler surface for plasticizer. The schemes on Fig. 4.14 explain the gain of maximum packing fraction. With surfactant, interparticle attractive interactions are reduced. Thus, filler is better dispersed with less dissipative contacts. By the way, a more compact packing can be achieved.

Figure 4.11 shows gain in maximum packing fraction for XS, M and XXL filler. For XXL filler, its low specific surface (0.01 m^2/g) means that there is nearly no surface to compatibilize, then benefit of using surfactant is limited (1-2 %). On the contrary, XS filler has a high specific surface (1.03 m^2/g). Surfactant has a major impact here in filler/DINCH compatibility, justifying an increase of 18% in maximum packing fraction. On a general level, the smaller the filler particle size, the more efficient the surfactant is. It is worth noting to remark that the compacity achieved with decanoic acid (66%) is very close to the value obtained when using the same filler industrially treated with fatty acid on its surface (Filler XS-treated, 64%), showing the relevancy of our measurements. Increase of filler compacity when having stearic acid on filler was also reported by Cook et. al. [191] while performing oil absorption tests. Similarly to our work, the gain was higher for fillers with smaller particle sizes.

Complementary to maximum packing fraction measurements, rheological experiments have been performed. Figure 4.12 shows viscosity of filler M suspended in plasticizer at 47% without surfactant or with SDBS, decanoic acid or stearic acid (0.002g/g of filled, denoted 0.2 wt%). Decanoic acid is soluble in plasticizer. For other surfactants, they are dispersed in plasticizer. Then suspension is prepared following usual protocol. Using a surfactant leads to a decrease of viscosity (factor 2-3) on the whole shear rate range. Best is using decanoic acid. Stearic acid is a little bit less efficient for low-shear viscosity. In the following, we keep decanoic acid as efficient compatibilizer for filler. Figure 4.13 displays viscosity of filler M dispersed in plasticizer at 25 s^{-1}. Adding decanoic acids shifts maximum packing fraction to 61.5 % (+9%). This increase is slightly higher than the one measured with plasticizer absorption test (+7%).

4.2.4 Impact of water

Water has also a great impact on rheology of these organic-based suspensions. Water is insoluble is plasticizer. Adding 1 wt % of water (0.01g/g of filler) greatly increases the viscosity of filler suspension (see Fig. 4.15), particularly at low shear rate. Water wets well the hydrophilic filler surface. Adding water in the suspension enables the creation of multiple capillary bridges between particles [112, 111], increasing by more than one decade the low-shear viscosity. As for PVC dispersion D2, these attractive interactions are broken at high shear rate, explaining the small viscosity change at high shear rate.

Instead of intentionally adding water, we focus also on the effect of residual moisture in filler powder. Fig. 4.16 shows viscosity curves for a suspension of filler M particles at 47 % with a filler used without any treatment or a filler dried in a oven at 120 °C for one night.

There is no major change. The low-shear viscosity is a little bit lower because the drying step slightly decreases the hydrophily of the filler surface. Thus, interparticle attractive interactions are a little bit weaker, explaining the lower viscosity at low shear rate [243].

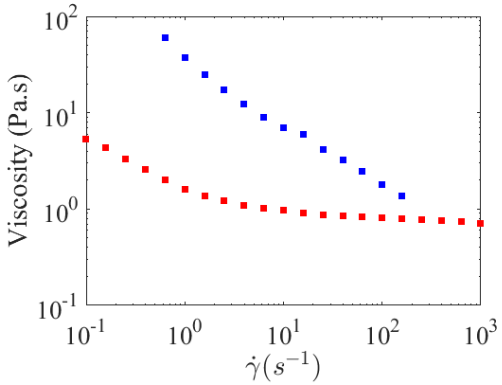

Figure 4.15: Viscosity of a 40 % suspension of filler (size M) in plasticizer (■) and same formulation with 1 wt % water (■).

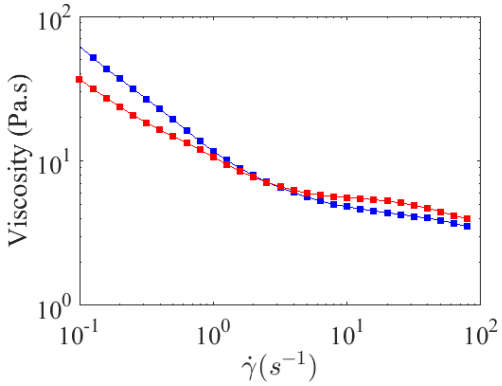

Figure 4.16: Viscosity of a suspension of filler (size M) in plasticizer at 47 % prepared with a filler dried in a oven at 120˚C (■) or with a filler used as received (■).

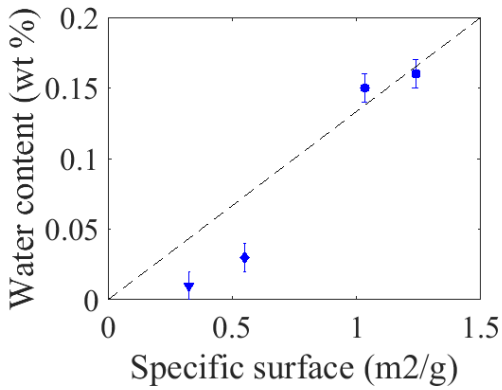

Figure 4.17: Moisture content of smallest fillers assessed by weighting before and after one night at 120 ˚C. Filler M (◆); S (▲); XS(●); XS-treated (■). Water content is roughly proportional to specific surface (dotted line).

Intrinsic water content is not critical for filler medium (most used industrially). We assume that for filler bigger than medium M, water content is insignificant (low specific surface). However, this is not necessarily the case for filler with smaller size. Indeed, to assess filler size role in rheological properties and maximum packing fraction, several fillers with different mean diameters will be used in the following. Water content was assessed combining different methods: thermo-gravimetry, weighting

after a night in a oven at 120 ˚C, Karl Fischer titration and freeze drying. All methods give consistent results. Results are plotted on figure 4.17 versus the specific surface. The smaller the filler, the higher the water content. This amount of water scales roughly with specific surface. Giving the relatively high amount of water in small size fillers, they will be used dried in the following to assess the true effect of size (decoupling the water effect).

Polar Calcium carbonate particles are not in good solvent when dispersed in fatty ester plasticizer, creating interparticle attractive interactions. Thus, at low volume fraction, these interactions are low and rheological behaviour is Newtonian. At higher volume fraction (around 35%), attractive interaction are responsible for a shear thinning behaviour at low shear rate. Unlike PVC with its brush, no repulsive interaction is present here, explaining why no shear thickening happens even at high volume fraction, close to the maximum packing fraction. Compatibility between filler and liquid plasticizer can be enhanced by using a surfactant that will cover particles surface. Different surfactants can be used as for example fatty acids. They increase the maximum packing fraction, thus decreasing the suspension viscosity. Water leads to an increase of viscosity at low shear rate by creating capillary bridges.

4.3 Dispersing together PVC and filler

In this section, suspensions are made by dispersing together PVC and filler in plasticizer in various concentrations. The two powders exhibit completely different rheological behaviours due to their difference in physico-chemical nature, size and shape as detailed previously (see parts 4.2 and 3.1.2). Thus, dispersing these two powders together in a liquid results in a more complex rheology which is rather poorly described in literature [244, 245, 246, 247].

In the following,

$$\phi_{PVC} = \frac{Volume(PVC)}{Volume(PVC) + Volume(Filler) + Volume(DINCH)} \tag{4.1}$$

is the partial volume fraction of PVC,

$$\phi_{Filler} = \frac{Volume(Filler)}{Volume(PVC) + Volume(Filler) + Volume(DINCH)} \tag{4.2}$$

the partial volume fraction of filler and $\phi_{tot} = \phi_{PVC} + \phi_{Filler}$ the total particle volume fraction.

All viscosity measurements were performed in a Couette cell geometry. For characterizing the ratio of PVC over filler, PVC fraction of total powder (PVC+ filler) is defined. It is denoted ξ_{PVC} and defined as the following: ξ_{PVC}=$\frac{\phi_{PVC}}{\phi_{PVC}+\phi_{filler}}$.

ξ_{PVC} = 1 means a suspension obtained by dispersing only PVC in DINCH. ξ_{PVC} = 0 accounts for suspension obtained by dispersing only filler in DINCH.

4.3.1 Variation of maximum packing fraction

Filler and PVC alone have very different maximum packing fractions (55 % for filler M and 69% for PVC 1). Here, the variation of maximum packing fraction for different PVC over filler ratio are measured using the plasticizer absorption test described in part 2.6.

4.3.1.1 Experimental results

Maximum packing fractions ϕ_{max} are measured using the plasticizer absorption test for filler/PVC composition from pure PVC suspensions to pure filler suspensions. Results are plotted on figure 4.18. For this graph and the followings, the x axis refers to the PVC fraction of total powder, denoted ξ_{PVC} (described just above). Industrial filled formulations are close to the ratio ξ_{PVC} = 0.5. In the following, our model formulation for an industrial filled suspension will be ϕ_{PVC} = 0.33 and ϕ_{filler} = 0.3, giving ξ_{PVC} = 0.524.

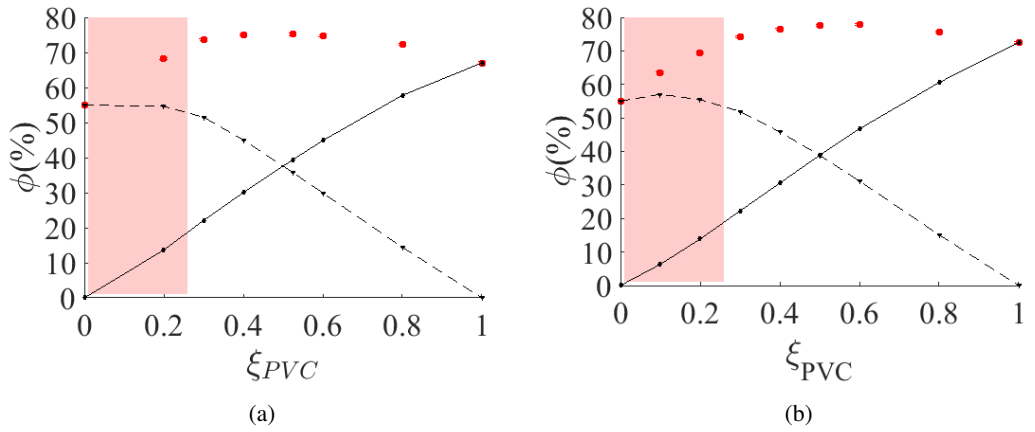

Figure 4.18: Measured maximum packing fractions (red dots) using plasticizer absorption test for various compositions of (a) PVC 1 and Filler M (b) PVC 2 and Filler M. Dotted line: partial volume fraction of filler (ϕ_{filler}). Solid black line: partial volume fraction of PVC (ϕ_{PVC}). Error bars are smaller than dots width.

Using either PVC 1 or PVC 2 results in the same trend as graphs from Fig. 4.18 are very similar. ϕ_{max} is higher when mixing PVC and filler together. The optimum is around ξ_{PVC} = 0.5 . A simple view can be to consider that PVC small particles fill voids between coarse filler particles. Thus, a mix of the two powders achieved the lowest porosity. This simple view is only valid at low ξ_{PVC} as shown by partial volume fraction (solid and dotted lines). For ξ_{PVC} up to around 0.2 (red zone on the figure), ϕ_{filler} volume fraction does not change, meaning that the increase of ϕ_{max} is only gained by PVC particle inserted between coarse filler particles (which are the majority in this zone). For higher content of PVC, ϕ_{filler} declined and ϕ_{PVC} raises, meaning that in this range, adding PVC replaces filler space and does not only fills voids.

4.3.1.2 Filler size dependance

The same measurements as previously are done (also with PVC 1) but the size of the filler is varied from the smallest (=XS) to the biggest (=XXL). Effect on maximum packing fraction is given

on Fig. 4.19a. For filler XS mixed with PVC, resulting maximum packing fraction is roughly the mean between ϕ_{max} of PVC and ϕ_{max} of filler. The bigger the filler, the higher the maximum packing fraction achieved by mixing PVC and filler. The gain by mixing is more important than the initial gain by using a filler with a wider size distribution: for example, even if filler S alone has a better compacity than filler XXL due to its wider size distribution, mixing PVC and filler S does not reach ϕ_{max} as high as those achieved with PVC/filler XXL.

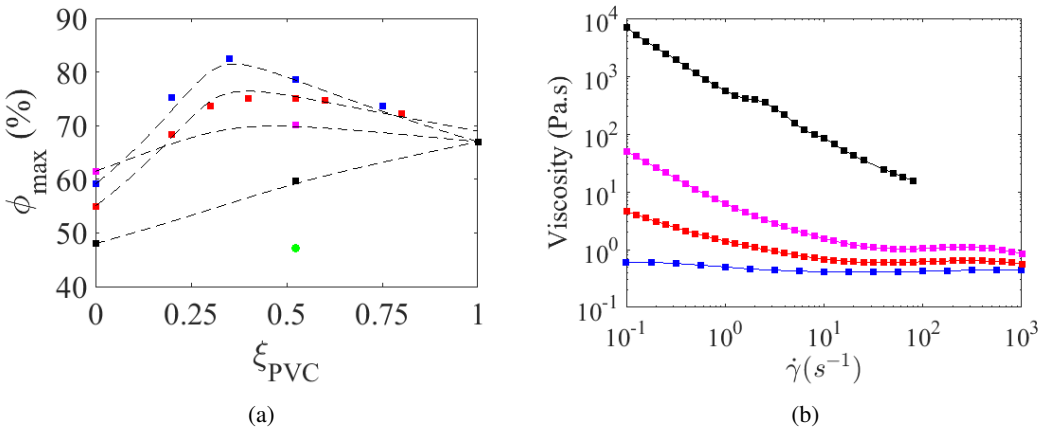

Figure 4.19: (a) Evolution of ϕ_{max} versus ξ_{PVC} for filler XS (■),S (■), M (■), XXL (■). Error bars are smaller than dots width. Dotted lines come from the model detailed in the next part. (b) Viscosity of suspensions made of 24.6 % of PVC 1 and 22.5 % of filler XS (■), S (■), M (■) and XXL (■). This formulation corresponds to the green point in graph (a).

Those differences obtained in ϕ_{max} for different filler sizes are even more visible when measuring the viscosity in a Couette cell geometry. We focus on formulation ratio ξ_{PVC} = 0.524 close to industrial formulations. Studied volume fraction is 24.6 % of PVC 1 and 22.5 % filler (Fig. 4.19b) . Naturally, the lowest viscosity is achieved by the formulation with highest ϕ_{max}.

4.3.1.3 Packing model description

One of the first model proposed in the literature to fit variations of packing fractions when mixing two powders was proposed by Furnas [248]. The resulting packing fraction depends both on the particle size ratio and the fine particle proportion ξ. However, one of the main hypothesis is to consider a large size ratio between the two particle sizes, i.e. $d_1/d_2 > 10$. However, in our case, for the filler M, S or XS, the condition is not fulfilled.

For cases when the size ratio is not so large (< 10), one has to take into account geometrical interactions between particles of different size . Various models have been developed [249, 250, 251]. We choose to use the compressible packing model developed by De Larrard [251] a widely used model [252] with industrial applications for example in concrete industry [253]. De Larrard model is a geometrical model which only considers space occupied by the particles. We consider the mixing of two powders: a coarse powder 1 (typical diameter d_1, maximum packing fraction $\phi_{max,1}$) and a fine powder 2 (typical diameter d_2, $\phi_{max,2}$) with $d_1 \geq d_2$. In all the following, the smaller subscript will be attributed to the coarsest particles. In our case, powder 1 corresponds to the filler and powder 2 to the PVC. Influence of particle size distribution is accounted via the packing fraction of the powder $\phi_{max,i}$.

In De Larrard's model, two different limiting cases are discriminated: the first when the coarse particles are dominant and the second where the fine particles are dominant. The first case corresponds to a state where fine particles fill voids between coarse particles (majority of coarse). The second case corresponds to a state where coarse particles are embedded in a fine particle matrix (majority of fine). Due to their limited size span, adding powder 2 will perturb packing of powder 1 and vice versa. Those perturbations are calculated through two contributions:

— **loosening effect** (coarse particles dominant): when one fine particle is inserted into a packing of coarse particles and the particle is not small enough to fill the empty space between the coarse, it will induce a local perturbation of the coarse packing which become slightly looser than expected (cf. Fig. 4.20a)

— **wall effect** (fine particles dominant): when one coarse particle is inserted into a packing of fine particles, the coarse particle will perturb the packing of the fines close to it. This wall effect induces a decrease in the overall fine particle density (cf. Fig. 4.20b).

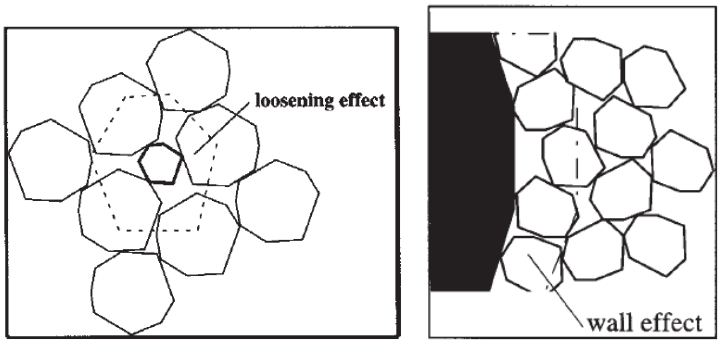

(a) (b)

Figure 4.20: Scheme for (a) Loosening effect, (b) Wall effect [251].

The virtual packing density corresponds to defined as the maximum packing density achievable with a given mixture, each particle keeping its original shape and being placed one by one [251]. Here ϕ_i stands for the volume fraction of powder i. We define for the following the fraction of powder i over the total powder. It is denoted ξ_i with i=1 or 2 the particle i proportion defined as:

$$\xi_i = \frac{\phi_i}{\phi_1 + \phi_2} \tag{4.3}$$

with $\xi_1 + \xi_2 = 1$

The first limiting case corresponds to a state where coarse particles are dominant. We can write:

$$\phi_{1,mix} = \frac{\phi_{max,1}}{1 - \xi_2(1 - a_{12}\frac{\phi_{max,1}}{\phi_{max,2}})} \tag{4.4}$$

where ξ_2 is the fraction of powder 2 (PVC) over the total powder a_{12} is the loosening effect coefficient. If $d_1 \gg d_2$, $a_{12} = 0$ as small particles do not disturb coarse particles packing (no interaction). On the contrary, d_1=d_2 corresponds to the case a_{12}=1 (total interaction).

The second limiting case is where fine particles are dominant. In that case, one gets:

$$\phi_{2,mix} = \frac{\phi_{max,2}}{1 - \xi_1(1 - \phi_{max,2} + b_{12}(\phi_{max,2} - \frac{\phi_{max,2}}{\phi_{max,1}}))} \tag{4.5}$$

The virtual packing density is thus written as:

$$\phi_{mix} = min(\phi_{1,mix}, \phi_{2,mix}) \tag{4.6}$$

where b_{12} is the wall effect coefficient.

Experimental measurements enable to determine a_{12} and b_{12} coefficients. However, in real life, the virtual packing density is not achieved and depends on the process to build the packing. The packing fraction experimentally achieved is denoted actual packing fraction $\phi_{mix,real}$. The difference is computed using a constant K called compaction index which considers the difference between actual packing density and virtual packing density and characterizes therefore the placing process.

The actual packing fraction $\phi_{mix,real}$ is defined by:

$$K = \sum_{i=1}^{2} \frac{\xi_i / \phi_{max,i}}{1/\phi_{mix,real} - 1/\phi_{i,mix}} \tag{4.7}$$

with K the compaction index, a variable which depends on the process. K is empirically ranging from 4 to 10 [251]. For example, for dry granular media, measuring packing just by vibration results in K = 4. Vibration followed by compaction at 10 kPa allows to be closer the virtual packing fraction (K = 9). K = + ∞ would stand for the case where the obtained packing is the maximum mathematically achievable.

4.3.1.4 Application: mixing one PVC and one filler

In our case, there are three unknown parameters a_{12}, b_{12} and K as $\phi_{max,i}$ (pure powder) is experimentally measured. As a reminder, subscript 1 stands for the filler (coarse particle) and subscript 2 for the PVC. Results from the model are directly plotted on experimental results (see Fig . 4.19). Parameters used for the model are listed in table 4.2.

PVC	Filler	a_{12}	b_{12}	K
PVC 1	XS	0.85	0.85	8
PVC 1	S	0.65	0.65	8
PVC 1	M	0	0.25	8
PVC 1	XXL	0	0	8

Table 4.2: Parameters of De Larrard model used for fitting data on Fig. 4.19

K should be the same for all experiments and is characteristic to our plasticizer absorption test which is used for all packing measurements. K is chosen from fitting data of mixing PVC and filler XXL. In such case, the size difference is higher than 10, corresponding to the case of non-interacting particles (a and b are taken to 0): the small PVC particles fill the voids between coarse fillers without

perturb its packing. Fitting with such conditions (a and b = 0) well captures experimental data for K = 8 (same holds for PVC 2 instead of PVC 1 as seen further). In the following, K = 8 is used for all fits. The value is closed to K = 6.9, a value found for similar super-plasticizer absorption test for wet granulars [251]

When the filler size is decreased, the particles are more and more in interaction from a geometrical point of view, meaning that adding PVC disturbs more and more filler packing and vice versa. This trends is visible in the choice of coefficients a and b needed to well the data. The smaller the filler, the higher a and b. They are highest for the case PVC 1- filler XS. Chosen coefficient are close the case of totally interacting particles (a=1 b=1 when d_1=d_2) which makes sense as their typical size are close (d50 =2.7 μm for filler XS; d50 =2 μm for PVC 1). Such a model explains our experimental results from Fig . 4.19.

The highest packing fraction obtained with biggest fillers is explained by the fact that small PVC particles better fill voids in that case. For smaller filler, the packing is less efficient as small PVC particles perturbs coarse filler packing. As a conclusion, the higher the size gap between particles, the highest the achieved maximum packing fraction even if the filler size distribution is quite narrow (as for XXL).

4.3.1.5 Mixing one PVC and two fillers

De Larrard's model was previously described for a binary mix. However, the model can be extended to a mixture of n powders. We detail here for three powders: 1 PVC and 2 fillers. Up to now, only one filler was mixed with PVC and the best packing fraction was obtained using filler XXL. We can complicate a little the problem by using together 2 fillers because real formulations contain several PVC and fillers. The goal is to find the formulation window which achieves the highest compacity. Contrary to last paragraphs, we focus here on PVC 2 as it has wider applications. Fillers M and XXL are used.

Only final equations are given here. Further details can be found in [251]. The virtual packing density is computed from each contribution:

$$\phi_{i,mix} = \frac{\phi_{max,i}}{1 - \sum_{j=1}^{i-1}(1 - \phi_{max,i} + b_{ij}\phi_{max,i}(1 - 1/\phi_{max,j}))\xi_j - \sum_{j=i+1}^{n}(1 - a_{ij}\phi_{max,i}/\phi_{max,j})\xi_j} \tag{4.8}$$

The actual packing fraction $\phi_{mix,real}$ is defined by:

$$K = \sum_{i=1}^{n} \frac{\xi_i/\phi_{max,i}}{1/\phi_{mix,real} - 1/\phi_{i,mix}} \tag{4.9}$$

Following the same logic as previously, 1 refers to the coarsest particle (filler XXL), 2 to filler M and 3 to PVC.

Preliminary experiments To apply the model in the case of three powders, one has to found the interactions parameters between powders: $\begin{pmatrix} & a_{12} & a_{13} \\ b_{21} & & a_{23} \\ b_{31} & b_{32} & \end{pmatrix}$

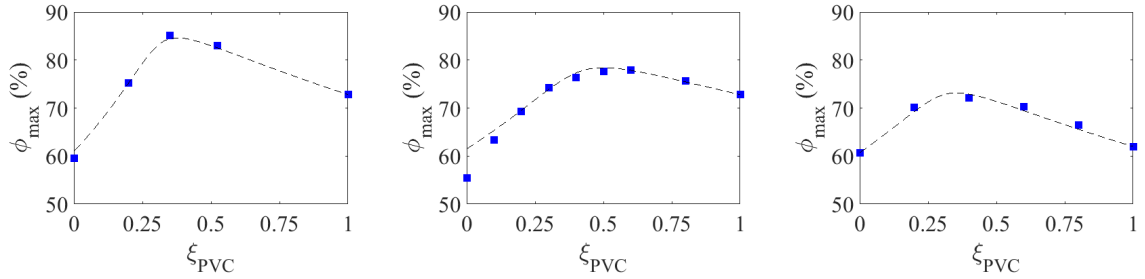

(a) (b) (c)

Figure 4.21: Maximum packing fraction from plasticizer absorption tests for each binary mix (a) PVC 2 - Filler XXL (b) PVC 2 - Filler M and (c) Filler M - Filler XXL. Horizontal axis always refers to percentage of the finer powder. Dotted line are fits using De Larrard model.

K is fixed to 8 like in previous fits. Values of all interactions parameters a_{ij} and b_{ij} are determined by measuring packing fraction variation for each binary mix and then fitting data with model for binary mix detailed previously. $\begin{pmatrix} & 0.35 & 0 \\ 0.3 & & 0.5 \\ 0 & 0.2 & \end{pmatrix}$

Figure 4.21 shows the measured values of ϕ_{max} for the three needed binaries. Fits from Delarrard model are also plotted and well match data. A discrepancy exists for PVC 2 - Filler M at high filler content ($\xi_{PVC} < 0.25$). The best fitting shown here is achieved by using the ϕ_{max} of the compatibilized filler with decanoic acid as a surfactant (61.5 % instead of 55). Using 55 % does not enable to well capture data for the whole range of ξ_{PVC} . This choice can be justified by the following: De Larrard model is purely geometric (filling spaces with particles) and was developed for dry granulars. In particular, it does not tackle possible problems related to a badly dispersed state. In our case, the filler is not in a good solvent when dispersed in plasticizer. Thus, compacity is artificially lowered when filler is a majority. This side effect of the compacity is not accounted by De Larrard model. Using compacity from the surfactant-covered filler enables to get rid of this side effect. The fit gives us a first hint that surfactant on filler surface is only decreasing suspension viscosity for very high loading of filler and does not play a role otherwise. This discrepancy is not seen with filler XXL as the specific surface is low and problem of compatibility is thus minor. For the mix Filler M- Filler XXL, experiments where done with the surfactant to get rid of incompatibility problem and focus on geometrical packing only.

Model prediction for ternary diagram Once all parameters have been determined by preliminary binary experiments, using De Larrard model allows the computation of maximum packing fraction over the whole formulation window. It gives a predictive ternary diagram showed in figure 4.22 based on experimental points from binaries. Axis x refers to filler XXL fraction of total powder (ξ_1 in the model). Similarly, axis y refers to filler M fraction of total powder (ξ_2 in the model).

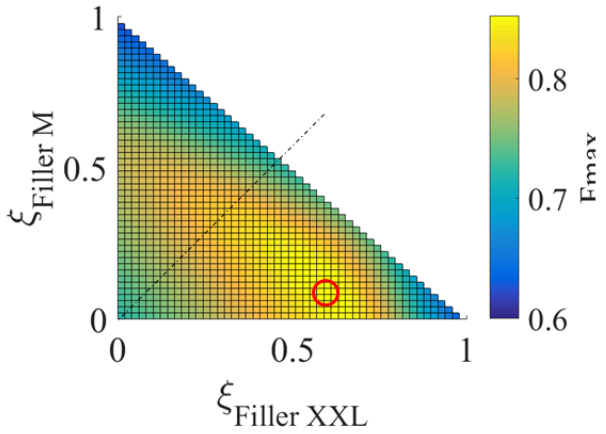

Figure 4.22: Prediction on maximum packing fraction for a ternary mix made of PVC 2- Filler M - Filler XXL using De Larrard's model and experimental data from binary mixes. The model will be checked on formulations following the black dotted line (cf. Fig. 4.23). The highest maximum packing fraction using the ternary mix reaches 85.2 % (red circle).

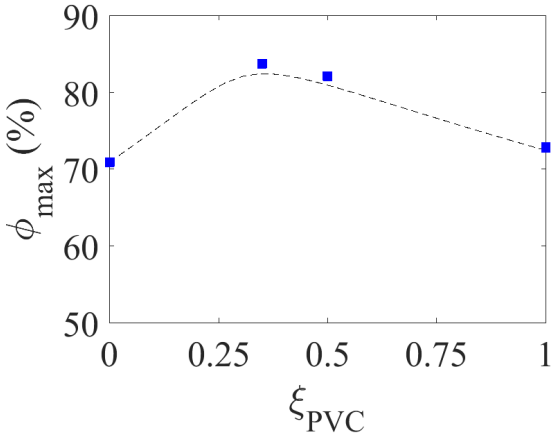

Figure 4.23: Comparison between experiments (■) and predictions (solid line) from De Larrrard model for the following formulation: Filler XXL x; Filler M: x, PVC: $1-2x$ with x from 0 to 0.5 (see dotted line on Fig. 4.22)

To check the validity of this approach, predictions from the model and experimental results are compared for the following formulation: Filler XXL x; Filler M: x, PVC: $1-2x$ with x from 0 to 0.5 (see dotted line on 4.22). Experimental data and model prediction are plotted on Fig. 4.23. A good agreement is observed: in particular the trend and the maximum position is well predicted. Values are however a little bit underestimated.

The highest maximum packing fraction using the ternary mix reaches 85.2 % (cf. 4.22). This value is very close to the maximum obtained by dispersing only PVC 2 and filler XXL (84.6 %). Thus using three fillers only achieved a small gain of 0.6 %

Variations of maximum packing fraction when mixing PVC and filler have been measured. It has been observed that a large size difference between PVC and filler enables the best maximum packing fraction. Especially, it is better to have a large size difference than a polydisperse filler.

These results are in good agreement with De Larrard model. From the experimental binaries, the model can be also used for compacity prediction of more complex formulations. The principle has been shown on a ternary mix (1 PVC and 2 fillers) and showed good predictive abilities. Even if more preliminary experiments are needed to measure some parameters, the model turns out to be a efficient tool for compacity prediction in such PVC/filler suspensions.

4.3.2 Rheological behaviour

Once maximum packing fraction has been investigated, we now turn the viscosity measurements of filled suspensions. First part is dedicated to measuring the viscosity for a wide range of filler/PVC ratio (varying ξ_{PVC}). The second part discusses about a simple model accounting for experimental results. **We focus here on Filler M, the reference filler** with a D50 of 20 μm.

4.3.2.1 From PVC to filler suspensions

Filler suspensions exhibit a shear-thinning behaviour at low shear rate followed by a Newtonian plateau. PVC suspensions are shear thinning at low shear rate but, on the contrary, shear thickening at higher shear rate. Thus mixing the two powders would give a priori unknown flow curves.

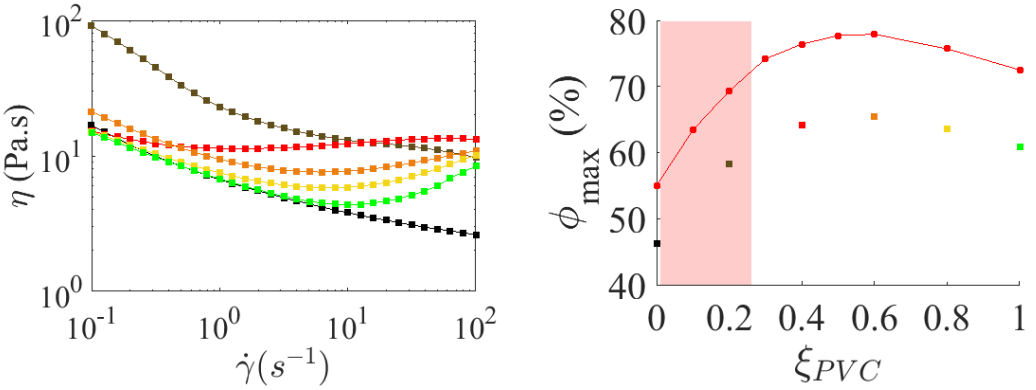

(a) (b)

Figure 4.24: (a) Flow curves for different PVC/filler ratio: 100% (■); 80% (■); 60% (■); 40%; (■); 20% (■) and 0% (■). To offset large maximum packing fraction variation, each composition is taken at 0.84 ϕ_{max} (b) Corresponding coordinates in formulation diagram. Solid red line is experimental points for maximum packing fraction. Red zone corresponds to the zone underlined previously where filler is the majority with few PVC particles inserted in the voids (cf. part 4.3.1.1).

In figure 4.24a is plotted the viscosity VS shear rate for different ξ_{PVC}. As packing fraction varies a lot when mixing powders, experiments are carried out at fixed distance from experimentally measured maximum packing fraction ($0.84\phi_{max}$, cf. Fig. 4.24b). Changing Filler/PVC ratio results in a gradual change in the shape of rheological curves. The shear thickening behaviour disappears gradually when filler replaces PVC. Besides, the low-shear viscosity increases progressively. At intermediate content, the viscosity curve is not so far from Newtonian behaviour (red curve). When filler is further increased, the behaviour changes drastically to shear thinning with a net increase of viscosity at low shear rate. This transition occurs around $\xi_{PVC} \sim 0.3$. For $\xi_{PVC} < 0.3$, the sample behaves closely to pure filler in DINCH. This zone corresponds to the zone underlined previously (in compacity measurements) where

filler is the majority and few PVC particles fills the voids in between (cf. part 4.3.1.1). Thus, logically, rheological behaviour in this zone is dominated by filler contribution. Followings experiments will help to understand the physics governing the viscosity of our filled suspension.

4.3.2.2 Adding filler

Starting from the reference industrial filled formulation (33% PVC, 30 % filler), if the filler is virtually removed, one obtains a suspension of PVC at ϕ = 33 / (33+37) = 47.1 %. Here, a reference formulation of PVC in plasticizer at 47.1 % is prepared. Filler is added to this suspension with different volume: 0, 25, 42.8 and 66.7 %. Recalculated formulations are given in the following table (4.3):

Added filler	Resulting formulation			ξ_{PVC}
	% PVC	% filler	% liquid	
0 %■	47.1	0	52.9	1
+25 % filler (■)	37.7	20	42.3	0.65
+42.8 % filler (■)	33	30	37	0.52
+66.7 % filler (■)	28.3	40	31.7	0.41

Table 4.3: Formulations from which rheology is measured and displayed in Fig 4.25. Position on the formulation diagram is displayed later (Fig. 4.26).

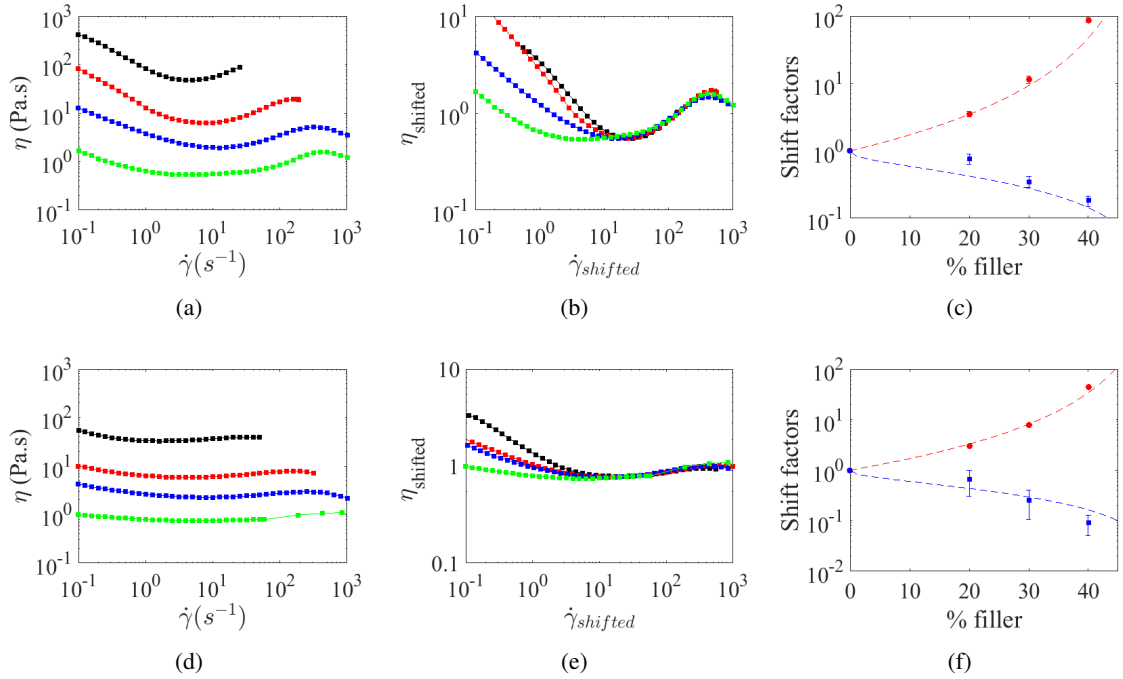

Figure 4.25: (a) Flow curves of D1 47.1 % with no filler added (■) and with adding extra 25% (■); 42.8% (■); 66.7% (■) filler (size M). (b) Rescaled curves: viscosity is divided by a shift factor η_{sf} and shear rate multiplied by a shift factor $\dot{\gamma}_{sf}$ (c) Shift factors η_{sf} and $\dot{\gamma}_{sf}$ plotted versus volume fraction of filler in the mix. Dotted lines are predictions from Eq. 4.12 and Eq. 4.17. (d)(e)(f) Same with D2 at 47.1 % as the suspending medium.

Viscosity is measured for these formulations using filler M with PVC 1 (Fig. 4.25a) or PVC 2 (Fig. 4.25d). Results concerning mix of PVC 1 and filler shows that the shear-thickening behaviour (increase of viscosity at the highest shear rates) is very similar whatever the filler content. It can be checked when curves are superposed using two shift factors: a vertical one η_{sf} increasing the viscosity and a horizontal one $\dot{\gamma}_{sf}$ shifting shear thickening at lower shear rate. Superposed curves and shift factors are plotted on Fig. 4.25. Very good superposed curves are obtained in the shear-thickening regime, meaning that the shear thickening is the same whatever the filler content and depend only on the PVC relative concentration $\frac{\phi_{PVC}}{\phi_{PVC}+\phi_{liq.}}$ (here 47.1 %). However, viscosity at low shear rate is not superposed: high filler content results in a higher low-shear viscosity than expected.

Our approach consists in adding inert coarse particles (non-shear thickening) into a shear-thickening medium made of smaller particles. Such systems have not been widely studied except some recent papers [244, 245, 246, 247]. In the two first references, non-Brownian particles are added to a colloidal shear-thickening suspension. For the two latter, fine and coarse particles are non-Brownian. But, in all of these studies, the size ratio between coarse and fine particles is always 10 or larger, and therefore the shear thickening medium made of small particles can be treated as a continuous medium for coarse particles. In our case, such condition is not completely fulfilled especially for the PVC 2: filler has a D50 of 22 μm but with a non-negligible part of particles under 10 μm. PVC 1 size distribution is centred around 2 μm and PVC 2 has two peaks one at 700 nm but also one peak at 5-6 μm.

More generally, these studies focus on suspensions dispersed in a Non-Newtonian phase. In the above works, the Non-Newtonian liquid phase is made of the small particles and is shear thickening. First work concerning suspensions in a Non-Newtonian fluids deals with spherical non-colloidal particles in polymer solutions and melts [254]. Strikingly, it was observed that flow curves can be rescaled onto the suspending fluid at a constant shear stress using a single rescaling parameter [254, 255, 243]:

$$\eta_{sf} = \left.\frac{\eta(\phi)}{\eta(\phi=0)}\right|_{\sigma} \tag{4.10}$$

meaning that when flow curves are plotted versus σ, rescaling is done only by a vertical shift. As the shear stress is continuous in the sample, we can write

$$\dot{\gamma}_{sf} = \left.\frac{\dot{\gamma}(\phi)}{\dot{\gamma}(\phi=0)}\right|_{\sigma} = \frac{1}{\eta_{sf}} \tag{4.11}$$

For coarse suspensions dispersed into a shear-thickening medium made of smaller particles, such scaling was found valid at low coarse particle volume fraction ($\phi < 0.15$)[244] and invalid at higher loadings [244, 247]. Here, the simple scaling is also not satisfied. Both the stress and viscosity should be altogether shifted.

4.3.3 Modelling viscosity of a PVC-filler dispersion

Simple models are here developed to account for η_{sf} and $\dot{\gamma}_{sf}$. Predictions from such models are then compared to experimental data.

4.3.3.1 First Model: Description

Vertical shift factor η_{sf}: Except at low shear rate, increasing levels of added filler particles do not change the shape of the flow curve. Filler is thus here supposed to be non-interacting and only to fill geometrical space. In such cases, it has been empirically found that adding particles in a liquid medium causes a rise in viscosity well described by [243]:

$$\eta_{sf} = (1 - \frac{\phi}{\phi_{max}})^{-n} \tag{4.12}$$

where ϕ_{max} and n are parameters.

In my work, n is adjustable but contrary to most of previous works, ϕ_{max} is here determined from experiments of plasticizer absorption test. More precisely, we take advantage of the measured variation of packing fraction over the whole range of formulation from part 4.3.1. Indeed ϕ_{max} from Eq. 4.12 is determined by the intersection of the formulation path and the maximum packing fraction border experimentally obtained (cf. Fig. 4.26). The formulation path corresponds to the explored zone when adding increasing amounts of filler to a PVC suspension initially at 47.1 %.

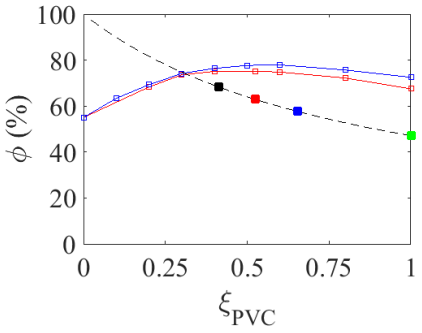

Figure 4.26: Dotted line: Formulation path followed when adding filler to a PVC suspension initially at 47.1 %. Coloured dots corresponds to formulations from which rheology is measured in Fig. 4.25. The dotted line intersects the maximum packing fraction curve of PVC 1 - filler (red solid line) for ξ_{PVC} = 0.314 and ϕ = 73.9 %, corresponding to a maximum volume fraction of filler ϕ_{max} = 50.7 %. For PVC 2 -filler (blue solid line), intersection occurs for ξ_{PVC} = 0.307 and ϕ = 74.4 %, corresponding to a maximum volume fraction of filler ϕ_{max} = 51.6 %.

Horizontal shift factor $\dot{\gamma}_{sf}$: When adding filler, shear thickening occurs at lower shear rates. As the level of filler is increased, small PVC particles will be more and more confined between filler coarse particles. PVC particles thus feel local higher shear rates.

Using a toy model, the local shear rate $\dot{\gamma}_{local}$ felt by PVC particles (in between coarse filler particles) can be expressed as a function of the macroscopic shear rate $\dot{\gamma}_{macro}$ [247]. Related picture is on Fig. 4.27.

$$\dot{\gamma}_{local} = \frac{2U}{2h} \tag{4.13}$$

where U is the speed for coarse particle and h the distance between two particles surface.

$$\dot{\gamma}_{macro} = \frac{2U}{2a + 2h} \tag{4.14}$$

where a is the particle radius.

Combining Eq 4.13 and Eq 4.14:

$$\dot{\gamma}_{local} = \frac{2a+2h}{2h} * \dot{\gamma}_{macro} = (\frac{a}{h}+1) * \dot{\gamma}_{macro} \tag{4.15}$$

Now, one needs a relation for the interparticle distance 2h as a function of the volume fraction fraction. For a sufficient concentration, a simple geometric model gives a relation for the interparticle distance h in the suspension [244, 194, 45]:

$$\frac{h}{a} = (\frac{\phi_{max}}{\phi})^{1/3} - 1 \tag{4.16}$$

where a is the particle radius.

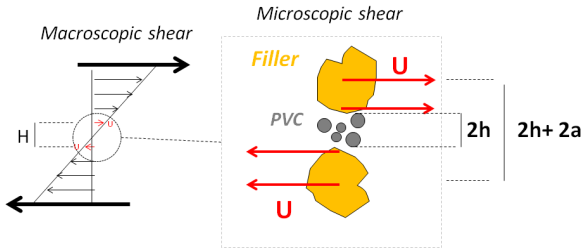

Figure 4.27: Macroscopic shear rate $\dot{\gamma}_{macro}$ and local shear rate $\dot{\gamma}_{local}$ felt by small PVC particles in between coarse filler particles.

Therefore, using Eq. 4.16 and Eq. 4.15, the horizontal shift factor can be expressed as:

$$\dot{\gamma}_{sf} = \frac{\dot{\gamma}_{macro}}{\dot{\gamma}_{local}} = \frac{1}{1+\frac{\beta'}{(\frac{\phi_{max}}{\phi})^{1/3}-1}} \tag{4.17}$$

where we introduced β' as a geometrical factor. This factor aims at accounting for the real complex local shear rate distribution compared to our toy model used for calculating a single local shear rate.

Finally, the viscosity of the total suspension is written in this model as

$$\eta_{total}(\dot{\gamma}_{macro}) = \eta_{\text{PVC in DINCH}}(\dot{\gamma}_{local}) * \eta_{sf} = \eta_{\text{PVC in DINCH}}(\frac{\dot{\gamma}_{macro}}{\dot{\gamma}_{sf}}) * (1-\frac{\phi}{\phi_{max}})^{-n} \tag{4.18}$$

where ϕ is the volume fraction of added filler and ϕ_{max} the maximum volume fraction of filler which can be added to the suspensions (determined experimentally from plasticizer absorption test, cf. Fig. 4.26).

4.3.3.2 Validity and limitations

Predicted shift factors (η_{sf} for viscosity and $\dot{\gamma}_{sf}$ for shear rate) are plotted versus the filler volume fraction on Fig. 4.25c and 4.25f.

— For η_{sf}, the only adjustable parameter n is fixed to 2.5, slightly higher than often reported factor 2 but still coherent and already observed [243]. The parameter ϕ_{max} is experimentally determined to be 50.7 % for PVC 1 -filler and 51.6 % for PVC 2 - filler (cf. Fig 4.26).

— For $\dot{\gamma}_{sf}$, the only adjustable parameter β' is chosen to 1/2 for both cases (PVC 1 + filler and PVC 2 + filler). $\beta' < 1$ means that the averaged local shear rate is less important than the one found using the toy model.

Finally, a good agreement is obtained for both shift factors even used models are very simple.

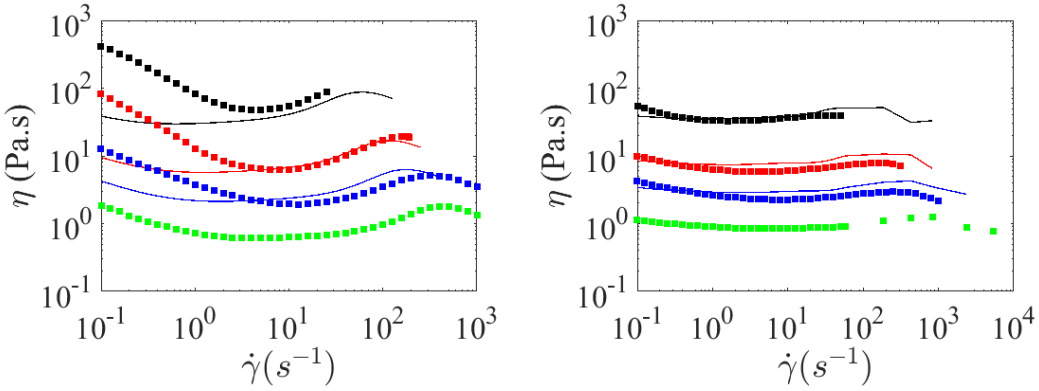

Figure 4.28: a) Flow curves of a 20 % PVC 1 suspension with no filler added (■) or with 20% (■); 30% (■); 40% (■) filler (size M). Solid lines corresponds to prediction from 1^{st} model (b) Same with PVC 2.

Applying theses shift factors to predict the flow curve of filled suspensions is displayed on Fig. 4.28. For PVC 1 and filler, shear-thickening behaviour and minimum viscosity are quite well predicted. Major discrepancy occurs for predicting the low-shear viscosity. It could have been foreseen as the shifting superposition already failed at low shear rates. The problem is less present for PVC 2 - filler where no such over-expected increase is low shear is observed. For this case, predicting the viscosity through our approach fits well experimental data. Discrepancy at low shear rate can be explained by the hypothesis from our model. Filler was considered as non-interacting, i.e only geometrically filling space. The model considers only PVC-PVC interactions with the flow curve of the suspending medium. Thus, both filler-filler and filler-PVC were neglected. But such interactions seem to exist due to high experimental viscosity measured at low shear rate.

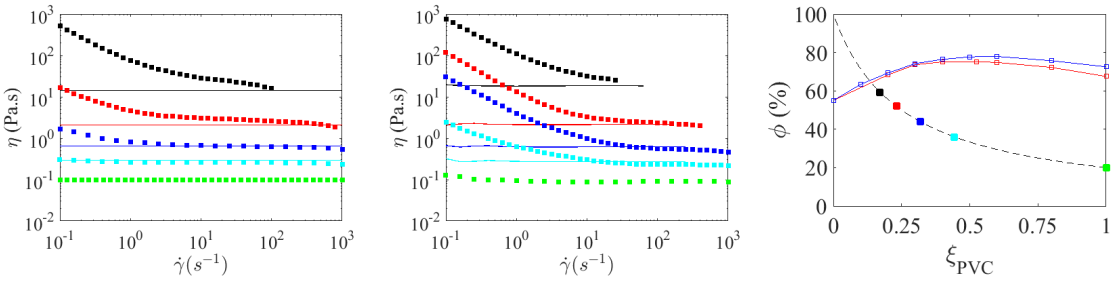

Figure 4.29: (a) Flow curves of D1 at 20 % with no filler added (■) or with 20 % (■); 30% (■); 40% (■); 49% (■) filler (size M). Solid lines corresponds to prediction from 1^{st} model (b) Same with PVC 2. (c) Corresponding coordinates in formulation diagram. Solid red line is experimental points for maximum packing fraction. Dotted line: formulation path followed when adding filler to a 20 % PVC suspension. Intersection giving $\phi_{max,filler}$ is 55.6% for PVC 1-filler and 56.8 % for PVC 2-filler

Limits of the model are also underlined when investigating suspensions with higher filler ratios. For example is displayed on figure 4.29 the rheology for increasing levels of filler added to a more dilute PVC suspension at 20 %. As previously, viscosity is measured for the dilute suspension of PVC at 20 % and for three different amount of added filler. Here, the rheology of the suspending phase is Newtonian because of the low concentration of PVC. Predictions of the model are then Newtonian as the liquid phase curve. They reach very good predictions for high shear rate viscosity. However, low shear rate viscosity is not well estimated, certainly due to PVC-filler interaction and especially filler-filler interactions. Indeed, the flow curve of the global suspension has the same behaviour as filler dispersed in DINCH (cf. part 4.2) as the formulation tends to the zone (red zone underlined previously) where rheology is rather filler-dominated.

In order to try to account for these filler-filler interactions, a second simple model is developed below. Predictions from this second model are then compared to ones from first model and to experimental data.

4.3.3.3 Second model

To try to fit the experimental viscosity at low shear rate, we develop a second approach. We focus on highly filled formulations where the viscosity profile is similar to those of pure filler suspensions (only filler in DINCH). The global suspension is seen as a suspension of filler suspended in DINCH but in which the interstitial liquid phase is not pure DINCH but a dilute suspension of PVC in DINCH (20 % in the example above).

The viscosity of the suspensions can thus be written:

$$\eta_{total}(\dot{\gamma}_{macro}) = \eta_{filler/DINCH}(\dot{\gamma}_{macro}) * \frac{\eta_{\text{PVC in DINCH}}(\dot{\gamma}_{local})}{\eta_{DINCH}} \tag{4.19}$$

where $\eta_{\text{PVC in DINCH}}$ is for the example detailed here the viscosity of the PVC suspension at 20 %.

Filler-filler interactions are accounted because the rheology of concentrated filler suspension is taken as an input in the model ($\eta_{filler/DINCH}$). Applied like this, such model failed to predict the viscosity curve (nor high-shear neither low shear rate). The approach used here implies a large size difference between particles to be valid (PVC particles 10 times at least smaller than filler). Such an hypothesis is not validated for our case. Consequently, the model implies a maximum packing fraction ϕ_{max} larger than the actual one $\phi_{max,actual}$. Indeed, as explained in part 4.3.1.3, $\phi_{max,actual} < \phi_{max}$ due to geometrical interactions in a packing when the size ratio between particles is under ~ 10.

To make the viscosity from our model diverging at $\phi_{max,actual}$, the viscosity prediction is corrected:

$$\eta_{total,actual} \sim \eta_{total} * \frac{(1 - \frac{\phi}{\phi_{max,actual}})^{-n}}{(1 - \frac{\phi}{\phi_{max}})^{-n}} \tag{4.20}$$

Here again, $\phi_{max,actual}$ comes from experiments with plasticizer absorption test. ϕ_{max} is obtained with the De Larrard model when simulating the packing in the virtual case of geometrically non-interacting particles: a = b = 0 (cf. Fig. 4.30)

Figure 4.31 presents the results obtained with this model for the case of adding filler to D1 at 47.1 % (Fig. 4.31a), adding filler to D1 at 20 % (Fig. 4.31b), D2 at 20 % suspensions (Fig. 4.31)c). In all

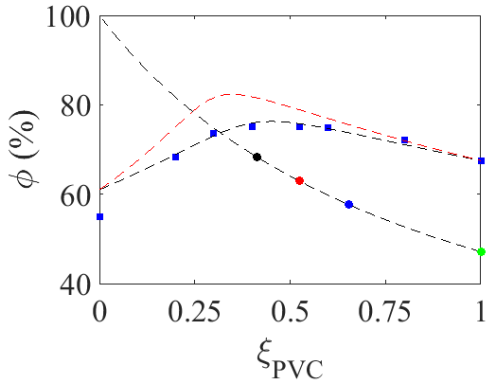

Figure 4.30: Example for PVC2 - Filler M: experimental points for ϕ_{max} (■) fitted with the De Larrard model (black dotted line). Intersection with formulation path gives a maximum filler content $\phi_{max,actual}$= 50.3 %. Red dotted line correspond to the maximum packing fraction which would be obtained in the virtual case of a large size difference between particles (a = b = 0 in De Larrard model). Intersection with formulation path gives for the filler ϕ_{max} = 59.3 %.

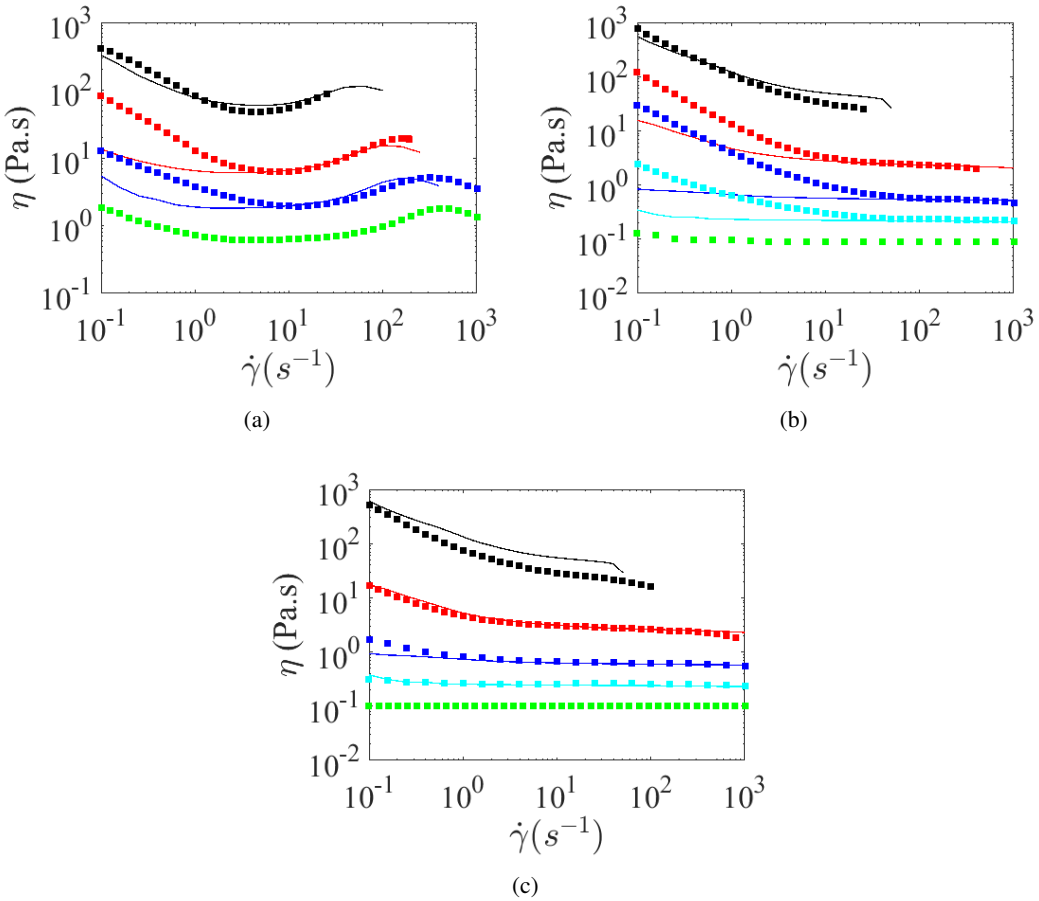

Figure 4.31: (a) 2^{nd} model applied to data from 4.25a (D1 at 47 %+ added filler); (b) 2^{nd} model applied to data from 4.29b (D1 at 20 % + added filler); (c) 2^{nd} model applied to data from 4.29b (D2 at 20 % + added filler).

cases, n was also taken to 2.5. For PVC 1 (Fig. 4.31a and b), low shear viscosity is well predicted at very high filler content for both initial PVC concentrations (20 and 47.1 %). Accounting for filler-filler

interactions matches experimental data, underlying the major importance of them at high filler content. At intermediate filler content, prediction is better than the 1^{st} model but still insufficient. Filler-PVC interactions are certainly here important and not really accounted here, explaining the discrepancy. However, this problem is not encountered for PVC 2 (Fig. 4.31c). Here, the 1^{st} model was accurate for initial concentration 47.1 %. For 20 %, the 2^{nd} model predicts well experimental results.

4.3.3.4 Back to first rheological experiments

We now turn back to first experiments concerning the rheology of filled suspensions with PVC 2 + filler M (cf. part 4.3.2.1). Figure is reminded on 4.32a. Such curves can be reanalyzed at the light of insights gained in previous sections. In the regime of $\xi_{PVC} \geq 0.4$ (red, orange, yellow curves), rheology is similar with pure PVC dispersed in DINCH (green curve). Adding filler lowers the actual concentration of PVC explaining the decrease in the shear thickening intensity. The case corresponds well to 1^{st} model. On the contrary, in the regime of $\xi_{PVC} \leq 0.3$ (brown and black curves); the rheological behaviour is similar to pure filler dispersed in DINCH, Filler-filler interactions have to be taken into account, i.e. using 2^{nd} model.

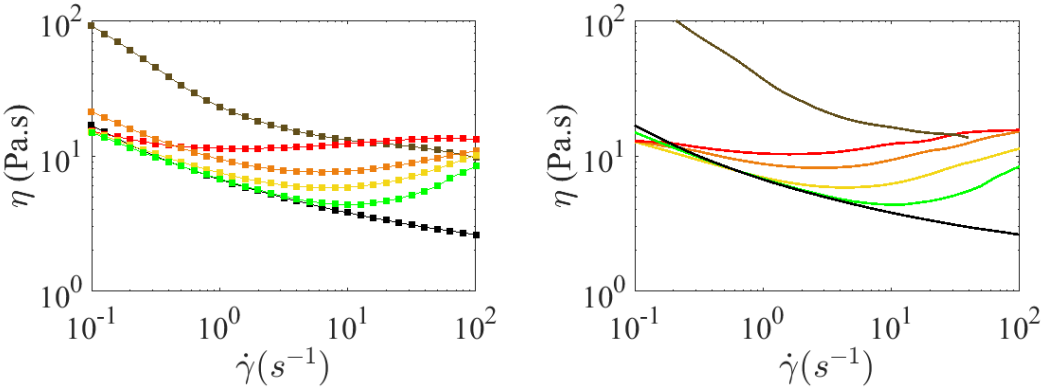

Figure 4.32: Left: flow curves form presented in 4.3.2.1. Right: prediction from model

Predicted flow curves obtained using either model 1 or 2 as described above are displayed on Fig. 4.32b. Very good agreement is obtained, meaning that contributions of filler and PVC to the global rheological curve is well understood.

4.3.3.5 Practical application

Such models can be used in a program for simulating rheological curves within the whole formulation window. For example, it can be used to calculate the viscosity at 100 s^{-1} for any formulation. At this shear rate, the first model was perfectly valid. Indeed, discrepancy for high filler content was only at low shear rate. We will use it as an example.

The logic of the program is the following:

— For any formulation, compute the real concentration of PVC $\frac{\phi_{PVC}}{\phi_{PVC}+\phi_{liq.}}$.

— Measure its rheological behaviour. To be more efficient, only a few concentrations can be measured and curve for any concentration can be generated by fitting viscosity with a Krieger Dougherty law for any shear rate (cf. Fig. 4.33).

— Find the maximum packing fraction when adding filler from intersection of formulation path and experimental compacity curve (plasticiser absorption test).

— Run the model for computing the viscosity and plot the results (cf. Fig. 4.34).

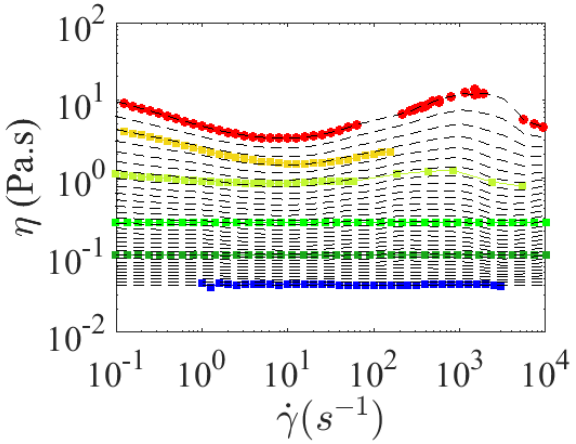

Figure 4.33: Interpolation of D2 flow curve for any concentration based on few experimental data (circles, from below to top): 0%; 20%; 35%; 47.1%; 60%. Predictions (dotted lines) derive from a fit with a Krieger-Dougherty law for any each shear rate.

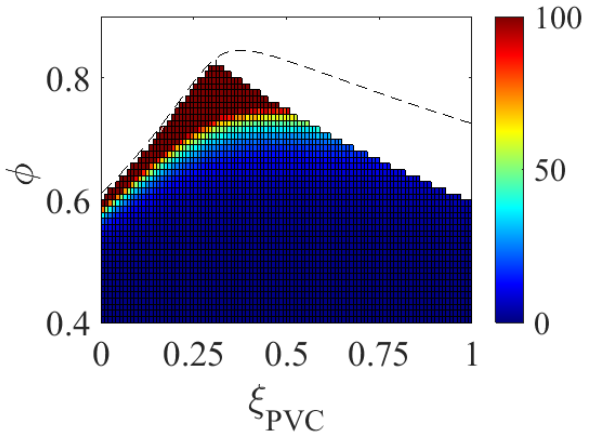

Figure 4.34: Viscosity prediction at 100 s^{-1} on nearly the whole formulation window with PVC 2 and filler M (first model). Dotted line represents the maximum packing fraction. Coloured scale bar is constrained to 0-100 Pa.s which correspond approximately to the range of viscosity processable during the coating step (knife over roll).

Procedure here works for any shear rate and could be implemented in more complex formulations, giving guidelines for the engineer which designs new formulations.

As a conclusion, we developed here a simple model enabling to predict rheological changes induced by filler addition. Using as input only the maximum packing fraction variation and the rheology of PVC in DINCH, the first model predicts well the viscosity for moderate filler content

(including filler content typically used in industrial formulations). As the predicted viscosity is based on the measured viscosity of pure PVC which is shifted to lower shear rate (and higher viscosity), the flow curve of the PVC suspension must be measured at sufficient shear rate. This could be performed with capillary rheometry (air compressed for example) described throughout the PhD thesis. The limit in our case (PVC 2 - Filler M) was ξ_{PVC} = 0.3. For higher filler content, filler-filler interactions cannot be neglected. Model 2 uses input from model 1 combined with the rheology of pure filler in DINCH. Again, the predictions match quite well the experimental data. In both models, some discrepancy has been observed at low shear rate when using PVC 1 in the formulation, probably linked with PVC-Filler interactions not accounted in the model. The discrepancy is far less present when using PVC 2 instead of PVC 1.

4.3.4 Impact of surfactant on filler surface

From the literature (cf. part 1.8.4.1), results are scarce and rather controversial as Cook et. al. [191] observed no impact; Oregui et. al. [190] reported an increase of viscosity when using a filler coated with stearic acid and Lambla et. al [189] reported a fluidization of the sample with filler coated with stearic acid.

From measurements of part 4.2.3, we have shown that the viscosity of a filler suspension can be significantly reduced using a surfactant as it increases the maximum packing fraction of filler when dispersed in DINCH. We wonder here if such effect are still visible when filler is mixed together with PVC. Following work for filler suspension, we focus here on decanoic acid as a surfactant.

4.3.4.1 Rheological curves

We showed in part 4.2.3 that filler compatibilization can be achieved with decanoic acid solubilized directly in DINCH. Here we try the same but on filled plastisol, i.e. a suspension with both filler and PVC. We choose the following formulation 33 % PVC, 30% Filler (ξ_{PVC} = 0.524) close to industrial formulations.

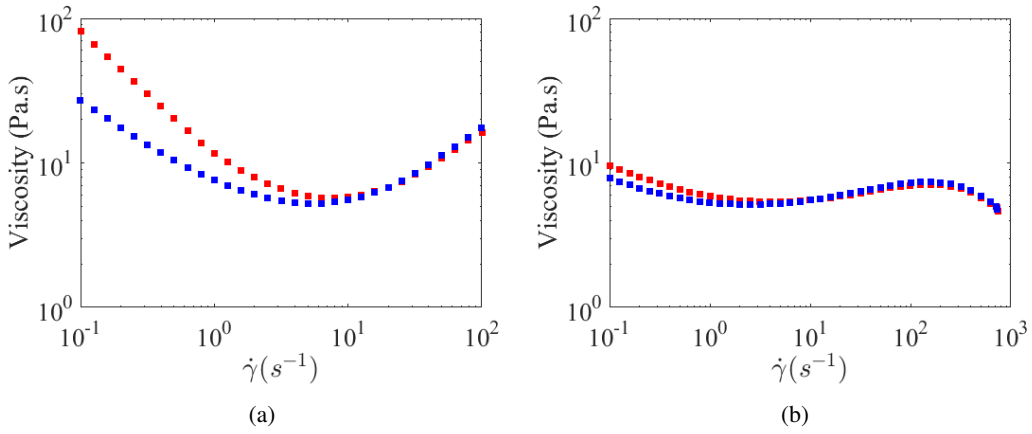

Figure 4.35: Viscosity of a suspension 33% PVC + 30 % filler M without (■) and with 0.2 wt% decanoic acid (■) when using (a) PVC 1 or (b) PVC 2.

Impact of adding 0.2 wt% (relative to filler mass) decanoic acid is displayed on Fig. 4.35 in the case of filler M. For PVC 1, a reduction of viscosity is observed but only limited to low shear rate, shear-thickening behaviour and minimum viscosity remains unmodified. Using the more polydisperse PVC 2 in the formulation does not modify the viscosity. Finally, even if adding decanoic acid for a suspension of pure filler decreases significantly the viscosity (2-3 times), the drop in viscosity for the whole flow curve is not observed for filled suspensions close to industrial formulations.

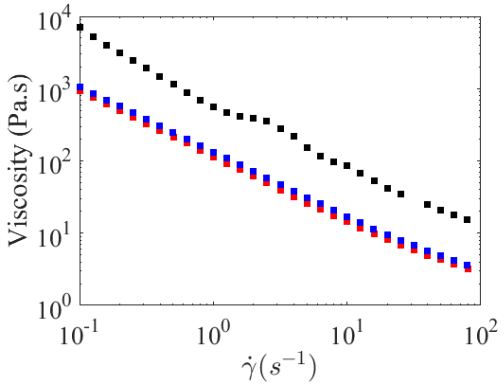

Figure 4.36: Viscosity of a suspension 24.6 % PVC 1 + 22.5 % filler size XS without (■) and with 0.2 wt% decanoic acid (■). Same formulation using filler XS industrially pre-treated with stearic acid (■).

To check filler size influence on possible effect of surfactant on the viscosity, the same as before is done but using filler XS instead of M (see Fig. 4.36). As filler XS contains non-negligible amounts of water, it is used after one night drying in an oven. As maximum packing fraction with filler XS is far lower than filler M (cf part 4.3.1.2), experiments are carried out on a diluted formulation (24.6 % PVC + 22.5 % filler) but keeping the same PVC ratio (ξ_{PVC} = 0.524). First, the behaviour is only shear-thinning. Using a filler with small particle size (i.e high specific surface) results in numerous attractive filler-filler interactions due to bad compatibility between hydrophilic filler surface and hydrophobic DINCH [243], explaining the high low shear viscosity and the shear-thinning behaviour.

However, adding decanoic acid in the formulation greatly reduces the viscosity by around one decade (see Fig. 4.36). We can suggest that in this case, the compatibilization of filler explains the drop of viscosity. This is confirmed by using filler XS industrially treated with stearic acid (modified filler "XS-treated" used without further modification) which achieves the same viscosity drop as filler + decanoic acid in solution, showing that the decanoic does go to filler surface. By the way, using either decanoic acid or stearic acid as a compatibilizer results in the same effect. This could have been guessed from Fig 4.12 where both chemicals enable the same viscosity reduction for pure filler dispersed in DINCH.

4.3.4.2 Impact on packing fraction

To try to explain previous results, maximum packing fractions are measured in suspensions with 0.2 % of decanoic acid. Suspensions are composed of PVC 1 and different filler sizes XS, M, XXL (see. Fig. 4.37). We focus on PVC 1 as it contains no surfactant which could influence our results. For the filler XS and M, the gain in packing fraction when using surfactant is the highest for pure filler and reduces progressively when adding PVC (increasing ξ_{PVC}).

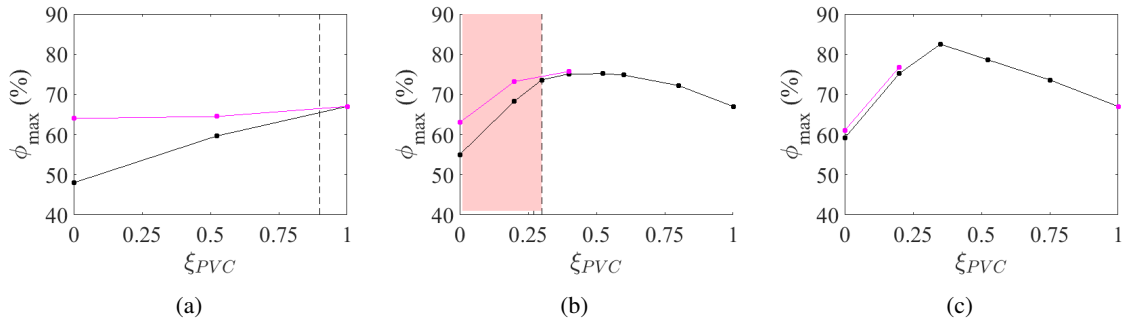

Figure 4.37: Maximum packing fraction when mixing PVC 1 with filler (a) XS (b) M (c) XXL with 0.2 wt% decanoic acid (■) or without surfactant (■).

For the filler XS, a significant increase in compacity ($\geq$ a few %) is achieved for filler content up to $\xi_{PVC}^{boundary} \approx 0.9$ (see dotted line on Fig. 4.37a). It means in particular that for the $\xi_{PVC} = 0.524$ corresponding to previous experiments, the increase of packing fraction is visible with adding decanoic acid, thus explaining the viscosity drop observed in Fig. 4.36. For filler M, the gain in compacity is limited to filler content up to $\xi_{PVC}^{boundary} \approx 0.3$ (similar boundary when using PVC 2) as displayed on Fig. 4.37b. Thus, for previous experiments ($\xi_{PVC} = 0.524$), no gain of maximum packing fraction is achieved with decanoic acid, also explaining the results of Fig. 4.35, especially the unchanged minimum viscosity. It is interesting to note than the formulation window for which the surfactant reduces the viscosity matches quite well the zone for which the rheology is filler dominated (red zone on the graph). For the filler XXL, the gain in compacity is small and only limited to formulation range very close to pure filler. As a conclusion, decanoic acid causes a viscosity drop for a sufficient amount of filler in suspension; the bigger the filler, the higher this critical amount of filler. Results from maximum packing fraction measurements are in line with viscosity measurements.

For the case of PVC 2 instead of PVC 1 in the filled formulation, adding decanoic acid did not reduce the viscosity neither. However, some SDBS (surfactant) is present at PVC particle surface and SDBS was proved to be a efficient compatibilizer too (cf. part 4.2.3). We thus may wonder if filler was already compatibilized by some SDBS coming from PVC particles.

Considering that SDBS takes the same area per molecule on filler particle and on PVC particle, surfaces of PVC and filler are equal for a PVC/filler ratio of:

$$\xi_{PVC,c} = \frac{\rho_{filler}}{\rho_{filler} + A\rho_{PVC}} \tag{4.21}$$

with A the ratio of specific surfaces defined as A = S_{PVC}/S_{filler}

For PVC 2 and filler M, it gives $\xi_{PVC,c} = 0.28$ which is very close to $\xi_{PVC}^{boundary}$. For lower ξ_{PVC}, the surfactant on PVC surface would not be sufficient to cover filler surface and compatibilization with decanoid could help to decrease the viscosity. For higher ξ_{PVC}, even without surfactant from PVC, compatibilization of filler is rapidly useless. And surfactant from PVC particles could compatibilize filler a little bit if needed. Globally, surfactant on PVC particles does not change our conclusions: decanoic acid causes a viscosity drop only for a sufficient amount of filler in suspension which depends on the characteristics of the two powders and especially filler particle size.

4.3.5 Impact of residual water

Using a filler dried in the oven results in nearly the same viscosity (see Fig. 4.38). Such results are consistent with results for pure filler (cf. Fig. 4.16) where only a slight modification was observed.

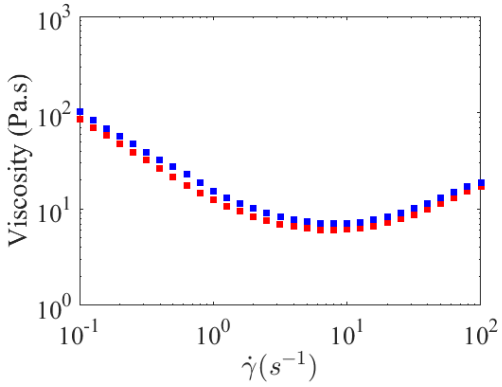

Figure 4.38: Viscosity of a suspension 33% PVC 1 + 30 % filler size M when filler is used as received (■) or dried in a oven (■).

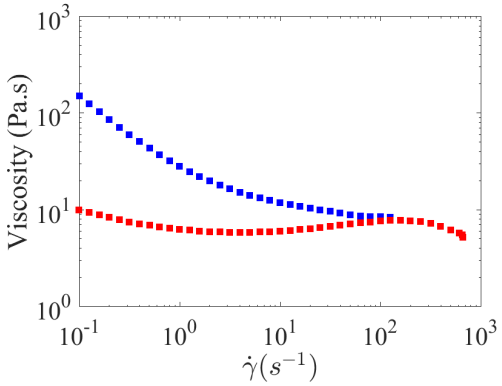

Figure 4.39: Flow curve with 1 wt% water (■) and without added water (■) for a suspension a suspension 33% PVC 2 + 30 % filler size M.

As displayed in Fig. 4.39, adding 1 % wt water logically increases the low shear viscosity at it was the case for Filler-plasticizer (cf. part 4.2.4) and for PVC 2 - plasticizer (cf part. 4.1.2.1). Again, this is microscopically explained by capillary bridges formation. Such capillary bridges are broken at high shear rate, explaining the convergence of flow curves with and without water for $\dot{\gamma} > 100\ s^{-1}$.

4.4 Chapter conclusion

The role of surfactant on PVC suspension has been first investigated. It impacts the suspension viscosity at low shear rate. In particular, the low-shear viscosity may be significantly increased. Besides, we do not measure any effect in postponing the shear-thickening transition. For our system, plasticizer was chosen to have a great affinity with PVC. Thus, interparticles attractive interactions are low. Adding surfactant perturbs the dispersion state. Moreover, in our system, the repulsive forces overcome during shear-thickening originates from small layer of solvated PVC at particle surface. Adding surfactant

cannot expand this layer, condition for a postponed shear thickening. Water content is quite complex and depends both on surfactant and the way water is dispersed in the system.

Before studying filled formulation (PVC-Filler-Plasticizer), we investigated the rheology of filler dispersed in plasticizer. A high viscosity is measured at low shear rate with a shear-thinning behaviour. Indeed, contrary to PVC, filler has a hydrophilic surface. So, there is a bad compatibility with hydrophobic plasticizer, resulting in filler-filler attractive interactions (=high low-shear viscosity). At high shear rate, those interactions are broken and a Newtonian behaviour is observed. Compatibility between the filler and the plasticizer can be enhanced by using a surfactant. Better compacity is achieved enabling a significant viscosity reduction. Adding water creates capillary bridges.

Dispersing together PVC and filler in the suspension changes greatly the maximum packing fraction. The latter is experimentally measured for different formulation with a plasticizer absorption test. ϕ_{max} could be higher than single powders alone when filler particle size is bigger than PVC one. The greater the difference, the highest ϕ_{max} achievable. All results are rationalized using the De Larrard model initially developed for granular packings in cement industry. Using insight from binary mixes, the model is able to predict ϕ_{max} for more complex formulations.

We then turn to the rheology of these filled formulations when a part of PVC powder is relaxed by filler particles. For moderate filler/PVC ratio, the shear thickening intensity is diminished and increase low shear viscosity. At high filler/PVC ratio, the viscosity profiles is only shear thinning similar for pure filler suspensions (rheological behaviour is thus filler-dominated). In particular, we notice that the shear thickening intensity is set by the PVC relative concentration $\frac{\phi_{PVC}}{\phi_{PVC}+\phi_{liq.}}$. Viscosity of filled paste can be rescaled onto the suspension without filler thanks to two shift factors. This scaling implies that the filler is considered as non-interacting. Except at low shear rate for PVC 1, the hypothesis appears to be valid. We have developed simple models that match quite well experimental data for both of them, allowing a prediction of the viscosity. This approach holds for moderate filler/PVC ratio. For high filler/PVC ratio when viscosity is dominated by filler-filler interactions, the latter are accounted and this second model which well predicts viscosity for such a filler content.

Finally, the role of surfactant on filler surface is also investigated. We show that filler covering with a surfactant decreases the viscosity only for high filler/PVC ratio where rheology is dominated by filler-filler interactions. This is reminiscent of the gain in maximum packing fraction achieved with surfactant on suspensions of pure filler. The filler relative content at which adding the surfactant results in a viscosity drop depends greatly on the filler particle size: lower for smaller filler particle size and vice versa. Except in this zone of high filler content, the viscosity will be mainly controlled by the maximum packing fraction. Increasing the latter could achieve significant viscosity reduction.

4.5 Summary

— PVC suspensions are well stabilized by DINCH. Adding surfactant may destabilize the suspension (high low shear viscosity).
— Impact of water on the rheology is complex and depends both on the surfactant present and water repartition in the system.
— Filler in DINCH: no shear thickening. Interparticles attractive forces (visible at low shear rate).
— Surfactant improves the filler affinity for plasticizer (i.e increases ϕ_{max} of filler). Different surfactant can be used.
— Maximum packing fraction is highly dependant on formulation and filler size. Highest ϕ_{max} are obtained with filler as big as possible. It is the main leverage for controlling the viscosity of a plastisol.
— De Larrard model developed initially for modelling packing in concrete pastes can be used for compacity predictions in plastisol.
— Surfactant on filler surface diminishes viscosity of filled suspensions only for high filler/PVC ratio. This effect is reminiscent of the compatibilization of the filler.

Chapter 5

Flow instabilities during the coating process

Using the new insights in the flow behaviour of concentrated suspensions from previous chapters, we investigate in this chapter the high-speed coating of plastisols. Coating of suspensions are quite widespread in the industry with different processes: roll over roll, knife over roll, slot die... We focus here on the knife-over-roll coating where the goal is to obtain an homogeneous coating as fast as possible. However, in some cases, some coating defects appear. We focus here on one defect encountered at Tarkett in some cases and investigate its root cause.

5.1 Industrial relevance

5.1.1 Defect presentation

We focus on one defect appearing while coating a plastisol at high speed on a substrate. The industrial coating process used here is knife-over-roll process (cf. Fig. 5.1a). Plastisol to be coated is pumped through pipes and is poured just behind knife. Knife angle and position (typical coating gap between 0.2 and 1 mm) are adjusted. It can have different shapes (cf. Fig. 5.1b). Substrate speed ranges typically from 5 to 20 m/min.

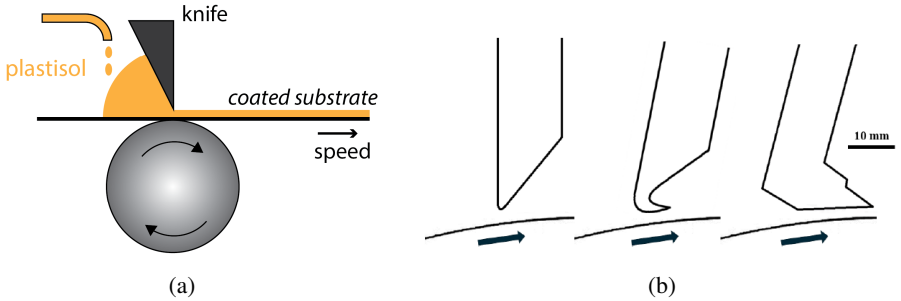

Figure 5.1: (a) Schematic view of knife-over-roll process. Substrate to be coated goes at a speed V. Coating gap is adjusted with knife position. Input flow of plastisol comes directly behind knife. (b) Different geometries of coating knifes used in the industry [256].

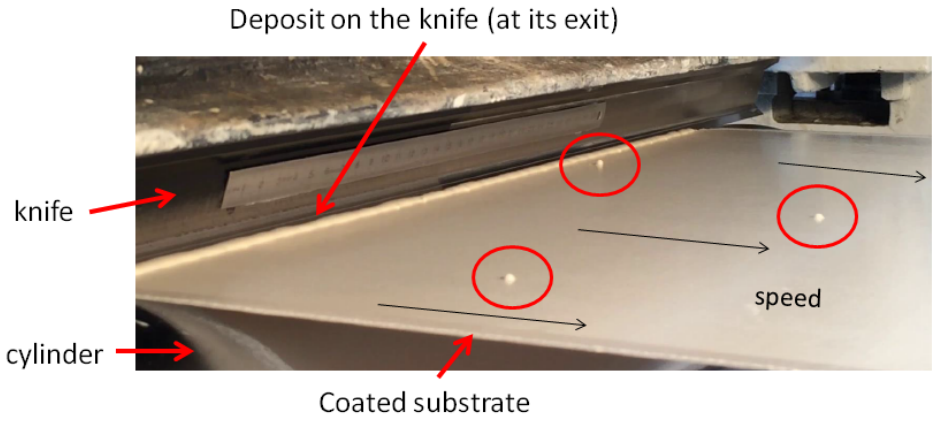

Figure 5.2: View of coating process at knife exit. Small droplets appears on flat coating (red circles). They are randomly distributed downstream from the coating knife. After oven step, these droplets become solid and are still present on the flat flooring product which is unacceptable for quality standards [256].

Under certain operational conditions, downstream from the coating step, small droplets are encountered (cf. Fig. 5.2) onto the flat coated surface. Depending on the following process steps, these droplets still exist onto the final product after gelation in an oven. These defects (solid droplets) are obviously unacceptable for the quality of a flat and regular floor product.

5.1.2 State of the art

Defects encountered in concentrated suspensions coating are quite various due to their complex rheology [257]. In most of the cases reported, particles are dispersed in a polymeric phase. For example, extrusion through a cylindrical die leads sometimes to self filtration with particles intermittent jamming [258]. Haw [259] pointed out arch-like patterns of particles at the capillary entrance, explaining intermittent jamming. There is however very few studies reporting flow coating instability with shear thickening fluids. One study [260] reports some defects in a different process (slot die coating) but they are different from us. There is however one recent PhD thesis which focuses on this defect encountered when coating a plastisol with knife over roll coating [256].

Indeed, in her PhD thesis [256], Y. Abdesselam studied this coating defect on a pilot line at Tarkett R& I center (coating width = 50 cm). Coating is performed, like for the industrial process, on a glass veil substrate. Thus, experiments are limited in time (substrate length). Droplets encountered on coated substrate are released from a deposit on the knife (at its exit). In particular, defects occurrence can be split into two phases: a first step includes a deposit creation at knife exit and its growth. A second step occurs when the deposit reaches a critical size: droplets are released. In this phase, the deposit has a steady-state size as droplet release and deposit growth are balanced. The whole kinetics of defects is displayed on Fig. 5.3. Snapshots are taken downstream from the knife. At the beginning, the knife is clean. During coating, a white deposit of plastisol begins to form on the knife (downstream) at different spots. During its growth, all these spots merge together and a quite homogeneous deposit is obtained (white irregular strip at knife exit). At a critical size, droplets are released from time to time from the deposit onto the coated substrate. The two phases (deposit formation and droplet release) are illustrated on Fig. 5.4.

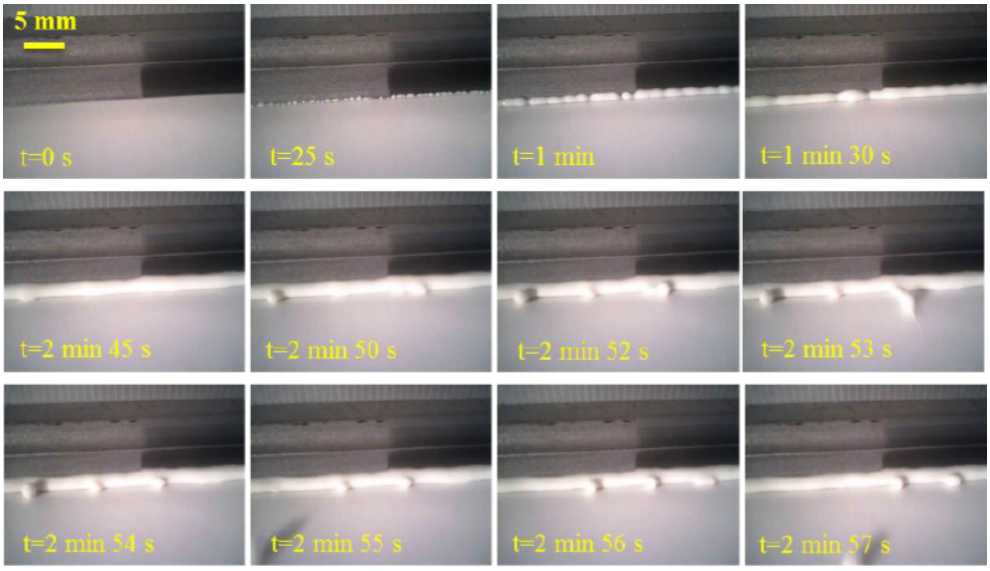

Figure 5.3: Pictures showing the kinetic of defect formation: clean knife (t=0 s); deposit starting from some spots (25 s) which progressively merge (1' < t < 2'45) while deposit is growing; finally droplets are released from the latter on substrate (t > 2'50) [256].

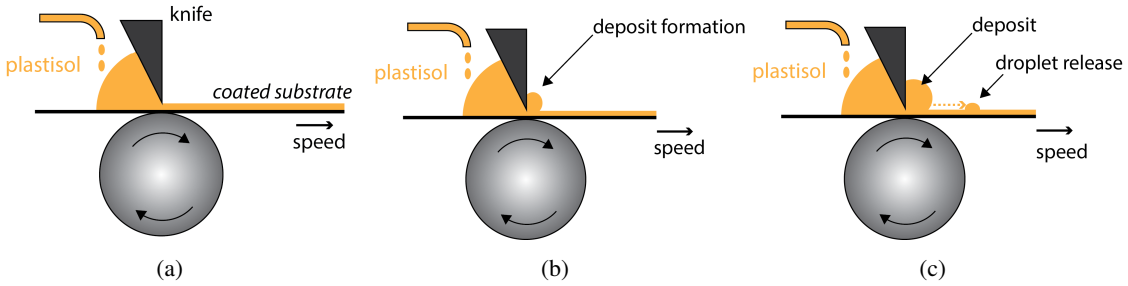

Figure 5.4: Scheme showing the defect formation (a) no defect; (b) deposit formation at knife output; deposit is growing (c) deposit reaches a critical size and droplets (coming from the deposit) are released on the coated substrate.

Keys parameters were studied by Y.Abdesselam. Defects are observed for both unfilled formulations (PVC-plasticizer) and filled formulations (Filler-PVC-plasticizer) and also on industrial formulations as well as for simplified formulations. They report that more droplets are observed if substrate speed is increased or coating gap is decreased. Thus, importance of coating shear rate is underlined. Besides, rate of droplets release is found to be nearly proportional to shear rate. In fact, as described in the chapter "flow modelisation", local shear rate is not constant under knife with complex geometries (cf. Fig. 5.1b) and maximum shear rate can be higher than mean shear rate (substrate speed over gap).

Several parameters have been discussed:

— **Solid loading** ϕ: Droplets appear faster (at fixed shear rate) with increasing solid fraction. Rate of droplet release is higher also.

— **Filler**: Defects are observed from a lower shear rate for filled plastisols (range of shear rate encountered in industrial process) than unfilled plastisol (critical shear rate higher than ones encountered in industrial process). Besides, rate of droplet release is higher also for filled formulations. Impact of filler size is not clear.

— **Position of knife** compared to center of cylinder (knife aligned with cylinder center or not) has no impact.
— **Dependence of angle** was explained by the shear rate variation when turning knife.
— **Nature of substrate** (glass veil or silicone paper) has no visible effect

Y.Abdesselam managed to analyse the composition of one deposit (case of filled formulation). Deposit was found to be less concentrated than mother suspension (57 instead of 64 %). However, it does not change anything on concentration of coated suspension as deposit flow rate is far lower than coated plastisol flow rate (typically 1000 times lower). Besides, this analysis was done only for filled suspension (with big filler particles). Furthermore, the deposit formation is not limited to knife over roll process. In her work, Y. Abdesselam [256] developed a capillary rheometer with a rectangular die. They found that a deposit (similar do die swell) is formed at shear rate similar to the ones needed for defect on knife over roll coating.

As a conclusion, key factors influencing defect formation have been pointed out but the root cause of the defect is still unknown. Moreover, no direct link between defects appearance and viscosity curve (neither level of viscosity nor "shape" of curve) can be established. For example, in some cases, a formulation with a lower viscosity can lead to a higher number of defects. In order to better investigate the root cause of this defect, we decide to build a lab-scale coating machine.

5.2 Lab-scale coating machine

5.2.1 Presentation

Pilot trials have a number of drawbacks: limited time of coating (finite size of the substrate coil), several people needed to run a test, $\sim$ 5-10 kilos of plastisol are needed for one test... In order to circumvent these drawbacks, we designed and manufactured in the mechanical workshop of the laboratory a lab-scale coating machine (cf. Fig. 5.5). Coating is performed at a 50-mm scale on a cylinder (30 mm diameter). Rotation is accurately controlled by an electronic motor (precision of 1 rpm). Knife is for now limited to a simple straight blade (0.3 mm thickness). Its thickness is 1/100 of cylinder diameter, so we assume the cylinder to be locally flat under the knife. Knife angle can be adjusted with a goniometer but we keep it vertical in this study. Knife centring and coating thickness are adjusted by two micrometric translation stages. During this study, gap between 100 and 2000 μm will be investigated. A camera is placed in front of the prototype to image the knife exit and follow possible deposit formation and droplet release. In the following, all snapshots will be taken from this camera.

5.2.2 Qualitative behaviour

We first validate our approach by checking that defects are qualitatively well reproduced at the lab scale. 50 mL of D2 at 62 % are prepared and poured into the tank of the prototype. Some viscous paste is entrained with the cylinder when it rotates. This dragged paste comes to the knife and is coated. At the exit, a thin layer (thickness $\sim$ coating gap) lies on the cylinder.

At low speed, the knife stays clean and the coating goes well (see Fig. 5.6a). At moderate speed, a slight deposit appears on the knife (see Fig. 5.6b-c) as observed in the industrial process. At higher

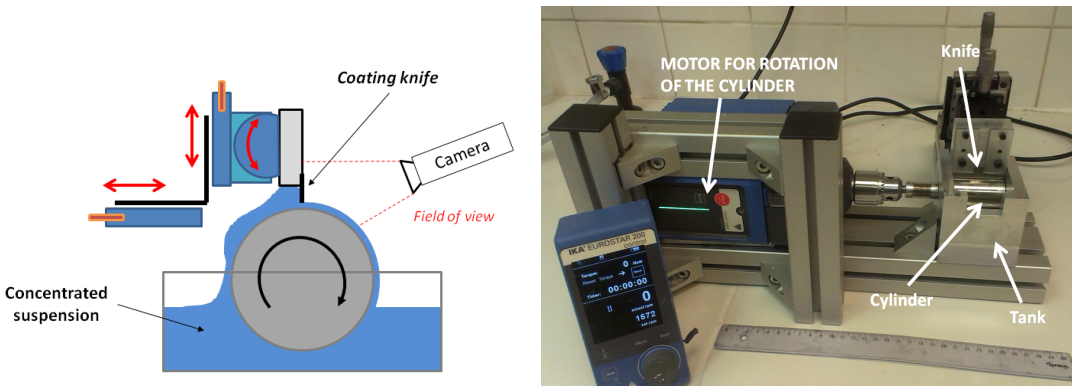

(a) (b)

Figure 5.5: (a) Schematic view of lab-scale prototype mimicking knife over roll coating process. (b) Picture of the lab-scale prototype. The ruler in the foreground is 30 cm long.

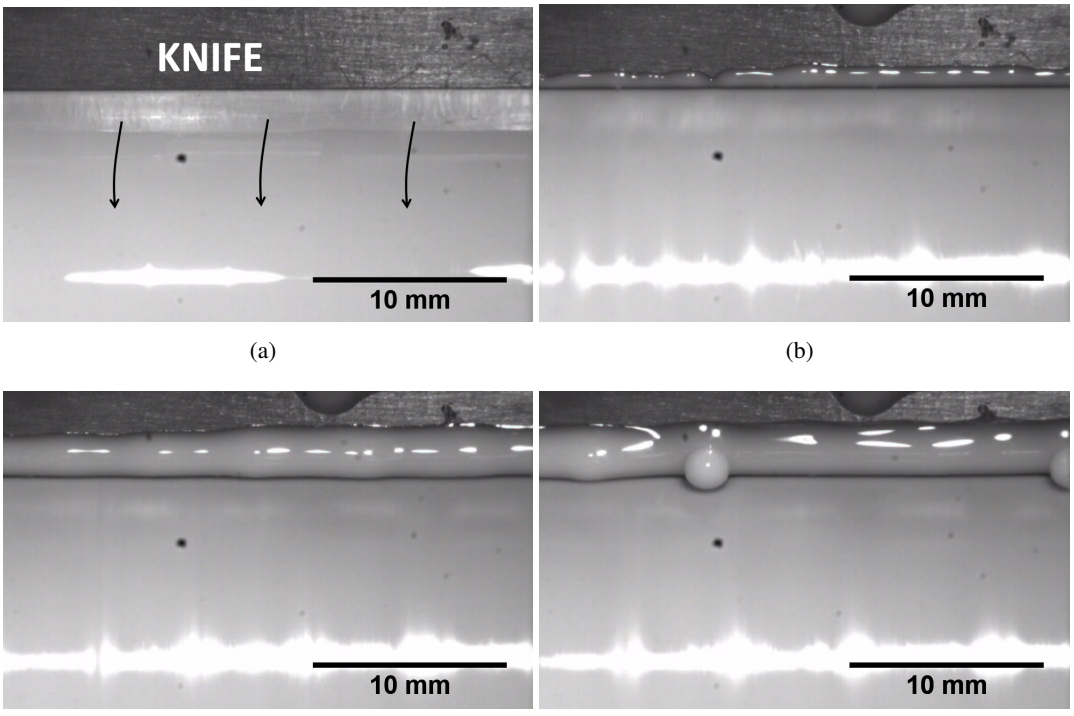

(a) (b)

(c) (d)

Figure 5.6: Pictures of a coating of D2 at $\phi = 62\%$ with increasing cylinder speed. Gap = 800 μm. Same defects as in industrial line are reproduced: (a) coating goes well at low speed; (b)(c) a deposit appears at knife exit at moderate speed; (d) droplet of suspensions are finally released downstream. All pictures presented in this chapter are taken from the front (looking at knife exit, cf Fig. 5.5). Thus, the upper grey part is the knife and the white part is the plastisol flowing in the observer's direction. The white line at the bottom is only light reflection.

coating speed, deposit is larger and begins to release droplets of suspensions (see Fig. 5.6d). Thus, our prototype displays the same phenomenology of defects as encountered in the industrial coating.

Concerning our lab-scale prototype, the coating runs in a closed loop. It is nearly the same layer of suspension which is sheared at each rotation. Thus, temperature on the cylinder is carefully controlled to avoid any heating (viscous dissipation). In the following, we focus on the deposit appearance,

especially its root cause as droplets are only a consequence of deposit formation. All experiments were done in a air conditioned room (T = 23 ˚C). Due to viscous dissipation, temperature on the cylinder was often at around 24-27 ˚C. All data are rescaled to T = 25 ˚C knowing the temperature dependence of DINCH viscosity (cf. part 2.1.3).

5.3 Ribbing induced by normal stress differences

We focus here on the first formulation investigated: D2 at ϕ = 62%. We study the coating progressively starting from the rest position and then increasing the speed (i.e. the shear rate). Contrary to work of Abdesselam et. al. [256], the speed can be infinitely varied and many different coating speeds can be chosen during one experiment (from 0 to 2000 rpm).

5.3.1 Description

All pictures presented in this chapter are taken when facing the knife exit (cf. field of view on Fig. 5.5). Thus, the upper grey part is the knife and the lower part is the plastisol flowing in the observer's direction. At very low shear rate, the coating is homogeneous with no visible pattern or defects (cf. Fig. 5.7a). At a critical speed, some tiny lines appear at the surface of coated plastisol (cf. Fig. 5.7b). They are oriented parallel to the flow direction (perpendicular to knife). Moreover, the maxima of these lines do not spatially evolve during the experiments: they are like pinned.

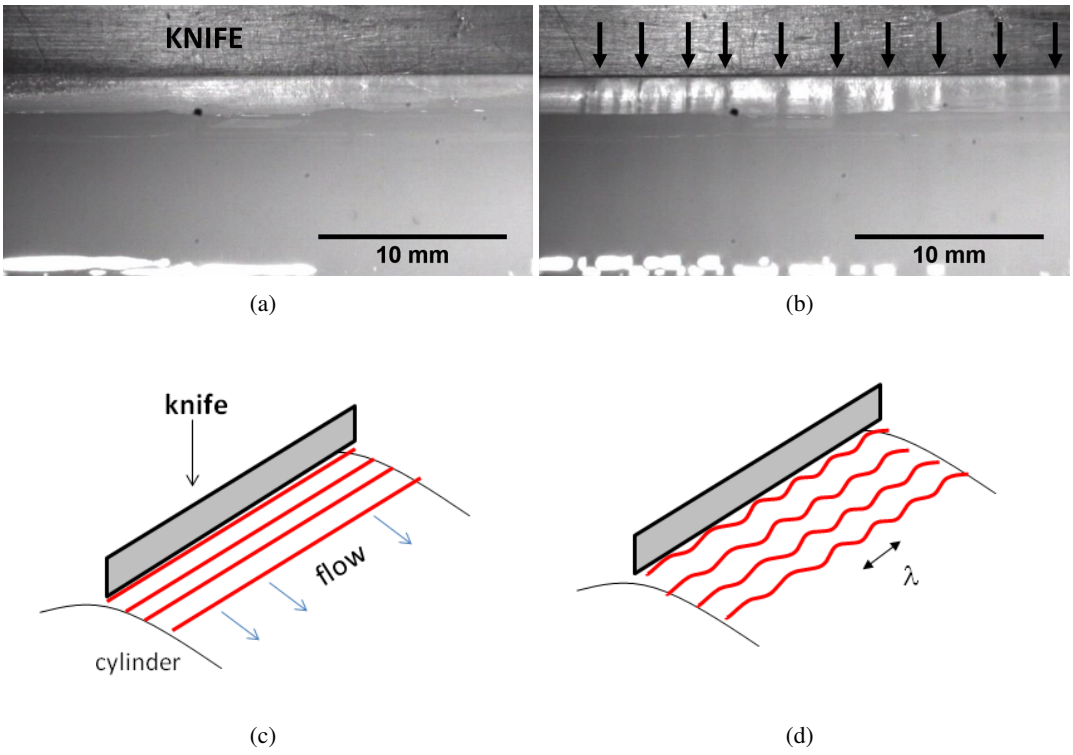

Figure 5.7: Picture of a coating of D2 62% at a gap of 500μm. Cylinder speed is (a) 10 rpm ($\dot{\gamma} = 31\ s^{-1}$) (b) 40 rpm ($\dot{\gamma} = 126\ s^{-1}$). Picture are taken 10 s after experiment start. Arrows represent the maxima of the surface oscillation. (c) Scheme of picture (a); (d) Scheme of picture (b).

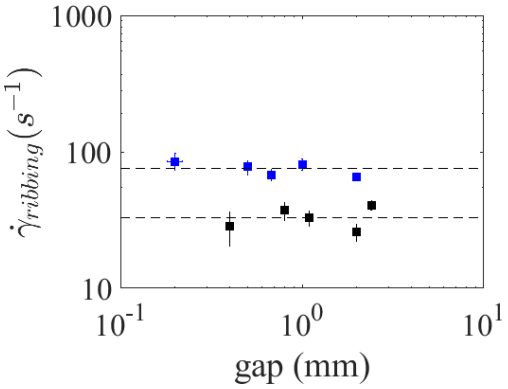

Figure 5.8: (a) Critical shear rate $\dot{\gamma}_{ribbing}$ for ribbing appearance versus gap for D2 62%. Measurements are done either after 20 s of rotation (■) or 2 min of rotation (■). Dotted line stands for respectively 75 s^{-1} and 33 s^{-1}.

The critical speed for the instability appearance is followed for different gaps (cf. Fig. 5.8). The resulting critical shear rate $\dot{\gamma}_{ribbing}$ (calculated as the critical velocity divided by the gap) obtained depends on the waiting time. The higher waiting time, the lower critical shear rate $\dot{\gamma}_{ribbing}$. Indeed, it could take 2 min for the instability to take place and be visible. For practical reasons, 2 min of applied speed was the maximum waiting time. The critical shear rate for this instability $\dot{\gamma}_{ribbing}$ is the same for all gaps, showing that the instability onset is characterized by a single shear rate. It is worthy noting that close to or just above $\dot{\gamma}_{ribbing}$, only the instability is observed; no deposit is formed even if the coating is done over a long time.

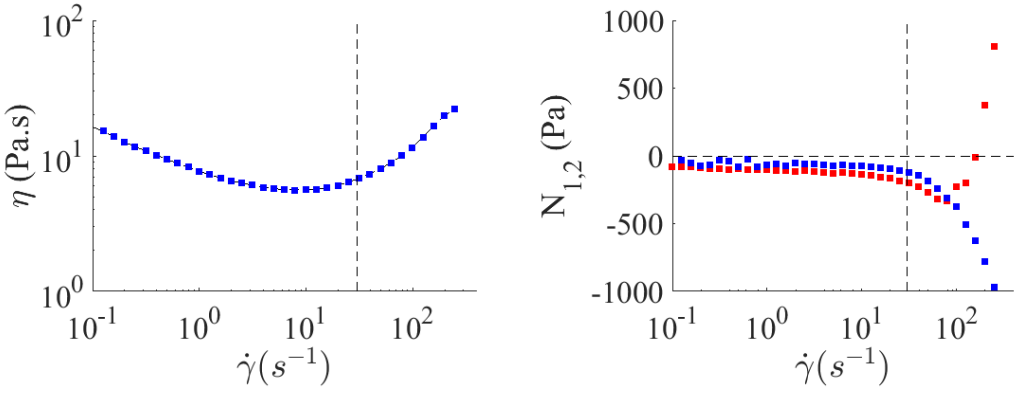

Figure 5.9: Dotted line: critical shear rate $\dot{\gamma}_{ribbing}$ of D2 62% plotted on flow curve: (a) viscosity and (b) first and second normal stresses difference: N_1 (■) and N_2 (■).

We correlate this critical shear rate with the viscosity and normal stress difference (N_1 and N_2) measured previously (cf. Fig. 5.9). The instabilities seem to appear when shear thickening starts. More precisely, the instability arises when N_1 and N_2 begin to be non-zero and negative. We assume that the instability is caused by normal forces differences. Besides, we do not observe any instability with a Newtonian oil of similar viscosity (η = 12 Pa.s). By the way, the instability phenomenon occurs also

when coating is performed only on a partial width of the roll so as to remove possible influence of side walls (industrial coating is performed on a flat sheets with no wall boundaries).

In the literature, a ribbing instability is often encountered in coating processes more precisely in roll coatings where it happen even for Newtonian fluids. It is also called printer's instability and is similar to the phenomenon of viscous fingering (Saffman-Taylor) [261]. In that case (roll coating), the instability sets up because of an interaction between the pressure distribution just before the knife exit and an interfacial pressure controlled by surface tension just at the exit. The threshold is thus hydrodynamically described with a critical capillary number [262].

For knife coating, the reports are scarce [261]. Knife coating is less sensitive to defect (not happening for Newtonian rheology) but is dependant on knife geometry (length, angle...) [261]. For all geometries, instabilities are experimentally enhanced when the fluid has viscoelastic properties [263, 264]. Here, we have to take account of visco-elasticity (via normal stress difference). We will see that the instability onset is determined by the appearance of normal stress, and thus we think that we are very far from the pure hydrodynamic instability. We keep the term ribbing for the instability but this does not mean that this instability is related to Saffman-Taylor instability.

5.3.2 Comparison with a dilute polymer solution

All previously cited studies were carried out using polymeric samples when considering viscoelasticity, i.e. N_1 and $N_2 > 0$ which is different from our case of plastisol. We test here the coating of a viscoelastic polymer solution in our setup. We test here the coating of a dilute polymer solution with viscoelastic properties. A solution of Poly(acrylamide-acrylic acid, sodium salt) (MW > 10^7, 40% carboxy, supplied by Polysciences, Inc) at 7000 ppm (0.7 %) in water is used. Such dilute polymer solution exhibit large normal stresses upon shearing (cf. Fig. 5.12).

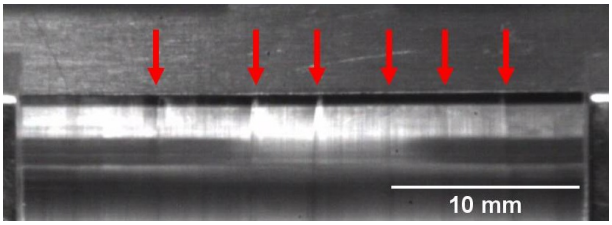

Figure 5.10: Picture of ribbing when coating a viscoelastic dilute polymer solution (7000 ppm) at a gap of $800\mu m$ (200 rpm). Arrows represent the maxima of the surface oscillation. On the contrary to plastisol, maxima spatially move over time (no pinning).

While coating the polymer, a ribbing phenomenon occurs (cf. Fig. 5.10 with red arrows). However, unlike for the ribbing lines of plastisol which were like pinned, the instability here is dynamic and lines are moving during coating. Moreover, even if the onset shear rate of normal stress difference is similar for our PVC particle concentrated suspension and the polymer solution, signs are different. For the polymer solution, both N_1 and N_2 are positive whereas for D2 62 %, N_2 is negative and N_1 slightly negative then highly positive. Moreover, even at very high shear rate (15 000 s^{-1}), no deposit is formed as for the industrial defect investigated in the plastisol.

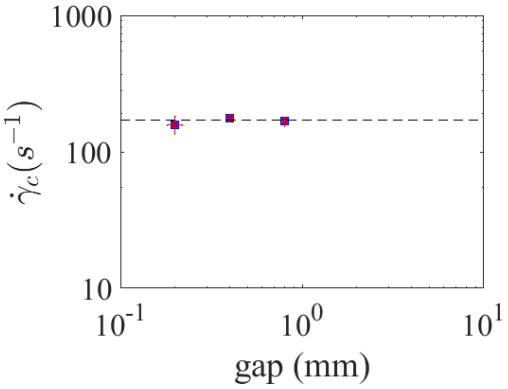

Figure 5.11: Critical shear rate for ribbing appearance ($\dot{\gamma}_{ribbing}$) versus gap for a viscoelastic dilute polymer solution (7000 ppm).

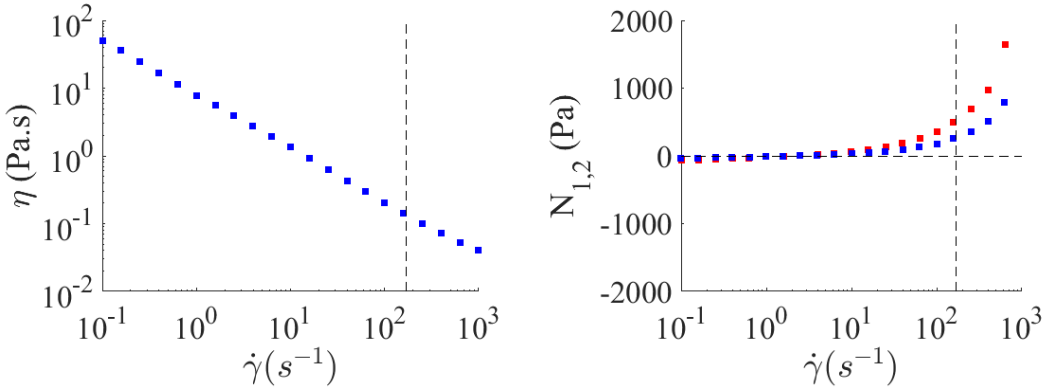

(a) (b)

Figure 5.12: (a) Flow curve and (b) normal stress differences : N_1 (■) and N_2 (■) for a viscoelastic dilute polymer solution (7000 ppm). Dotted line represents critical shear rate for ribbing appearance $\dot{\gamma}_{ribbing}$.

5.3.3 Wavelength of ribbing

We come back to coating of D2 at ϕ = 62 %. A wavelength λ can be defined for the instability by measuring the mean distance between two maxima. The wavelength λ depends on the gap (cf. Fig. 5.13). The smaller the gap, the smaller the wavelength. More precisely, the instability wavelength is proportional to the gap (cf. Fig. 5.14). A good fitting is obtained for $\lambda = 7.4 * h$ where h is the coating gap.

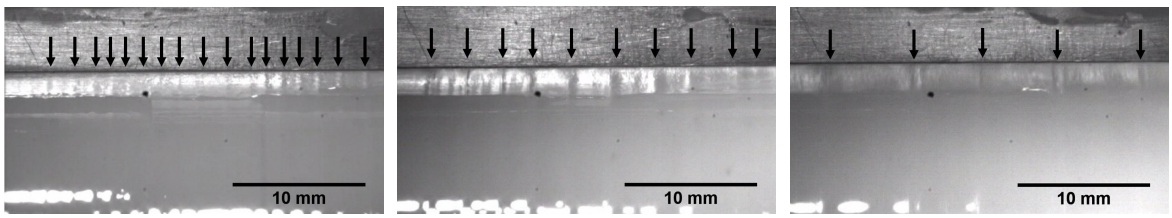

(a) (b) (c)

Figure 5.13: Pictures of ribbing induced by normal stress differences when coating D2 62% at a gap of (a) 200μm (b) 500μm and (c) 1000μm.

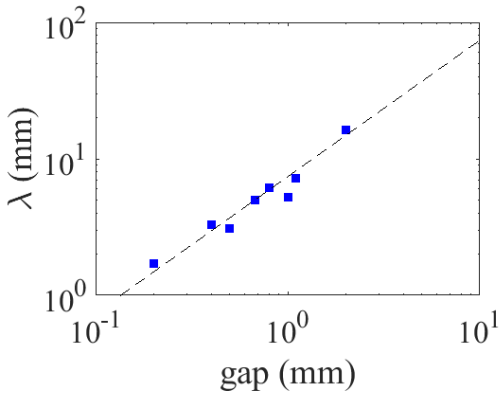

Figure 5.14: Ribbing wavelength λ function of gap for PVC 2 at 62%. Dotted line has a slope of 1.

5.3.4 Toward deposit formation

At shear rate higher than $\dot{\gamma}_{ribbing}$, secondary maxima appear sometimes (cf. Fig. 5.15 with blue arrows). They are less regular than the fundamental oscillation and do not exist very close to $\dot{\gamma}_{ribbing}$. We suggest than increasing normal stress differences further enhance surface destabilization.

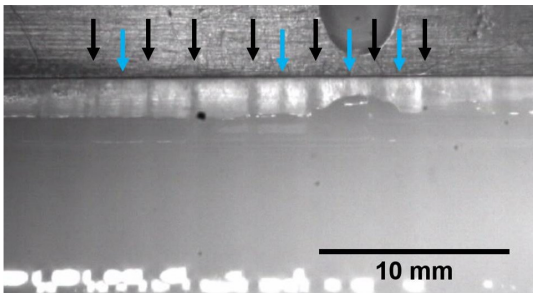

Figure 5.15: Picture of the coating of D2 62% at a shear rate above $\dot{\gamma}_{ribbing}$. Local maxima (blue arrows) are visible between main maxima (black arrows) on the surface.

Ribbing is an intermediate state as we know that high speed coating will generate the deposit and eventually droplet release. Thus, we now focus on the transition from the surface instability to the deposit observed industrially. We start by increasing continuously the speed (increasing shear rate starting from $\dot{\gamma}_{ribbing}$). The following phenomenology is observed (cf. Fig. 5.16) :

— ribbing phenomena with no deposit on the knife even over a long time (cf. Fig 5.16a)
— deposit appears at difference spots corresponding to the maxima of the surface oscillation (cf. Fig 5.16b)
— new spots of deposit appear in between previous spots, certainly related to oscillation of high harmonics highlighted previously (cf. Fig 5.16c)
— Deposit spot begin to merge during its growth : deposit is now nearly continuous. Original appearance points are not visible any more but the discrete nature of deposit growth is still present (cf. Fig 5.16d)
— Deposit is now continuous and continues to grow (cf. Fig 5.16e). This state is the usual one visible in industrial coatings when suspensions are directly highly sheared.

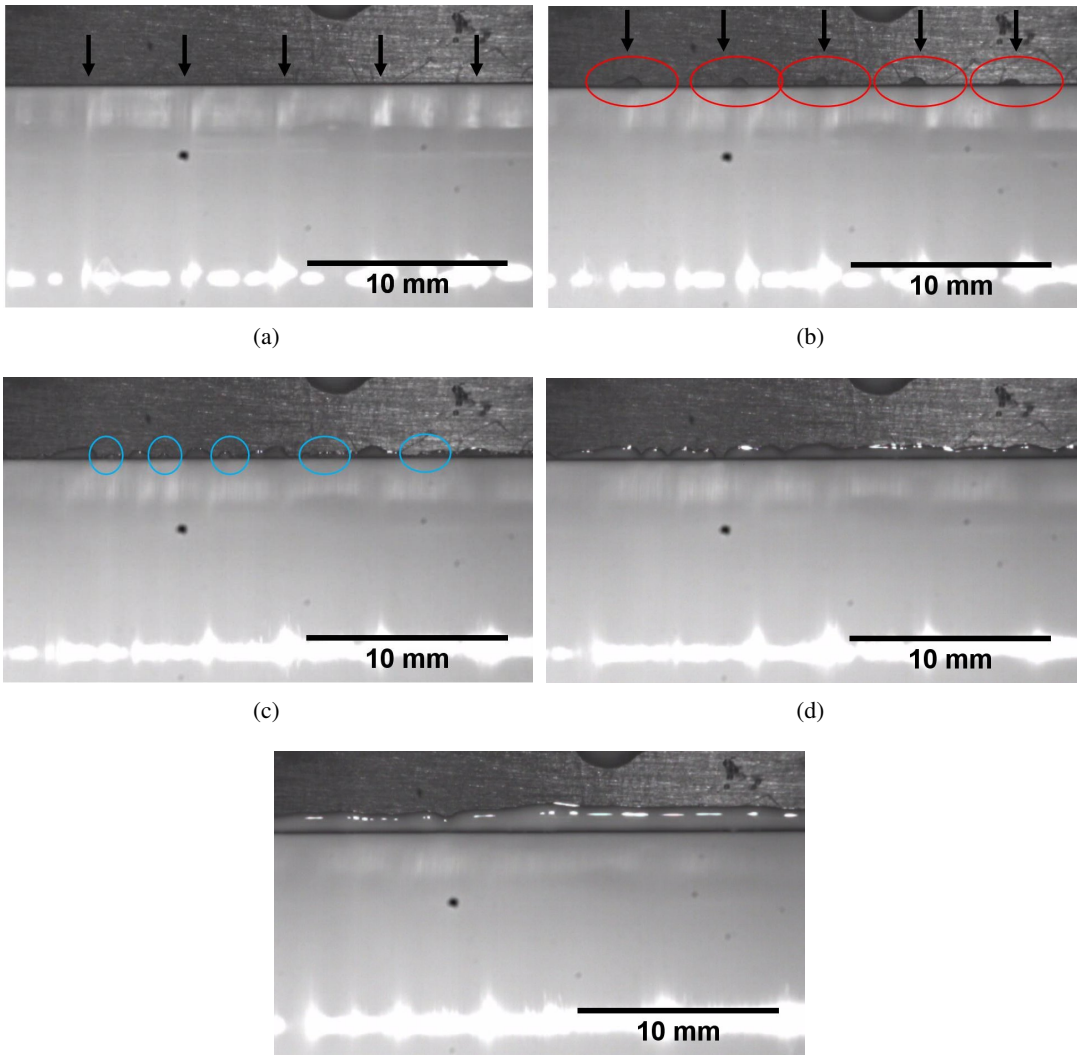

(a) (b) (c) (d) (e)

Figure 5.16: Pictures of the coating of D2 62% at a gap of 800μm while increasing shear rate from $\dot{\gamma}_{ribbing}$: (a) no defect (ribbing maxima are shown with arrows); (b) first spots of deposit on knife appear at the instability maxima (see red circles); (c) defects appears in between first spots (blue circles); (d)(e) all spots join together into a continuous deposit.

Thus, we observed that the deposit stems from the surface instability (ribbing) at moderate shear rate. In particular, occurrence of ribbing can be split into two phases: the first where only ribbing is present and the second where ribbing is present but a deposit starts also to form at different spots on the knife. We focus now on the transition at which a deposit begins to form on the knife.

5.4 Deposit formation

We now investigate the critical speed at which deposit begin to form on the knife. We still focus on D2 62 %.

5.4.1 Influence of coating speed

We first plot the time of first droplet release (droplet time) versus the coating speed for different gaps (see Fig. 5.17). The time when first droplet is released diverges at a critical speed determined by fitting data with a inverse function $\frac{a}{v-v_c}$ with a is a proportional factor and v_c is the critical rotation speed. Resulting critical velocities are plotted versus gap on Fig. 5.18 (black points). As we showed previously that viscosity depends on the gap size (cf. part 3.6.2), all critical velocities are rescaled for the case of infinite gap size (where suspension has a viscosity of η(infinite gap)) by multiplying the critical velocity by the factor $\frac{\eta(\text{considered gap})}{\eta(\text{infinite gap})}$ (assuming a linear rescaling of the critical velocity with the viscosity ratio). We use the measurements obtained for D2 60% (no data for D2 62 %, cf. part 3.6.2).

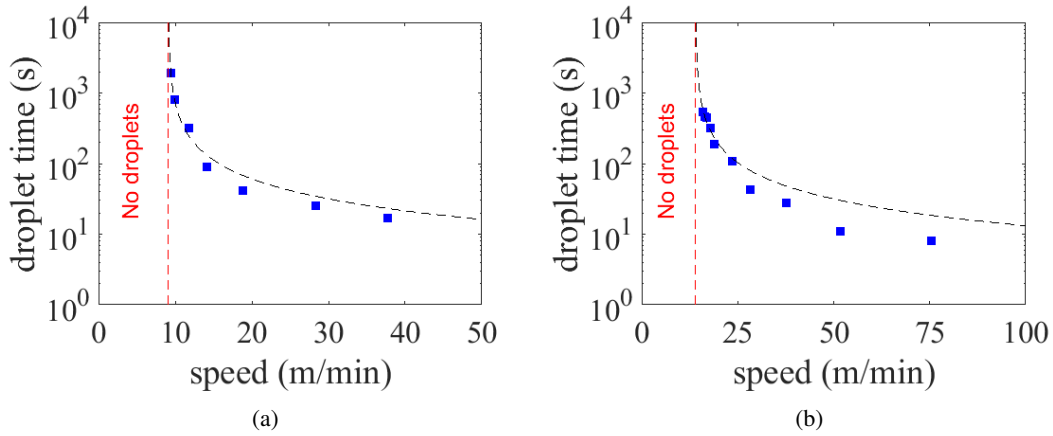

Figure 5.17: Typical curves for time of first droplet release (droplet time) versus the coating speed v of D2 at 62%. Examples: (a) gap = 250 μm; (b) gap = 820 μm. Dotted line is a fit using inverse function $\frac{a}{v-v_c}$ with a a proportional factor and v_c the critical speed . Critical speeds v_c are respectively 9.1 and 14.0 m/min for (a) and (b) (red dotted lines).

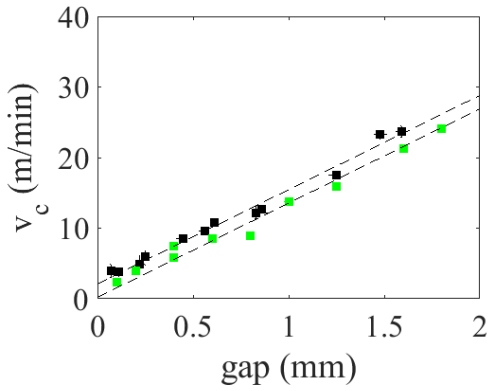

Figure 5.18: Critical velocity for defect appearance v_c versus gap. Measurements are done either following time needed for first droplet release (■) or by tracking first deposit appearance on knife (■). As viscosity depends on gap, critical velocities are rescaled for an infinite gap.

In addition, we also determine a critical coating speed by looking at the knife with a camera equipped with a macro- objective. The critical speed correspond here to the velocity at which deposit begins to form on knife (first spot of around 100 μm on the knife). Critical speeds found using this

method are also plotted versus gap on Fig. 5.18 (green points). Both methods results in the same trend: a quasi linear increasing trend. Using the method with appearance of macroscopic droplets, an offset of speed is found compared to the other method, meaning that this method reaches critical speed always a little bit higher than following microscopic appearance of droplets

5.4.2 Critical shear rate $\dot{\gamma}_c$

Instead of plotting critical velocity, we plot now critical shear rate $\dot{\gamma}_c$ defined as the ratio between critical velocity v_c (rescaled for infinite gap) and the gap. Results are on Fig. 5.19. In fact, critical speed do not vary exactly linearly with the gap. Instead of this, a range from 180 to 380 s^{-1} is found for critical shear rate $\dot{\gamma}_c$ at which deposit appears (red zone).

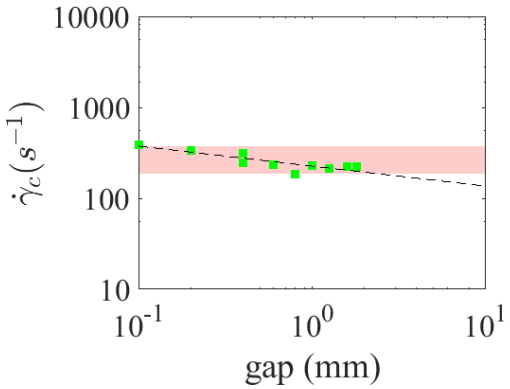

Figure 5.19: Critical shear rate $\dot{\gamma}_c$ versus coating gap for D2 62 %. Red zone represents the range of shear rate for defect appearance.

5.4.3 Other formulations

In addition to D2 62 %, we screen several other formulations: D1 55%; D1 60 %; the reference filled formulation PVC 2 33%, Filler M 30% and also a formulation of pure filler dispersed in DINCH : filler M at 54 % (with decanoic acid as compatibilizer). For D1 (55 % and 60 %), speeds are rescaled for infinite gap using experimental data for D1 60 % (cf. part 3.6.2). For PVC 2 33%, Filler M 30 %, speeds are rescaled for infinite gap using experimental data for D2 62 %.

For all formulations, a single critical shear rate is not found (cf. Fig. 5.20). It is worthy to note that slip at the wall could appear for filler M at 54 % as it was observed in rheological experiments for $\phi_{filler} > \sim 45\%$. For other formulations no wall slip occurs. Again, the waiting time has an impact (minor). Waiting for a longer time enable to find slightly lower critical shear rate.

5.4.4 Correlation with rheological properties of the suspension

We correlate the range of critical shear rates found in previous experiments with their related rheology especially the normal stress differences N_1 and N_2 (cf. Fig. 5.21). There is no clear correlation between the appearance of the deposit and the viscosity. However, there is a clear correlation between the shear rate at which N_1 rise (>0) and the defect occurrence for the three formulations where we have data for both N_1 and N_2 and also for D1 60 % where we have only N_1 (cf. Fig. 5.22)

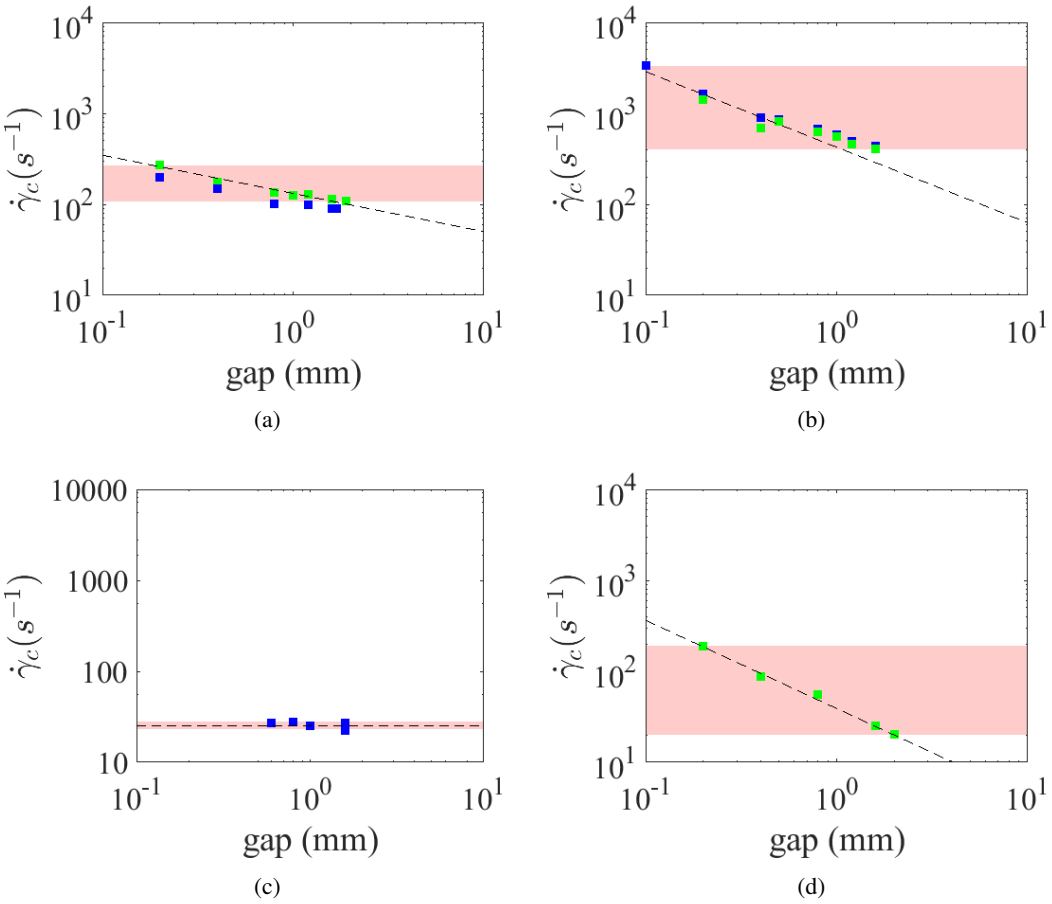

Figure 5.20: Critical shear rate versus coating gap for different formulations: (a) PVC 2 (33%) + Filler M (30%) (b) D1 55% (c) D1 60% (d) Filler M 54% (with decanoic acid as compatibilizer). Measurements are done either by waiting 2 min (■) or 5 minutes (■) at a fixed gap and speed before looking for first deposit appearance on knife. Red zone represents the range of shear rate for defect appearance.

As a remark, for filler 54 %, only measurements from cross-hatched plate/plate were performed. So we access only $N_1 - N_2$. Measurements were not correct with usual cone/plate due to the large size of filler particles compared to the truncature gap (normally a size ratio of 10 is needed to ensure good experiments). It could have been possible using the procedure of Marsh and Pearson [121] that employs a finite gap D (higher than usual truncature gap) between the cone tip and the plate to obtain a second relation between the two normal stress differences (as a function of gap spacing C). For the filled suspension PVC 2 33 % + Filler M 30 %, no difficulty was encountered while using a cone and plate certainly due to the limited number of big particles.

Even if only $N_1 - N_2$ is measured, the defect occurrence well corresponds to normal stress increase for filler 54 % (cf. Fig. 5.22). More generally, this sample shows that deposit and droplets can appear even if the sample is not shear thickening. The rise in normal stress difference, especially N_1 is rather the key parameter to observe the defect as shear thickening is not an essential prerequisite.

Unveiling the link between the defect and a positive rise in N_1 allows us to rationalize some of the trends observed by Abdesselam et. al. [256]. For example, they observed defects at lower shear rate for suspensions are more concentrated. Indeed, as seen in part 3.1.3 and in the literature [121, 54],

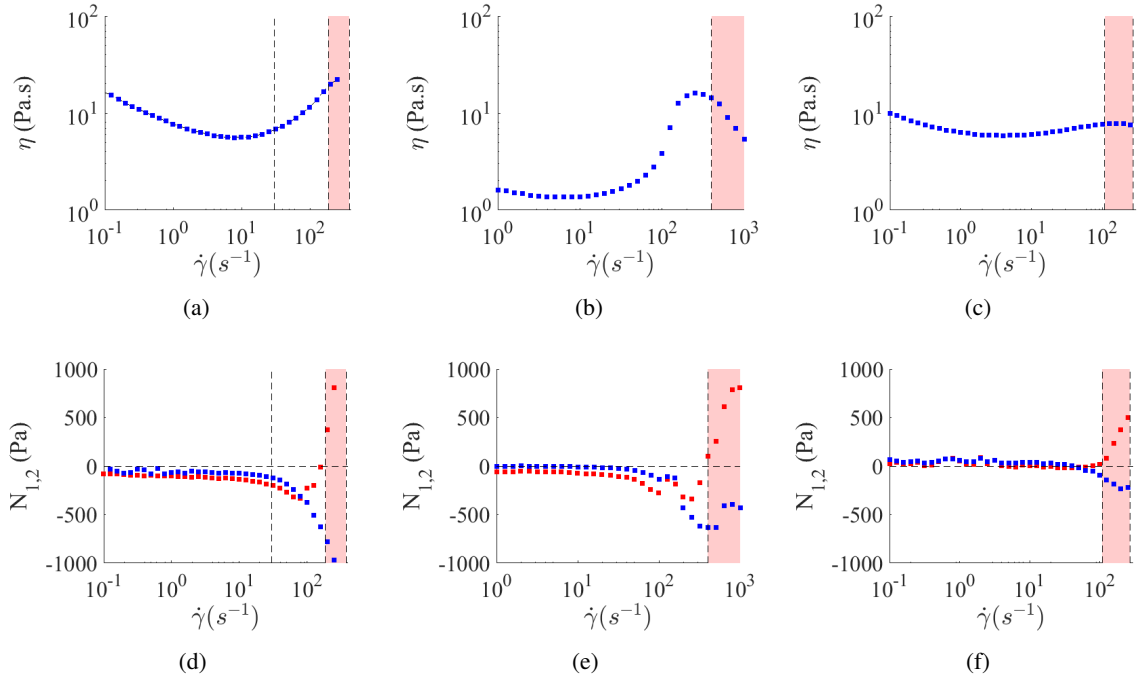

Figure 5.21: Pale red zone: range of shear rate for defect appearance from fig 5.20: (a)(d) D2 62%. First dotted line was the ribbing onset previously underlined (30 s^{-1}; (b)(e) D1 (55%); (c)(f) PVC 2 (33%) + Filler M (30%). For normal stresses difference measurements, both N_1 (■) and N_2 (■) are measured.

increasing the volume fraction of particles shifts the onset of N_1 to lower rate, thus indicating that defect would occur at a lower shear rate. Abdesselam et. al. also reported defects at lower shear rate for filled plastisols than unfilled plastisols. We do observe the same trend. Again, from insights of chapter 4, adding filler shifts the shear thickening transition to lower shear rates, thus defects should also be observed at lower shear rate when substituting part of PVC particles by $CaCO_3$ particles.

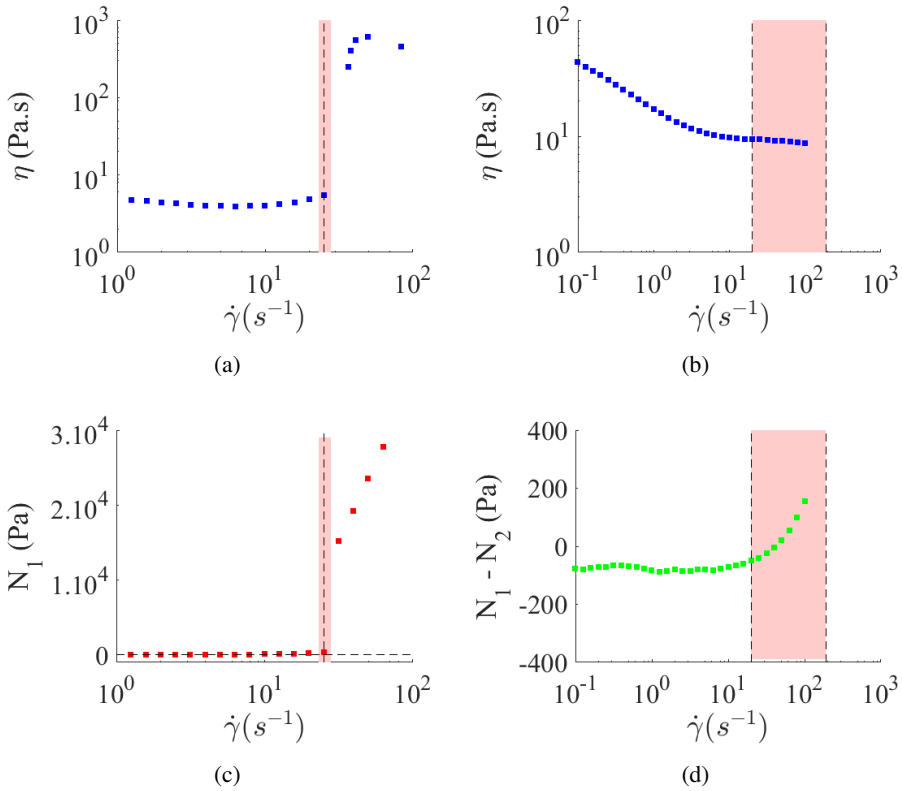

Figure 5.22: Critical shear rate range from fig 5.20 plotted on their respective flow curves and normal stresses difference measurements: (a)(c) D1 60%; (b)(d) Filler M 54%; . Pale red zone represents the range of shear rate for defect appearance. For (c) N_1 is plotted (■). For (d) $N_1 - N_2$ is plotted (■).

5.5 Suggested mechanism

Based on experiments shown above, a mechanism for defect formation can be suggested (cf. Fig. 5.23). At low shear rate where the suspension exhibits no normal stress difference, the coating is homogeneous. At a critical shear rate $\dot{\gamma}_{ribbing}$ linked with normal stress difference appearance (N_1 slightly negative, large N_2 negative), a surface instability develops with a oscillation on the surface (parallel to the flow direction). This is very similar to a ribbing instability but rather triggered by normal stress difference. Following notation from 5.23, N_1 and N_2 are written:

$$N_1 = \sigma_{11} - \sigma_{22} \text{ and } N_2 = \sigma_{22} - \sigma_{33} \tag{5.1}$$

with σ_{11}, σ_{22} and σ_{33} the normal stresses (shear stress = σ_{12}) where 1, 2 and 3 refer to the direction of velocity, velocity gradient and vorticity respectively (cf. Fig. 5.23). Normal stress difference are important as they can induce secondary flows, in particular orthogonal to the main flow direction. In particular, N_2 negative means a high $\sigma_{33} - \sigma_{22}$. Thus, vorticity lines (in direction 3) are expected to dilate in the 2-3 plane, resulting in the observed surface oscillation (ribbing). As we saw previously, ridges do not move over time. However, we do not have any explanation yet for this pinning in the surface instability.

At $\dot{\gamma} > \dot{\gamma}_c$, N_1 turns positive which is linked with a dilation of the suspension. Thus, the surface instability at the knife exit is "pushed" upwards in a phenomenon similar to the famous die swelling.

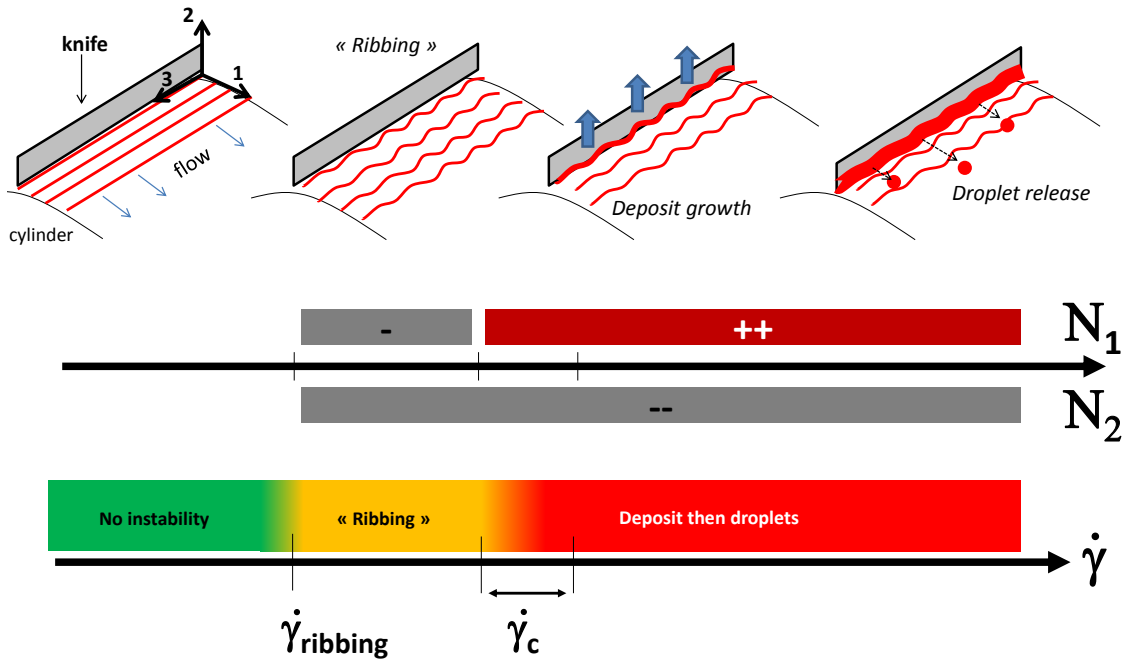

Figure 5.23: Suggested mechanism for defect formation: (i) Low shear rate ($< \dot{\gamma}_{ribbing}$) : homogeneous flow; (ii) $\dot{\gamma}_{ribbing} < \dot{\gamma} < \dot{\gamma}_c$: ribbing surface instability with normal stress appearance; (iii) $\dot{\gamma} > \dot{\gamma}_c$: deposit when N_1 goes to positive values (dilation) then droplets release.

The oscillating plastisol surface begins to wet the knife at the exact position of the maxima. Birth of the deposit occurs thus in a discrete way (spots). For higher speed, deposit will emerge in multiple points as evidenced by some harmonics observed in the instability. Once the knife is wetted in some points, it becomes easier for future dilated plastisol to further wet the knife and make deposit growing.

It is interesting to note that a small gap in a coating step will exacerbate defect formation for two reasons:

— For a constant speed, shear rate will be higher, thus normal stress difference too.

— A small gap implies a lower wavelength, i.e maxima of the oscillation will be closer generating a higher density of nucleation points (spots on the knife) of the deposit.

5.6 Practical solutions for defects reduction or elimination

5.6.1 Changing coating knife position

One way to avoid consequences of droplet release on the final product is to avoid the release of droplet onto the downstream coated substrate. By modifying the knife position (cf. Fig. 5.24), the deposit can flow back into the batch. Thus no droplet are formed as deposit does not grow enough. This geometry can be slightly modified with two options: (i) either there is a "hole" between the knife and the support (black lines linking the green knife and the red holder on the scheme Fig. 5.24) so as to the deposit can flow back into the batch or (ii) there is no hole and deposit flowing down is trapped and thus would be easily retrieved for analysis. A top view of a typical experiment is shown on Fig. 5.25 (case with a solid piece of metal to trap the flowing deposit).

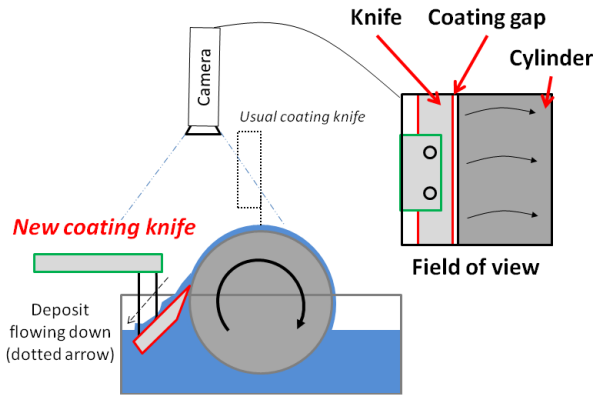

Figure 5.24: Schematic view of new positioned knife which replaces the usual coating deposit. Deposit flows down to the batch. Thus, droplets are not formed.

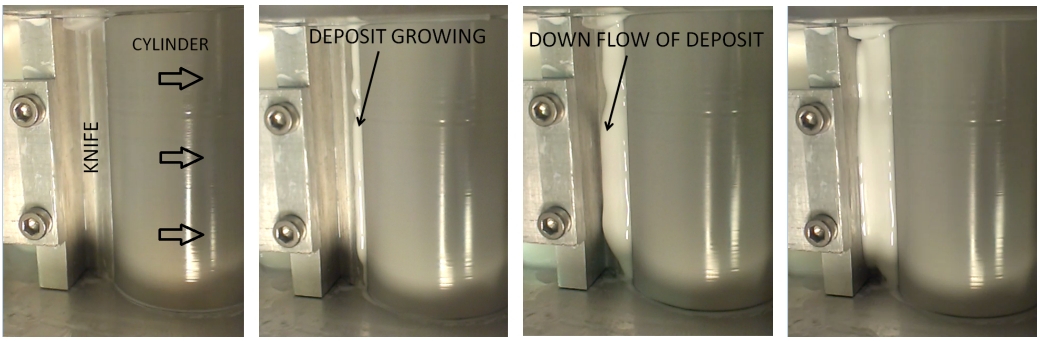

(a) (b) (c) (d)

Figure 5.25: Top view of the cylinder and the new knife following the scheme on 5.24. Here is the case with a solid piece of metal to trap flowing deposit for further analysis. (a) just at rotation beginning. The surface is smooth far from the knife. The two furrows nearby are likely due to knife defect/dust below the knife; (b) a deposit appears on the knife; (c)(d) the deposit is flowing down avoiding accumulation at knife exist, so droplets are not released on the substrate.

From Fig. 5.25, we can confirm that deposit flows down to the batch and is not accumulated at knife exit. Thus no downstream droplet release is observed using this modified knife geometry. **As a conclusion, using gravity and modified coating knife to avoid droplet release is a relevant idea to circumvent the droplet issue.**

5.6.2 Roughness

We measure viscosity of D1 63 % in plate/plate geometry (diameter 25 mm) using either smooth surfaces (no slip at the wall in our case) or cross-hatched surface. The pattern is the same for the bottom and the top plate (square pyramid) but the peak to peak roughness is different (0.45 mm for top plate and 0.22 mm for bottom plate). The gap is 200 μm (zero done by the rheometer). Strikingly, the viscosity is lower when using cross-hatched plates (cf. Fig 5.26), which cannot be explained by slip at the wall. Besides, the shear thickening is shifted to higher shear rates. However, it has been shown in the literature [265] that correct measurements with rough surface can be performed only by correcting the gap by an effective gap taking into account the sample located within the roughness.

We can estimate this effective gap by taking data from [265]. With two surfaces with same pattern as us (roughness of each surface 0.675 mm), they show that the effective gap is larger of 0.4 mm. Considering our case (0.45 + 0.22 mm of roughness) leads to an extra 0.2 mm. So the effective gap to take into account is 400 μm. Shear rate and viscosity are recalculated from the torque and rotation speed (cf. Fig. 5.26). Viscosity from measurements with smooth surfaces is recovered. A discrepancy exist for the critical shear rate but we saw previously that it depends on the geometry. In conclusion, the drop in viscosity seen with rough surfaces is only due to an experimental artefact.

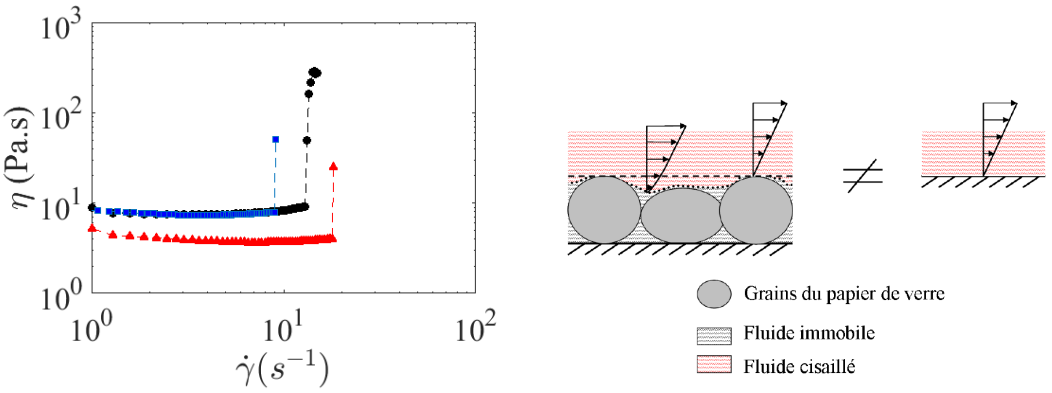

(a) (b)

Figure 5.26: (a) Viscosity of D1 63 % in plate/plate geometry (gap = 200 μm, diameter = 25 mm) using either smooth surfaces (●) or cross-hatched surface without gap correction (▲) or correcting by the effective gap (■). (b) Volume of partially sheared sample in roughness spaces not accounted (case of sandpaper) [265].

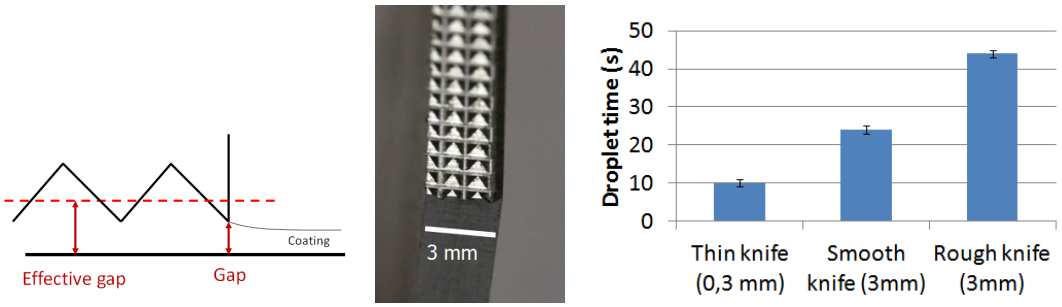

(a) (b) (c)

Figure 5.27: (a) Gap is adjusted by checking with a feeler gauge the distance between the cylinder and the hatching tops. (b) Machined cross-hatched knife. Its width is 3 mm and peak to peak roughness is similar to hatched plates from the rheometer (0.4 mm). Gap is adjusted by checking with a feeler gauge the distance between the cylinder and the hatching tops. The knife exit (on the right of the picture) is straight to ensure a regular coating (no thickness pattern from the hatched surface) ; (c) Time for first droplet release for smooth and hatched knife (gap = 100 μm, $\dot{\gamma}$ = 12 000 s^{-1})

Then, we turn back to the coating in knife-over-roll geometry of D2 62 %. A knife with similar roughness than hatched plate from the rheometer has been manufactured (cf. Fig. 5.27a). Its width is 3 mm. To avoid possible impact of knife width, a similar smooth knife, also 3 mm wide is also machined. Fig. 5.27b shows the time for first droplet release in the case of different knifes (gap = 100 μm, $\dot{\gamma}$ = 12 000 s^{-1}). Gap is adjusted by checking with a feeler gauge the distance between the cylinder and the

hatching tops. The knife exit (on the right of the picture 5.27a) is straight to ensure a regular coating (no thickness pattern from the cross-hatched surface).

It is interesting to note that the geometry of the knife (thickness here between smooth 0.3 mm and 3 mm) has an impact on the defect. The rough knife doubles the time needed for droplet release compared to the smooth one. These results are in line with previous rheological experiments on D1 63 %. Indeed, the paste will be sheared with a higher effective gap (lower shear rate) which explains the slower growth of the deposit. But finally, the coating is performed with the same final thickness. Using rough surface under knife would be an interesting way of delaying droplet occurrence. However, these are only preliminary experiments and it would be insightful to further investigate this option (measure for different speeds and roughness).

5.7 Chapter conclusion

We studied in this chapter a defect encountered in industrial applications when coating a plastisol at high speed. In such cases, a deposit forms on the knife just at its exit and progressively grows until some droplets are released onto the coated substrate. We built a lab-scale prototype (coating on a cylinder, 5 cm width) which successfully mimics the industrial process. In fact, the prototype successfully reproduces defect phenomenology. We first point out a prior instability of plastisol at intermediate shear rate where a ribbing-like phenomenon appears. Pinned ridges appears at a critical shear rate $\dot{\gamma}_{ribbing}$ which we correlate with normal stress differences appearance (N_2 negative, N_1 slightly negative). By carefully increasing the shear rate, we then show that the deposit observed industrially is first formed at ridges maxima from the plastisol ribbing instability. The shear rate at which deposit appears on the knife is not unique but very well corresponds to the N_1 positive rise. Following N_1 versus the shear rate is thus a relative easy measurement to predict a priori deposit and droplet occurrence.

5.8 Summary

- The defect observed in industrial knife-over-roll coating reproduced at the lab scale : deposit growth on knife at its exit and then droplets release.
- Normal stress differences (N_2 negative, N_1 slightly negative) triggers a ribbing-like instability visible at plastisol surface.
- N_1 positive at high shear rate correlated to deposit growth on the knife (dilation) from the instability. It is an easy criteria to a priori predict deposit and droplet occurrence.
- Instability and defects are thus correlated to normal stress difference of plastisols at high shear rate.
- Shear thickening is not a prerequisite for obtaining deposit and droplets.
- Two ideas for defect reduction are detailed: new knife position and knife roughness.

Chapter 6

General conclusion and Perspectives

My PhD thesis focuses on the macroscopic properties over a large range of shear rates ($0.1\ s^{-1}\ \dot{\gamma} < 10^4 s^{-1}$) of formulations based on PVC particles in plasticizer (plastisol). The identified rheological behaviours (shear-thinning/shear-thickening) depending on the shear rate domains, are explained by various interactions between particles at microscopic scale. In particular, effects of polydispersity, particle volume fraction ϕ, impact of fillers and different kinds of additives such as surfactants and water are assessed. Furthermore we successfully develop a lab-scale proptotype in order to mimic the industrial coating process and elucidate the industrial issue.

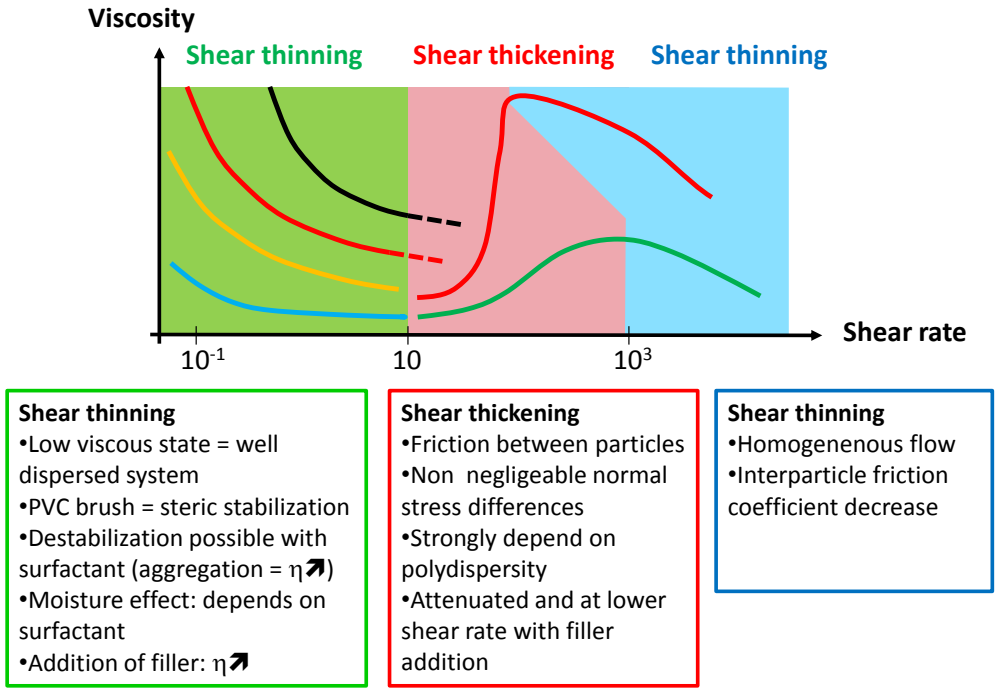

Figure 6.1: Different flow regimes in PVC concentrated suspensions: shear thinning at low shear and high shear rate. Shear thickening in-between. Main factors influencing the rheological behaviour in each regime are underlined.

Flow curves for different concentrations and different powders (PVC 1 and PVC 2) were accurately measured over a wide range of shear rates by combining different rheological tools: rotational rheometer

and capillary rheometers (a home-made and a commercial). Several regimes are underlined when studying the influence of shear rate on the viscosity. Indeed, suspensions are shear-thinning at low shear rate (typically $\dot{\gamma} < 10\ s^{-1}$) and at high shear rate (typically $\dot{\gamma} \sim 1000 s^{-1}$ for suspensions with polydisperse PVC). In between, they exhibit shear thickening at intermediate shear rate (cf. Fig. 6.1).

The low shear rate regime is very sensitive to attractive interparticles interactions. In our system, particles are stabilized by steric interactions due to a thin swelled PVC brush on the surface. This polymer brush comes from the slow diffusion of plasticizer into particles. Plasticizer is already optimized to minimize attractive interactions between particles (high affinity PVC/plasticizer). We have shown that a higher number of small particles results in a higher low-shear viscosity due to the increase of interparticles interactions. More critically, we noticed that polar surfactant (insoluble in DINCH) remaining from the water-based PVC synthesis could also be responsible for high low-shear viscosity by inducing particles aggregation. In the best case, the surfactant does not change viscosity. This low-shear behaviour can also be tuned by the water content. Effects are complex and highly dependant on surfactant nature. Moreover, we have shown that water repartition in the system is also a critical parameter. For industrial polydisperse PVC powder, shear thickening can be "hidden" by high low-shear viscosity, resulting in a apparent shear-thinning behaviour on the whole shear rate range.

The shear-thickening behaviour is strongly dependant on the PVC particle size distribution; a more polydisperse powder reduces the shear thickening intensity. PVC suppliers have well noticed this phenomenon and offer now PVC powder with bidispersity (or more) so as to limit the shear thickening. Furthermore, we unveiled its microscopic origin. Indeed, using an Atomic Force Microscope, we were able, for the first time, to experimentally link the macroscopic stress, at which shear-thickening appears, with the microscopic stress needed for particles to enter a frictional regime. Thus, shear thickening appears in PVC concentrated suspension when the PVC brush on surface becomes unable to keep particles separated by a lubrication film (onset of frictional forces). Besides, large normal stress differences (N_1 and N_2 have been measured along shear thickening). Positive N_1 and negative N_2 are reported.

Finally, the shear thinning regime beyond shear thickening is experimentally pointed out through the flow in a capillary. Thanks to X-ray radiography, we do not evidence any heterogeneity or self-filtration. Moreover no slip at the wall occurs , showing the relevancy of this regime. Its origin is however not clearly addressed in the literature. The only reported explanation comes from the elastohydrodynamic model. Such model should probably be called into question as fitting can be achieved only with a prefactor far smaller than 1 (0.01-0.15). Moreover, it implies a lubrication film which is in fact broken at lower stress during the shear-thickening transition. From preliminary experiments with AFM, we suggest that friction coefficient decreases at very high load.

We have also investigated the different regimes encountered at different volume fraction of particles ϕ (cf. Fig. 6.2) for PVC 1 and PVC 2. The plastisol composed of PVC 1 (D1) well follows the phenomenology derived from the theory of Wyart and Cates [57]. For example, below ϕ_{CST}, plastisols are Newtonian. They exhibit moderate shear thickening above ϕ_{CST}. Above ϕ_{DST}, shear thickening becomes then discontinuous. Jamming density in frictional regime (ϕ_m) and in frictionless regime (ϕ_{RCP}) are derived from a fit of respectively low-shear and high-shear viscosity for different volume fraction ϕ. We checked also the shear thickening transition is a stress- controlled phenomena; the critical stress is linked to the interparticle repulsion force (PVC brush). Using X-ray radiography and

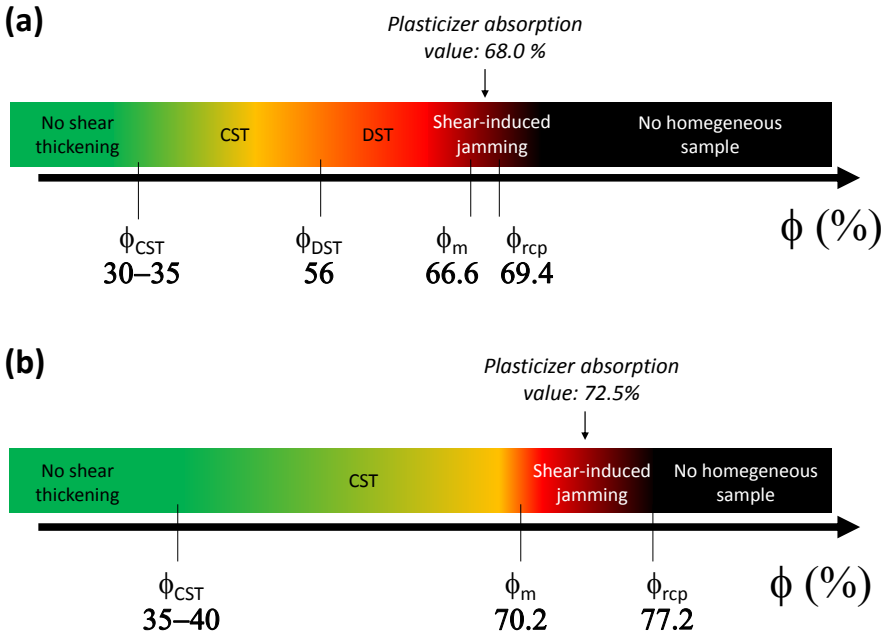

Figure 6.2: Characterization of the different rheological behaviours for the two dispersions (a) D1 and (b) D2. For D1, we observe a shear thickening for volume fraction higher than 45 %. Upon 56 %, sample exhibit discontinuous shear thickening at a critical shear which is smaller and smaller when ϕ is increased. Upon 66.6 %, the sample flows only for very low shear rate near to zero and shear-thickened state is expected to flow inhomogeneously or exhibit fracture. Random close packing which corresponds to the most concentrated obtainable sample is 69.4 %. For D2, the behaviour is almost the same except that DST is absent even at high concentration. Transitions between regimes occurs at higher volume fraction than for D1.

ultrasounds, we shows that the regime between ϕ_{DST} and ϕ_m does imply a transition between two viscous flowing state as expected from the theory of Wyart and Cates. In particular, we pointed out new non-local phenomena in the flow of concentrated suspensions: a smaller gap leads to a smaller viscosity.

We then studied the change in rheological properties when a part of PVC powder is replaced by $CaCO_3$ particles. These particles are very different from PVC ones for chemical composition and shape (angular shape). We first studied the filler alone dispersed in plasticizer. The rheology is shear-thinning at low shear rate due to bad compatibility between hydrophobic plasticizer and hydrophilic filler. At high shear rate, where such interaction are broken, rheology is Newtonian. Compatibility between filler and plasticizer can be enhanced with a surfactant resulting in a lower viscosity (i.e. higher maximum packing fraction).

With the plasticizer absorption test, we are able to measure the change of maximum packing fraction ϕ_{max} when filler/PVC ratio is changed (cf. Fig. 6.3, the horizontal scale referring to ξ_{PVC}=$\frac{\phi_{PVC}}{\phi_{PVC}+\phi_{filler}}$.). Increase of ϕ_{max} compared to pure PVC is obtained when filler has a larger particle size (size ratio > $\sim$ 3-4). In particular, the bigger filler particle size, the higher ϕ_{max} achieved . We observed also that the gain achieved by the size difference is more important than a gain possibly stemming from polydispersity of pure powder (cf. Fig. 6.4a).

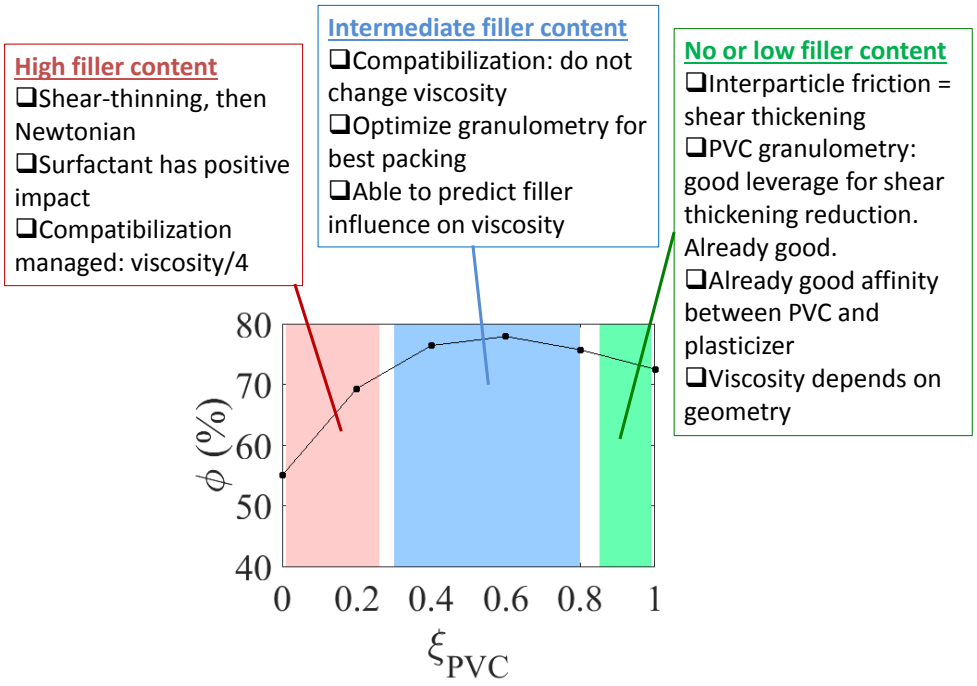

Figure 6.3: Black dots: maximum packing fraction measured from plasticizer absorption test when mixing together PVC 2 and filler M. Different regimes can be underlined depending on filler/PVC ratio: low (green), intermediate (blue) or high (red). This is characterized by the number ξ_{PVC}=$\frac{\phi_{PVC}}{\phi_{PVC}+\phi_{filler}}$. For each regime, main features concerning rheology are reminded.

Concerning the rheological behaviour, we identified different regimes depending on filler content. For low filler content ($\xi_{PVC} >\sim 0.8$, see green zone on Fig. 6.3), rheology is dominated by PVC-PVC interactions and is thus hardy changed from pure PVC suspensions. At moderate filler content, where most industrial formulations are ($0.4 < \xi_{PVC} < 0.8$, see blue zone), the intensity of shear thickening is attenuated and depends on PVC real concentration $\frac{\phi_{PVC}}{\phi_{PVC}+\phi_{liq.}}$. Considering filler as non interacting, we rationalize viscosity measurements within a simple model which takes advantage of our experimentally measured ϕ_{max}. For high filler load ($\xi_{PVC} < 0.25$, see red zone) , the rheology is now filler dominated: no shear thickening is displayed, shear thinning is observed like in pure filler suspensions. Modelling viscosity can be done by considering the rheology of pure filler in a liquid composed of a dilute suspension of PVC particles. Surfactant on filler surface was found to decrease suspension viscosity only when rheology is filler dominated (cf. Fig. 6.4b). Transitions between regimes are smooth and depends on filler and PVC used, especially the filler size.

Using these new insights in the flow behaviour of concentrated suspensions, we now investigate some instabilities when coated at high speed. We developed a lab scale prototype which mimics industrial coating step and reproduces same defects sometimes encountered: a deposit is progressively formed on the knife, downstream. The deposit grows and resulting in a release of suspension droplet on the flat coated substrate. We showed that at moderate shear rate (before deposit appearance), where N_1 and N_2 become to be non-zero, a ribbing-like instability appears with a wavelength proportional to the coating gap. A higher speed, where N_1 becomes positive, the deposit begin to form at maxima of the ribbing instability and invades progressively the total length of the knife. We thus pointed out a simple

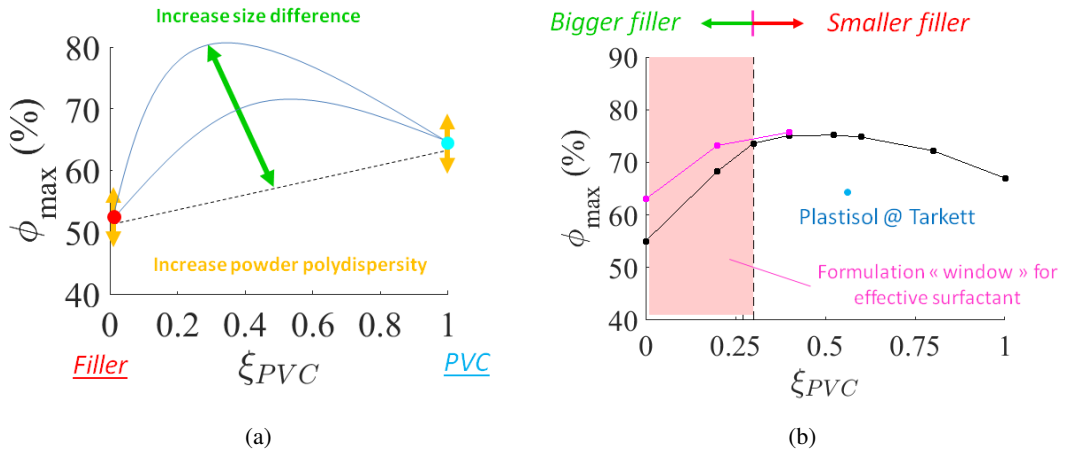

(a) (b)

Figure 6.4: (a) Gain of maximum packing fraction when mixing PVC and filler. Gain due to mixing different sizes can be much higher than gain from more polydisperse pure powder(b) Formulation window for effective viscosity reduction due to compatibilized filler. Frontier is dependant on filler size.

criteria for anticipating defect appearance. Moreover, practical solutions to avoid defects consequences are suggested.

The topic of this thesis is broad. Although many breakthrough in the understanding of the plastisol behaviour under shear, some future investigations are possible in the future. From an academic point of view, the origin of shear thinning regime beyond shear thickening is not clearly pointed out. Preliminary results concerning a decrease of frictional coefficient at high load is promising and would constitute an alternative theory to elastohydrodynamic limit as we proved that shear thickening implies interparticles solid friction. Moreover, particles local concentrations were followed by X-ray at a concentration between ϕ_{DST} and ϕ_m where we observe no shear-induced particle migration. It would be interesting to run the same experiments at a concentration above ϕ_m. According to Wyart and Cates [57], samples cannot flow in this regime and would fracture and separate into different phases. Such phase separation would remind results obtained in a cornstarch suspension [81].

Concerning the formulation, we showed that surfactant on PVC surface (remaining from PVC synthesis) induces an aggregation of suspension, explaining the high low shear viscosity observed in some cases. However, the microscopic origin of these attractive forces induced by surfactant remains an open question. Moreover, it would be interesting to test on other formulations our model for viscosity prediction of filled suspensions. Especially, for different reasons, some coarse PVC extender particles are sometime used in formulation. Their granulometry in similar to the one of filler ($\sim 20\ \mu m$). More generally, several PVC and several fillers are used in industrial formulations, each of them with a specific granulometry. It would be insightful to test our simple models predicting the viscosity of filled suspensions on these more complex formulations.

For the instability, it would be interesting to do more experiments with different knife geometries: width and surface state (smooth or roughened). Moreover the reason of a non-unique critical shear rate $\dot{\gamma}_c$ should also be investigated. Finally, as the deposit on knife has been correlated with N_1 positive

burst, it would be of great interest to extend the model developed in chapter 4 which predicts the viscosity of filled plastisol. In particular, the shift of shear-thickening behaviour at lower shear rate upon filler incorporation was quite well predicted. As N_1 rises concomitantly with shear thickening, the model may be able to predict the onset shear rate for positive N_1 of a filled plastisol by knowing the N_1 profile of unfilled interstitial phase (PVC + DINCH).

Bibliography

[1] Yves Georget. Mise en oeuvre des plastisols, 1994.

[2] Yoël Forterre and Olivier Pouliquen. Flows of Dense Granular Media. *Annual Review of Fluid Mechanics*, 40(1):1–24, January 2008.

[3] Pierre Jop, Yoël Forterre, and Olivier Pouliquen. A constitutive law for dense granular flows. *Nature*, 441(7094):727–730, June 2006.

[4] Frédéric da Cruz, Sacha Emam, Michaël Prochnow, Jean-Noël Roux, and François Chevoir. Rheophysics of dense granular materials: Discrete simulation of plane shear flows. *Physical Review E*, 72(2), August 2005.

[5] François Boyer, Élisabeth Guazzelli, and Olivier Pouliquen. Unifying Suspension and Granular Rheology. *Physical Review Letters*, 107(18):188301, October 2011.

[6] Anaël Lemaître, Jean-Noël Roux, and François Chevoir. What do dry granular flows tell us about dense non-Brownian suspension rheology? *Rheologica Acta*, 48(8):925–942, October 2009.

[7] G. K. Batchelor and J. T. Green. The hydrodynamic interaction of two small freely-moving spheres in a linear flow field. *Journal of Fluid Mechanics*, 56(02):375, November 1972.

[8] D. Quemada. Rheology of concentrated disperse systems II. A model for non-newtonian shear viscosity in steady flows. *Rheologica Acta*, 17(6):632–642, November 1978.

[9] Irvin M. Krieger. A Mechanism for Non-Newtonian Flow in Suspensions of Rigid Spheres. *Journal of Rheology*, 3(1):137, 1959.

[10] Jan Mewis and Norman J. Wagner. *Colloidal suspension rheology*. Cambridge University Press, 2012.

[11] Irvin M. Krieger and Miguel Eguiluz. The Second Electroviscous Effect in Polymer Latices. *Transactions of the Society of Rheology*, 20(1):29–45, March 1976.

[12] F.M. Horn, W. Richtering, J. Bergenholtz, N. Willenbacher, and N.J. Wagner. Hydrodynamic and Colloidal Interactions in Concentrated Charge-Stabilized Polymer Dispersions. *Journal of Colloid and Interface Science*, 225(1):166–178, May 2000.

[13] Brent J. Maranzano and Norman J. Wagner. Thermodynamic properties and rheology of sterically stabilized colloidal dispersions. *Rheologica Acta*, 39(5):483–494, October 2000.

[14] S. L. Elliott and W. B. Russel. High frequency shear modulus of polymerically stabilized colloids. *Journal of Rheology*, 42(2):361, 1998.

[15] Gary Biebaut. *Rheology of colloical suspensions: Effects of stabilizer layer thickness*. PhD thesis, 1999.

[16] Stephen Tanurdjaja, Carolina Tallon, Peter J. Scales, and George V. Franks. Influence of dispersant size on rheology of non-aqueous ceramic particle suspensions. *Advanced Powder Technology*, 22(4):476–481, July 2011.

[17] I. Sushumna, R. K. Gupta, and E. Ruckenstein. Effective dispersants for concentrated, nonaqueous suspensions. *Journal of Materials Research*, 7(10):2884–2893, October 1992.

[18] Lucia Ferrari, Josef Kaufmann, Frank Winnefeld, and Johann Plank. Interaction of cement model systems with superplasticizers investigated by atomic force microscopy, zeta potential, and adsorption measurements. *Journal of Colloid and Interface Science*, 347(1):15–24, July 2010.

[19] Hyun Joon Kong, Stacy G. Bike, and Victor C. Li. Effects of a strong polyelectrolyte on the rheological properties of concentrated cementitious suspensions. *Cement and Concrete Research*, 36(5):851–857, May 2006.

[20] Jennifer A. Lewis, Hiro Matsuyama, Glen Kirby, Sherry Morissette, and J. Francis Young. Polyelectrolyte Effects on the Rheological Properties of Concentrated Cement Suspensions. *Journal of the American Ceramic Society*, 83(8):1905–1913, December 2004.

[21] Fabrice Toussaint, Cédric Roy, and Pierre-Henri Jézéquel. Reducing shear thickening of cement-based suspensions. *Rheologica Acta*, 48(8):883–895, October 2009.

[22] H. Lombois-Burger, P. Colombet, J. L. Halary, and H. Van Damme. On the frictional contribution to the viscosity of cement and silica pastes in the presence of adsorbing and non adsorbing polymers. *Cement and Concrete Research*, 38(11):1306–1314, November 2008.

[23] Lisa R. Murray, Chetali Gupta, Newell R. Washburn, and Kendra A. Erk. Lignopolymers as viscosity-reducing additives in magnesium oxide suspensions. *Journal of Colloid and Interface Science*, 459:107–114, December 2015.

[24] Norio Tobori and Takeshi Amari. Rheological behavior of highly concentrated aqueous calcium carbonate suspensions in the presence of polyelectrolytes. *Colloids and Surfaces A: Physicochemical and Engineering Aspects*, 215(1-3):163–171, March 2003.

[25] Deng Deng, Volodymyr Boyko, Sabrina Montero Pancera, Nikolaus Nestle, and Tharwat Tadros. Rheology investigations on the influence of addition sodium polyacrylate to calcium carbonate suspensions. *Colloids and Surfaces A: Physicochemical and Engineering Aspects*, 372(1-3):9–14, December 2010.

[26] Koffi Leon Konan, Claire Peyratout, Manuella Cerbelaud, Agnes Smith, Jean-Pierre Bonnet, and Alain Jacquet. Influence of two dispersants on the rheological behavior of kaolin and illite in concentrated calcium hydroxide dispersions. *Applied Clay Science*, 42(1-2):252–257, December 2008.

[27] J Yuan. Influence of dispersants on the solubility of calcined kaolin. *Applied Clay Science*, 13(2):137–147, August 1998.

[28] Marie Sjöberg, Lennart Bergström, Anders Larsson, and Eva Sjöström. The effect of polymer and surfactant adsorption on the colloidal stability and rheology of kaolin dispersions. *Colloids and Surfaces A: Physicochemical and Engineering Aspects*, 159(1):197–208, November 1999.

[29] Simge Çınar and Mufit Akinc. Ascorbic acid as a dispersant for concentrated alumina nanopowder suspensions. *Journal of the European Ceramic Society*, 34(8):1997–2004, August 2014.

[30] Piotr Tomasik, Christopher H Schilling, Ryszard Jankowiak, and Jong-Cheol Kim. The role of organic dispersants in aqueous alumina suspensions. *Journal of the European Ceramic Society*, 23(6):913–919, May 2003.

[31] H. A. Barnes. Shear-thickening ("Dilatancy") in Suspensions of Nonaggregating Solid Particles Dispersed in Newtonian Liquids. *Journal of Rheology*, 33(2):329–366, February 1989.

[32] H. Freundlich and H. L. Röder. Dilatancy and its relation to thixotropy. *Transactions of the Faraday Society*, 34(0):308–316, January 1938.

[33] Hans Martin Laun. Rheological properties of aqueous polymer dispersions. *Die Angewandte Makromolekulare Chemie*, 123(1):335–359, August 1984.

[34] B.J. Maranzano and N.J. Wagner. The effects of interparticle interactions and particle size on reversible shear thickening: Hard-sphere colloidal dispersions. *Journal of Rheology*, 45(5):1205–1222, August 2001.

[35] X. Cheng, J. H. McCoy, J. N. Israelachvili, and I. Cohen. Imaging the Microscopic Structure of Shear Thinning and Thickening Colloidal Suspensions. *Science*, 333(6047):1276–1279, September 2011.

[36] Colin D. Cwalina and N. J. Wagner. Material properties of the shear-thickened state in concentrated near hard-sphere colloidal dispersions. *Journal of Rheology*, 58(4):949–967, June 2014.

[37] A. Kate Gurnon and Norman J. Wagner. Microstructure and rheology relationships for shear thickening colloidal dispersions. *Journal of Fluid Mechanics*, 769:242–276, April 2015.

[38] Abdoulaye Fall, François Bertrand, Guillaume Ovarlez, and Daniel Bonn. Shear thickening of cornstarch suspensions. *Journal of Rheology*, 56(3):575, 2012. arXiv: 1206.1717.

[39] Didier Lootens, Henri van Damme, Yacine Hémar, and Pascal Hébraud. Dilatant Flow of Concentrated Suspensions of Rough Particles. *Physical Review Letters*, 95(26):268302, December 2005.

[40] Eric Brown and Heinrich M. Jaeger. Dynamic Jamming Point for Shear Thickening Suspensions. *Physical Review Letters*, 103(8):086001, August 2009.

[41] Ryan J. Larsen, Jin-Woong Kim, Charles F. Zukoski, and David A. Weitz. Fluctuations in flow produced by competition between apparent wall slip and dilatancy. *Rheologica Acta*, 53(4):333–347, March 2014.

[42] Eric Brown and Heinrich M. Jaeger. Shear thickening in concentrated suspensions: phenomenology, mechanisms and relations to jamming. *Reports on Progress in Physics*, 77(4):046602, 2014.

[43] Young S. Lee, E. D. Wetzel, and N. J. Wagner. The ballistic impact characteristics of Kevlar® woven fabrics impregnated with a colloidal shear thickening fluid. *Journal of Materials Science*, 38(13):2825–2833, July 2003.

[44] Norman J. Wagner and John F. Brady. Shear thickening in colloidal dispersions. *Physics Today*, 62(10):27–32, October 2009.

[45] Jonathan Bender and Norman J. Wagner. Reversible shear thickening in monodisperse and bidisperse colloidal dispersions. *Journal of Rheology*, 40(5):899–916, September 1996.

[46] P. Coussot and C. Ancey. Rheophysical classification of concentrated suspensions and granular pastes. *Physical Review E*, 59(4):4445–4457, April 1999.

[47] Abdoulaye Fall, Anaël Lemaître, François Bertrand, Daniel Bonn, and Guillaume Ovarlez. Shear Thickening and Migration in Granular Suspensions. *Physical Review Letters*, 105(26):268303, December 2010.

[48] R. L Hoffman. Discontinuous and dilatant viscosity behavior in concentrated suspensions. II. Theory and experimental tests. *Journal of Colloid and Interface Science*, 46(3):491–506, March 1974.

[49] Ronald G. Egres and N. J. Wagner. The rheology and microstructure of acicular precipitated calcium carbonate colloidal suspensions through the shear thickening transition. *Journal of Rheology*, 49(3):719–746, May 2005.

[50] Dennis P. Kalman and Norman J. Wagner. Microstructure of shear-thickening concentrated suspensions determined by flow-USANS. *Rheologica Acta*, 48(8):897–908, October 2009.

[51] Abdoulaye Fall, N. Huang, F. Bertrand, G. Ovarlez, and Daniel Bonn. Shear Thickening of Cornstarch Suspensions as a Reentrant Jamming Transition. *Physical Review Letters*, 100(1):018301, January 2008.

[52] Eric Brown and Heinrich M. Jaeger. The role of dilation and confining stresses in shear thickening of dense suspensions. *Journal of Rheology (1978-present)*, 56(4):875–923, July 2012.

[53] Eric Brown, Nicole A. Forman, Carlos S. Orellana, Hanjun Zhang, Benjamin W. Maynor, Douglas E. Betts, Joseph M. DeSimone, and Heinrich M. Jaeger. Generality of shear thickening in dense suspensions. *Nature Materials*, January 2010.

[54] John R. Royer, Daniel L. Blair, and Steven D. Hudson. Rheological Signature of Frictional Interactions in Shear Thickening Suspensions. *Physical Review Letters*, 116(18):188301, May 2016.

[55] Safa Jamali, Arman Boromand, Norman Wagner, and Joao Maia. Microstructure and rheology of soft to rigid shear-thickening colloidal suspensions. *Journal of Rheology (1978-present)*, 59(6):1377–1395, November 2015.

[56] Chiara Neto, Drew R. Evans, Elmar Bonaccurso, Hans-Jürgen Butt, and Vincent S. J. Craig. Boundary slip in Newtonian liquids: a review of experimental studies. *Reports on Progress in Physics*, 68(12):2859, 2005.

[57] M. Wyart and M. E. Cates. Discontinuous Shear Thickening without Inertia in Dense Non-Brownian Suspensions. *Physical Review Letters*, 112(9):098302, March 2014.

[58] Nicolas Fernandez, Roman Mani, David Rinaldi, Dirk Kadau, Martin Mosquet, Hélène Lombois-Burger, Juliette Cayer-Barrioz, Hans J. Herrmann, Nicholas D. Spencer, and Lucio Isa. Microscopic Mechanism for Shear Thickening of Non-Brownian Suspensions. *Physical Review Letters*, 111(10):108301, September 2013.

[59] B. M. Guy, M. Hermes, and W. C. K. Poon. Towards a Unified Description of the Rheology of Hard-Particle Suspensions. *Physical Review Letters*, 115(8):088304, August 2015.

[60] Michiel Hermes, Ben M. Guy, Guilhem Poy, Michael E. Cates, Matthieu Wyart, and Wilson C. K. Poon. Unsteady flow and particle migration in dense, non-Brownian suspensions. *arXiv:1511.08011 [cond-mat, physics:physics]*, November 2015. arXiv: 1511.08011.

[61] Krishnamurthy, N.J Wagner, and Mewis. Shear thickening in polymer stabilized colloidal dispersions. *Journal of Rheology*, 49(6):1347–1360, October 2005.

[62] Richard L. Hoffman. Explanations for the cause of shear thickening in concentrated colloidal suspensions. *Journal of Rheology (1978-present)*, 42(1):111–123, January 1998.

[63] Zhongcheng Pan, Henri de Cagny, Bart Weber, and Daniel Bonn. S-shaped flow curves of shear thickening suspensions: Direct observation of frictional rheology. *Physical Review E*, 92(3):032202, September 2015.

[64] W. J. Frith and A. Lips. The rheology of concentrated suspensions of deformable particles. *Advances in Colloid and Interface Science*, 61:161–189, January 1995.

[65] Romain Mari, Ryohei Seto, Jeffrey F. Morris, and Morton M. Denn. Nonmonotonic flow curves of shear thickening suspensions. *Physical Review E*, 91(5):052302, May 2015.

[66] Willem H. Boersma, P.J.M. Baets, Jozua Laven, and Hans N. Stein. Time dependent behavior and wall slip in concentrated shear thickening dispersions. *Journal of Rheology*, 35(6):1093–1120, August 1991.

[67] Didier Lootens, Henri Van Damme, and Pascal Hébraud. Giant Stress Fluctuations at the Jamming Transition. *Physical Review Letters*, 90(17):178301, April 2003.

[68] Neil Y. C. Lin, Ben M. Guy, Michiel Hermes, Chris Ness, Jin Sun, Wilson C K Poon, and Itai Cohen. Hydrodynamic and Contact Contributions to Continuous Shear Thickening in Colloidal Suspensions. *Physical Review Letters*, 115(22):228304, November 2015.

[69] Romain Mari, Ryohei Seto, Jeffrey F. Morris, and Morton M. Denn. Shear thickening, frictionless and frictional rheologies in non-Brownian suspensions. *Journal of Rheology (1978-present)*, 58(6):1693–1724, November 2014.

[70] Ryohei Seto, Romain Mari, Jeffrey F. Morris, and Morton M. Denn. Discontinuous Shear Thickening of Frictional Hard-Sphere Suspensions. *Physical Review Letters*, 111(21):218301, November 2013.

[71] Christopher Ness and Jin Sun. Shear thickening regimes of dense non-Brownian suspensions. *Soft Matter*, 12(3):914–924, January 2016.

[72] Romain Mari, Ryohei Seto, Jeffrey F. Morris, and Morton M. Denn. Discontinuous shear thickening in Brownian suspensions by dynamic simulation. *Proceedings of the National Academy of Sciences*, 112(50):15326–15330, December 2015.

[73] Cécile Clavaud, Antoine Bérut, Bloen Metzger, and Yoël Forterre. Revealing the frictional transition in shear-thickening suspensions. *Proceedings of the National Academy of Sciences*, page 201703926, May 2017.

[74] M. I. Smith, R. Besseling, M. E. Cates, and V. Bertola. Dilatancy in the flow and fracture of stretched colloidal suspensions. *Nature Communications*, 1:114, November 2010.

[75] Eric Brown. Friction's Role in Shear Thickening. *Physics*, 6, November 2013.

[76] Matthieu Roché, Eglind Myftiu, Mitchell C. Johnston, Pilnam Kim, and Howard A. Stone. Dynamic Fracture of Nonglassy Suspensions. *Physical Review Letters*, 110(14):148304, April 2013.

[77] Scott R. Waitukaitis and Heinrich M. Jaeger. Impact-activated solidification of dense suspensions via dynamic jamming fronts. *Nature*, 487(7406):205–209, July 2012.

[78] M. I. Smith. Fracture of Jammed Colloidal Suspensions. *Scientific Reports*, 5:14175, September 2015.

[79] Ivo R. Peters, Sayantan Majumdar, and Heinrich M. Jaeger. Direct observation of dynamic shear jamming in dense suspensions. *Nature*, 532(7598):214–217, April 2016.

[80] Endao Han, Ivo R. Peters, and Heinrich M. Jaeger. High-speed ultrasound imaging in dense suspensions reveals impact-activated solidification due to dynamic shear jamming. *Nature Communications*, 7:12243, July 2016.

[81] A. Fall, F. Bertrand, D. Hautemayou, C. Mezière, P. Moucheront, A. Lemaître, and G. Ovarlez. Macroscopic Discontinuous Shear Thickening versus Local Shear Jamming in Cornstarch. *Physical Review Letters*, 114(9):098301, March 2015.

[82] M. E. Cates, M. D. Haw, and C. B. Holmes. Dilatancy, jamming, and the physics of granulation. *Journal of Physics: Condensed Matter*, 17(24):S2517, 2005.

[83] Michael E. Cates and Matthieu Wyart. Granulation and bistability in non-Brownian suspensions. *Rheologica Acta*, 53(10-11):755–764, November 2014.

[84] J. Bergenholtz, J. F. Brady, and M. Vicic. The non-Newtonian rheology of dilute colloidal suspensions. *Journal of Fluid Mechanics*, 456:239–275, April 2002.

[85] Sudhir S. Shenoy, Norman J. Wagner, and Jonathan W. Bender. E-FiRST: Electric field responsive shear thickening fluids. *Rheologica Acta*, 42(4):287–294, July 2003.

[86] Ji Young Moon, Shaocong Dai, Li Chang, Joon Sang Lee, and Roger I. Tanner. The effect of sphere roughness on the rheology of concentrated suspensions. *Journal of Non-Newtonian Fluid Mechanics*, 223:233–239, September 2015.

[87] Roger Tanner and Shaocong Dai. Particle roughness and rheology in noncolloidal suspensions. *Journal of Rheology*, 60(4):809–818, July 2016.

[88] Stany Gallier, Elisabeth Lemaire, François Peters, and Laurent Lobry. Rheology of sheared suspensions of rough frictional particles. *Journal of Fluid Mechanics*, 757:514–549, October 2014.

[89] Didier Lootens. *Ciments et suspensions concentrées modèles. Écoulement, encombrement et floculation.* PhD, 2004.

[90] T. H. Phan, M. Chaouche, and M. Moranville. Influence of organic admixtures on the rheological behaviour of cement pastes. *Cement and Concrete Research*, 36(10):1807–1813, October 2006.

[91] Dimitri Feys, Ronny Verhoeven, and Geert De Schutter. Fresh self compacting concrete, a shear thickening material. *Cement and Concrete Research*, 38(7):920–929, July 2008.

[92] D. Lootens, P. Hébraud, E. Lécolier, and H. Van Damme. Gelation, Shear-Thinning and Shear-Thickening in Cement Slurries. *Oil & Gas Science and Technology*, 59(1):31–40, January 2004.

[93] Martin Cyr, Claude Legrand, and Michel Mouret. Study of the shear thickening effect of superplasticizers on the rheological behaviour of cement pastes containing or not mineral additives. *Cement and Concrete Research*, 30(9):1477–1483, September 2000.

[94] Jan Mewis and Gary Biebaut. Shear thickening in steady and superposition flows effect of particle interaction forces. *Journal of Rheology*, 45(3):799–813, April 2001.

[95] Sudhir S. Shenoy and Norman J. Wagner. Influence of medium viscosity and adsorbed polymer on the reversible shear thickening transition in concentrated colloidal dispersions. *Rheologica Acta*, 44(4):360–371, April 2005.

[96] Wufang Yang, Yang Wu, Xiaowei Pei, Feng Zhou, and Qunji Xue. Contribution of Surface Chemistry to the Shear Thickening of Silica Nanoparticle Suspensions. *Langmuir*, 33(4):1037–1042, January 2017.

[97] Xiaoping Yan, Scott S. Perry, Nicholas D. Spencer, Stéphanie Pasche, Susan M. De Paul, Marcus Textor, and Min Soo Lim. Reduction of Friction at Oxide Interfaces upon Polymer Adsorption from Aqueous Solutions. *Langmuir*, 20(2):423–428, January 2004.

[98] Uri Raviv, Suzanne Giasson, Nir Kampf, Jean-François Gohy, Robert Jérôme, and Jacob Klein. Lubrication by charged polymers. *Nature*, 425(6954):163–165, September 2003.

[99] Vito DePalma and Nolan Tillman. Friction and wear of self-assembled trichlorosilane monolayer films on silicon. *Langmuir*, 5(3):868–872, May 1989.

[100] Fang Ye, Wei Zhu, Wanquan Jiang, Zhiyuan Wang, Qian Chen, Xinglong Gong, and Shouhu Xuan. Influence of surfactants on shear-thickening behavior in concentrated polymer dispersions. *Journal of Nanoparticle Research*, 15(12):2122, December 2013.

[101] Maranzano and Norman Wagner. The effects of particle size on reversible shear thickening of concentrated colloidal dispersions. *The Journal of Chemical Physics*, 114(23):10514–10527, June 2001.

[102] George V. Franks, Zhongwu Zhou, Nanda J. Duin, and David V. Boger. Effect of interparticle forces on shear thickening of oxide suspensions. *Journal of Rheology*, 44(4):759, 2000.

[103] Shuangbing Li, Jixiao Wang, Wei Cai, Song Zhao, Zhi Wang, and Shichang Wang. Effect of acid and temperature on the discontinuous shear thickening phenomenon of silica nanoparticle suspensions. *Chemical Physics Letters*, 658:210–214, August 2016.

[104] Neil Y. C. Lin, Christopher Ness, Michael E. Cates, Jin Sun, and Itai Cohen. Tunable shear thickening in suspensions. *Proceedings of the National Academy of Sciences*, 113(39):10774–10778, September 2016.

[105] K. Abraham Vaynberg, Norman J. Wagner, Ravi Sharma, and Peter Martic. Structure and Extent of Adsorbed Gelatin on Acrylic Latex and Polystyrene Colloidal Particles. *Journal of Colloid and Interface Science*, 205(1):131–140, September 1998.

[106] Hélène Babin, Eric Dickinson, Helen Chisholm, and Steve Beckett. Interactions in dispersions of sugar particles in food oils: influence of emulsifier. *Food Hydrocolloids*, 19(3):513–520, May 2005.

[107] G. Arnold, S. Schuldt, Y. Schneider, J. Friedrichs, F. Babick, C. Werner, and H. Rohm. The impact of lecithin on rheology, sedimentation and particle interactions in oil-based dispersions. *Colloids and Surfaces A: Physicochemical and Engineering Aspects*, 418:147–156, February 2013.

[108] Georges Bossis, Yan Grasselli, Alain Meunier, and Olga Volkova. Tunable discontinuous shear thickening with magnetorheological suspensions. *Journal of Intelligent Material Systems and Structures*, page 1045389X17704915, April 2017.

[109] V. Gopalakrishnan and C. F. Zukoski. Effect of attractions on shear thickening in dense suspensions. *Journal of Rheology*, 48(6):1321, 2004.

[110] Sidhant Pednekar, Jaehun Chun, and Jeffrey F. Morris. Simulation of shear thickening in attractive colloidal suspensions. *Soft Matter*, 13(9):1773–1779, March 2017.

[111] E. Koos and N. Willenbacher. Capillary Forces in Suspension Rheology. *Science*, 331(6019):897–900, February 2011.

[112] K. Cavalier and F. Larché. Effects of water on the rheological properties of calcite suspensions in dioctylphthalate. *Colloids and Surfaces A: Physicochemical and Engineering Aspects*, 197(1–3):173–181, February 2002.

[113] Erin Koos, Julia Johannsmeier, Linda Schwebler, and Norbert Willenbacher. Tuning suspension rheology using capillary forces. *Soft Matter*, 8(24):6620–6628, May 2012.

[114] Jan Mewis and Norman J. Wagner. Thixotropy. *Advances in Colloid and Interface Science*, 147–148:214–227, March 2009.

[115] J. Vermant and M. J. Solomon. Flow-induced structure in colloidal suspensions. *Journal of Physics: Condensed Matter*, 17(4):R187, 2005.

[116] Francis A Gadala-Maria. The rheology of concentrated suspensions[Ph. D. Thesis]. 1979.

[117] Isidro E. Zarraga, Davide A. Hill, and David T. Leighton. The characterization of the total stress of concentrated suspensions of noncolloidal spheres in Newtonian fluids. *Journal of Rheology*, 44(2):185–220, February 2000.

[118] Anugrah Singh and Prabhu R. Nott. Experimental measurements of the normal stresses in sheared Stokesian suspensions. *Journal of Fluid Mechanics*, 490:293–320, September 2003.

[119] François Boyer, Olivier Pouliquen, and Élisabeth Guazzelli. Dense suspensions in rotating-rod flows: normal stresses and particle migration. *Journal of Fluid Mechanics*, 686:5–25, November 2011.

[120] T. Dbouk, L. Lobry, and E. Lemaire. Normal stresses in concentrated non-Brownian suspensions. *Journal of Fluid Mechanics*, 715:239–272, January 2013.

[121] Chaiwut Gamonpilas, Jeffrey F. Morris, and Morton M. Denn. Shear and normal stress measurements in non-Brownian monodisperse and bidisperse suspensions. *Journal of Rheology*, 60(2):289–296, February 2016.

[122] Shaocong Dai, Bertevas, Qi, and Tanner. Viscometric functions for noncolloidal sphere suspensions with Newtonian matrices. *Journal of Rheology*, 57(2):493–510, January 2013.

[123] Étienne Couturier, François Boyer, Olivier Pouliquen, and Élisabeth Guazzelli. Suspensions in a tilted trough: second normal stress difference. *Journal of Fluid Mechanics*, 686:26–39, November 2011.

[124] Jeffrey F. Morris and Boulay. Curvilinear flows of noncolloidal suspensions: The role of normal stresses. *Journal of Rheology*, 43(5):1213–1237, August 1999.

[125] Colin D. Cwalina, Kelsey J. Harrison, and Norman J. Wagner. Rheology of cubic particles in a concentrated colloidal dispersion suspending medium. *AIChE Journal*, pages n/a–n/a, August 2016.

[126] M Lee, M Alcoutlabi, J.J. Magda, C Dibble, M. J. Solomon, Xuetao Shi, and G.B. McKenna. The effect of the shear-thickening transition of model colloidal spheres on the sign of N1 and on the radial pressure profile in torsional shear flows. *Journal of Rheology*, 50(3):293–311, April 2006.

[127] David R. Foss and John F. Brady. Structure, diffusion and rheology of Brownian suspensions by Stokesian Dynamics simulation. *Journal of Fluid Mechanics*, 407:167–200, March 2000.

[128] John R. Melrose and Robin. C Ball. Continuous shear thickening transitions in model concentrated colloids—The role of interparticle forces. *Journal of Rheology*, 48(5):937–960, September 2004.

[129] John R. Melrose and Robin. C Ball. "Contact networks" in continuously shear thickening colloids. *Journal of Rheology*, 48(5):961–978, September 2004.

[130] M. E. Cates, J. P. Wittmer, J.-P. Bouchaud, and P. Claudin. Jamming, Force Chains, and Fragile Matter. *Physical Review Letters*, 81(9):1841–1844, August 1998.

[131] Zhongcheng Pan, Henri de Cagny, Mehdi Habibi, and Daniel Bonn. Normal stresses in shear thickening granular suspensions. *Soft Matter*, 13(20):3734–3740, May 2017.

[132] A. Sierou and J. F. Brady. Rheology and microstructure in concentrated noncolloidal suspensions. *Journal of Rheology*, 46(5):1031, 2002.

[133] Kyongmin Yeo and Martin R. Maxey. Dynamics of concentrated suspensions of non-colloidal particles in Couette flow. *Journal of Fluid Mechanics*, 649:205–231, April 2010.

[134] Stany Gallier, Elisabeth Lemaire, Laurent Lobry, and Francois Peters. Effect of confinement in wall-bounded non-colloidal suspensions. *Journal of Fluid Mechanics*, 799:100–127, July 2016.

[135] Gadala-Maria and Andreas Acrivos. Shear Induced Structure in a Concentrated Suspension of Solid Spheres. *Journal of Rheology*, 24(6):799–814, December 1980.

[136] David Leighton and Andreas Acrivos. The shear-induced migration of particles in concentrated suspensions. *Journal of Fluid Mechanics*, 181:415–439, August 1987.

[137] Dima Merhi, Elisabeth Lemaire, Georges Bossis, and Fadl Moukalled. Particle migration in a concentrated suspension flowing between rotating parallel plates: Investigation of diffusion flux coefficients. *Journal of Rheology*, 49(6):1429–1448, October 2005.

[138] Ronald J. Phillips, Robert C. Amstrong, Robert A. Brown, Alan L. Graham, and James R. Abbott. A constitutive equation for concentrated suspensions that accounts for shear-induced particle migration. *Physics of Fluids A: Fluid Dynamics*, 4(1):30–40, January 1992.

[139] Guillaume Ovarlez, François Bertrand, and Stephane Rodts. Local determination of the constitutive law of a dense suspension of noncolloidal particles through magnetic resonance imaging. *Journal of Rheology*, 50(3):259–292, April 2006.

[140] R.E. Hampton, A.A. Mammoli, Alan L. Graham, and N Tetlow. Migration of particles undergoing pressure-driven flow in a circular conduit. *Journal of Rheology*, 41(3):621–640, May 1997.

[141] Steven Sinton and Andrea Chow. NMR flow imaging of fluids and solid suspensions in Poiseuille flow. *Journal of Rheology*, 35(5):735–772, July 1991.

[142] S.A. Altobelli, R.C. Givler, and Eiichi Fukushima. Velocity and concentration measurements of suspensions by nuclear magnetic resonance imaging. *Journal of Rheology*, 35(5):721–734, July 1991.

[143] M. K. Lyon and L. G. Leal. An experimental study of the motion of concentrated suspensions in two-dimensional channel flow. Part 1. Monodisperse systems. *Journal of Fluid Mechanics*, 363:25–56, May 1998.

[144] Christopher J. Koh, Philip Hookham, and L. G. Leal. An experimental investigation of concentrated suspension flows in a rectangular channel. *Journal of Fluid Mechanics*, 266:1–32, May 1994.

[145] John Benbow and J. Bridgwater. *Paste flow and extrusion*. Clarenton press edition, 1993.

[146] Andrea Chow, Steven Sinton, and Joseph Iwamiya. Shear-induced particle migration in Couette and parallel-plate viscometers: NMR imaging and stress measurements. *Physics of Fluids*, 6(8):2561–2576, August 1994.

[147] Daniel Lhuillier. Migration of rigid particles in non-Brownian viscous suspensions. *Physics of Fluids*, 21(2):023302, February 2009.

[148] Prabhu R. Nott, Elisabeth Guazzelli, and Olivier Pouliquen. The suspension balance model revisited. *Physics of Fluids (1994-present)*, 23(4):043304, April 2011.

[149] Francois BOYER. Suspensions concentrées (expériences originales de rhéologie). 2011.

[150] Anaïs Coline Machado. *Contribution à la rhéologie des suspensions: migration, rhéoépaississement*. PhD thesis, Bordeaux, 2016.

[151] T. Dbouk, E. Lemaire, L. Lobry, and F. Moukalled. Shear induced particle migration: Predictions from experimental evaluation of the particle stress tensor. *Journal of Non-Newtonian Fluid Mechanics*, 198:78–95, August 2013.

[152] Guillaume OVARLEZ and Elisabeth GUAZZELLI. Migration induite par cisaillement dans les suspensions. *21ème Congrès Français de Mécanique, 26 au 30 août 2013, Bordeaux, France (FR)*, 2013.

[153] Dennis P. Kalman. *Microstructure and rheology of concentrated suspensions of near hard-sphere colloids*. PhD thesis, Delaware, 2010.

[154] Manojkumar Chellamuthu, Eric M. Arndt, and Jonathan P. Rothstein. Extensional rheology of shear-thickening nanoparticle suspensions. *Soft Matter*, 5(10):2117–2124, May 2009.

[155] Amanda S. Lim, Sergey L. Lopatnikov, Norman J. Wagner, and John W. Gillespie. An experimental investigation into the kinematics of a concentrated hard-sphere colloidal suspension during Hopkinson bar evaluation at high stresses. *Journal of Non-Newtonian Fluid Mechanics*, 165(19–20):1342–1350, October 2010.

[156] Francisco J. Galindo-Rosales, Francisco J. Rubio-Hernández, and José F. Velázquez-Navarro. Shear-thickening behavior of Aerosil® R816 nanoparticles suspensions in polar organic liquids. *Rheologica Acta*, 48(6):699–708, July 2009.

[157] Chinedum O. Osuji, Chanjoong Kim, and David A. Weitz. Shear thickening and scaling of the elastic modulus in a fractal colloidal system with attractive interactions. *Physical Review E*, 77(6):060402, June 2008.

[158] Jianbin Qin, Guangcheng Zhang, and Xuetao Shi. Study of a Shear Thickening Fluid: The Suspensions of Monodisperse Polystyrene Microspheres in Polyethylene Glycol. *Journal of Dispersion Science and Technology*, 0(ja):null, August 2016.

[159] Ashok C. Shah and David J. Poledna. Review of PVC dispersion and blending resin products. *Journal of Vinyl and Additive Technology*, 9(3):146–154, September 2003.

[160] J Leadbitter, J.A. Day, and J.L. Ryan. *PVC: Compounds, Processing and Applications*. Rapra review report edition, January 1994.

[161] N. Nakajima, J. D. Isner, and E. R. Harrell. Gelation and fusion mechanism of PVC plastisols observed by changes of morphology, viscoelastic properties, and ultimate mechanical properties. *Journal of Macromolecular Science, Part B*, 20(3):349–364, October 1981.

[162] J. López, R. Balart, and A. Jiménez. Influence of crystallinity in the curing mechanism of PVC plastisols. *Journal of Applied Polymer Science*, 91(1):538–544, January 2004.

[163] Pierre Verrier. Plastifiants.

[164] S. J. Willey. Steady Shear Rheological Behavior of PVC Plastisols. *Journal of Rheology*, 22(5):525–545, October 1978.

[165] S. J. Willey. Solvation Effects on Dilatancy in Concentrated PVC Plastisols. *Journal of Rheology*, 26(6):557, 1982.

[166] J. R. Darby, N. W. Touchette, and Kern Sears. Dielectric constants of plasticizers as predictors of compatibility with polyvinyl chloride. *Polymer Engineering & Science*, 7(4):295–309, October 1967.

[167] C. E. Wilkes, J. W. Summers, C. A. Daniels, and Mark T. Berard. *PVC Handbook*. 2005.

[168] George Wypych, editor. *Handbook of plasticizers*. ChemTec Pub, Toronto, 2nd ed edition, 2012.

[169] Mridula Chandola and Sujata Marathe. A QSPR for the plasticization efficiency of polyvinylchloride plasticizers. *Journal of Molecular Graphics and Modelling*, 26(5):824–828, January 2008.

[170] N. Nakajima and C. A. Daniels. Plastisols of poly(vinyl chloride); particle size distribution, morphology, rheology, and mechanism of aging. *Journal of Applied Polymer Science*, 25(9):2019–2044, September 1980.

[171] D. J. Hoffmann and L. G. Garcia. Rheology of PVC plastisols II Effect of time and temperature. *Journal of Macromolecular Science, Part B*, 20(3):335–348, October 1981.

[172] N. Nakajima and E. R. Harrell. Viscosity aging of poly(vinyl chloride) plastisol: The effect of the resin type and plasticizer type. *Journal of Applied Polymer Science*, 95(2):448–464, January 2005.

[173] M. G. Rasteiro and E. Antunes. Correlating the Rheology of PVC-Based Pastes with Particle Characteristics. *Particulate Science and Technology*, 23(4):361–375, October 2005.

[174] M.g. Rasteiro, A. Tomás, L. Ferreira, and S. Figueiredo. PVC paste rheology: Study of process dependencies. *Journal of Applied Polymer Science*, 112(5):2809–2821, June 2009.

[175] A. Marcilla, J. C. García, and M. Beltrán. Study of the flow properties and the ageing process in PVC pastisols from commercial PVC resins. *European Polymer Journal*, 33(5):753–759, May 1997.

[176] Edward A Collins, D. J Hoffmann, and Pravin L Soni. Rheology of PVC dispersions. I. Effect of particle size and particle size distribution. *Journal of Colloid and Interface Science*, 71(1):21–29, August 1979.

[177] A. Tomás, M. G. Rasteiro, L. Gando-Ferreira, and S. Figueiredo. Rheology of poly(vinyl chloride) plastisol: Effect of a particular nonionic cosurfactant. *Journal of Applied Polymer Science*, 115(1):599–607, January 2010.

[178] Hassane Boudhani, René Fulchiron, and Philippe Cassagnau. Rheology of physically evolving suspensions. *Rheologica Acta*, 48(2):135–149, September 2008.

[179] Hassane Boudhani, Carole Lainé, René Fulchiron, and Philippe Cassagnau. Rheology and gelation kinetics of PVC Plastisols. *Rheologica Acta*, 46(6):825–838, June 2007.

[180] R. L. Hoffman. Discontinuous and Dilatant Viscosity Behavior in Concentrated Suspensions. I. Observation of a Flow Instability. *Transactions of The Society of Rheology (1957-1977)*, 16(1):155–173, March 1972.

[181] N. Nakajima and E.R. Harrell. Rheology of PVC Plastisol: Formation of Immobilized Layer in Pseudoplastic Flow. *Journal of Colloid and Interface Science*, 238(1):116–124, June 2001.

[182] N. Nakajima and E. R. Harrell. Rheology of PVC Plastisol III. Analyses of Dilatancy and Fracture. *Journal of Colloid and Interface Science*, 241(2):492–496, September 2001.

[183] N. Nakajima and E. R. Harrell. Rheology of poly(vinyl chloride) plastisol for super-high-shear-rate processing. II. *Journal of Applied Polymer Science*, 123(3):1377–1383, February 2012.

[184] Eva G. Barroso, Fernando M. Duarte, Miguel Couto, and João M. Maia. High strain rate rheological characterization of low viscosity fluids. *Polymer Testing*, 29(4):419–424, June 2010.

[185] N. Nakajima and E. R. Harrell. Rheology of poly(vinyl chloride) plastisol for superhigh shear-rate processing. I. *Journal of Applied Polymer Science*, 115(6):3605–3609, March 2010.

[186] Yamina Abdesselam, Jean-François Agassant, Romain Castellani, Rudy Valette, Yves Demay, Diego Gourdin, and Richard Peres. Rheology of plastisol formulations for coating applications. *Polymer Engineering & Science*, pages n/a–n/a, November 2016.

[187] N. Nakajima and E. R. Harrell. Rheology of PVC Plastisol IV. Force Balance among Osmotic Pressure, Normal Stress, and Dilatational Stress. *Journal of Colloid and Interface Science*, 241(2):497–501, September 2001.

[188] N. Nakajima and E. R. Harrell. Rheology of PVC Plastisol - V: Storage Modulus and Network Formed by Particle Contact. *Journal of Colloid and Interface Science*, 254(2):362–366, October 2002.

[189] M. Lambla and H. P. Schreiber. Relations entre les caracteristiques physico-chimiques des charges et les proprietes mecaniques des polymeres (PVC) plastifies et charges. *European Polymer Journal*, 16(3):211–218, January 1980.

[190] X. Oregui, A. Santamaría, J. M. Hiriart, and J. Etcheveste. Influence of the components in the flow properties and physical aging of spray coating PVC plastisols. *Journal of Vinyl Technology*, 7(3):98–102, September 1985.

[191] John A Cook. *Relationships between PVC plastisol rheology and partical size distribution for filled and unfilled systems*. PhD thesis, \copyright John Alan Cook, 1986.

[192] Leonard. *Encyclopedia of PVC*, volume 3. Marcel Dekker, 1992.

[193] A. Winter. Extender resins to enhance processing and end product properties in paste applications. *Plastics, Rubber and Composites*, 37(9-10):421–424, December 2008.

[194] Willem H. Boersma, Jozua Laven, and Hans N. Stein. Shear thickening (dilatancy) in concentrated dispersions. *AIChE Journal*, 36(3):321–332, March 1990.

[195] B. Hochstein, N. Willenbacher, Albert Co, L. G. Leal, Ralph H. Colby, and A. Jeffrey Giacomin. Influence of Water Content on the Flow Behaviour of PVC Plastisols. *AIP Conference Proceedings*, 1027(1):761–763, July 2008.

[196] J. Maybury, J. C. M. Ho, and S. A. M. Binhowimal. Fillers to lessen shear thickening of cement powder paste. *Construction and Building Materials*, 142:268–279, July 2017.

[197] N. Nakajima and E. R. Harrell. Normal stresses in flow of polyvinyl chloride plastisols. *Journal of Applied Polymer Science*, 103(5):2769–2775, March 2007.

[198] N. Nakajima and E.R. Harrell. Rheology of PVC Plastisol - VI: Criteria for Yielding and Fracture of an Immobilized Layer. *Journal of Colloid and Interface Science*, 254(2):367–371, October 2002.

[199] Tarkett. Private Communication, Tarkett.

[200] Gary E. Williams, James T. Bergen, and Gary W. Poehlein. Rheological Behavior of High-Resin-Level Plastisols. *Journal of Rheology (1978-present)*, 23(5):591–616, October 1979.

[201] Faith A Morrison. *Understanding rheology*. Oxford University Press, USA, 2001.

[202] B Rabinowitsch. Uber die viskostat und elastizitat von solen. *Z. Phys. Chem. A*, 145:141, 1929.

[203] E. B. Bagley. End Corrections in the Capillary Flow of Polyethylene. *Journal of Applied Physics*, 28(5):624–627, May 1957.

[204] Melvin Mooney. Explicit Formulas for Slip and Fluidity. *Journal of Rheology*, 2(2):210–222, April 1931.

[205] S. Manneville, L. Bécu, and A. Colin. High-frequency ultrasonic speckle velocimetry in sheared complex fluids. *The European Physical Journal Applied Physics*, 28(3):361–373, December 2004.

[206] Mohammad Gholami, Nicolas Lenoir, David Hautemayou, Guillaume Ovarlez, and Sarah Hormozi. Time-resolved 2d concentration maps in flowing suspensions using X-ray. 2017.

[207] Alan Kastengren and Christopher F. Powell. Synchrotron X-ray techniques for fluid dynamics. *Experiments in Fluids*, 55(3):1686, March 2014.

[208] Changning Wu, Yi Cheng, Yulong Ding, Fei Wei, and Yong Jin. A novel X-ray computed tomography method for fast measurement of multiphase flow. *Chemical Engineering Science*, 62(16):4325–4335, August 2007.

[209] Morton M. Denn and Jeffrey F. Morris. Rheology of Non-Brownian Suspensions. *Annual Review of Chemical and Biomolecular Engineering*, 5(1):203–228, 2014.

[210] Jean Comtet, Guillaume Chatté, Antoine Niguès, Lydéric Bocquet, Alessandro Siria, and Annie Colin. Pairwise frictional profile between particles determines discontinuous shear thickening transition in non-colloidal suspensions. *Nature Communications*, 8:15633, May 2017.

[211] Adam Feiler, Ian Larson, Paul Jenkins, and Phil Attard. A Quantitative Study of Interaction Forces and Friction in Aqueous Colloidal Systems. *Langmuir*, 16(26):10269–10277, December 2000.

[212] Nicolas Fernandez, Juliette Cayer-Barrioz, Lucio Isa, and Nicholas D. Spencer. Direct, Robust Technique for the Measurement of Friction between Microspheres. *Langmuir*, 31(32):8809–8817, August 2015.

[213] A. Niguès, A. Siria, P. Vincent, P. Poncharal, and L. Bocquet. Ultrahigh interlayer friction in multiwalled boron nitride nanotubes. *Nature Materials*, 13(7):688–693, July 2014.

[214] M. Labardi and M. Allegrini. Noncontact friction force microscopy based on quartz tuning fork sensors. *Applied Physics Letters*, 89(17):174104, October 2006.

[215] Khaled Karrai and Robert D. Grober. Piezoelectric tip sampledistance control for near field optical microscopes. *Applied Physics Letters*, 66(14):1842–1844, April 1995.

[216] Richard Villey, Emmanuelle Martinot, Cécile Cottin-Bizonne, Magali Phaner-Goutorbe, Liliane Léger, Frédéric Restagno, and Elisabeth Charlaix. Effect of Surface Elasticity on the Rheology of Nanometric Liquids. *Physical Review Letters*, 111(21):215701, November 2013.

[217] Samuel Leroy, Audrey Steinberger, Cécile Cottin-Bizonne, Frédéric Restagno, Liliane Léger, and Élisabeth Charlaix. Hydrodynamic Interaction between a Spherical Particle and an Elastic Surface: A Gentle Probe for Soft Thin Films. *Physical Review Letters*, 108(26):264501, June 2012.

[218] Eckhard. Goernitz and Helmut. Zecha. Interactions in PVC-plasticizer dispersions. *Langmuir*, 3(5):738–741, September 1987.

[219] JN Israelachvili. Intermolecular and Surface Forces (revised 3rd edition) Academic Press. *Waltham, MA*, 2011.

[220] Jacob Klein. Shear of polymer brushes. *Colloids and Surfaces A: Physicochemical and Engineering Aspects*, 86:63–76, July 1994.

[221] John E. Sader and Suzanne P. Jarvis. Accurate formulas for interaction force and energy in frequency modulation force spectroscopy. *Applied Physics Letters*, 84(10):1801–1803, March 2004.

[222] J. Klein. Shear, Friction, and Lubrication Forces Between Polymer-Bearing Surfaces. *Annual Review of Materials Science*, 26(1):581–612, 1996.

[223] Jacob Klein, Eugenia Kumacheva, Diana Mahalu, Dvora Perahia, and Lewis J. Fetters. Reduction of frictional forces between solid surfaces bearing polymer brushes. *Nature*, 370(6491):634–636, August 1994.

[224] Anne-Sophie Bouchet, Colette Cazeneuve, Nawel Baghdadli, Gustavo S. Luengo, and Carlos Drummond. Experimental Study and Modeling of Boundary Lubricant Polyelectrolyte Films. *Macromolecules*, 48(7):2244–2253, April 2015.

[225] Phillip A. Schorr, Thomas C. B. Kwan, S. Michael Kilbey, Eric S. G. Shaqfeh, and Matthew Tirrell. Shear Forces between Tethered Polymer Chains as a Function of Compression, Sliding Velocity, and Solvent Quality. *Macromolecules*, 36(2):389–398, January 2003.

[226] K. V. Shooter and D. Tabor. The Frictional Properties of Plastics. *Proceedings of the Physical Society. Section B*, 65(9):661, 1952.

[227] D.S. Keller and D.V. Keller. The effect of particle size distribution on the antithixotropic and shear thickening properties of coal–water dispersions. *Journal of Rheology*, 35(8):1583–1607, November 1991.

[228] Robson F. Storey, Kenneth A. Mauritz, and B. Dwain Cox. Diffusion of various dialkyl phthalate plasticizers in PVC. *Macromolecules*, 22(1):289–294, January 1989.

[229] Ann Yoshimura and Robert K. Prud'homme. Wall Slip Corrections for Couette and Parallel Disk Viscometers. *Journal of Rheology*, 32(1):53–67, January 1988.

[230] Guillaume Ovarlez. Private Communication, Guillaume Ovarlez.

[231] K. A. Reddy, Y. Forterre, and O. Pouliquen. Evidence of Mechanically Activated Processes in Slow Granular Flows. *Physical Review Letters*, 106(10):108301, March 2011.

[232] Antoine Le Bouil, Axelle Amon, Sean McNamara, and Jérôme Crassous. Emergence of Cooperativity in Plasticity of Soft Glassy Materials. *Physical Review Letters*, 112(24):246001, June 2014.

[233] J. Goyon, A. Colin, G. Ovarlez, A. Ajdari, and L. Bocquet. Spatial cooperativity in soft glassy flows. *Nature*, 454(7200):84–87, July 2008.

[234] Julie Goyon, Annie Colin, and Lydéric Bocquet. How does a soft glassy material flow: finite size effects, non local rheology , and flow cooperativity. *Soft Matter*, 6(12):2668–2678, 2010.

[235] Lydéric Bocquet, Annie Colin, and Armand Ajdari. Kinetic Theory of Plastic Flow in Soft Glassy Materials. *Physical Review Letters*, 103(3):036001, July 2009.

[236] Pierre Jop, Vincent Mansard, Pinaki Chaudhuri, Lydéric Bocquet, and Annie Colin. Microscale Rheology of a Soft Glassy Material Close to Yielding. *Physical Review Letters*, 108(14):148301, April 2012.

[237] Vincent Mansard, Annie Colin, Pinaki Chauduri, and Lyderic Bocquet. A kinetic elasto-plastic model exhibiting viscosity bifurcation in soft glassy materials. *Soft Matter*, 7(12):5524–5527, June 2011.

[238] Ken Kamrin and Georg Koval. Nonlocal Constitutive Relation for Steady Granular Flow. *Physical Review Letters*, 108(17):178301, April 2012.

[239] David L. Henann and Ken Kamrin. A predictive, size-dependent continuum model for dense granular flows. *Proceedings of the National Academy of Sciences*, 110(17):6730–6735, April 2013.

[240] Mehdi Bouzid, Martin Trulsson, Philippe Claudin, Eric Clément, and Bruno Andreotti. Nonlocal Rheology of Granular Flows across Yield Conditions. *Physical Review Letters*, 111(23):238301, December 2013.

[241] Olivier Pouliquen and Yoel Forterre. A non-local rheology for dense granular flows. *Philosophical Transactions of the Royal Society of London A: Mathematical, Physical and Engineering Sciences*, 367(1909):5091–5107, December 2009.

[242] Vincent Mansard, Lydéric Bocquet, and Annie Colin. Boundary conditions for soft glassy flows: slippage and surface fluidization. *Soft Matter*, 10(36):6984–6989, August 2014.

[243] Howard A Barnes. A review of the rheology of filled viscoelastic systems. *Rheology reviews*, pages 1–36, 2003.

[244] Colin D. Cwalina and Norman J. Wagner. Rheology of non-Brownian particles suspended in concentrated colloidal dispersions at low particle Reynolds number. *Journal of Rheology (1978-present)*, 60(1):47–59, January 2016.

[245] Colin D. Cwalina, Kelsey J. Harrison, and Norman J. Wagner. Rheology of cubic particles suspended in a Newtonian fluid. *Soft Matter*, 12(20):4654–4665, May 2016.

[246] Yasaman Madraki, Sarah Hormozi, Guillaume Ovarlez, Élisabeth Guazzelli, and Olivier Pouliquen. Enhancing shear thickening. *Physical Review Fluids*, 2(3):033301, March 2017.

[247] Maxime Liard, Nicos S. Martys, William L. George, Didier Lootens, and Pascal Hebraud. Scaling laws for the flow of generalized Newtonian suspensions. *Journal of Rheology (1978-present)*, 58(6):1993–2015, November 2014.

[248] C. C. Furnas. Grading Aggregates - I. - Mathematical Relations for Beds of Broken Solids of Maximum Density. *Industrial & Engineering Chemistry*, 23(9):1052–1058, September 1931.

[249] R Ben Aim and P Le Goff. Effet de paroi dans les empilements désordonnés de sphères et application à la porosité de mélanges binaires. *Powder Technology*, 1(5):281–290, 1968.

[250] JA Dodds. The porosity and contact points in multicomponent random sphere packings calculated by a simple statistical geometric model. *Journal of colloid and interface science*, 77(2):317–327, 1980.

[251] Francois De Larrard. *Concrete mixture proportioning: a scientific approach*. CRC Press, 1999.

[252] Vu, Guillaume Ovarlez, and X. Chateau. Macroscopic behavior of bidisperse suspensions of noncolloidal particles in yield stress fluids. *Journal of Rheology*, 54(4):815–833, June 2010.

[253] François de Larrard and Thierry Sedran. Mixture-proportioning of high-performance concrete. *Cement and Concrete Research*, 32(11):1699–1704, November 2002.

[254] D. J. Highgate and R. W. Whorlow. Rheological properties of suspensions of spheres in non-Newtonian media. *Rheologica Acta*, 9(4):569–576, November 1970.

[255] N. Ohl and W. Gleissle. The characterization of the steady state shear and normal stress functions of highly concentrated suspensions formulated with viscoelastic liquids. *Journal of Rheology*, 37(2):381–406, March 1993.

[256] Yamina Abdesselam. *Rhéologie des plastisols et leurs procédés d'enduction*. PhD thesis, 2016.

[257] Dilhan M. Kalyon and Seda Aktaş. Factors Affecting the Rheology and Processability of Highly Filled Suspensions. *Annual Review of Chemical and Biomolecular Engineering*, 5(1):229–254, 2014.

[258] P. Yaras, Prof D. M. Kalyon, and U. Yilmazer. Flow instabilities in capillary flow of concentrated suspensions. *Rheologica Acta*, 33(1):48–59, January 1994.

[259] M. D. Haw. Jamming, Two-Fluid Behavior, and "Self-Filtration" in Concentrated Particulate Suspensions. *Physical Review Letters*, 92(18):185506, May 2004.

[260] Sunilkumar Khandavalli and Jonathan P. Rothstein. The effect of shear-thickening on the stability of slot-die coating. *AIChE Journal*, 62(12):4536–4547, December 2016.

[261] Dennis J. Coyle. Knife and Roll Coating. In Stephan F. Kistler and Peter M. Schweizer, editors, *Liquid Film Coating*, pages 539–571. Springer Netherlands, 1997. DOI: 10.1007/978-94-011-5342-3_15.

[262] Timothy M. Sullivan and Stanley Middleman. Roll Coating in the Presence of a Fixed Constraining Boundary. *Chemical Engineering Communications*, 3(6):469–482, November 1979.

[263] T. Bauman, T. Sullivan, and S. Middleman. Ribbing Instability in Coating Flows: Effect of Polymer Additives. *Chemical Engineering Communications*, 14(1-2):35–46, February 1982.

[264] F. Varela López, L. Pauchard, M. Rosen, and M. Rabaud. Non-Newtonian effects on ribbing instability threshold. *Journal of Non-Newtonian Fluid Mechanics*, 103(2):123–139, March 2002.

[265] Quentin Barral. *Superposition d'écoulements orthogonaux dans des fluides complexes: mise en place de l'expérience, application aux suspensions et aux fluides à seuil*. PhD thesis, Paris Est, 2011.

BIBLIOGRAPHY

Résumé

Nous étudions des suspensions concentrées de particules non-colloïdales de PVC. Ces suspensions, appelées plastisols, sont utilisées principalement pour la fabrication de revêtements de sols.

Elles présentent notamment un phénomène de rhéoépaississement (hausse de la viscosité en cisaillant). Nous montrons que cela provient des forces de frottement entre particules. En effet, à l'aide d'un microscope à force atomique, nous sommes pour la 1ère fois capable de relier directement la contrainte macroscopique d'apparition du rhéo-épaississement à la contrainte microscopique d'apparition de la friction solide entre particules.

Nous caractérisons la viscosité de la suspension jusqu'à 10^5 s^{-1} et nous observons qu'une plus grande polydispersité limite le rhéoépaississement. Les différences de contraintes normales N_1 et N_2 sont aussi mesurées. Par ailleurs, des mesures à l'aide de rayons X ou d'ultrasons ne montrent aucune migration de particules sous cisaillement.

Nous montrons également que la géométrie a un fort impact sur l'écoulement de la suspension concentrée. Un entrefer plus petit provoque une baisse de la viscosité et retarde le rhéoépaississement. Une approche non-locale permet de rationaliser les résultats.

La substitution de particules de PVC par des particules de $CaCO_3$ modifie profondément la viscosité et la densité d'empilement maximum. Nous développons alors des modèles simples pour modéliser ces effets. En outre, nous mesurons l'impact sur la rhéologie d'un éventuel surfactant à la surface des particules.

Nous avons pu finalement étudier des instabilités observées en étalant ces suspensions à haute vitesse. Une instabilité de surface est d'abord observée. A plus haute vitesse, un dépôt se forme en aval sur le couteau. Nous corrélons ces instabilités avec l'apparition de différences de contraintes normales.

Mots Clés

Suspensions concentrées, rhéologie, rhéoépaississement, PVC, différences de contraintes normales, instabilité d'écoulement

Abstract

Highly concentrated and non-colloidal suspensions consisting of micrometric PVC particles dispersed in a liquid phase, were studied. These suspensions, called plastisol, are mostly used in vinyl flooring manufacture.

A key feature of these suspensions is shear-thickening, since viscosity greatly increases as a function of the applied shear rate. This phenomenon is explained as being related to frictional forces between particles. Indeed, using an Atomic Force Microscope, we were able, for the first time, to link the macroscopic stress, at which shear-thickening appears, with the microscopic stress needed to enter a frictional regime.

We then characterize the suspension viscosity up to 10^5 s^{-1}. We observed that shear thickening is lowered with a more polydisperse powder. Large normal stress differences N_1 and N_2 were also measured, along with shear thickening. In addition, using both X-ray radiography and ultrasound, no particle migration in the sheared suspension could be detected.

We also found that geometry plays a major role in the features of the flow of concentrated suspensions. For a smaller gap, the viscosity is lower and shear-thickening is pushed to higher shear rates. A non-local approach accounts for our experimental results.

Replacing a number of PVC particles with $CaCO_3$ particles changes both the viscosity and the maximum packing fraction quite dramatically. For both of these, we developed simple models that matched quite well with the experimental data. Moreover, we elucidate the rheological changes resulting from adding surfactant at the surface of each particle type.

Finally, we investigated some instabilities observed while coating at high speed. At a moderate speed, a ribbing phenomenon appears. At a higher speed, a deposit is formed on the knife (downstream). The appearance of these instabilities correlates with normal stress differences

Keywords

Concentrated suspensions, rheology, shear-thickening, PVC, normal stress differences, flow instability